



# UNIVERSITY OF MANITOBA

## Magnetic Fields and Ultracold Neutron Production

Studies Towards the Future Neutron Electric Dipole Moment Experiment at TRIUMF

by

Taraneh Andalib

A Thesis submitted to the Faculty of Graduate Studies of

The University of Manitoba

in partial fulfilment of the requirements of the degree of

Doctor of Philosophy

Department of Physics and Astronomy  
University of Manitoba  
Winnipeg

Copyright © 2018 by Taraneh Andalib



# Abstract

The existence of a non-zero neutron Electric Dipole Moment (nEDM) confirms the theoretical models of Physics beyond the Standard Model which provide extra sources of CP violation. Based on Sakharov Criteria, CP violation is one of the main ingredients to create the baryon asymmetry in the universe. The current upper limit of the neutron EDM was found to be  $3.0 \times 10^{-26}$  e·cm, which is below the theoretical models predictions. As a result, there is a worldwide quest to find a finite nEDM.

The typical experimental method to measure the nEDM uses the Ultracold Neutrons (UCN) and employs Ramsey method of separated oscillatory fields. In this method, the Larmor precession frequency of UCN is measured in the presence of aligned Electric and Magnetic fields orientations. Such precision measurements require high UCN statistics and very stable and homogeneous magnetic fields. The work presented in this thesis is focused on these two aspects of the future nEDM measurement at TRIUMF.

The TUCAN's (TRIUMF UltraCold Advanced Neutron source) collaboration goal is to measure the nEDM to the sensitivity level of  $10^{-27}$ . For this measurement, the  $< 1$  pT magnetic stability requirement could be met by using magnetic shields with high magnetic permeability ( $\mu$ ), such as Mumetal, to nullify the external magnetic fields. However, external sources such as ambient temperature fluctuations could give rise to a change in the magnetic properties such as  $\mu$ . The result of the temperature dependence of  $\mu$  measurements and related simulations are presented here. These measurements set a limit on the temperature control level for the future nEDM measurement at TRIUMF.

The TUCAN collaboration's goal is to design a next-generation UCN source to increase the UCN statistics and reach the required nEDM sensitivity. In 2016, the vertical UCN source that was previously developed at RCNP was shipped to TRIUMF. In 2017 the first UCN experiments were conducted with the source. The status of the current UCN facility at TRIUMF and the result of the first UCN production tests are presented here.



# Contents

<b>1</b>	<b>Introduction</b>	<b>1</b>
1.1	History of Fundamental Symmetries . . . . .	1
1.2	Baryon Asymmetry of the Universe . . . . .	2
1.3	Neutron Electric Dipole Moment and Symmetry Breaking . . . . .	3
1.4	Ultracold Neutrons . . . . .	4
1.5	Superthermal UCN sources . . . . .	7
1.5.1	Basic Idea of Superthermal UCN Sources . . . . .	7
1.5.2	UCN Production by Superfluid $^4\text{He}$ . . . . .	8
1.5.3	UCN production by Solid Deuterium . . . . .	14
1.5.4	Comparison between sD <sub>2</sub> and superfluid helium sources . . . . .	19
1.5.5	Other UCN Sources [60–62] . . . . .	19
1.6	Current Status of UCN sources Worldwide . . . . .	20
1.7	Summary . . . . .	22
<b>2</b>	<b>Future nEDM Measurement at TRIUMF</b>	<b>23</b>
2.1	Ramsey Method of Separated Oscillating Fields . . . . .	24
2.2	Statistical and Systematic Errors . . . . .	25
2.2.1	Statistical Sensitivity . . . . .	25
2.2.2	Systematic Errors . . . . .	25
2.3	TRIUMF nEDM Components . . . . .	26
2.3.1	New UCN Source . . . . .	26
2.3.2	UCN Handling and Transport . . . . .	26
2.3.3	Magnetic Components . . . . .	28
2.3.4	EDM Cells and High Voltage System . . . . .	32
2.3.5	Comagnetometry . . . . .	32
2.4	nEDM Status Worldwide . . . . .	33
<b>3</b>	<b>Temperature Dependence of Magnetic Permeability</b>	<b>37</b>
3.1	Sensitivity of Internally Generated Field to Permeability of the Shield $B_0(\mu)$ . . . . .	38
3.2	Measurements of $\mu(T)$ . . . . .	40
3.2.1	Previous Measurements and their Relationship to nEDM Experiments . . . . .	40
3.2.2	Axial Shielding Factor Measurements . . . . .	42
3.2.3	Transformer Core Measurements . . . . .	48
3.3	Relationship to nEDM experiments . . . . .	52
3.4	Conclusion . . . . .	53

<b>4 Current UCN Facility at TRIUMF</b>	<b>55</b>
4.1 UCN Beam-line (BL1U) . . . . .	55
4.2 Tungsten Spallation Target . . . . .	58
4.3 Vertical UCN Source at TRIUMF . . . . .	59
4.3.1 Neutron D <sub>2</sub> O Moderators . . . . .	59
4.3.2 Helium Circulation and Superfluid Helium Condensation . . . . .	60
4.4 Data Acquisition System . . . . .	62
4.5 UCN Detectors . . . . .	64
4.5.1 <sup>6</sup> Li Detector . . . . .	64
4.5.2 <sup>3</sup> He Detector . . . . .	66
<b>5 UCN Production and Detection</b>	<b>69</b>
5.1 UCN Cycle of Measurement . . . . .	69
5.2 Data Quality Checks . . . . .	71
5.3 UCN Count Measurements . . . . .	73
5.3.1 UCN Yield Versus Proton Beam Current . . . . .	74
5.3.2 UCN Yield Versus Target Irradiation Times . . . . .	76
5.3.3 UCN Yield Versus Isopure Helium Temperature . . . . .	76
5.3.4 Steady-state UCN Production . . . . .	78
5.3.5 UCN Yield Over the Experiment Period . . . . .	78
5.4 UCN Storage Lifetime . . . . .	80
5.4.1 Storage Lifetime Versus Beam Current and Irradiation Time . . . . .	81
5.4.2 Storage Lifetime Versus Isopure Helium Temperature . . . . .	82
5.4.3 Storage Lifetime Over Experimental Period . . . . .	82
5.5 PENTtrack Simulations . . . . .	84
5.5.1 UCN Guide Diffusivity . . . . .	84
5.5.2 UCN Yield and Storage Lifetime Simulations . . . . .	85
5.5.3 Heater Test Versus Proton Beam Current . . . . .	88
5.6 Summary . . . . .	90
<b>6 Conclusion</b>	<b>93</b>
<b>Appendices</b>	<b>95</b>
<b>A Review of Quantum Mechanics [153]</b>	<b>97</b>
A.1 Spin-1/2 Particle in a Magnetic Field . . . . .	97
A.2 Larmor precession . . . . .	98
A.3 Effect of RF Pulses and NMR Lineshape . . . . .	99
<b>B Derivation of Ramsey's Method [153]</b>	<b>103</b>
<b>C Geometric phase effect [153]</b>	<b>109</b>
C.1 Geometric phase effect as a Bloch-Siegert shift . . . . .	109
C.1.1 T <sub>1</sub> ,T <sub>2</sub> , GPE redux . . . . .	112
C.1.2 Why is it called a geometric phase? . . . . .	113
<b>D Vertical Source Gas Flow Diagram</b>	<b>117</b>

<b>E Heat Conductivity in Superfluid Helium [156]</b>	<b>119</b>
E.0.1 Theoretical Models . . . . .	121
E.1 Measurement Result . . . . .	121
<b>References</b>	<b>125</b>



# List of Figures

1.1	The phase diagram of $^4\text{He}$ . Here the normal fluid phase or He-I and the superfluid phase or H-II are shown. . . . .	9
1.2	[43] Dispersion relation of superfluid helium (c) and of the free neutron (a). Neutrons with $E \simeq 1$ meV and wavenumber $q \simeq 0.7/\text{\AA}$ can excite a single phonon with the same energy and momentum and be downscattered to UCN energy range. The UCN production rate (b)(circles) shows the dominance of this single phonon process with respect to multiphonon processes at higher momentum $q$ . . . . .	10
1.3	The energy spectrum of the incident cold neutron flux from three sources compared to the dynamic scattering function $S(q, \omega = \frac{\alpha k^2}{2}) / \text{meV}$ as a function of $q / \text{\AA}$ . . . . .	12
1.4	[42] Multiphonon scattering function at SVP (Saturated Vapour Pressure) and 20 bar. The extrapolation to short wavelength of Korobkina <i>et al.</i> [41] at SVP is linear in $k$ , whereas the calculation of Schott <i>et al.</i> [48] is based on the static structure factor of the superfluid helium. The data point ( $A$ ) is taken from Ref. [49]. The one-phonon peaks are indicated by vertical arrows: SVP (dotted line) and 20 bar (solid line). . . . .	13
1.5	UCN production cross-section of sD <sub>2</sub> with 98% ortho concentration. UCN energy range 0-150 neV inside the solid D <sub>2</sub> . Solid line: cross-section calculated in incoherent approximation. Dashed line: one-quasi-particle contribution. Dotted line: two-quasi-particle contribution. □: data from measurements at PSI [55]. . . . .	16
1.6	[52] $S(q, \omega)$ ( $q = Q, \omega = E$ ) (arb. units) of 95.2% solid o-D <sub>2</sub> at $T = 4$ K. Data from IN4 measurements. Black parabola: dispersion of the free neutron. . . . .	16
1.7	[52] UCN production cross-section solid o-D <sub>2</sub> of 95.2% [52]. A UCN energy range of 0-150 neV inside the solid D <sub>2</sub> is assumed. Sample: fast frozen solid deuterium ( $T = 4$ K); data from IN4 measurements. Blue □: $E_0 = 17.2$ meV. Red filled ○: $E_0 = 67$ meV, ■: direct UCN production data from measurements at PSI [55]. . . . .	17
1.8	[52] Calculated UCN production rate of sD <sub>2</sub> with 98% ortho concentration for different Maxwellian neutron spectra with effective neutron temperature $T_n$ . UCN energy range:0-150 neV inside the sD <sub>2</sub> . Neutron capture flux $10^{14} / \text{cm}^2 \text{s}$ . Solid line: total production rate (one- and two- particle excitations). Dashed line: one-particle production rate. Dotted line: two-particle production rate. . . . .	18

- |     |  |    |
|-----|--|----|
| 1.9 | [58] Left- Data points are measured sD <sub>2</sub> lifetimes as a function of temperature, with the para-fraction fixed at 2.5%. Only the statistical errors are shown. Solid lines show the predicted temperature dependence. The dashed line is the predicted effect of departure from the solid lifetime model due to the upscattering from the D <sub>2</sub> gas in the guide. Right- sD <sub>2</sub> lifetimes as a function of para-fraction for all of the data taken below 6 K. The solid line is the model prediction of the para-fraction dependence at an average temperature of 5.6 K. . . . .               | 18 |
| 2.1 | Ramsey method of separated oscillating fields. Left shows the scheme of a measurement procedure and right shows the data points. The blue points are the UCN counts with the spin up and the red points are the UCN with spin down (data from the PSI-nEDM collaboration). The width at half height $\Delta\nu$ of the central fringe is approximately $1/2T$ , the four vertical lines indicate the working points (see text). . . . .  | 24 |
| 2.2 | Conceptual design of the proposed UCN source and nEDM experiment. Protons strike a tungsten spallation target. Neutrons are moderated in the LD <sub>2</sub> cryostat and become UCN in a superfluid <sup>4</sup> He bottle, which is cooled by another cryostat located farther downstream. UCN pass through guides and the superconducting magnet (SCM) to reach the nEDM experiment located within a magnetically shielded room (MSR). Simultaneous spin analyzers (SSA's) detect the UCN at the end of each nEDM experimental cycle. . . . .   | 27 |
| 2.3 | The 3D model of the proposed UCN source and the LD <sub>2</sub> cryostat. Protons strike a tungsten spallation target liberating neutrons, which are moderated in surrounding volumes of graphite (not shown), D <sub>2</sub> O, and LD <sub>2</sub> . Neutrons are downscattered in the UCN production volume containing superfluid <sup>4</sup> He. They are bottled within a horizontal guide up to a UCN valve. When the valve is opened, UCN are transported to room temperature UCN guides. . . . .  | 28 |
| 2.4 | A 3D model of the UCN delivery and the future nEDM experiment at TRI-UMF. UCN exit the source by passing through the SCM spin polarizer, and UCN switch and detector system, where they then enter the proposed nEDM experiment. UCN are loaded into the measurement cells within a MSR/coil system. At the end of the measurement cycle, UCN are counted by simultaneous spin analyzers (SSA's) including detectors. An ambient magnetic compensation system, and thermally controlled room, will surround the nEDM apparatus (not shown). For scale, the innermost layer of the MSR is a 1.8 m side-length cube. . . . . | 29 |
| 2.5 | Schematic drawing for the TUCAN nEDM magnetics. From outside in: The active compensation system followed by several layers of magnetically shielded room and passive shields nullify the environmental magnetic field. The magnetometers inside the active shielding monitor the changes in the magnetic field internal to that region. The internal coil system ( $B_0$ and $B_1$ coils) generate the magnetic fields for the Ramsey cycle. The UCN and the co-magnetometers are internal to the coils. . . . .   | 30 |
| 2.6 | The prototype active compensation system at the University of Winnipeg. . . . .  | 31 |

2.7	Three layers of the prototype passive magnetic shield at the University of Winnipeg. The 4th layer is not shown in this picture. . . . .	32
2.8	3D drawing of the double EDM cell with vacuum chamber and UCN guides	33
2.9	The history of the nEDM measurements [93] . . . . .	34
3.1	Upper: Magnetic field at the coil center as a function of magnetic permeability of the surrounding magnetic shield for a geometry similar to the ILL nEDM experiment as discussed in the text. Lower: $\frac{\mu}{B_0} \frac{dB_0}{d\mu}$ vs. permeability. The solid curve is the exact calculation for the ideal spherical coil and shield from Ref. [113]; the dashed curve is the approximation of Eq. 3.2. The circles and squares are the FEMM-based simulations for the spherical and solenoidal geometries with discrete currents. Since the spherical simulation was in agreement with the calculation, it is omitted from the lower graph. For the exact calculation and the two simulations, currents were chosen to give $B_0 = 1 \mu\text{T}$ at $\mu_r = 20,000$ . . . . .	39
3.2	The hysteresis or $B - H$ curve. Some commonly used terminology is shown. $H_c$ or coercivity is a measure of the ability of the material to withstand external magnetic fields and is at $B = 0$ . Initial permeability or $\mu_i$ is the slope of the initial magnetization curve. The initial magnetization or idealization curve is achievable after degaussing the high $\mu$ material. . . . .	41
3.3	(color online) Axial shielding factor measurement setup. The witness cylinder with an inner diameter of 5.2 cm and a length of 15.2 cm is placed inside a solenoid (shown in red) with a diameter of 30.8 cm and a length of 35.5 cm, containing 14 turns. The thickness of the witness cylinder is $1/16'' = 0.16 \text{ cm}$ . The loop coil (shown in blue) is mechanically coupled to the witness cylinder and has a diameter of 9.7 cm. . . . .	44
3.4	Ambient temperature and shielded magnetic field amplitude, measured over a 70 hour period. (a) temperature of the witness cylinder as a function of time. (b) magnetic field amplitude measured by fluxgate at center of witness cylinder vs. time. (c) magnetic field vs. temperature with linear fit to data giving $\frac{1}{B_s} \frac{dB_s}{dT} = -0.75\%/\text{K}$ (evaluated at $23^\circ\text{C}$ ). In panels (d), (e), and (f), the same quantities are shown for a 20-hour run with a copper cylinder in place of the witness cylinder with the linear fit giving $\frac{1}{B_s} \frac{dB_s}{dT} = -0.03\%/\text{K}$ . . . . .	46
3.5	Photograph of a witness cylinder showing transformer windings (left) and schematic of the transformer measurement (right). The primary coil was driven by the sine-out of an SR830 lock-in amplifier, which was also used to demodulate induced voltage $V(t)$ in the secondary coil. The driving current $I(t)$ was sensed by measuring the voltage across a stable $1 \Omega$ resistor. . . . .	49
3.6	$\dot{B}_{m,X}$ and $\dot{B}_{m,Y}$ as a function of amplitude of the applied $H_m$ field at 1 Hz. Points show the acquired data. Curves display the simulation based on the model described in the text. . . . .	50
4.1	A map of TRIUMF. The UCN facility is located at the Meson Hall area shown in Blue. . . . .	56
4.2	TRIUMF cyclotron and the three beam-lines. . . . .	56
4.3	The kicker, septum and dipole (bender) magnets define the front two sections of BL1U. . . . .	57

4.4	UCN beam structure. The top graph shows the 120 $\mu\text{A}$ BL1A in 1 ms period of beam followed by a 50-100 $\mu\text{s}$ of no beam. The middle graph shows the same beam-line when the kicker magnet is on. The bottom graph shows the 1/3 of the beam that goes to the UCN area. . . . .	57
4.5	Two quadrupole magnets which focus the proton beam onto a 12 cm thick tungsten spallation target, located inside a hermetically-sealed target crypt. Also shown is the UCN shielding pyramid, which encases both the spallation target and the UCN source, and is designed to meet the dose rate requirements specified by the TRIUMF Safety Group. . . . .	58
4.6	(a) Tungsten Target Blocks from the spallation target at KEK. The target blocks are plated with tantalum. (b) Present design for the tungsten spallation target at the TRIUMF UCN facility. The target blocks have a cross-section of $5.7 \times 7.8 \text{ cm}^2$ , and thicknesses of 2.0, 2.0, 3.0, and 5.0 cm, respectively. . . . .	59
4.7	Schematic diagram of the vertical UCN source at TRIUMF. Spallation neutrons are moderated in warm D <sub>2</sub> O vessel and become cold neutrons in Iced D <sub>2</sub> O. The cold neutrons then enter the superfluid helium bottle where they become UCN by phonon excitations in the superfluid. The isotopically pure superfluid helium is cooled down to below 1 K via a <sup>3</sup> He pot. The <sup>3</sup> He pot is cooled down to 0.7 K via the 1 K pot and further pumping (see text for more details). . . . .	60
4.8	A photograph of the UCN experimental area during the mini shutdown in October 2017. Some experimental components are shown and are labeled. The yellow concrete blocks are blocking the radiation during the target irradiation times. The vertical UCN cryostat could be seen because of the removal of some radiation shielding. . . . .	61
4.9	The 4 K reservoir filling during the cool down test in April 2017. . . . .	61
4.10	A photograph of the PLC in the meson hall. The grey terminal blocks are used to connect the signal from the devices to the computing modules. The first two top rows include the computing modules. Each sensor is connected to a specific terminal on a specific module. The bottom row is where the power supplies and the fuses are positioned. . . . .	63
4.11	EPICS thermal screen. The approximate location of each temperature sensor is shown. The thermal screen is intended to contain all the information about temperatures, and controls for compressors and heaters. . . . .	64
4.12	TUCAN MIDAS web interface . . . . .	65
4.13	3D drawing of the <sup>6</sup> Li detector and its enclosure. The enclosure is made of Al, and the rim of the adapter flange which UCN can hit is coated with 1 $\mu\text{m}$ Ni by thermal evaporation. . . . .	66
4.14	<sup>3</sup> He detector and paraffin blocks for neutron moderation. . . . .	67
5.1	Schematic drawing of a simple UCN source. $V_1$ is the production volume with $N_1$ number of UCN, $V_2$ is the secondary volume where $N_2$ number of UCN exist, and $V_3$ is the detector with $N_3$ number of UCN. . . . .	69
5.2	The UCN source and the guide geometry at TRIUMF . . . . .	71

5.3	The figure shows the UCN rate at 60 s irradiation time, and 1 $\mu\text{A}$ beam current. In this case, the UCN gate valve is opened immediately after the end of target irradiation. At this time, the UCN rate reaches the peak of about 2000 UCN/s. The UCN rate decays down to the background level. The valve is left open for 120 s. . . . .	71
5.4	PSD versus $Q_L$ for all of the PMTs for a standard 1 $\mu\text{A}$ proton beam current and 60 s target irradiation time . . . . .	72
5.5	Number of UCN events for each channel. The total number of UCN events decrease as we move towards the corner channels. . . . .	73
5.6	Three measurement cycles for 1 $\mu\text{A}$ beam current, 60 s irradiation time, and 0 s valve open delay time. The dashed lines show the start of the target irradiation, the dotted lines show the end of the irradiation and the valve open time for each cycle and the solid lines show the end of a cycle, which is the valve close time. . . . .	74
5.7	The total UCN counts versus the applied proton beam current. The labels show the full range of the superfluid helium temperature for that measurement. The dashed line is the fit to the UCN counts at low beam currents. . . . .	75
5.8	Zoomed in screenshot of the EPICS temperature monitoring screen 4.11. TS11 is located at the UCN heat exchanger bottom, TS12 is located at the UCN double tube bottom, TS14 is located at the heat exchanger double tube top and TS16 is located at the UCN double tube top. For further information about the source schematic see Section 4.3 . . . . .	76
5.9	Number of UCN extracted from the source after irradiating the target for different times with different beam currents. The dashed lines extrapolate the data for irradiation times below 60 s using exponential saturation curves. The labels show the saturation time constant for each beam current. . . . .	77
5.10	UCN yield versus the superfluid helium temperature. At a particular UCN counts, there are several values for the temperature of the superfluid helium. This is due to the discrepancy in the temperature sensor readings as described in the text. . . . .	77
5.11	UCN rate at the steady-state production mode with 0.3 $\mu\text{A}$ proton beam current. The UCN rate reaches a constant value of 450 UCN counts/s. . . . .	78
5.12	The UCN rate at 3 $\mu\text{A}$ beam current at 10 min irradiation time at the steady-state mode of operation. The UCN valve is left open throughout the measurement cycle. Quickly after the start of the target irradiation the UCN rate in the detector goes up. The target irradiation creates a heatload on the cryostat and the superfluid helium. This gives rise to a slow temperature increase in the source. As a result, the UCN rate goes down due to the higher upscattering rate. . . . .	79
5.13	The temperature of the superfluid helium (TS12) for the steady state mode of operation at 3 $\mu\text{A}$ beam current and 10 min target irradiation. After the irradiation stops, the temperature starts to decrease. . . . .	79
5.14	The total UCN counts extracted from the source for 1 $\mu\text{A}$ beam current and 60 s irradiation time at different days during the experimental run. . . . .	80
5.15	UCN cycles at different valve open delay times for 1 $\mu\text{A}$ beam current and 60 s target irradiation time. . . . .	81

5.16 The total UCN counts at different valve open delay times for 1 $\mu\text{A}$ beam current and 60 s irradiation time. The red line is the one exponential fit.	81
5.17 Storage lifetime in the source at different irradiation times and proton beam currents. Different markers refer to different target irradiation times. At longer irradiation times and higher beam currents, the storage lifetime decreases due to the increased heat load in the source, and an increase in the superfluid helium temperature. . . . .	82
5.18 Storage lifetime of UCN at different isopure helium temperatures. In this experiment, the temperature of the superfluid helium was set using heater tapes around the UCN bottle. The vertical axis shows the storage lifetime in seconds and the horizontal axis shows the superfluid helium temperature in Kelvin. As the temperature increases, the storage lifetime decreases. This is due to higher upscattering rate in the superfluid helium at higher temperatures. . . . .	83
5.19 Storage lifetime of the source over the experimental run. A 2% daily decrease in the storage lifetime is observed possibly due to the contamination in the source after opening the UCN valve. . . . .	83
5.20 UCN rate with two exponential fit shown in red. The rise time and fall time are labeled. . . . .	86
5.21 Comparison of fall time $\tau_2$ in the experimental data and the simulations with different diffuse-reflection probabilities. The boxes indicate the second and third quartile of the experimental data. The empty circle indicates its average. . . . .	86
5.22 Comparison of rise time $\tau_{\text{rise}}$ in experimental data and simulations with different diffuse-reflection probabilities. The boxes indicate the second and third quartile of the experimental data. The empty circles indicate the average. . . . .	87
5.23 MCNP model of the source. Red dots indicate the temperature sensors used to determine the temperature of the superfluid. . . . .	88
5.24 Number of UCN extracted from the source at different superfluid helium temperatures after irradiating the target with 1 $\mu\text{A}$ proton beam current for 60 s(filled circles). The lines are interpolations of simulated data to guide the eye. . . . .	89
5.25 Storage lifetime of UCN in the source at different superfluid helium temperatures (filled circules). The lines are interpolations of simulated data to guide the eye. . . . .	89
5.26 Histogram of measured UCN rates and temperatures from all four temperature sensors while the target is continuously irradiated with the UCN valve open. The simulated data (empty squares and triangles) slightly overestimate the UCN rate. The lines are interpolations of simulated data to guide the eye. . . . .	90
5.27 Steady-state UCN production data for 1.5 $\mu\text{A}$ proton beam current. The top graph shows the UCN rate over time, the middle graph shows the superfluid helium temperature (TS12) over time and the bottom graph shows the ${}^3\text{He}$ flow rate versus time. Detail provided in text. . . . .	91

A.1	The solid blue line shows the probability of the transition from spin-up to spin-down with $\omega_1 t = \pi$ . The dashed line shows the envelope of the transition probability, which is the simply $1/(1+x^2)$ . . . . .	102
B.1	The graph above shows the transition probability of spin down using Ramsey technique of separated oscillating fields. In this graph $T = 8\tau$ and $b\tau = \frac{\pi}{4}$ . . . . .	107
C.1	Effective magnetic field in the rotating coordinate system . . . . .	111
D.1	Gas flow diagram for the vertical UCN source . . . . .	117
E.1	The heat conductivity function of the Van Sciver and HEPAK models. The vertical axis shows the temperature gradient along the channel and the horizontal axis shows the input heat flux [156]. The arrows on the graph indicate the temperature of the superfluid helium . . . . .	122
E.2	The comparison between the April heater test data and the Van Sciver theoretical model of heat conductivity. The lines show the Van Sciver model's heat conductivity function at different superfluid helium bath temperatures. The black data points show the measured raw data of the heater tests. The blue points are the the values where the Joule-Thomson effect is considered and its heat input is added to the raw data plus the calculated background heat. The red points show the raw data with the assumed 50 mW background heat input. . . . .	123
E.3	Theoretical model of Van Sciver for the superfluid helium heat conductivity at different temperature ranges and the November heater test data. The vertical axis shows the temperature difference between the base and the saturation temperature for temperature sensors. The horizontal axis shows the heat input from the heaters plus the background heat. . . . .	124



# List of Tables

1.1	Symmetry properties of all bilinear covariants . . . . .	4
1.2	Symmetry properties of different components of the EDM Hamiltonian . . . . .	4
1.3	Commonly used names for neutrons in different energy ranges and their corresponding velocity, temperature and wavelenght . . . . .	5
1.4	Candidates for a superthermal source . . . . .	20
1.5	Existing and future UCN sources worldwide. The existing or proposed sources at the following sites is listed: Institut Laue-Langevin (ILL) in France, Reasearch Center for Nuclear Physics (RCNP) in Japan, KEK and J-PARC in Japan, TRIUMF in Canada, Petersburg Nuclear Physics Institute (PNPI) in Russia, Los Alamos National Lab (LANL), PULSTAR and SNS in the US, Mainz and FRM II in Germany. . . . .	21
3.1	Summary of data acquired for the AC axial shielding factor measurements, in chronological order. Data with an applied field of $\sim 1 - 6\mu T$ and a measurement frequency of 1 Hz are included. Data which used daily fluctuations of the temperature from 21-24°C over a 10-80 hour period are included. Other data acquired for systematic studies are not included in the table. . . . .	47
3.2	Summary of OPERA and FEMM simulations and shielding factor measurements, resulting in extracted temperature slopes of $\mu$ . . . . .	48
3.3	Summary of data acquired for the transformer core measurements. Three different witness cylinders, arbitrarily labeled $\alpha$ , $\beta$ , and $\gamma$ , were used for the measurements. A 1 Hz excitation frequency was used with amplitudes for $H_m$ ranging from 0.1 to 0.3 A/m. Fluctuations in the temperature ranged from 21-24°C and measurement times over a 10-80 hour period are included. Other data acquired for systematic studies are not included in the table. . . . .	52
4.1	Properties of the glass scintillators . . . . .	65
5.1	Material parameters used in PENTrack simulation. [145–147] . . . . .	85
E.1	The heater power, and the base and saturation temperatures from the temperature sensors in the superfluid helium, and in the $^3\text{He}$ pot, for the April and November heat tests [156] . . . . .	120



# Chapter 1

## Introduction

The work presented in this thesis is focused on the two important factors for successfully measuring the neutron Electric Dipole Moment (nEDM) at TRIUMF. Those include having a very stable magnetic field environment as well as high Ultra Cold Neutron (UCN) statistics. The TRIUMF Advanced Ultracold Neutron source (TUCAN) collaboration's goal is to measure the nEDM to the  $10^{-27}$  e·cm sensitivity level.

This chapter provides some information on why nEDM is interesting to measure and how finding a nonzero nEDM would answer questions regarding the matter-antimatter or Baryon asymmetry of the universe. Chapter 2 gives a brief description of the future nEDM measurement at TRIUMF and its experimental setup components. The method of measurement is also presented in that chapter. Chapter 3 is focused on the work towards the temperature dependence of magnetic permeability  $\mu$  which helps to set an upper limit on the temperature stability of the nEDM measurement setup. Chapter 4 presents the current UCN facility at TRIUMF where the first UCN were produced with the vertical UCN source that was built at RCNP. Chapter 5 presents the result of those measurements with UCN. The final remarks and notes are available in chapter 6.

### 1.1 History of Fundamental Symmetries

Over the last few decades the interest in the invariance of the discrete symmetries has been increased. Such studies revealed the internal structure of the elementary particles and helped develop the underlying theories.

There are three significant symmetries in physics as Charge conjugation ( $C$ ), Parity ( $P$ ) and Time-reversal ( $T$ ).  $C$ -symmetry simply describes physical laws under a charge-conjugation transformation. Parity transformation, is simply the inversion of spatial coordinates and Time-reversal transformation is changing the direction of time. Tests of Charge  $C$ ,  $P$  and  $T$  symmetries established the structure of the Standard Model (SM) [1].

In 1956, fall of discrete symmetries started with the famous  $\theta - \tau$  paradox in the K-mesons decay. The paradox was that two particles previously known as  $\theta^+$  and  $\tau^+$ , which had the same mass and lifetime, decayed into products with different parities

$$\begin{aligned}\theta^+ &\rightarrow \pi^+ + \pi^0 \\ \tau^+ &\rightarrow \pi^+ + \pi^+ + \pi^-.\end{aligned}\tag{1.1}$$

At first, it was assumed that the initial states should also have different parities, but precise measurements revealed that this is not the case. Yang and Lee suggested that

the paradox is originated from a  $P$  violation in the weak interactions [2]. Immediately after, an experimental search was suggested by Ramsey for Parity violation in the  $\beta$  decay of Co-60. Within a few months,  $P$  violation was demonstrated by three different experiments [3–5]. After the observation of  $P$  violation, Landau showed that Electric Dipole Moments (EDMs) are forbidden by  $T$  symmetry [6] and then it was suggested that  $T$  symmetry should also be checked experimentally [7].

One of the most fundamental symmetries in physics is the  $CPT$  (Charge-Parity-Time) symmetry. The simultaneous operation of  $C$ ,  $P$  and  $T$  leave the system unchanged. To date, there is no experimental evidence for  $CPT$  symmetry breaking. Because of the  $CPT$  invariance, breakdown of  $CP$  symmetry should be accompanied by violation of Time-reversal symmetry.

A finite EDM provides a good source of  $CP$  violation. EDMs caused by  $CP$  violation in the Standard Model are negligible. But most extensions of the Standard Model such as supersymmetry naturally produce EDMs that are comparable to or larger than the present experimental limits.

The search for EDMs can be traced back to 1950, when Purcell and Ramsey tested the possibility of finding EDMs for particles and nuclei. Smith, Purcell and Ramsey started an experiment to search for neutron EDM  $d_n$ , and they achieved the upper limit of  $d_n < 5 \times 10^{-20} \text{ e} \cdot \text{cm}$  [8]. Over the years, the upper limit on the neutron EDM has been improved by many orders of magnitude. Measurement of particle EDMs provide some of the tightest constraints on the extensions to the Standard Model to probe  $CP$  violation. The most recent upper limit on the neutron EDM is found to be  $|d_n| < 3.0 \times 10^{-26} \text{ e} \cdot \text{cm}$  [9].

## 1.2 Baryon Asymmetry of the Universe

The neutron EDM provides a highly sensitive diagnostic for  $CP$  violation, which is an important element for the observed baryon asymmetry in the universe. The dominance of matter over antimatter in the universe can be characterized by [10]

$$\eta = \frac{n_b - \bar{n}_b}{n_\gamma} \simeq 6 \times 10^{-10} \quad (1.2)$$

where  $n_b$  is the number of baryons,  $\bar{n}_b$  is the number of anti-baryons and  $n_\gamma$  is the number of photons in the Cosmic Microwave Backgorund.

It is possible to assume that, maybe, the universe is baryon symmetric in a very large scale, and it is split into regions that are made of only baryons or anti-baryons. If that was the case, an excess of gamma rays in between these separated regions was expected to be observed due to annihilation. But, even in the least dense regions of the space, there is hydrogen gas cloud.

### Sakharov criteria

There are three key ingredients needed to create baryon asymmetry known as Sakharov conditions [11]:

- Baryon number violation
- $C$  and  $CP$  violation

- Departure from the thermal equilibrium.

The first condition is obvious. It simply means, in a reaction, if the net baryon number is zero, there would be no baryon asymmetry. In the reactions that violate baryon number, if there is no  $C$  and  $CP$  violations, the net baryon number would be zero, and this is because, the reactions that create excessive baryons will be counter-balanced by the reactions that create excessive anti-baryons. [12]. The third condition is essential for a net nonzero baryon asymmetry, since the equilibrium average of  $B$  vanishes. Sakharov suggested that baryogenesis took place immediately after the big bang, at a temperature not far below the Planck scale of  $10^{19}$  GeV, when the universe was expanding so rapidly that many processes were out of thermal equilibrium [13].

## 1.3 Neutron Electric Dipole Moment and Symmetry Breaking

A permanent nEDM is an intrinsic property of a neutron. This fundamental property is a measure for the separation of positive and negative charges internal to the neutron. However, no nEDM has been measured so far.

The interaction of a the EDM  $d$  of a spin-1/2 particle with the electromagnetic field strength  $F_{\mu\nu}$  in the relativistic invariant form can be written as

$$H_d = \frac{d}{2} \bar{\psi} \gamma_5 \sigma_{\mu\nu} \psi F_{\mu\nu} . \quad (1.3)$$

Similarty, the interaction of a magnetic moment with the electromagnetic field strenght  $F_{\mu\nu}$  is

$$H_d = \frac{\mu}{2} \bar{\psi} i \sigma_{\mu\nu} \psi F_{\mu\nu} . \quad (1.4)$$

To study the transformation properties of the Hamiltonian, it is interesting to see how all bilinear covariants behave under discrete symmetries transformation. In four-vector notation, the parity operator as a  $4 \times 4$  matrix is

$$p = \begin{pmatrix} 1 & 0 & 0 & 0 \\ 0 & -1 & 0 & 0 \\ 0 & 0 & -1 & 0 \\ 0 & 0 & 0 & -1 \end{pmatrix} , \quad (1.5)$$

the time-reversal symmetry is

$$p = \begin{pmatrix} -1 & 0 & 0 & 0 \\ 0 & 1 & 0 & 0 \\ 0 & 0 & 1 & 0 \\ 0 & 0 & 0 & 1 \end{pmatrix} . \quad (1.6)$$

The transformation of all bilinear covariants is listed in Table 1.3.

The interaction of a nonrelativistic neutron with the electromagnetic field can be descibed by the follwoing hamiltonian

$$H = -\boldsymbol{\mu}_n \cdot \mathbf{B} - \mathbf{d}_n \cdot \mathbf{E} \quad (1.7)$$

	current	P	C	T
Scalar	$\bar{\psi}_1 \psi_2$	$\eta_1 \eta_2^* \bar{\psi}_1 \psi_2$	$\xi_1 \xi_2^* \bar{\psi}_1 \psi_2$	$\zeta_1 \zeta_2^* \bar{\psi}_1 \psi_2$
Vector	$\bar{\psi}_1 \gamma_\mu \psi_2$	$\eta_1 \eta_2^* \bar{\psi}_1 \gamma_\mu \psi_2$	$-\xi_1 \xi_2^* \bar{\psi}_1 \gamma_\mu \psi_2$	$-\zeta_1 \zeta_2^* \bar{\psi}_1 \gamma_\mu \psi_2$
Tensor	$\bar{\psi}_1 \sigma_{\mu\nu} \psi_2$	$\eta_1 \eta_2^* \bar{\psi}_1 \sigma_{\mu\nu} \psi_2$	$-\xi_1 \xi_2^* \bar{\psi}_1 \sigma_{\mu\nu} \psi_2$	$-\zeta_1 \zeta_2^* \bar{\psi}_1 \sigma_{\mu\nu} \psi_2$
Pseudo-vector	$\bar{\psi}_1 \gamma_\mu \gamma_5 \psi_2$	$-\eta_1 \eta_2^* \bar{\psi}_1 \gamma_\mu \gamma_5 \psi_2$	$\xi_1 \xi_2^* \bar{\psi}_1 \gamma_\mu \gamma_5 \psi_2$	$\zeta_1 \zeta_2^* \bar{\psi}_1 \gamma_\mu \gamma_5 \psi_2$
Pseudo-scalar	$\bar{\psi}_1 \gamma_5 \psi_2$	$-\eta_1 \eta_2^* \bar{\psi}_1 \gamma_5 \psi_2$	$\xi_1 \xi_2^* \bar{\psi}_1 \gamma_5 \psi_2$	$\zeta_1 \zeta_2^* \bar{\psi}_1 \gamma_5 \psi_2$

Table 1.1: Symmetry properties of all bilinear covariants

where  $\boldsymbol{\mu}_n$  is the magnetic moment of the neutron interacting with the magnetic field  $\mathbf{B}$ , and  $\mathbf{d}_n$  is the electric dipole moment of the neutron interacting with the electric field  $\mathbf{E}$ .

The properties of the Hamiltonian under discrete symmetries is summarized in Table 1.3. Based on this, the first term is *CP*-even and *T*-even, and the second term is *cp*-odd and *T*-odd. Because of the *CPT*-invariance, a nonzero EDM may exist if both Parity and Time-reversal symmetries are broken.

	C	P	T
<b>B</b>	-	+	-
<b>E</b>	-	-	+
<b><math>\mu</math></b>	-	+	-
<b>d</b>	-	+	-

Table 1.2: Symmetry properties of different components of the EDM Hamiltonian

The nEDM measurement technique and a breif survey of the current nEDM measurement sites worldwide are presented in chapter 2.

## 1.4 Ultracold Neutrons

The measurement of the nEDM is strongly correlated with having high neutron statistics. Table 1.4 shows the energy regime of neutrons and their corresponding velocity, temperature and de Broglie wavelength via

$$E = \frac{1}{2}mv^2 = \frac{3}{2}k_B T = \frac{h^2}{2m\lambda^2} \quad (1.8)$$

where  $m$  is the mass of the neutron,  $v$  is the neutron velocity,  $k_B$  is the Boltzmann constant,  $T$  is the equivalent temperature,  $h$  is the Planck's constant and  $\lambda$  is the de Broglie wavelength.

Ultracold Neutrons (UCN) are neutrons with kinetic energies  $\lesssim 300$  neV corresponding to a velocities of  $\lesssim 8$  m/s or temperatures  $\lesssim 3$  mK. UCN move so slowly that they

Name	Energy $E$	Velocity $v$	Temperature $T$	Wavelength $\lambda$
Fast	10 MeV	$4.4 \times 10^7$ m/s	$7.7 \times 10^{10}$ MK	9.0 pm
Thermal	0.0254 eV	$2.2 \times 10^3$ m/s	290 K	0.2 nm
Cold	1 meV	500 m/s	8 K	3 nm
Ultracold	300 neV	8 m/s	3 mK	50 nm

Table 1.3: Commonly used names for neutrons in different energy ranges and their corresponding velocity, temperature and wavelength

can populate traps made of matter, magnetic, and gravitational fields, and could be stored and manipulated for several hundreds of seconds in such traps. Because of their properties, UCN are a valuable tool for precise measurements in fundamental physics.

High precision studies of neutrons and their interactions provide important data for the particle physics and cosmology. In addition, they enable sensitive searches for new physics. Examples of the experiments using UCN, which aim to discover new physics, are searches for a permanent electric dipole moment (EDM) of the neutron [14–18], precision measurements of the neutron lifetime [19–23], and  $\beta$ -decay correlation parameters [24, 25], as well as quests for dark matter candidates [26, 27], axion-like particles [28–30], Lorentz invariance violations [31] and the measurements of the quantum states of UCN in the gravitational field of the earth [32].

Neutron is an electrically neutral hadron and it participates in all four fundamental interactions as described below.

### The Gravitational Interaction

A neutron has a mass of  $m_n \approx 940$  MeV/c<sup>2</sup>, and therefore, it has a potential in the Earth's gravitational field as

$$V_g = mgh. \quad (1.9)$$

Here  $h$  is the vertical displacement and  $g = 9.8$  m/s<sup>2</sup> is the acceleration due to the Earth's gravitational field. In experiments using thermal or cold neutrons, the effects of gravity can usually be negligible due to the short survival times of the neutrons. However, with the UCN experiments, since they are confined for up to several hundred of seconds, gravity has a significant influence.

Here

$$mg = 102 \text{ neV/m} \quad (1.10)$$

which is comparable to the UCN kinetic energy. This means, a UCN of energy 200 neV can rise by at most 2 m.

### The Weak Interaction

The weak interaction governs the radioactive  $\beta$ -decay of neutrons. UCN decay into a proton, an electron, and an electron antineutrino via

$$n \longrightarrow p + e^- + \bar{\nu}_e. \quad (1.11)$$

The value of the neutron lifetime sets the maximum time constant with which UCN can be stored. The current value of the neutron lifetime is  $880.2 \pm 1.0$  s [33].

## The Electromagnetic Interaction

Neutron is an electrically neutral, spin-1/2 particle that possesses a magnetic dipole moment due to its internal structure through which it interacts with a magnetic field  $\mathbf{B}$  as

$$V_m = -\boldsymbol{\mu}_n \cdot \mathbf{B} \quad (1.12)$$

where

$$|\boldsymbol{\mu}_n| = 60 \text{ neV/T}. \quad (1.13)$$

In an inhomogeneous magnetic field, UCN experience a force described by

$$\mathbf{F}_m = -\nabla V_m = \pm |\boldsymbol{\mu}_n| \nabla \mathbf{B}. \quad (1.14)$$

In the nEDM measurements, the interaction of UCN with the magnetic field is used to polarize UCN and to measure its polarization at the end of the measurement cycle (see Section 2.1). In Eqn. 1.14, the sign  $\pm$  corresponds to the relative orientation between the magnetic moment and the magnetic field. UCN of anti-parallel spin to the magnetic field (magnetic moment parallel) are called *high field seekers*, have negative  $V_m$ , accelerate towards strong magnetic fields, and are attracted to it. UCN with parallel spin (and thus magnetic moment anti-parallel) to the magnetic field, are called *low field seekers*, have positive  $V_m$ , and are repelled by the magnetic field.

Eqn. 1.14 is true only if UCN move adiabatically through the magnetic field. This condition will be fulfilled when the Larmor precession frequency of UCN is smaller than the changes in the magnetic field in the rest frame of UCN. However, since UCN have low speeds, this condition is easily fulfilled. If the UCN spin adiabatically traces the magnetic field, it will be fully polarized, which can be achieved by passing UCN through a strong  $\sim 6$  T magnetic field.

## The strong Interaction

Neutrons and protons are bound in the nucleus by the strong interaction. However, this interaction has a short range and it only affects the neighbouring nuclei. The Woods-Saxon potential approximately describes the nucleons interaction inside the atomic nucleus

$$V(r) = -\frac{V_0}{1 + \exp\left(\frac{r-R}{a}\right)} \quad (1.15)$$

where  $V_0$  represents the potential well depth,  $a$  represents the surface thickness of the nucleus and  $R = r_0 A^{1/3}$  where  $r_0 = 1.25$  fm and  $A$  is the mass number. For neutrons and protons the depth is  $V \approx -40$  MeV. The UCN energy and their binding energy and the depth of the potential differ by many orders of magnitude. As a result, it is not possible to use perturbation theory to describe neutron scattering. Fermi realized that it is possible to introduce an equivalent potential which can be used to calculate the small changes in the wavefunction outside the range of the interaction by the perturbation theory.

The interaction of an incident neutron with a liquid or a solid could be described by sum of  $\delta$  functions

$$V(r) = \frac{2\pi\hbar^2}{m_N} \sum_i a_i \delta(r - r_i) \quad (1.16)$$

where  $m_N$  is the mass of neutron,  $r_i$  is the position of  $i$ th nucleus and  $a_i$  is the scattering length with the  $i$ th nucleus. This is the so-called Fermi pseudopotential. Because of UCN's large wavelength, this equation could be written as

$$V(r) = \frac{2\pi\hbar^2}{m_N} \sum_i N_i a_i \quad (1.17)$$

where  $N_i$  is the number density in the material  $i$ . In UCN physics, this potential is typically called neutron optical potential, since if the energy of the neutron is less than the optical potential  $E < V$  the neutron will be fully reflected from the material surface under any angle of incidence. This sets a limit on the UCN velocity.

UCN can be lost when it is reflected from the material walls. This is because of the upscattering in which UCN absorb energy or absorption in which UCN get absorbed by the nucleus of the reflecting material. To include the losses in the potential, the optical potential is usually written as

$$U(r) = V(r) - iW. \quad (1.18)$$

The ratio  $\eta = V/W$  is a measure of the loss per bounce probability of the material.

The strong interaction plays a crucial role in the nEDM measurements. Choosing certain materials enables us to store and guide UCN to the measurement cell. The highest known value for the optical potential is  $V_F = 335$  neV and is measured for  $^{58}\text{Ni}$ .

## 1.5 Superthermal UCN sources

In thermal UCN sources, neutrons are extracted from a distribution almost in thermal equilibrium with a moderation system. The UCN turbine source at the Institute Laue-Langevin (ILL) extracted very cold neutrons vertically from a cold source (liquid deuterium) and slowed them down using the mechanical action of a turbine [34, 35]. Here cold neutrons with velocities of  $\sim 40$  m/s are decelerated by reflection from a set of curved turbine blades moving with a velocity  $\sim 20$  m/s in the same direction as the neutrons. A UCN density of  $\sim 40$  UCN/cm<sup>3</sup> was achieved with this method [36, 37]. The current UCN density of this source is 110 UCN/cm<sup>3</sup> for neutrons with velocities  $< 7$  m/s[34].

In 1975 it was shown that, it is possible to achieve higher steady state UCN densities corresponding to temperatures much lower than the temperature of the moderator [38]. These are called superthermal converters. Here thermal or cold neutrons are inelastically scattered and transfer their kinetic energy to an excitation of the converter medium (e.g., to a phonon). Superthermal sources have the ability to provide much higher UCN densities (i.e., more UCN) than conventional sources such as the ILL turbine source. The best candidates for the superthermal converters to date are solid deuterium and liquid  $^4\text{He}$ .

### 1.5.1 Basic Idea of Superthermal UCN Sources

The mechanism of a superthermal UCN source is the following. An incident neutron can lose almost its entire energy in a single scattering event by creating excitations ( e.g., phonons) in a converter medium [36, 38]. Because of the loss in the kinetic energy, this process is called downscattering. The reverse process is called upscattering, where a UCN absorbs kinetic energy from the medium.

Consider a simple model for the medium as a two-level system with an energy gap  $E_0^*$ . A neutron can excite a quasi-particle from the lower state to the higher state by

transferring the energy  $E_0^*$ . A quasi-particle from the higher state can fall down to the lower state by transfer of the energy  $E_0^*$  to a neutron. The principle of detailed balance links the cross-section for upscattering  $\sigma(E_{\text{UCN}} \rightarrow E_{\text{UCN}} + E_0^*)$  and downscattering  $\sigma(E_{\text{UCN}} + E_0^* \rightarrow E_{\text{UCN}})$  [36]

$$\sigma(E_{\text{UCN}} \rightarrow E_{\text{UCN}} + E_0^*) = \frac{(E_{\text{UCN}} + E_0^*)}{E_{\text{UCN}}} e^{-\frac{E_0^*}{k_B T}} \sigma(E_{\text{UCN}} + E_0^* \rightarrow E_{\text{UCN}}) \quad (1.19)$$

where  $T$  is the temperature of the medium,  $E_{\text{UCN}}$  is the energy of the UCN, and  $k_B$  is the Boltzmann constant.

In general,  $\sigma(E_{\text{UCN}} + E_0^* \rightarrow E_{\text{UCN}})$  is practically independent of  $T$ , so that for  $E_0^* \gg k_B T \gg E_{\text{UCN}}$ , the upscattering cross-section for UCN can be made arbitrarily small by decreasing the temperature. If the converter is now placed in a neutron flux at a temperature  $T_n \geq E_0^*$ , there will be a significant number of downscattering events, and a negligible number of upscattering events.

If the converter is contained in a vessel whose walls are good UCN reflectors with potential  $V \gg V_m$ , where  $V_m$  is the UCN potential of the converter, and the walls are transparent to the neutrons of energy  $E_0^*$ , then UCN will build up in the moderator to a density until the rate of loss is equal to the rate of UCN production.

The steady-state UCN density in the source is given by

$$\rho_{\text{UCN}} = P_{\text{UCN}} \tau, \quad (1.20)$$

where  $P_{\text{UCN}}$  (UCN/cm<sup>3</sup>·s) is the UCN production rate, and  $\tau$  (s) is the UCN mean lifetime in the system. The mean lifetime  $\tau$  of the UCN in the vessel is restricted by a variety of possible loss mechanisms

$$\frac{1}{\tau} = \frac{1}{\tau_a} + \frac{1}{\tau_W} + \frac{1}{\tau_{up}} + \frac{1}{\tau_\beta}, \quad (1.21)$$

where  $1/\tau_a$  is the UCN absorption rate in the medium,  $1/\tau_W$  is the rate of the UCN loss on the walls,  $1/\tau_{up}$  is the neutron loss due to the upscattering in the medium and  $1/\tau_\beta$  is the  $\beta$ -decay losses.

Pure deuterium and liquid  ${}^4\text{He}$  are good candidates for superthermal conductors, possessing a balance of high production rate and small neutron absorption cross-section and upscattering rate.

### 1.5.2 UCN Production by Superfluid ${}^4\text{He}$

#### Superfluid ${}^4\text{He}$ Definition

${}^4\text{He}$  is an isotope of helium with two protons and two neutrons. It has an integer spin of zero, which makes it a boson. As a result, it follows the Bose-Einstein statistics. It has two liquid states known as He-I and H-II. The He-I phase is the normal fluid phase, and the He-II phase is the superfluid phase with zero viscosity, and zero entropy. Fig. 1.1 shows the phase transition diagram of  ${}^4\text{He}$ . The two phases are separated out by the  $\lambda$ -line. The phase transition happens at 2.172 K. Below the lambda line, the liquid can be described by the so-called two-fluid model, which consists of both phases. Below 1 K the liquid is mostly superfluid.

Because of its zero viscosity, superfluid helium has the ability to flow through very small capillaries or narrow channels without experience any friction at all. The flow of liquid helium along the surface is called film flow.

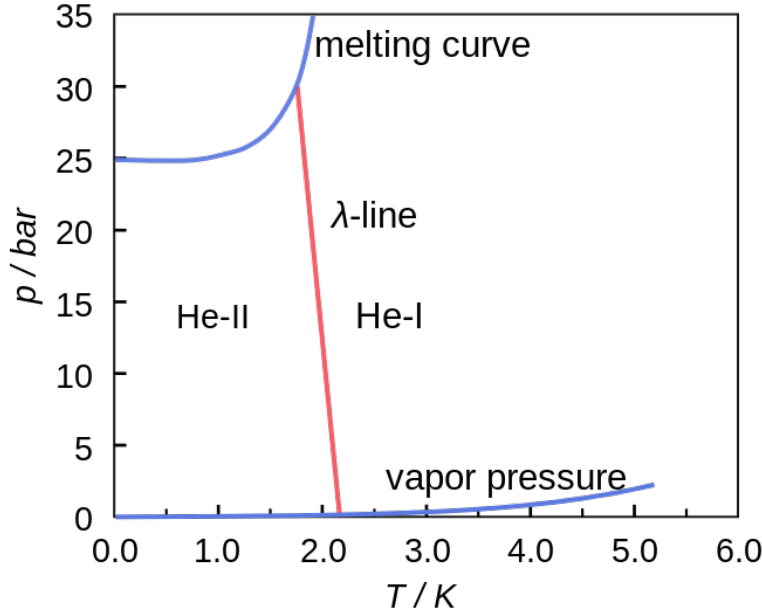


Figure 1.1: The phase diagram of  ${}^4\text{He}$ . Here the normal fluid phase or He-I and the superfluid phase or He-II are shown.

### Superfluid Helium Converter

The superfluid  ${}^4\text{He}$  is an attractive candidate as a UCN source, and was studied in Ref. [39]. It has zero neutron absorption cross-section, resulting in  $\tau_a \rightarrow \infty$ , which makes it a good candidate as a UCN source. In superfluid helium the upscattering losses become smaller than  $\beta$ -decay losses below  $T \sim 0.7$  K. The dominant production mechanism is the excitation of a single phonon at the crossing of the free neutron and phonon dispersion curves, with a momentum  $q \sim 0.7/\text{\AA}$  [40], and energy 1 meV corresponding to a neutron wavelength 8.9 Å. The availability of 8.9 Å cold neutrons is crucial and their flux must be maximized. There are two types of UCN sources based on superfluid helium: sources where experiment and source are combined in one apparatus, and the measurement is performed inside the superfluid helium, and extracted-UCN sources where the source is an apparatus on its own, and delivers neutrons to experiments at room temperature connected to it by UCN guides.

### UCN Production Rate with Single Phonon scattering in Superfluid helium [39, 41, 42]

UCN can be produced by one phonon excitation in superfluid helium when the energy of the incident neutrons is equal to that of the one phonon excitation in the medium. The incident neutrons then scatter down to UCN by creating one-phonon excitations in the converter medium. Fig. 1.2 shows the dispersion relation of the superfluid helium and a free neutron. A neutron at rest can absorb energy  $\hbar\omega$  and momentum  $\hbar q$  with

$$\omega = \frac{\hbar q^2}{2m}, \quad (1.22)$$

where  $m$  is the mass of the neutron. A neutron with this energy and momentum can come to rest after transferring its energy and momentum to the superfluid  ${}^4\text{He}$ . For

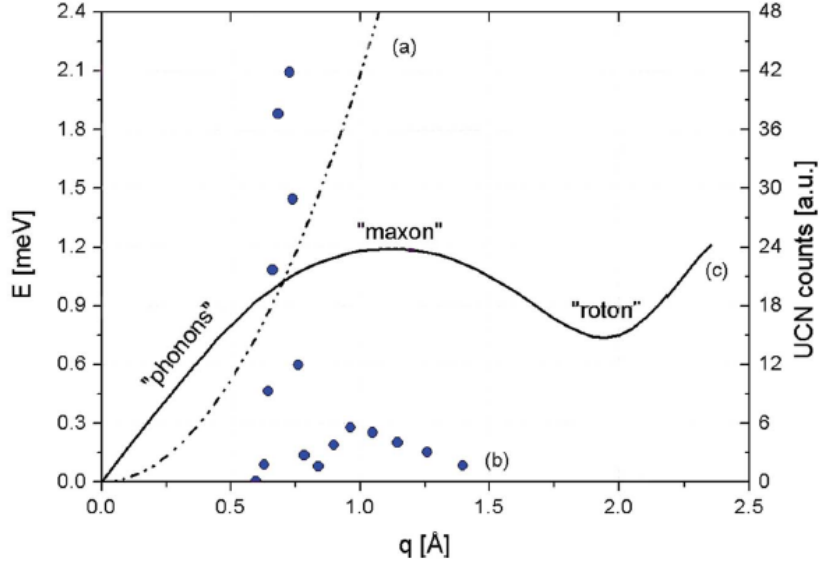


Figure 1.2: [43] Dispersion relation of superfluid helium (c) and of the free neutron (a). Neutrons with  $E \simeq 1$  meV and wavenumber  $q \simeq 0.7/\text{\AA}$  can excite a single phonon with the same energy and momentum and be downscattered to UCN energy range. The UCN production rate (b)(circles) shows the dominance of this single phonon process with respect to multiphonon processes at higher momentum  $q$ .

single phonon interactions, which are usually dominant, the superfluid can only exchange quantities of energy and momentum that are related by the dispersion curve

$$\omega = \omega(q) = cq, \quad (1.23)$$

where  $\omega$  is the energy of the phonon,  $q$  is the phonon's momentum, and  $c$  is the speed of sound in the moderator. The second equal sign in Eqn. (1.23) is an approximation to simplify the discussion. The neutrons can only come to rest by emission of a single phonon, if they have the resonant energy  $E_0^*$  given by the intersection of Eqns. (1.22) and (1.23)

$$\omega(q) = cq = \frac{\hbar q^2}{2m}, \quad (1.24)$$

and so

$$q^* = \frac{2mc}{\hbar}. \quad (1.25)$$

The differential cross-section for neutron scattering is given by the dynamic scattering function  $S(q, \omega)$ , which is the Fourier transform of the Van Hove correlation function  $G(r, t)$  in space and time of the superfluid helium [44]:

$$\frac{d\sigma}{d\omega} = b^2 \frac{k_2}{k_1} S(q, \omega) d\Omega, \quad (1.26)$$

where  $b$  is the bound neutron scattering length for  ${}^4\text{He}$ ,  $\hbar k_1$  is the momentum of the incident neutrons, and  $\hbar k_2 = \hbar k_{\text{UCN}}$  is the momentum of UCN. The quantity  $S(q, \omega)$  has been measured in great detail [45–47]. Performing the change of variables,

$$d\Omega = 2\pi \sin \theta d\theta = 2\pi \frac{qdq}{k_1 k_2} \quad (1.27)$$

gives

$$\frac{d\sigma}{d\omega} = 2\pi b^2 \frac{k_2}{k_1} S(q, \omega) \frac{qdq}{k_1 k_2} = 2\pi b^2 S(q, \omega) \frac{qdq}{k_1^2}. \quad (1.28)$$

This may effectively be integrated over the limits on  $q$  which are

$$k_1 - k_2 < q < k_1 + k_2. \quad (1.29)$$

Since

$$k_2 = k_{\text{UCN}} \ll k_1, \quad q \sim k_1, \quad (1.30)$$

we may write  $dq = 2k_{\text{UCN}}$ . This results in the cross-section being related to  $S(q, \omega)$  evaluated on the incident neutron's dispersion curve:

$$\frac{d\sigma}{d\omega} = 4\pi b^2 \frac{k_{\text{UCN}}}{k_1} S\left(k_1, \omega = \frac{\alpha k_1^2}{2}\right), \quad (1.31)$$

where  $\alpha = \frac{\hbar}{m} = 4.14 \text{ meV}/\text{\AA}^2$ , and  $S(q, \omega)$  assumed to be constant over the narrow range  $dq$ . The approximation

$$\omega = \frac{\hbar(k_1^2 - k_2^2)}{2m} = \frac{\alpha}{2}(k_1^2 - k_2^2) \approx \frac{\alpha}{2}k_1^2 \quad (1.32)$$

has also been used.

The UCN production rate is given by

$$P(E_{\text{UCN}})dE_{\text{UCN}} = N_{\text{He}} \int \frac{d\Phi(E_1)}{dE} \cdot \frac{d\sigma}{d\omega}(E_1 \rightarrow E_{\text{UCN}})dE_1 dE_{\text{UCN}}, \quad (1.33)$$

where  $\frac{d\Phi(E_1)}{dE}$  is the differential incident neutron flux,  $N_{\text{He}}$  is the atomic density in the liquid helium, and  $\frac{d\sigma}{d\omega}(E_1 \rightarrow E_{\text{UCN}})$  is the energy differential cross-section for the inelastic neutron scattering or the probability of the incident neutrons with energy  $E_1$  to scatter from the helium nucleus and become UCN. Then

$$\begin{aligned} \int_0^{E_c} P(E_{\text{UCN}})dE_{\text{UCN}} &= N_{\text{He}} 4\pi b^2 \alpha^2 \left[ \int \frac{d\Phi(k_1)}{dE} S\left(k_1, \omega = \frac{\alpha k_1^2}{2}\right) dk_1 \right] \int_0^{k_c} k_{\text{UCN}}^2 dk_{\text{UCN}} \\ &= N_{\text{He}} 4\pi b^2 \alpha^2 \left[ \int \frac{d\Phi(k_1)}{dE} S\left(k_1, \omega = \frac{\alpha k_1^2}{2}\right) dk_1 \right] \frac{k_c^3}{3} \text{ UCN/cm}^3 \text{s}, \end{aligned} \quad (1.34)$$

where  $E_c$  and  $k_c$  are the critical UCN energy and wave vector of the walls of the storage chamber. This way of writing the UCN production rate is more general, and it is useful to calculate the single phonon and multiphonon contributions to the UCN production rate. The one phonon production rate is found by evaluating Eqn. (1.34) over the one phonon peak ( $q^* = 0.7/\text{\AA}$ ). Thus

$$P_{\text{UCN}} = 9.44 \times 10^{-9} \frac{d\Phi(E_1^*)}{dE_1^*} \text{ UCN/cm}^3, \quad (1.35)$$

where  $E_1^*$  is the energy of the incident neutrons at the one phonon peak.

### Multiphonon Scattering Contribution in UCN Production in Superfluid helium [41, 42]

For polychromatic neutron sources, UCN can also be produced by multiphonon processes in superfluid  $^4\text{He}$ . Multiphonon production of UCN with various energy spectrum of the neutron flux has been studied in Ref. [41]. Fig. 1.3 shows the energy spectrum of neutron flux  $\frac{d\phi}{dE}$  for three sources as a function of momentum  $q$ , and are compared to the dynamic scattering function  $S(q, \omega = \hbar q^2/2m)$ . The peak at  $q = 0.7/\text{\AA}$  corresponds to the one phonon excitation by superfluid helium. The values of  $S$  above  $1.2/\text{\AA}$  are extrapolated. The value of  $S$  above  $2/\text{\AA}$  are essentially zero. The UCN production from one phonon and multiphonon processes have been calculated for three input neutron spectrums: SNS ballistic guide, PULSTAR MC flux and HMI polarized flux. The multiphonon contribution to the UCN production is calculated by using Eqn. (1.34), and calculating  $\int \Phi(E_1)S(k_1, \omega = \frac{\alpha k_1^2}{2})dk_1$ . The result showed that, for sources where helium is exposed to the total thermal flux or at a dedicated spallation source, the multiphonon contribution can amount to slightly more than a factor of 2 increase in the UCN production.

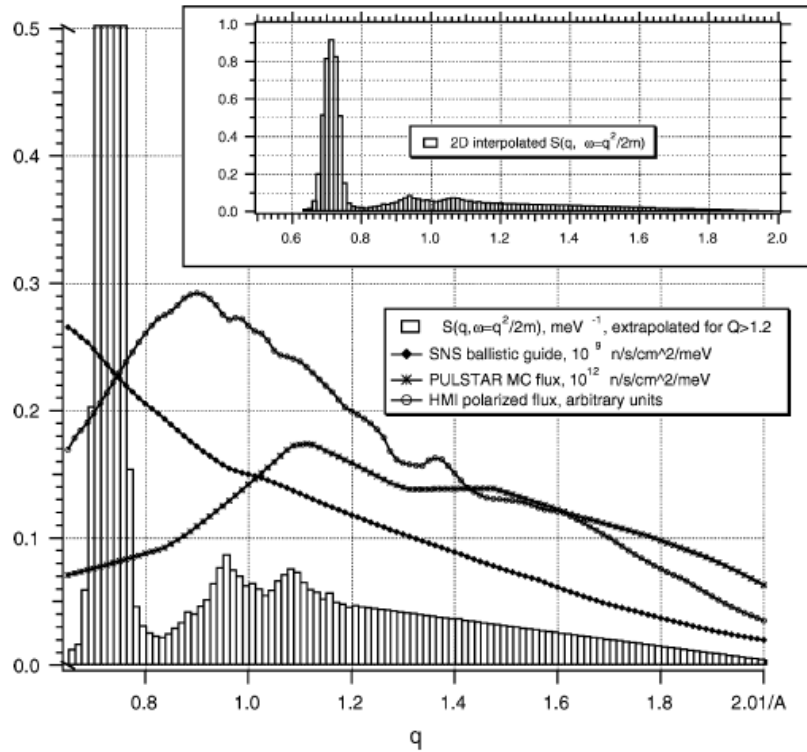


Figure 1.3: The energy spectrum of the incident cold neutron flux from three sources compared to the dynamic scattering function  $S(q, \omega = \frac{\alpha k_1^2}{2}) / \text{meV}$  as a function of  $q / \text{\AA}$ .

UCN production by multiphonon emission in superfluid helium under pressure is studied in Ref. [42]. The dynamic scattering function  $S(q, \omega)$  of the superfluid helium strongly depends on pressure, leading to a pressure-dependent differential UCN production rate. The expression for the multiphonon part of  $S$  describing UCN production is derived from the inelastic neutron scattering data. Application of pressure to superfluid helium in-

creases the velocity of sound, such that the dispersion curves of the  $^4\text{He}$  and of the free neutron cross at shorter neutron wavelength.

Since for neutron beams from a liquid deuterium cold source, the differential flux density  $\frac{d\Phi}{dE}$  in the range 8–9 Å normally increases for decreasing wavelength of the cold neutron flux, and also since pressure increases the density of He-II, it was expected to observe an increase in the single phonon UCN production rate, and different multiphonon contribution with pressure increase. It was observed that, both the single and the multiphonon scattering functions change with pressure. The single phonon excitation moves to a shorter wavelength (see Fig. 1.4) and the value for  $S$  decreases. It leads to a reduction in one-phonon UCN production. The multiphonon excitations increase with pressure, and the peak of the scattering function  $S$  moves to shorter incident-neutron wavelengths, see Fig. 1.4. However, the UCN production rate decreases with pressure increase. Only if the cold neutron flux at 8.3 Å exceeds by more than 2.5 times that at 8.9 Å, an increase in the UCN production rate may be expected. However, it has to be considered that the application of pressure requires a window for UCN extraction which causes severe UCN losses. Therefore, UCN production in superfluid helium under pressure is concluded not to be attractive.

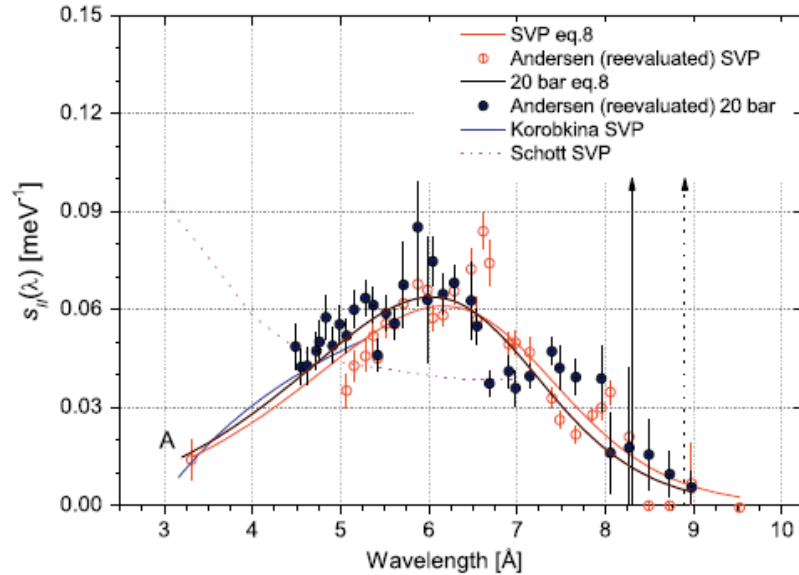


Figure 1.4: [42] Multiphonon scattering function at SVP (Saturated Vapour Pressure) and 20 bar. The extrapolation to short wavelength of Korobkina *et al.* [41] at SVP is linear in  $k$ , whereas the calculation of Schott *et al.* [48] is based on the static structure factor of the superfluid helium. The data point (*A*) is taken from Ref. [49]. The one-phonon peaks are indicated by vertical arrows: SVP (dotted line) and 20 bar (solid line).

### UCN upscattering and UCN lifetime in superfluid helium

Superfluid  $^4\text{He}$  has a zero neutron absorption cross-section, and if the converter is kept at sufficiently low temperatures (typically  $\lesssim 1$  K), thermal upscattering of UCN is sufficiently suppressed. This allows the produced UCN to survive in the converter for times dominated by the wall losses of the vessel, typically  $>100$  s [50].

The upscattering of neutrons is caused by the interactions between a neutron at rest, and excitations in superfluid helium at different temperatures. These excitations can be categorized in three groups: one phonon absorption, two-phonon scattering, and roton-phonon scattering. The total upscattering rate can be written as

$$\frac{1}{\tau_{up}} = \frac{1}{\tau_{1-ph}} + \frac{1}{\tau_{2-ph}} + \frac{1}{\tau_{rot-ph}}, \quad (1.36)$$

where

$$\frac{1}{\tau_{1-ph}} = Ae^{-(12K)/T} \quad (1.37)$$

is the one phonon absorption contribution,

$$\frac{1}{\tau_{2-ph}} = BT^7 \quad (1.38)$$

is the two-phonon scattering contribution (one phonon absorbed and one phonon emitted), and

$$\frac{1}{\tau_{rot-ph}} = CT^{3/2}e^{-(8.6K)/T} \quad (1.39)$$

is the contribution from roton-phonon scattering with the absorption of one roton followed by a phonon emission.

The values of  $A$ ,  $B$  and  $C$  are extracted from data for temperatures up to 2.4 K [50]. The comparison between the UCN production and upscattering rate to the theoretical temperature dependence of these processes showed that, the main contribution is from two-phonon scattering  $\frac{1}{\tau_{up}} = BT^7$  with  $B = (4 - 16) \times 10^{-3} /(\text{s K}^7)$  [50].

### 1.5.3 UCN production by Solid Deuterium

Solid deuterium ( $sD_2$ ) is a material with small absorption cross-section, small incoherent scattering cross-section (to minimize upscattering), and the presence of numerous phonon modes, which can inelastically scatter neutrons down to UCN energies. A converter based on  $sD_2$  should be operated at temperatures below 10 K in order to avoid subsequent upscattering of UCN by phonons within solid deuterium.

Solid deuterium has an almost perfect hcp crystal structure, when prepared under suitable conditions (low pressure and  $T > 5$  K). The  $D_2$  molecule has internal rotational modes, which are described by the rotational quantum number  $J$ . The rotational excitations give rise to additional modes in the solid deuterium. Deuterium in the states with even  $J$  is called ortho-deuterium ( $o-D_2$ ), whereas deuterium in the states with odd  $J$  is called para-deuterium ( $p-D_2$ ). An increase of the concentration of the  $p-D_2$  molecules leads to a larger neutron upscattering rate. Theoretically and experimentally, it has been shown that  $sD_2$  at sufficiently low temperatures (around 5K) with high enough purity and with high ortho concentration can be used to produce a high density UCN [51].

#### UCN Production Cross-Section and UCN Production Rate in Solid Deuterium [36, 52, 53]

The formula for the UCN production in solid deuterium is very similar to that of the superfluid helium shown in Eqn. (1.33), with replacing  ${}^4\text{He}$  atomic density  $N_{\text{He}}$  with

molecular density of solid deuterium  $N_{D_2}$ , and noting that in sD<sub>2</sub> the neutron scattering cross-section may be written as a sum of coherent and incoherent contributions:

$$\frac{d\sigma}{d\omega} = \left[ \frac{k_2}{k_1} b_{coh}^2 S_{coh}(q, \omega) + \frac{k_2}{k_1} b_{inc}^2 S_{inc}(q, \omega) \right] d\Omega. \quad (1.40)$$

In Ref. [52] the UCN production cross-section  $\sigma$  was determined by two ways. One way is the determination of the quasi-particle (phonons and rotational excitations of the D<sub>2</sub> molecule) density of states  $G_1(E)$  (incoherent approximation) from the measured neutron cross-section  $\frac{d\sigma}{d\omega}$ , and the other method is the direct integration of the dynamical neutron cross-section  $\frac{d\sigma}{d\omega}$  ( $\hbar = 1$ ) in the kinematical region along the free-neutron dispersion parabola.

**UCN production cross-section: Incoherent approximation.** With the knowledge of the quasi-particle density of states  $G_1(E)$ , it is possible to calculate the dynamical neutron cross-section  $\frac{d\sigma}{d\omega}$  (averaged over the scattering angle, thus  $q$ ). Vice versa it is also possible to extract  $G_1(E)$  from a measured dynamical neutron cross-section [54]. If  $G_1(E)$  is known, it is possible to calculate one-phonon and multiphonon contributions to the neutron cross-section  $\frac{d\sigma}{d\omega}$ .

The method for the determination of  $G_1(E)$  from the measured neutron scattering data in solid deuterium is studied in Ref. [53]. In the determination of  $G_1(E)$ , contributions of higher order multiphonons to  $\frac{d\sigma}{dE}$  are incorporated.

In the case of UCN production, the energy transfer of the downscattered neutron  $E = E_1 - E_{UCN}$  is approximately equal to the initial neutron energy  $E_1$  ( $E_{UCN} \ll E_1$ ,  $E_{UCN}$ : UCN energy). The total cross-section for UCN production can be calculated by

$$\sigma_{UCN}(E_1) = \int_0^{E_{UCN}^{max}} \frac{d\sigma(E_1)}{dE} dE_{UCN}. \quad (1.41)$$

The calculated cross-section shown in Fig. 1.5, is in agreement with data on UCN production using a cold neutron beam ( $E_1 \sim 1.4$  meV to 20 meV). Here the one-quasi-particle and two-quasi-particle excitations are included in the calculations. The UCN production cross-section is mainly determined by one-quasi-particle excitation for energies below 15 meV. The two-quasi-particle contribution is non-negligible in the region of 5-25 meV.

The application of the incoherent approximation in the case of sD<sub>2</sub> has certainly to be questioned since the sD<sub>2</sub> crystal scatters neutrons more coherently than incoherently.

**UCN production cross-section: Direct determination.** The easiest way of determining the cross-section for UCN production is the use of the dynamical scattering function  $S(q, \omega)$  in the  $(q, \omega)$ -phase space along the free-neutron parabola, as shown schematically in Fig. 1.6.

This method allows the incorporation of all the coherent and incoherent contributions to the UCN production cross-section. Possible coherent contributions, which cannot be treated exactly with the incoherent approximation, appear directly in the deduced cross-section. Therefore, this method is superior in principle to the result obtained by the incoherent approximation.

The UCN production cross-section can be determined by

$$\sigma_{UCN}(E_1) = \frac{\sigma_1}{k_1} S(k_1, E_1) \frac{2}{3} k_{UCN}^{max} E_{UCN}^{max}, \quad (1.42)$$

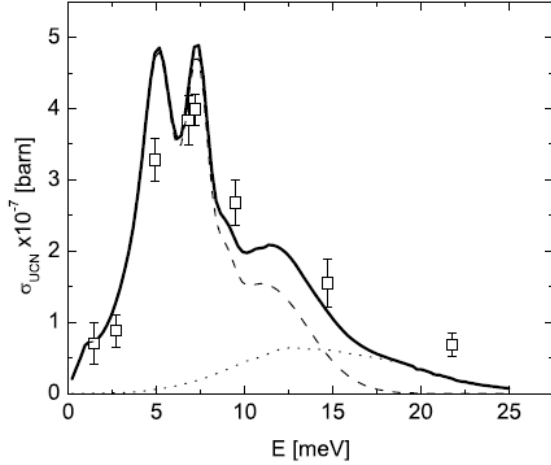


Figure 1.5: UCN production cross-section of sD<sub>2</sub> with 98% ortho concentration. UCN energy range 0-150 neV inside the solid D<sub>2</sub>. Solid line: cross-section calculated in incoherent approximation. Dashed line: one-quasi-particle contribution. Dotted line: two-quasi-particle contribution. □: data from measurements at PSI [55].

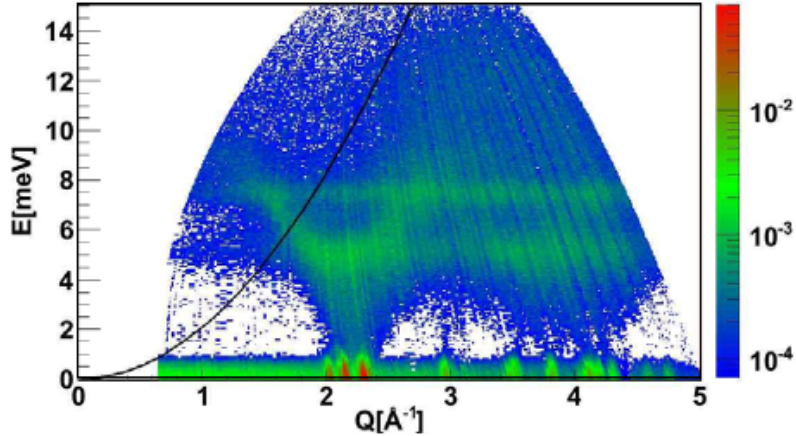


Figure 1.6: [52]  $S(q, \omega)$  ( $q = Q, \omega = E$ ) (arb. units) of 95.2% solid o-D<sub>2</sub> at  $T = 4$  K. Data from IN4 measurements. Black parabola: dispersion of the free neutron.

where  $E_1$  is the energy of the incoming neutrons in the downscattering process,  $\sigma_1$  is a constant, and  $k_{\text{UCN}}^{\max}$  and  $E_{\text{UCN}}^{\max}$  are the upper limits for the UCN momentum and energy. In order to obtain absolute cross-sections,  $S(q, \omega)$  has to be calibrated to absolute values. The result of this calibration and the determination of the UCN production cross-section as a function of the energy of the incoming neutrons, and a comparison with the measurements of this cross-section is shown in Fig. 1.7. This plot also contains the data, which were obtained with higher incoming-neutron energy ( $E_1 = 67$  meV).

The comparison of the calculated UCN production cross-section, extracted from the incoherent approximation and parabola method, shows (see Fig. 1.5 and Fig. 1.7) a discrepancy in the region of  $E \sim 6$  meV. The cross-section determined by the parabola method shows a pronounced maximum in the region of  $E \sim 6$  meV as compared to the incoherent approximation result. This peak corresponds to the coherent phonon

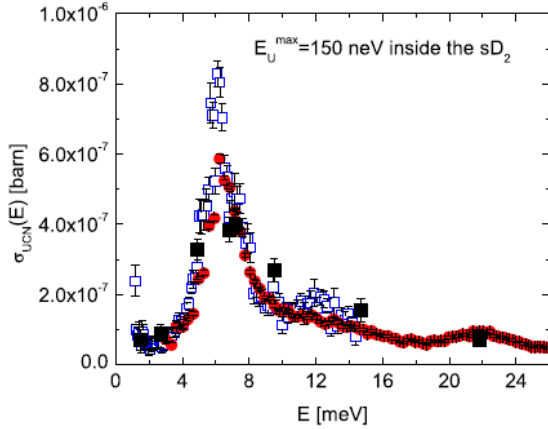


Figure 1.7: [52] UCN production cross-section solid o-D<sub>2</sub> of 95.2% [52]. A UCN energy range of 0–150 neV inside the solid D<sub>2</sub> is assumed. Sample: fast frozen solid deuterium ( $T = 4$  K); data from IN4 measurements. Blue  $\square$ :  $E_0 = 17.2$  meV. Red filled  $\circ$ :  $E_0 = 67$  meV,  $\blacksquare$ : direct UCN production data from measurements at PSI [55].

contribution to the UCN production cross-section. The double-peak structure in the UCN production cross-section by the incoherent approximation is not present in Fig. 1.7, and cannot be reproduced by the measured data shown in Figs. 1.5 and 1.7. This means, a new experiment at a more intense cold neutron beam with a better energy resolution would be desirable to study this effect further.

In Fig. 1.6, the parabola of the free neutron crosses the acoustical phonon dispersion curve at  $E \sim 6$  meV. At this point, the UCN production cross-section is predominantly determined by coherent scattering. This can explain a deviation from the production cross-section in incoherent approximation. Nevertheless, the general agreement of the incoherent approximation with the PSI data is remarkable (as shown in Fig. 1.5).

The result for the calculated UCN production rate in solid o-D<sub>2</sub>, exposed to a Maxwellian shaped neutron flux for different effective neutron temperatures is shown in Fig. 1.8. The main conclusion from these results was the new understanding of possible higher energetic loss channels (one-quasi-particle and two-quasi-particle) in solid deuterium for the downscattering of cold neutrons in the conversion process to UCN. The best value for the effective neutron temperature is in the region of  $T_n \sim 40$  K which is larger than what was previously expected ( $T_n \sim 30$  K [56]).

### UCN upscattering and UCN lifetime in sD<sub>2</sub> [57, 58]

The different molecular species, ortho-D<sub>2</sub> and para-D<sub>2</sub>, have significantly different UCN-phonon annihilation cross-sections [57]. The presence of even small concentrations of para-D<sub>2</sub> can dominate the upscattering rate which gives rise to reduced UCN lifetimes in the solid and orders of magnitude reduction in the achievable UCN density. In a D<sub>2</sub> solid, the populations of ortho and para states are typically determined by the ortho/para population of the gas phase before the D<sub>2</sub> is frozen into solid. After cooling down the D<sub>2</sub> to the solid phase ( $T \sim 6$  K), it normally takes months to reach the equilibrium of 99.999% o-D<sub>2</sub>. Since the elimination of para-D<sub>2</sub> is necessary to achieve UCN lifetimes comparable to the nuclear absorption time in solid deuterium, using a para-D<sub>2</sub> to ortho-D<sub>2</sub> converter

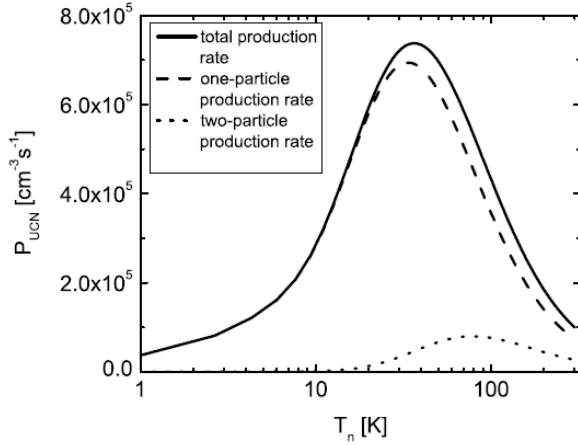


Figure 1.8: [52] Calculated UCN production rate of  $sD_2$  with 98% ortho concentration for different Maxwellian neutron spectra with effective neutron temperature  $T_n$ . UCN energy range: 0-150 neV inside the  $sD_2$ . Neutron capture flux  $10^{14} / \text{cm}^2 \text{s}$ . Solid line: total production rate (one- and two- particle excitations). Dashed line: one-particle production rate. Dotted line: two-particle production rate.

is crucial.

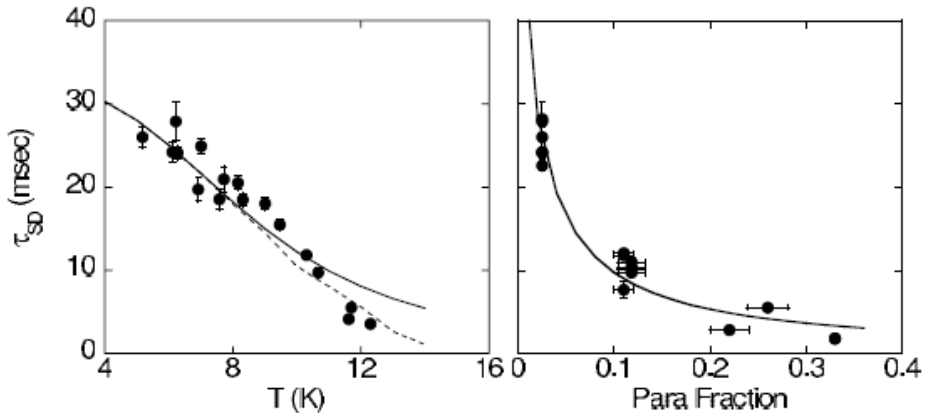


Figure 1.9: [58] Left- Data points are measured  $sD_2$  lifetimes as a function of temperature, with the para-fraction fixed at 2.5%. Only the statistical errors are shown. Solid lines show the predicted temperature dependence. The dashed line is the predicted effect of departure from the solid lifetime model due to the upscattering from the  $D_2$  gas in the guide. Right-  $sD_2$  lifetimes as a function of para-fraction for all of the data taken below 6 K. The solid line is the model prediction of the para-fraction dependence at an average temperature of 5.6 K.

The lifetime of the UCN in  $sD_2$  is limited by factors such as upscattering from phonons in the solid, upscattering from p- $D_2$  contamination, and absorption inside the vessel. Reducing the time UCN spend inside the  $sD_2$  can reduce the average absorption rate. This led to the proposal of a thin-film source where a thin layer of solid  $D_2$  coats the inside of a storage bottle that is embedded in a cold neutron flux [59]. The possibility

of a smaller source volume combined with the higher operating temperature of the thin film source offers significant technical simplification.

The UCN lifetime in the solid deuterium as a function of the temperature and para/ortho fractions has been measured [58]. The total loss rate can be written as

$$\frac{1}{\tau_{SD}} = \frac{1}{\tau_{phonon}} + \frac{1}{\tau_{para}} + \frac{1}{\tau_{Dabs}} + \frac{1}{\tau_{Habs}}, \quad (1.43)$$

where  $\frac{1}{\tau_{phonon}}$  is the upscattering rate from phonons in  $sD_2$ ,  $\frac{1}{\tau_{para}}$  is the upscattering rate from para deuterium molecules in the solid,  $\frac{1}{\tau_{Dabs}}$  is the upscattering rate from the absorption on deuterium and  $\frac{1}{\tau_{Habs}}$  is the upscattering rate from the absorption on the hydrogen impurities in the solid. The results for UCN lifetimes  $\tau_{SD}$  in  $sD_2$  as a function of the  $sD_2$  temperature and para/ortho fractions are shown in Fig. 1.9. The difference between the solid and dashed line demonstrates the need to include the effect of deuterium vapour in the guide on the lifetime at higher temperatures. With this correction, the measured lifetimes agree well with theoretical predictions of the upscattering rate.

#### 1.5.4 Comparison between $sD_2$ and superfluid helium sources

The main differences between  $sD_2$  and superfluid helium sources are the UCN lifetime and the UCN production rate. While UCN can stay in superfluid helium until it  $\beta$ -decays, UCN in solid deuterium are absorbed by the deuteron in 150 ms after they are produced. Once a superfluid helium source is cooled down to temperatures below 0.75 K, the upscattering rate is suppressed to a level comparable to neutron  $\beta$ -decay. Solid deuterium has a production rate two orders of magnitude greater than superfluid helium. Therefore, solid deuterium sources output higher UCN current compared to superfluid helium sources. However, the limiting production time in superfluid helium is four orders of magnitude longer than  $sD_2$ . Thus, even with a smaller UCN production rate, superfluid  $^4He$  can in principle achieve a UCN density larger than that of solid deuterium. The superthermal enhancement in solid deuterium is limited by the large nuclear absorption loss, and thus further cooling below 5 K will not significantly enhance the UCN yield.

#### 1.5.5 Other UCN Sources [60–62]

Superthermal UCN sources may be compared by

$$\sigma_s / \sigma_a, \quad (1.44)$$

where  $\sigma_s$  is the elastic scattering cross-section, and  $\sigma_a$  is the absorption cross-section. At low energies ( $< 1$  eV)  $\sigma_a \sim 1/v$  where  $v$  is the speed of the neutrons. This means, the absorption cross-section is much larger at lower energies. Table 1.4 shows a list of possible superthermal UCN sources [62]. The values of  $\sigma_a$  are for thermal neutrons.

Solid  $\alpha-^{15}N_2$  is a potential alternative to deuterium [60]. Its absorption cross-section is only 5% of that of  $D_2$ , and it has a negligible incoherent scattering cross-section. Additionally, rotation of the  $N_2$  molecules in the lattice is inhibited due to the anisotropy of the  $N_2$  inter-molecular potential. This leads to the dispersive modes for the rotational degrees of freedom (librons), which provide additional channels for neutron downscattering, and eliminates the rotational incoherent upscattering. Measurements [60] show that,

Isotope	$\sigma_a$ (barns)	$\sigma_s/\sigma_a$
$^2\text{D}$	0.000519	$1.47 \times 10^4$
$^4\text{He}$	0	$\infty$
$^{15}\text{N}$	0.000024	$2.1 \times 10^5$
$^{16}\text{O}$	0.00010	$2.2 \times 10^4$
$^{208}\text{Pb}$	0.00049	$2.38 \times 10^4$

Table 1.4: Candidates for a superthermal source

the production cross-section peaks near 6 meV, and the optimal incident cold neutron temperature is 40 K. It was found that, the variation in the cross-section is no more than 18% in the range from 5 to 25 K (increasing slightly with increasing temperature). The measured cross-section was found to be somewhat lower than that of D<sub>2</sub> and O<sub>2</sub>. A nitrogen-based source may benefit from operating at lower temperatures, if the upscattering cross-section can be further reduced at lower temperatures ( $\sim 1$  K) [60].

$^{208}\text{Pb}$  and solid deuterium have similar nuclear absorption cross-sections. The natural solid form of  $^{208}\text{Pb}$  would avoid the difficulties of growing cryogenic solids such as deuterium and oxygen. However, its heavy mass prevents the neutron momentum transfer to the solid phonon field. The heavy mass reduces the phonon creation cross-section by  $1/M$ . As a result, one would expect its UCN yield to be two orders of magnitude less than solid deuterium.

As other options, the properties of the new candidate converter materials including solid heavy methane (CD<sub>4</sub>) and solid oxygen (O<sub>2</sub>) have been investigated in the temperature range 8 K to room temperature by measuring the production of UCN from a cold neutron beam and the cold neutron transmission through the converter materials [61]. The liquid O<sub>2</sub>, D<sub>2</sub> and CD<sub>4</sub> have similar neutron scattering cross-sections.

$^4\text{He}$  and D<sub>2</sub> are still the best commonly pursued options, although there is a chance that other materials could lead to a breakthrough.

## 1.6 Current Status of UCN sources Worldwide

New UCN sources using superthermal technology are under development at various laboratories across the world. Neutrons are produced by two methods: proton-induced spallation off a heavy nuclear target (e.g., tungsten), and fission where neutrons are produced by a nuclear reactor. Table 1.5 shows a list of the present and future UCN sources worldwide.

Reactor sources place the moderators close to the reactor core (FRM II and Gatchina [63]), or use existing CN beam lines (ILL [64]). At FRM II, the sD<sub>2</sub> will be placed around a solid hydrogen cold-moderator close to the fuel element. The Gatchina superfluid  $^4\text{He}$  source will be placed inside their thermal column, using immense pumping power to cool the converter to 1.1 K, making rapid extraction necessary due to increased UCN upscattering at this temperature.

The SuperSUN and SUN-2 experiments are the logical extensions of the early superthermal source geometry at ILL. A novel feature of the SuperSUN experiment at ILL [65] is a magnetic multipole reflector for a drastic enhancement of the UCN density with respect to an existing prototype superfluid helium UCN source installed in a cold neutron beam. A multipole magnet can lead to a large gain in the saturated density of

Name	Source Type	Technology	Status
ILL	Turbine	Reactor, CN beam	Running
ILL SUN-2	LHe	Reactor, CN beam	Running
ILL SuperSUN	LHe	Reactor, CN beam	Future
RCNP/TRIUMF/KEK	LHe	Spallation	Installing/Future
PNPI Gatchina	LHe	Reactor	Future
LANL	sD <sub>2</sub>	Spallation	Running/Upgrading
PSI	sD <sub>2</sub>	Spallation	Running
Mainz	sD <sub>2</sub>	Reactor	Running
FRM II, Germany	sD <sub>2</sub>	Reactor	Future
NCSU PULSTAR	sD <sub>2</sub>	Reactor	Installing
SNS, Oakridge	LHe	Spallation	Future
J-PARC	Doppler Shifter	CN beam	Running

Table 1.5: Existing and future UCN sources worldwide. The existing or proposed sources at the following sites is listed: Institut Laue-Langevin (ILL) in France, Research Center for Nuclear Physics (RCNP) in Japan, KEK and J-PARC in Japan, TRIUMF in Canada, Petersburg Nuclear Physics Institute (PNPI) in Russia, Los Alamos National Lab (LANL), PULSTAR and SNS in the US, Mainz and FRM II in Germany.

low-field-seeking UCNs because the presence of the field reduces the number of neutrons hitting the material walls and reduces the energy and wall collision rate of those that do. In addition, it acts as a source-intrinsic UCN polarizer without need to polarize the incident beam, and hence avoiding associated losses.

The Los Alamos solid deuterium source [66] uses a proton beam of 900 MeV and a W target to produce neutrons. The neutrons get cooled down in a polyethylene cold moderator. The new design includes a flapper valve to isolate the neutrons from the sD<sub>2</sub> after the proton beam pulse.

The PSI UCN source [67] uses a 600 MeV proton beam to hit a Pb/Zr target for neutron production. They use a 30 L volume of sD<sub>2</sub> at 5 K as moderator and converter to produce UCN. This volume is surrounded by D<sub>2</sub>O thermal moderator. They also use a flapper valve for UCN extraction between the proton beam pulses to limit the losses. The UCN production has been running since 2012 with an on-going EDM experiment, with a peak density of 23 UCN/cm<sup>3</sup>.

The Mainz UCN source [68] is the only source that operates at a low power university reactor, and is the newest production source. The solid deuterium converter with a volume of  $V = 160 \text{ cm}^3$ , which is exposed to a thermal neutron fluence of  $4.5 \times 10^{13} \text{ n/cm}^2$ , delivers up to 240000 UCN ( $v \leq 6 \text{ m/s}$ ) per pulse outside the biological shield at the experimental area. UCN densities of  $\approx 10/\text{cm}^3$  are obtained in stainless-steel bottles of  $V \approx 10 \text{ L}$ . Their pulsed operation permits the production of high densities for storage experiments.

At the SNS UCN source, the 8.9 Å cold neutrons are selected using a monochromator, and are transported with neutron guides to two cells made out of acrylic (ultraviolet transmitting) and separated by a high voltage electrode. The neutrons entering the cell are polarized. Within the cell, the cold neutrons become ultra-cold neutrons via <sup>4</sup>He single-phonon process [69].

The UCN source at J-PARC is a doppler-shifter type of pulsed UCN source [70].

Very cold neutrons (VCNs) with 136 m/s velocity in a neutron beam supplied by a pulsed neutron source are decelerated by reflection on a wide-band multilayer mirror, yielding pulsed UCN. The mirror is fixed to the tip of a 2,000 rpm rotating arm moving with 68 m/s velocity in the same direction as the VCN. The repetition frequency of the pulsed UCN is 8.33 Hz and the time width of the pulse at production is 4.4 ms. In order to increase the UCN flux, a supermirror guide, wide-band monochromatic mirrors, focus guides, and a UCN extraction guide have been newly installed or improved. This source will be used to search for the nEDM.

The current UCN source at TRIUMF uses a W target to produce spallation neutrons from a 500 MeV proton beam on site. The cold neutrons are converted to UCN in superfluid helium. The future UCN source is projected to compete with the capabilities of the best planned future UCN sources. If TRIUMF's estimated UCN density of 680 UCN cm<sup>-3</sup> is achieved, it will be a new world record.

Other sources and nEDM experiments aim at similar goals of hundreds to thousands of UCN cm<sup>-3</sup> in the measurement volume. However, to date, superthermal sources have not produced considerably more UCN than the ILL turbine source.

## 1.7 Summary

Precision experiments involving UCN provide an attractive avenue to investigate physics beyond the standard model. Measurement of the neutron EDM is an example of such experiments. For such studies high densities of UCN are needed.

UCN are very slow neutrons with velocities < 8 m/s that can be trapped in matter, magnetic and gravitational fields. Superthermal UCN sources could produce high densities of UCN. Such sources should have a very small neutron absorption cross-section and upscattering rate, while having a high UCN production rate. So far, the best candidates are superfluid helium and solid deuterium.

Both <sup>4</sup>He and solid D<sub>2</sub> UCN sources use quantum excitations in the converter medium to create the UCN; these are phonons in the case of superfluid sD<sub>2</sub> and phonons and rotons in the case of <sup>4</sup>He. Since <sup>4</sup>He does not capture neutrons, and has a small upscattering probability for UCN, the superfluid <sup>4</sup>He source can be operated at lower currents for longer times, allowing a large density of neutrons to accumulate. In the case of superfluid helium, storage times of hundreds of seconds are achievable. The production rate in sD<sub>2</sub> is higher than in supefruid 4He, but the neutron storage lifetime is only tens of milliseconds.

The TRIUMF UCN project is the only spallation-driven superfluid-<sup>4</sup>He source proposed at this time in the world [71]. The spallation-driven UCN sources at PSI [67] and LANL [66] use the phonons in solid deuterium as an alternative method of UCN production. The TRIUMF's UCN source uses an optimum proton beam structure on the minute scale to produce the highest density of UCN in the world, while sD<sub>2</sub> spallation sources benefit from pulsing the beam, then isolate any UCN produced as quickly as possible to achieve high UCN densities. The detail of the current UCN facility at TRIUMF is presented in Chapter 4 and the result of the first UCN production with the vertical UCN source is discussed in Chapter 5.

# Chapter 2

## Future nEDM Measurement at TRIUMF

Finding a non-zero neutron electric dipole moment (nEDM) is directly linked to the extra sources of CP violation beyond the standard model. The next generation of nEDM experiments aim to measure  $d_n$  with proposed precision  $\delta d_n \lesssim 10^{-27} e\cdot\text{cm}$  [72–79]. The TUCAN (TRIUMF UltraCold Advanced Neutron source) collaboration proposes a world-leading experiment to measure the nEDM, improving the precision by a factor of thirty compared to the present world’s best experimental result. The current nEDM experiments suffer from low UCN statistics. As a result, TUCAN has intended to build the strongest UCN source in the world. To achieve this goal, extensive studies of the current vertical UCN source have been conducted (See Chapters 4 and 5).

To measure the nEDM, an ensemble of polarized UCN are put in the presence of aligned electric and magnetic fields. The Hamiltonian of the interaction of the UCN with electric and magnetic fields are described in Eqn. 1.7. The Larmor precession frequency of UCN is then measured in two orientations of parallel and anti-parallel electric and magnetic fields. For the parallel **E** and **B** fields, the Larmor precession frequency of UCN is written as

$$h\nu_{\uparrow\uparrow} = 2\mu_n|\mathbf{B}^{\uparrow\uparrow}| + 2d_n|\mathbf{E}^{\uparrow\uparrow}| , \quad (2.1)$$

and for anti-parallel **E** and **B** fields it is

$$h\nu_{\uparrow\downarrow} = 2\mu_n|\mathbf{B}^{\uparrow\downarrow}| + 2d_n|\mathbf{E}^{\uparrow\downarrow}| . \quad (2.2)$$

Here  $\uparrow\uparrow$  indicates the parallel electric and magnetic fields and  $\uparrow\downarrow$  represent the anti-parallel orientation of those fields. A nonzero nEDM is then extracted from any frequency shift between these two measurements:

$$d_n = \frac{h(\nu_{\uparrow\uparrow} - \nu_{\uparrow\downarrow}) - 2\mu_n(|\mathbf{B}^{\uparrow\uparrow}| - |\mathbf{B}^{\uparrow\downarrow}|)}{2(|\mathbf{E}^{\uparrow\uparrow}| - |\mathbf{E}^{\uparrow\downarrow}|)} . \quad (2.3)$$

The main reason to employ this method is because it is impossible to completely eliminate the **B** field to extract the neutron EDM. These measurements are either performed in two adjacent volumes with  $|\mathbf{E}^{\uparrow\uparrow}| = -|\mathbf{E}^{\uparrow\downarrow}|$ , and  $|\mathbf{B}^{\uparrow\uparrow}| - |\mathbf{B}^{\uparrow\downarrow}| = 0$ , or measured in the same volume where the configuration of the fields change in time. In the first case, it is essential to make sure that the magnetic field inside both volumes are the same, and there is no field gradient, and in the second method it is essential to make sure that the magnetic field is stable in time.

## 2.1 Ramsey Method of Separated Oscillating Fields

The Ramsey method of separated oscillating fields is the well-known measurement technique to extract the nEDM. Ramsey obtained an expression for the quantum mechanical transition probability of a system between two states, when the system is subjected to separated oscillating fields [80]. Fig. 2.1 [81] left shows a cycle of measurement. An ensemble of polarized UCN with the initial spin  $|\uparrow\rangle$  are exposed to a DC magnetic field  $B_0$ . A first RF pulse  $B_1 \cos(\omega_{rf}t)$ , prependicular to the  $B_0$  field, tips the spin of the neutrons to the transverse plane. The neutrons precess freely with their Larmor precession frequency  $\omega_0$  for some time  $T$ , while accumulating a phase  $\phi = \gamma_n B T$ . Then again, the second oscillating magnetic field pulse of  $B_1 \cos(\omega_{rf}t)$  is applied to the neutron ensemble. The essential idea is to compare the phase  $\phi$  with  $\omega_{rf}T$ , and if they are identical then  $B = \omega_{rf}/\gamma_n$ .

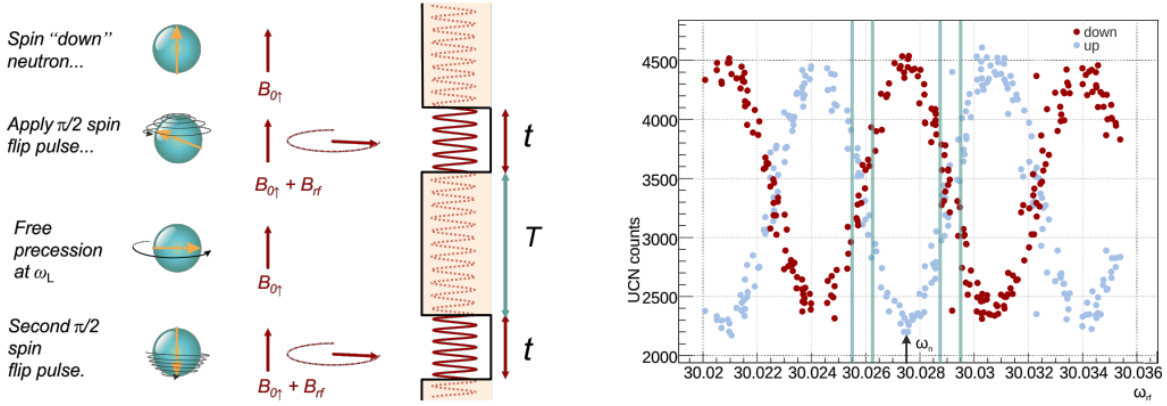


Figure 2.1: Ramsey method of separated oscillating fields. Left shows the scheme of a measurement procedure and right shows the data points. The blue points are the UCN counts with the spin up and the red points are the UCN with spin down (data from the PSI-nEDM collaboration). The width at half height  $\Delta\nu$  of the central fringe is approximately  $1/2T$ , the four vertical lines indicate the working points (see text).

The probability to find the UCN with spin up is

$$\begin{aligned} P(T, \omega_{rf}) &= \langle \uparrow | U(T, \omega_{rf}) | \uparrow \rangle \\ &= 1 - \frac{4\omega_1^2}{\Omega^2} \sin^2 \frac{\Omega t_{\pi/2}}{2} \left[ \frac{\Delta}{\Omega} \sin \frac{\Omega t_{\pi/2}}{2} \sin \frac{T\Delta}{2} - \cos \frac{\Omega t_{\pi/2}}{2} \cos \frac{T\Delta}{2} \right]^2, \end{aligned} \quad (2.4)$$

where  $U(T, \omega_{rf})$  is the time evolutions operator,  $\omega_1 = -\gamma_n B_1$ ,  $\Delta = \omega_{rf} - \omega_0$ , and  $\Omega = \sqrt{\Delta^2 + \omega_1^2}$ . When the spin-flipping pulses are optimized, we would have  $\gamma_n B_1 t_{\pi/2} = \pi/2$ . In this case, the central fringe range ( $\Delta \ll \omega_1$ ), and Eqn. 2.4 simplifies to

$$P(T, \omega_{rf}) = \frac{1}{2} (1 - \cos(T\Delta)) . \quad (2.5)$$

In a real measurement with  $N$  UCN inside a magnetic field region this becomes

$$N^\uparrow = \frac{N}{2} \left\{ 1 - \alpha(T) \cos \left[ (\omega_{rf} - \gamma_n B_0) \cdot \left( T + \frac{T + 4t_{\pi/2}}{\pi} \right) \right] \right\} , \quad (2.6)$$

where  $\alpha$  is the visibility of the central fringe with spin either up or down

$$\alpha^{\uparrow/\downarrow} = \frac{N_{max}^{\uparrow/\downarrow} - N_{min}^{\uparrow/\downarrow}}{N_{max}^{\uparrow/\downarrow} + N_{min}^{\uparrow/\downarrow}}. \quad (2.7)$$

The term  $4t_{\pi/2}/\pi$  is necessary to account for field inhomogeneities in  $B_1$  and  $B_0$ , which become relevant when the pulse length  $t_{\pi/2}$  is finite. The graph in Fig. 2.1 shows the Ramsey interference pattern by scanning  $\omega_{rf}$ , while everything else is kept the same. In the actual nEDM measurements, only 4 points with the highest sensitivity are measured. These points are referred to as the working points. For each configuration of the electric and magnetic fields (parallel or anti-parallel), Eqn. 2.6 is fitted to the data to extract the Larmor frequency. Taking the differences of those Larmor frequencies then give access to the nEDM

$$d_n = \frac{\hbar(\omega_0^{\uparrow\uparrow} - \omega_0^{\uparrow\downarrow})}{2(E^{\uparrow\uparrow} - E^{\uparrow\downarrow})} = \frac{\hbar\Delta\omega}{4E} \quad (2.8)$$

with the assumption that, the magnetic field is constant (see Eqn. 2.3).

## 2.2 Statistical and Systematic Errors

### 2.2.1 Statistical Sensitivity

The statistical sensitivity of the nEDM measurement per cycle is

$$\sigma(d_n) = \frac{\hbar}{2\alpha TE\sqrt{\bar{N}}}, \quad (2.9)$$

where visibility  $\alpha$  is a factor related to the neutrons polarization,  $\bar{N}$  is the average total number of detected UCN,  $T$  is the free precession time, and  $E$  is the electric field. The visibility depends on the longitudinal and transverse spin relaxation times  $T_1$  and  $T_2$  respectively. The transverse spin relaxation time  $T_2$  arises from inhomogeneities in the magnetic field as well as the  $T_1$  relaxation time as

$$\frac{1}{T_2} = \frac{1}{T'_2} + \frac{1}{T_1}, \quad (2.10)$$

where  $T'_2$  is the transverse relaxation time only due to the field inhomogeneities.

### 2.2.2 Systematic Errors

The dominant systematic errors in the previous best experiment arose due to magnetic field instability (uncorrelated with the electric field  $E$ ), and magnetic field inhomogeneity through the geometric phase effect (GPE) [82] (see Appendix C). The GPE could be understood by considering transverse fields originating from the gradient of the uniform  $B_0$  field in the axial direction ( $\partial B_{0z}/\partial z$ ), and the motion of UCN in the electric field ( $\mathbf{B}_v = (\mathbf{E} \times \mathbf{v})/c^2$ ), respectively. Radial fields like these rotate as the particle moves in the EDM cell, thereby inducing a Bloch-Siegert shift on the resonant frequency. To analyze this effect, the field rotations may be represented in terms of a perturbation on the precession phase. The phase is shifted in second order, resulting in a GPE. False EDM effects arise

from cross-terms between the radial component of the applied  $B_0$  field, and  $B_v$  in the second order perturbation.

The false EDM could be corrected by the frequency ratio of the neutrons to the co-magnetometer atoms ( $^{199}\text{Hg}$ ) used to sense the gradient. Graphing the measured neutron EDM as a function of this ratio then allows to correct to the zero gradient and hence discover the true neutron EDM. This is also supplemented by gradient determination using surrounding Cs magnetometers.

## 2.3 TRIUMF nEDM Components

The future nEDM experiment at TRIUMF will use a room-temperature nEDM apparatus, connected to a horizontal cryogenic UCN source Fig 2.2.

A proton beam at 480 MeV and  $40 \mu\text{A}$  impinges on a tungsten spallation target liberating neutrons. Over the target, a room-temperature neutron moderator/reflector system composed of Pb, graphite, and  $\text{D}_2\text{O}$  thermalizes the neutrons. Liquid deuterium ( $\text{LD}_2$ ) at 20 K creates a large flux of cold neutrons (CN) in a bottle containing superfluid  $^4\text{He}$  below 1 K. In the superfluid helium, the CN excite phonon and roton transitions, losing virtually all their kinetic energy to become UCN. Once a sufficient density of UCN is built up, the proton beam is turned off, and a cryogenic UCN valve opens. The UCN are transported out of the source by specular reflection on the surfaces of the UCN guides. A superconducting magnet (SCM) accelerates polarized UCN through barrier foils to a vacuum volume at room temperature. The UCN are then transported to the nEDM experiment by additional guides.

In 2016, the vertical UCN source from RCNP in Japan was shipped to TRIUMF for the research towards the development of the new horizontal UCN source. The details of the current UCN facility at TRIUMF is presented in Chapter 4. The result of the first set of UCN experiments with the vertical UCN source is available in Chapter 5.

A brief description of the main components of the future nEDM apparatus at TRIUMF is presented below.

### 2.3.1 New UCN Source

The future nEDM experiment at TRIUMF will use a new UCN source, which has quite some differences with the vertical UCN source described in Chapter 4. A schematic overview of the proposed UCN source upgrades, and the nEDM experiment is presented in Fig. 2.2. The new UCN source uses an  $\text{LD}_2$  cryostat to produce cold neutrons during the experiment, as opposed to the solid  $\text{D}_2\text{O}$  in the vertical source.  $\text{LD}_2$  increases the UCN production by factors, and reduces the uncertainty in the UCN source performance. A 3D model of the  $\text{LD}_2$  cryostat connected to the superfluid  $^4\text{He}$  cryostat is shown in Fig. 2.3.

### 2.3.2 UCN Handling and Transport

Efficient transport of polarized UCN is one of the major requirements for the nEDM measurement. This efficiency depends mainly on three parameters as described below:

The first parameter is the capacity of the guide walls to contain the UCN. UCN have a large wavelength compared to the lattice constants in solid matter (50 to 130 nm compared to 0.3 nm). Therefore, during a scattering process, a UCN interacts with

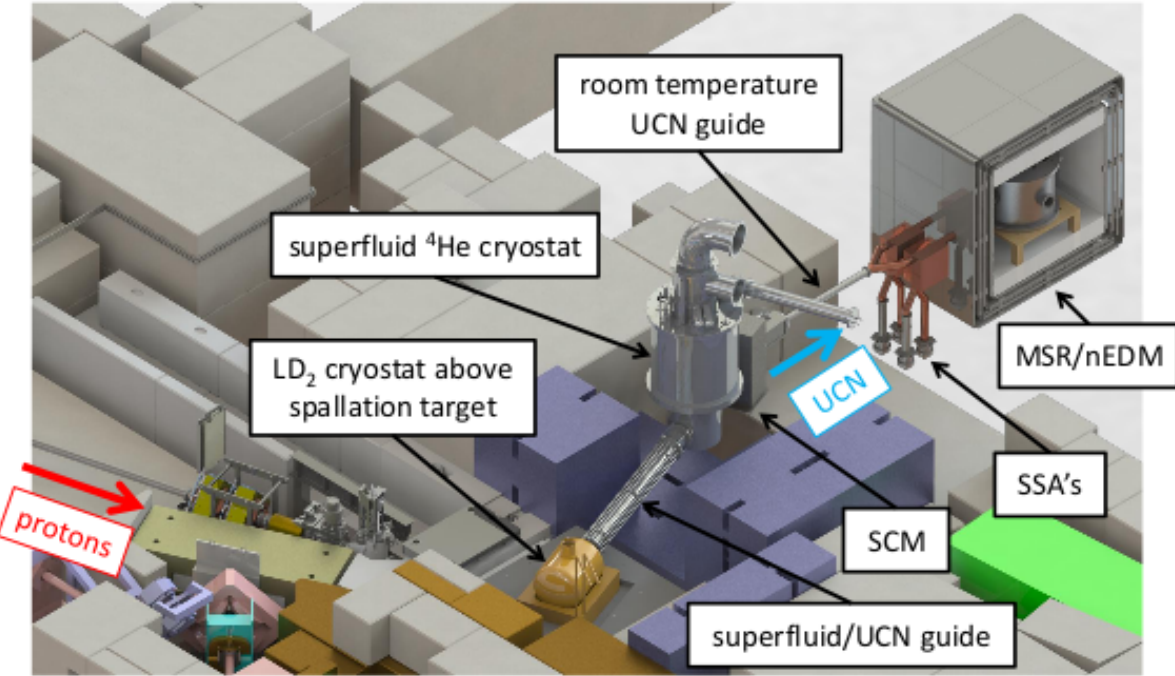


Figure 2.2: Conceptual design of the proposed UCN source and nEDM experiment. Protons strike a tungsten spallation target. Neutrons are moderated in the LD<sub>2</sub> cryostat and become UCN in a superfluid <sup>4</sup>He bottle, which is cooled by another cryostat located farther downstream. UCN pass through guides and the superconducting magnet (SCM) to reach the nEDM experiment located within a magnetically shielded room (MSR). Simultaneous spin analyzers (SSA's) detect the UCN at the end of each nEDM experimental cycle.

hundreds of nuclei. The mean nuclear potential experienced during the scattering, which is referred to as the Fermi potential, depends on the material. In order to store UCN, the Fermi potential must be as high as possible.

The second parameter is the roughness of the surface. Indeed, transportation is more efficient if the roughness is low. Then, the probability of having a specular reflection is increased. Empirically, a roughnesses should be lower than the UCN wavelength.

The last parameter is related to the polarization. UCN can be depolarized during a collision due to different processes. When selecting materials for UCN components, the mean depolarization rate per bounce should be as small as possible.

The main task of the UCN handling parts is to transport a large phase-space fraction of the UCN most efficiently to achieve the highest statistical sensitivity in the experiment as possible.

The parts that come in contact with UCN on the way from the UCN source to the EDM experiment, and the UCN detectors, constitute the neutron handling hardware: UCN guides, valves, switches and simultaneous spin analyzer (SSA) system. Fig. 2.4 shows the neutron handling parts for the future nEDM experiment at TRIUMF. UCN exiting the source are polarized by the SCM, and then enter the nEDM experiment.

Suitable guides and valves have optimized geometries: wall materials with large Fermi potentials, low upscattering and absorption cross sections for neutrons, and low roughness and depolarization. The plan is to use Be for the UCN production volume, and NiMo coatings for most other surfaces, on glass and Cu substrates, where non-magnetic

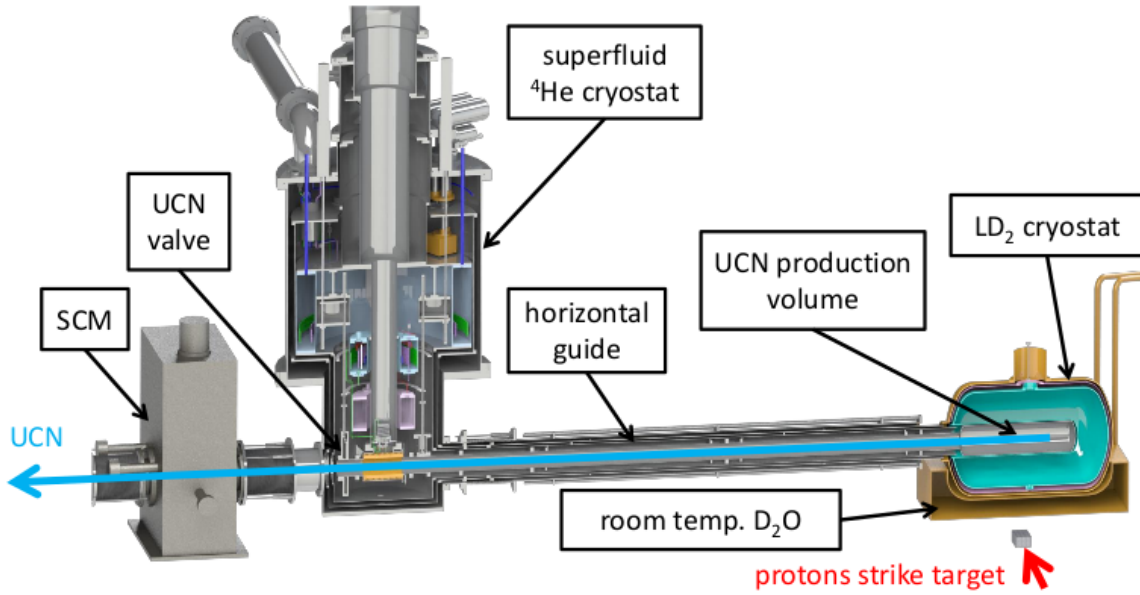


Figure 2.3: The 3D model of the proposed UCN source and the LD<sub>2</sub> cryostat. Protons strike a tungsten spallation target liberating neutrons, which are moderated in surrounding volumes of graphite (not shown), D<sub>2</sub>O, and LD<sub>2</sub>. Neutrons are downscattered in the UCN production volume containing superfluid <sup>4</sup>He. They are bottled within a horizontal guide up to a UCN valve. When the valve is opened, UCN are transported to room temperature UCN guides.

polarization preserving guides are required.

UCN spins will be measured by two separate simultaneous spin analyzer (SSA) systems (one for each cell). Its configuration allows simultaneous counting of both UCN spin states, and maximizes the visibility of the Ramsey fringes and counting efficiency. The UCN switches load the UCN into the nEDM experiment, and divert UCN exiting the experiment into the detectors. A prototype detector, based on scintillating lithium glass, and capable of handling the highest rates of UCN expected with the TRIUMF source has been developed and tested in the highest rate UCN beam available at PSI [83] (See Chapter 4).

### 2.3.3 Magnetic Components

To achieve the desired nEDM sensitivity of  $10^{-27}$  e·cm, an extremely stable and homogeneous  $B_0$  magnetic field is required. The magnetic stability upper limit for TUCAN's nEDM measurement is 1 pT and the magnetic homogeneity upper limit is 1 nT/m. Because of the challenges to achieve this level of magnetic stability, a <sup>199</sup>Hg co-magnetometer will be used to correct for the  $B_0$  field fluctuations. To achieve these specifications, both active and passive shielding will be utilized to nullify the uncontrolled and time-varying external fields. The desired internal magnetic field will be generated by using uniform and shim coils. Fig. 2.5 shows the schematic drawing of the magnetic components of the TUCAN nEDM experiment. Each magnetic component is explained below.

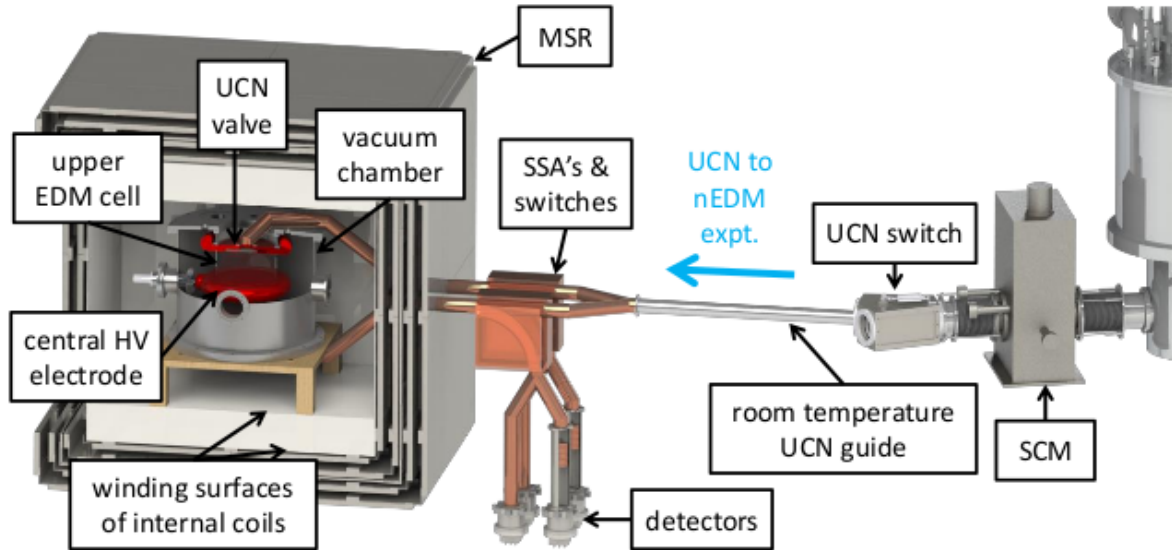


Figure 2.4: A 3D model of the UCN delivery and the future nEDM experiment at TRIUMF. UCN exit the source by passing through the SCM spin polarizer, and UCN switch and detector system, where they then enter the proposed nEDM experiment. UCN are loaded into the measurement cells within a MSR/coil system. At the end of the measurement cycle, UCN are counted by simultaneous spin analyzers (SSA's) including detectors. An ambient magnetic compensation system, and thermally controlled room, will surround the nEDM apparatus (not shown). For scale, the innermost layer of the MSR is a 1.8 m side-length cube.

### Active Shielding

The magnetic environment at the location of the planned nEDM experiment at TRIUMF is dominated by a  $400 \mu\text{T}$  static field due to the main cyclotron at TRIUMF, with 1 to 100 nT fluctuations due to the other external magnetic sources such as the electrical equipment or the displacement of large magnetic objects (e.g., vehicle traffic).

The TUCAN's plan is to reduce the static field to less than  $1 \mu\text{T}$  using dedicated compensation coils and constant-current supplies, with a readily achievable steability of  $10^{-3}$ , and to reduce the remaining static field and fluctuations by up to a factor of 100 through a separate set of compensation coils and current supplies, using fluxgate magnetometers for magnetic feedback. The fluxgate sensors will be placed in the region between the compensation coils and the passive shields as shown in Fig. 2.5. A prototype active compensation system has been built at the University of Winnipeg based on Refs. [84, 85]. The system employs a set of coils centered around a cylindrical passive magnetic shield system, using four 3-axis fluxgates for feedback (see Fig. 2.6). Overall, the active shielding system should be able to reduce the net background magnetic field to the level of tens of nT over the volume of the nEDM cell.

### Passive Shielding

Passive magnetic shielding system is generally composed of a multi-layer shield formed from thin shells of material with high magnetic permeability (e.g., mu-metal). The outer layers of the shield are normally cylindrical [72, 75] or form the walls of a magnetically shielded room [86, 87]. The innermost magnetic shield is normally a specially shaped

### Active Compensation/Shielding

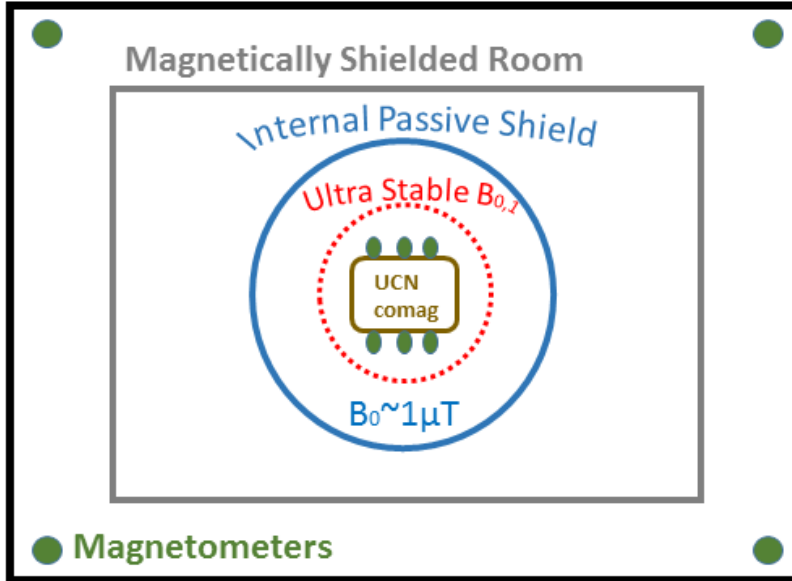


Figure 2.5: Schematic drawing for the TUCAN nEDM magnetics. From outside in: The active compensation system followed by several layers of magnetically shielded room and passive shields nullify the environmental magnetic field. The magnetometers inside the active shielding monitor the changes in the magnetic field internal to that region. The internal coil system ( $B_0$  and  $B_1$  coils) generate the magnetic fields for the Ramsey cycle. The UCN and the co-magnetometers are internal to the coils.

shield, where the design of the coil in relation to the shield is carefully taken into account to achieve adequate homogeneity [14, 74, 76]. Fig. 2.7 shows a picture of a prototype passive shield at the University of Winnipeg, which is in support of the precision magnetic field research for the future nEDM experiment to be conducted at TRIUMF. The shield system is a four-layer mu-metal shield formed from nested right-circular cylindrical shells with endcaps. The inner radius of the innermost shield is 18.44 cm, equal to its half-length. The radii and half-lengths of the progressively larger outer shields increase geometrically by a factor of 1.27. Each cylinder has two endcaps which possess a 7.5 cm diameter central hole. A stove-pipe of length 5.5 cm is placed on each hole, was designed to minimize leakage of external fields into the progressively shielded inner volumes. The design is similar to another smaller prototype shield discussed in Ref. [88].

The TUCAN's passive shielding system will nullify the residual background fields to the pT level. It will be a two-stage system: (1) a magnetically shielded room (MSR) with (2) a set of smaller shields that fit inside the room and surround the nEDM apparatus.

A magnetically shielded room (MSR) with quasi-static shielding factor of  $\sim 100,000$  is sufficient to reduce the magnetic fluctuations to the  $\sim \text{pT}$  level. A four-layer MSR with an inner cubic space of side-length 1.8 m and outer side-length 2.8 m produces this shielding factor, with mu-metal wall thicknesses 2 mm, 6 mm, 4 mm, 4 mm (inner to outer), equally spaced.

The innermost layer of the internal passive shields also serves as a return yoke for the magnetic flux generated by the internal coils for the shield-coupled coil designs. A degaussing (idealization) system will be used to stabilize the shields. A combined DC

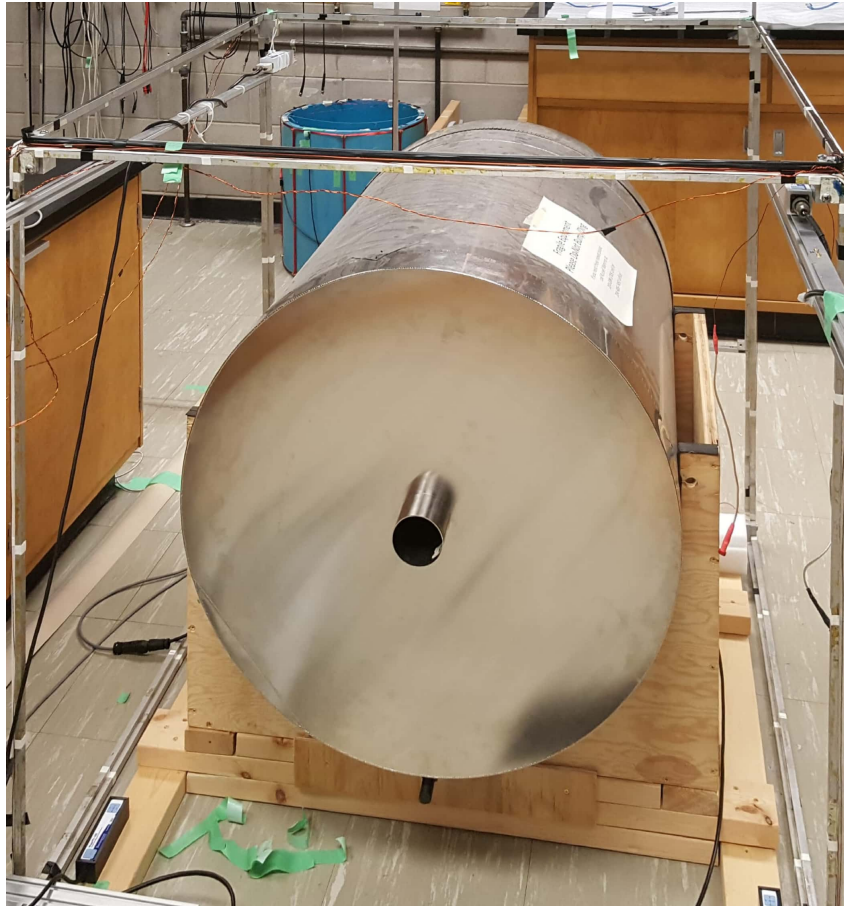


Figure 2.6: The prototype active compensation system at the University of Winnipeg.

shielding factor of the order of  $10^6$  is expected.

In principle, by utilizing both active and passive shielding, the magnetic field from external sources will be reduced to the level of tens of fT over the volume of the nEDM cell. There are two prototype four-layer mu-metal passive shields at the University of Winnipeg. The shields are used to facilitate a variety of magnetic field R&D. In addition, there are three small witness cylinders which are made of the same material and annealed in the same oven as the large passive shields. The design principles behind the small shield, shielding factor measurements, and comparison to simulation are described in Ref. [88]. The witness cylinders are used to evaluate the temperature dependence of the shield material properties, which could be an important consideration for internal field stability (see chapter 3).

### Internal Coils

For internal coils, self-shielded  $B_0$  coils and shim coils are considered surrounding the nEDM cells, since they provide immunity from the field perturbations induced by changes in the magnetic permeability of the passive shields arising from temperature fluctuations (see chapter 3). High-precision current supplies ( $\sim 1$  ppm) will be used to drive all internal coils, regardless of design. AC coils will apply  $\pi/2$  pulses for the UCN and comagnetometer species, to initiate free spin precession.



Figure 2.7: Three layers of the prototype passive magnetic shield at the University of Winnipeg. The 4th layer is not shown in this picture.

### 2.3.4 EDM Cells and High Voltage System

The nEDM measurement volume consists of two storage cells to enable simultaneous measurements with both up and down orientations of the electric field (see Fig. 2.8). The storage cells will be housed inside a non-magnetic vacuum chamber, providing insulating vacuum for the high voltage applied to the central electrode which separates the two cells. The cells are separated by a cylindrical wall of dielectric insulator. The insulator must have a large dielectric strength and low permittivity. An electric field of 12 kV/cm will be created between the electrodes with minimal leakage current ( $< 10 \text{ pA}$ ). The optical readout of the comagnetometer requires UV-transparent windows in the insulating side wall. The use of two cells with a central electrode allows first-order compensation of magnetic field drifts and a measurement of the magnetic field gradient.

### 2.3.5 Comagnetometry

A problem in a typical nEDM experiment is that, if the magnetic field  $B_0$  drifts over the course of the measurement period, it degrades the statistical precision with which  $d_n$  can be determined. If the magnetic field over one measurement cycle is determined to  $\delta B_0 = 10 \text{ fT}$ , it implies an additional statistical error of  $\delta d_n \sim 10^{-26} \text{ e}\cdot\text{cm}$  (assuming an electric field of  $E = 10 \text{ kV/cm}$ , which is reasonable for a neutron EDM experiment). Over 100 days of averaging, this would make a  $\delta d_n \sim 10^{-27} \text{ e}\cdot\text{cm}$  measurement possible. Unfortunately, the magnetic field in the experiment is never stable to this level. For this reason, experiments use a comagnetometer and/or surrounding atomic magnetometers to

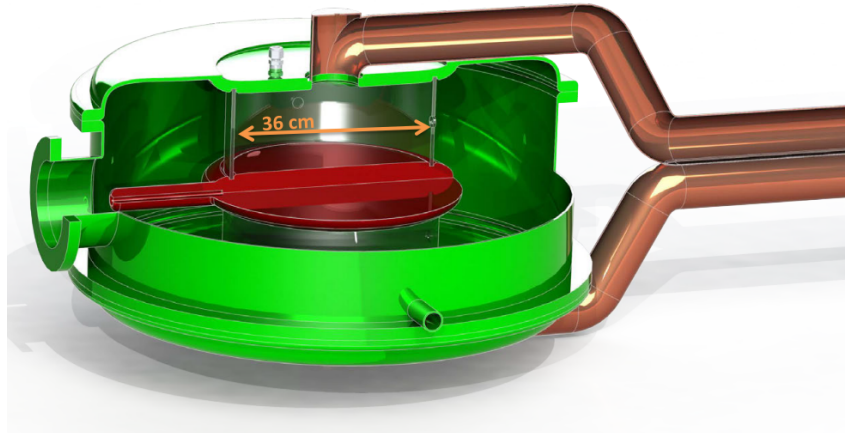


Figure 2.8: 3D drawing of the double EDM cell with vacuum chamber and UCN guides

measure and correct the magnetic field to this level [14, 85, 89]. Drifts of 1-10 pT in  $B_0$  may be corrected using the comagnetometer technique, setting a goal magnetic stability for the  $B_0$  field generation system in a typical nEDM experiment.

A false nEDM signal may arise due to a combination of a magnetic field gradient  $\partial B_z / \partial z$ , and motion in the electric field when species (neutrons and  $^{199}\text{Hg}$  atoms) are confined in the measurement cells. Comagnetometry offers the only way to correct for false EDMs caused by leakage currents. Each  $^{199}\text{Hg}$  atom is polarized using optical pumping techniques. Polarized atoms are introduced into the nEDM cell at the same time as UCN, and the spin-precession frequencies of them are measured simultaneously. The atoms are expected to have smaller EDMs than the neutrons, and so their precession frequencies may be used to normalize magnetic field drifts. The design of the  $^{199}\text{Hg}$  comagnetometer will be similar to that employed in the previous ILL experiment [14, 90].

## 2.4 nEDM Status Worldwide

In 1950, the first upper limit on neutron EDM was discussed by Purcell and Ramsey to be  $3 \times 10^{-18}$  [91]. Since then many groups around the world attempted to measure the nEDM and increase its sensitivity (see Fig. 2.9).

The most recent nEDM measurement at ILL found that to be  $d_n < 3.0 \times 10^{-26} \text{ e}\cdot\text{cm}$  (90% CL) [9]. The new  $^{199}\text{Hg}$  EDM measurement constrains the nEDM better than direct nEDM measurements,  $d_n < 1.6 \times 10^{-26} \text{ e}\cdot\text{cm}$ , although subject to uncertainty from Schiff screening [92].

There are several ongoing experiments seeking to measure the nEDM. Most groups are aiming initially for an improvement of the uncertainty on  $d_n$  to the  $10^{-27} \text{ e}\cdot\text{cm}$  level, ultimately improving to the  $10^{-28} \text{ e}\cdot\text{cm}$  level over time.

Here is a brief survey of the nEDM measurement sites.

The PSI nEDM experiment uses an improved version of the former Sussex- RAL-ILL single-cell apparatus. Several innovations have been made at PSI, including a new  $\text{SD}_2$  spallation-driven UCN source. The experiment employs several Cs magnetometers outside the EDM cell, and a  $^{199}\text{Hg}$  comagnetometer. Active magnetic shielding and other environmental controls have been improved. A new detector that can simultaneously count both spin states of UCN has also been implemented. The final sensitivity expected

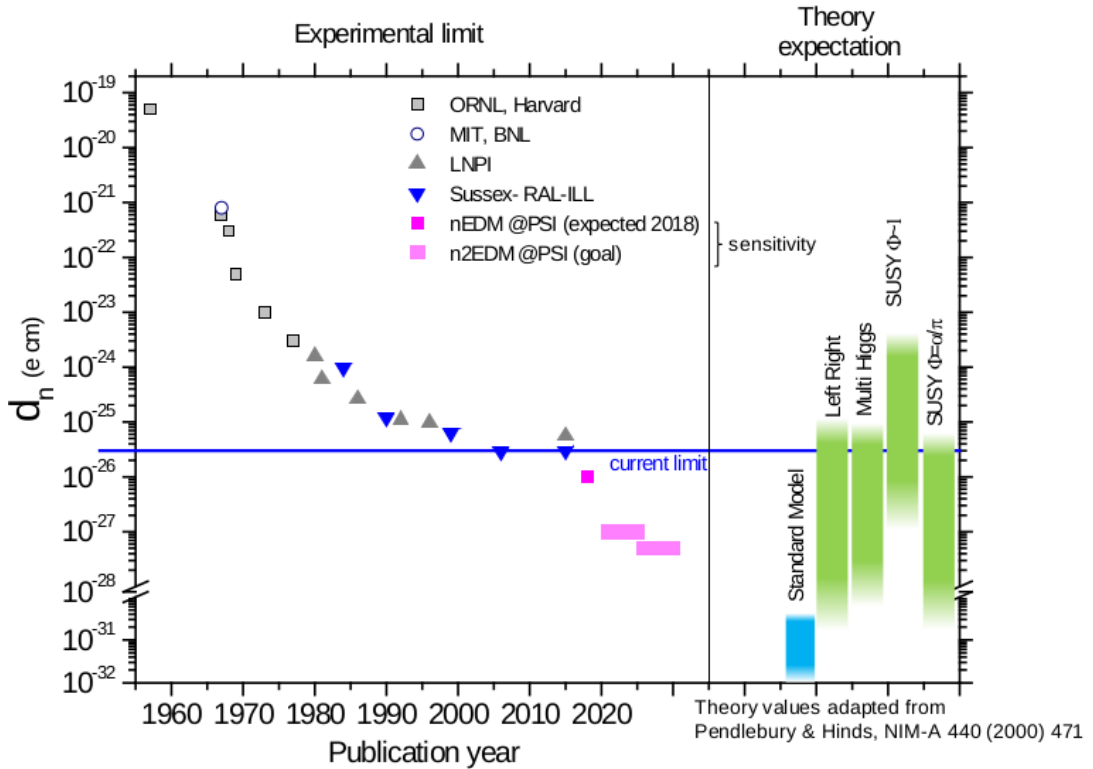


Figure 2.9: The history of the nEDM measurements [93]

is  $\simeq 10^{-26}$  e·c [81]. Some of the chief improvements made at PSI recently have been in the area of nearby alkali atom (Cs) magnetometry, Hg comagnetometry, and neutron magnetometry. A recent achievement at PSI is the understanding of the Cs magnetometer signals in terms of magnetic field gradients internal to the magnetic shielding. This has led to a detailed understanding of the false EDM of the Hg comagnetometer [94]. Another recent achievement is in using the neutrons themselves to measure gradients [95]. PSI also aims to improve their magnetometry with  $^3\text{He}$  magnetometers inside the electrodes of the double EDM measurement cells for their future n2EDM effort. They have performed R&D using Cs magnetometers to sense the free-induction decay signal from  $^3\text{He}$ , which resulted in a new high-precision magnetometer possessing excellent long-term stability [96]. The precision goal for n2EDM is  $5 \times 10^{-28}$  e·cm [75, 93].

The nEDM collaboration at SNS plans to measure  $d_n \approx 2 \times 10^{-28}$  e·cm, two orders of magnitude improvement from the current limit [97]. They plan to use a unique experimental technique. A Cold Neutron (CN) beam from the SNS will impinge upon a volume of superfluid  $^4\text{He}$  creating UCN. The nEDM measurement will also be conducted in the superfluid. A small amount of polarized  $^3\text{He}$  introduced into the superfluid  $^4\text{He}$  will act as both a comagnetometer and spin analyzer for the UCN. The  $^3\text{He}$  neutron capture rate is strongly spin dependent, and will beat at the difference of the Larmor precession frequencies of the neutrons and  $^3\text{He}$ . A non-zero EDM would change the beat frequency with E-reversal. Scintillation light produced in the superfluid will be used to detect the capture products. The target precision is  $10^{-28}$  e·cm. The false EDM of the  $^3\text{He}$  comagnetometer may be reduced by collisions in the surrounding  $^4\text{He}$  [98]. The group aims to commission the experiment at SNS by 2020.

A new room-temperature nEDM experiment will be conducted using an upgraded LANL UCN source [99]. The aim of the project is to increase the UCN density by a

factor of five to ten, which could then be used to carry out a  $\sim 10^{-27}$  e·cm determination of the nEDM. The experiment aims for completion of a  $10^{-27}$ -level result, to be completed in the years prior to the SNS nEDM experiment, which shares a number of collaborators. Two other room temperature nEDM experiments are being pursued at the FRM2 reactor in Munich [100] and at ILL [101]. Both experiments feature double measurement cells and Cs magnetometers internal to the innermost magnetic shield. The Munich effort features an impressive new effort in active and passive magnetic shielding [76, 86, 87, 102], and uses  $^{199}\text{Hg}$  comagnetometry. The ILL/Gatchina experiment has produced results at ILL [101]. This could be improved in further runs at ILL in the EDM position, or in runs using the superfluid He UCN source at ILL, where a statistical sensitivity of  $3.5 \times 10^{-27}$  e·cm could be obtained [103]. The group will build a UCN source at the WWR-M reactor in Gatchina in order to increase the UCN flux.



# Chapter 3

## Temperature Dependence of Magnetic Permeability

In the previous best experiment to measure nEDM [14, 18] which discovered  $d_n < 3.0 \times 10^{-26}$  e·cm (90% C.L), effects related to magnetic field homogeneity and instability were found to dominate the systematic error. To reduce the external magnetic fields several types of shielding such as active and passive shielding are essential for such precision measurements. In addition, internal coils that are usually coupled to the passive shields are used to generate the  $B_0$  field. As a result, a detailed understanding of passive and active magnetic shielding, magnetic field generation within shielded volumes, and precision magnetometry is expected to be crucial to achieve the systematic error goals for the next generation of experiments. Much of the research and development efforts for these experiments are focused on careful design and testing of various magnetic shield geometries with precision magnetometers [85, 86, 89, 104].

In nEDM experiments, the spin precession frequency  $\omega$  of neutrons placed in static magnetic  $B_0$  and electric  $E$  fields is measured (see Chapter 2). The measured frequencies for parallel  $\omega_+$  and antiparallel  $\omega_-$  relative orientations of the fields is sensitive to the neutron electric dipole moment  $d_n$

$$\hbar\omega_{\pm} = 2\mu_n B_0 \pm 2d_n E \quad (3.1)$$

where  $\mu_n$  is the magnetic moment of the neutron. In such experiments, typically  $B_0 = 1 \mu\text{T}$  is used to provide the quantization axis for the UCN. The  $B_0$  magnetic field generation system typically includes a coil placed within a passively magnetically shielded volume.

Mechanical and temperature changes of the passive magnetic shielding [105, 106], and the degaussing procedure [87, 106, 107] (also known as demagnetization, equilibration, or idealization), affect the stability of the magnetic field within magnetically shielded rooms. Active stabilization of the background magnetic field surrounding magnetically shielded rooms can also improve the internal stability [85, 105, 108]. The current supplied to the  $B_0$  coil is generated by an ultra-stable current source [89]. The coil must also be stabilized mechanically relative to the magnetic shielding.

One additional effect, which is the subject of this chapter, relates to the fact that the  $B_0$  coil in most nEDM experiments is magnetically coupled to the innermost magnetic shield. If the magnetic properties of the innermost magnetic shield change as a function of time, it then results in a source of instability of  $B_0$ . In the present work, we estimate this effect and characterize one possible source of instability: changes of the magnetic permeability  $\mu$  of the material with temperature.

While the sensitivity of magnetic alloys to temperature variations has been characterized in the past [109, 110], we sought to make these measurements in regimes closer to the operating parameters relevant to nEDM experiments. For these alloys, it is also known that the magnetic properties are set during the final annealing process [110–112]. In this spirit we performed our measurements on “witness” cylinders, which are small open-ended cylinders made of the same material and annealed at the same time as other larger shields are being annealed.

The chapter proceeds in the following fashion:

- The dependence of the internal field on magnetic permeability of the innermost shielding layer for a typical nEDM experiment geometry is estimated using a combination of analytical and finite element analysis techniques. This sets a scale for the stability problem.
- New measurements of the temperature dependence of the magnetic permeability are presented. The measurements were done in two ways in order to study a variety of systematic effects that were encountered.
- Finally, the results of the calculations and measurements are combined to provide a range of temperature sensitivities that takes into account sample-to-sample and measurement-to-measurement variations.

### 3.1 Sensitivity of Internally Generated Field to Permeability of the Shield $B_0(\mu)$

The presence of a coil inside the innermost passive shield turns the shield into a return yoke, and generally results in an increase in the magnitude of  $B_0$ . The ratio of this field inside the coil in the presence of the magnetic shield to that of the coil in free space is referred to as the reaction factor  $C$ , and can be calculated analytically for spherical and infinite cylindrical geometries [113, 114]. The key issue of interest for this work is the dependence of the reaction factor on the permeability  $\mu$  of the innermost shield. Although this dependence can be rather weak, the constraints on  $B_0$  stability are very stringent. As a result, even a small change in the magnetic properties of the innermost shield can result in an unacceptably large change in  $B_0$ .

To illustrate, consider here the model of a sine-theta surface current on a sphere of radius  $a$ , inside a spherical shell of inner radius  $R$ , thickness  $t$ , and linear permeability  $\mu$ . The uniform internal field generated by this ideal spherical coil is augmented by the reaction factor in the presence of the shield, but is otherwise left undistorted. The general reaction factor for this model is given by Eq. (38) in Ref. [113]. In the high- $\mu$  limit, with  $t \ll R$ , the reaction factor can be approximated as

$$C \simeq 1 + \frac{1}{2} \left( \frac{a}{R} \right)^3 \left( 1 - \frac{3}{2} \frac{R}{t} \frac{\mu_0}{\mu} \right), \quad (3.2)$$

which highlights the dependence of  $B_0$  on the relative permeability  $\mu_r = \mu/\mu_0$  of the shield.

Fig. 3.1 (upper) shows a plot of  $B_0$  versus  $\mu_r$  for coil and shield dimensions similar to the ILL nEDM experiment [14, 115]:  $a = 0.53$  m,  $R = 0.57$  m, and  $t = 1.5$  mm. In addition to analytic calculations, the results of two axially symmetric simulations

### 3.1. SENSITIVITY OF INTERNALLY GENERATED FIELD TO PERMEABILITY OF THE SHIELD

conducted using FEMM [116] are also included to assess the effects of geometry and discretization of the surface current. The differences are small, suggesting that the ideal spherical model of Ref. [113] and the high- $\mu$  approximation of Eq. 3.2 provide valuable insight for the design and analysis of shield-coupled coils.

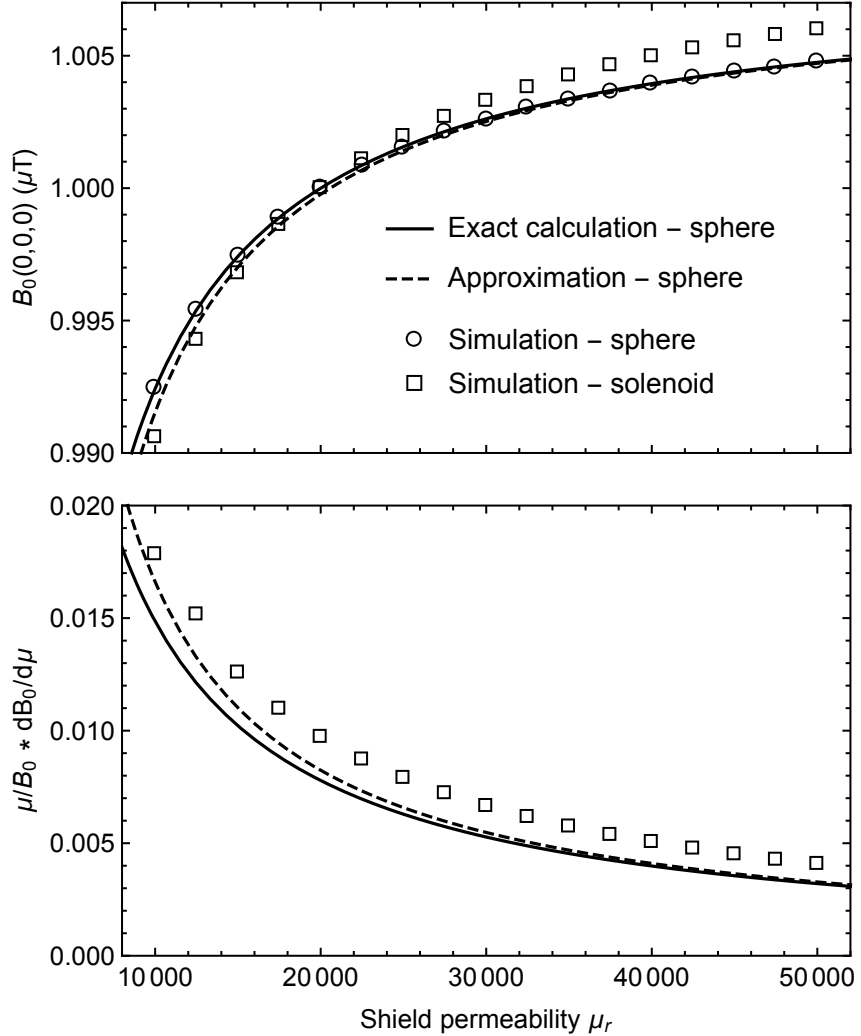


Figure 3.1: Upper: Magnetic field at the coil center as a function of magnetic permeability of the surrounding magnetic shield for a geometry similar to the ILL nEDM experiment as discussed in the text. Lower:  $\frac{\mu}{B_0} \frac{dB_0}{d\mu}$  vs. permeability. The solid curve is the exact calculation for the ideal spherical coil and shield from Ref. [113]; the dashed curve is the approximation of Eq. 3.2. The circles and squares are the FEMM-based simulations for the spherical and solenoidal geometries with discrete currents. Since the spherical simulation was in agreement with the calculation, it is omitted from the lower graph. For the exact calculation and the two simulations, currents were chosen to give  $B_0 = 1 \mu\text{T}$  at  $\mu_r = 20,000$ .

In the first simulation, the same spherical geometry was used as for the analytic calculations. However, the surface current was discretized to 50 individual current loops, inscribed onto a sphere, and equally spaced vertically (i.e. a discrete sine-theta coil). A square wire profile of side length 1 mm was used. As shown in Fig. 3.1, this simulation gave excellent agreement with the analytic calculations. In the second simulation, a solenoid

coil and cylindrical shield (length/radius = 2) were used with the same dimensions as above. Similarly, the coil was modelled as 50 evenly spaced current loops, with the distance from an end loop to the inner face of the shield endcap being half the inter-loop spacing. In the limit of tight-packing (i.e., a continuous surface current) and infinite  $\mu$ , the image currents in the end caps of the shield act as an infinite series of current loops, giving the ideal uniform field of an infinitely long solenoid [117, 118]. As shown in Fig. 3.1, the result is similar to the spherical case, with differences of order one part per thousand and a somewhat steeper slope of  $B_0(\mu_r)$ .

Fig. 3.1 (lower) shows the normalized slope  $\frac{\mu}{B_0} \frac{dB_0}{d\mu}$  of the curves from Fig. 3.1 (upper). In ancillary measurements of shielding factors (discussed briefly in Section 3.2.1), we found  $\mu_r = 20,000$  to offer a reasonable description of the quasistatic shielding factor of our shield. Using this value as the magnetic permeability of our shield material, Fig. 3.1 (lower) shows that  $\frac{\mu}{B_0} \frac{dB_0}{d\mu}$  varies by about 20% (from 0.008 to 0.01) for the spherical vs. solenoidal geometries. We adopt the value  $\frac{\mu}{B_0} \frac{dB_0}{d\mu} = 0.01$  as an estimate of this slope in our discussions in Section 3.3, acknowledging that the value depends on the coil and shield design.

For a high- $\mu$  innermost shield, the magnetic field lines emanating from the coil all return through the shield. This principle can be used to estimate the magnetic field  $B_m$  inside the shield material, and in our studies gave good agreement with FEA-based simulations. For the solenoidal geometry previously described and used for the calculations in Fig. 3.1,  $B_m$  is largest in the side walls of the solenoidal flux return, attaining a maximum value of 170  $\mu\text{T}$ . If we assume  $\mu_r=20,000$ , the  $H_m$  field is 0.007 A/m. Typically the shield is degaussed (idealized) with the internal coil energized. After degaussing,  $B_m$  must be approximately the same, since essentially all flux returns through the shield. However, the  $H_m$  field may become significantly smaller because after degaussing, it must fall on the ideal magnetization curve in  $B_m - H_m$  space. (For a discussion of the ideal magnetization curve, refer to Ref. [112] and see Fig. 3.2.) In principle, the  $H_m$  field could be reduced by an order of magnitude or more, depending on the steepness of the ideal magnetization curve near the origin. Thus  $B_m = 170 \mu\text{T}$  and  $H_m < 0.007 \text{ A/m}$  set a scale for the relevant values for nEDM experiments. Furthermore, the field in the nEDM measurement volume, as well as in the magnetic shield, must be stable for periods of typically hundreds of seconds (corresponding to frequencies  $< 0.01 \text{ Hz}$ ). This sets the relevant timescale for magnetic properties most relevant to nEDM experiments.

## 3.2 Measurements of $\mu(T)$

### 3.2.1 Previous Measurements and their Relationship to nEDM Experiments

Previous measurements of the temperature dependence of the magnetic properties of high permeability alloys have been summarized in Refs. [109, 112, 119]. These measurements are normally conducted using a sample of the material to create a toroidal core, where a thin layer of the material is used in order to avoid eddy-current and skin-depth effects [110, 119]. A value of  $\mu$  is determined by dividing the amplitude of the sensed  $B_m$ -field by the amplitude of the driving AC  $H_m$ -field (similar to the method described in Section 3.2.3). Normally the frequency of the  $H_m$ -field is 50 or 60 Hz. The value of  $\mu$  is then quoted either at or near its maximum attainable value by adjusting the amplitude of  $H_m$ . Depending on

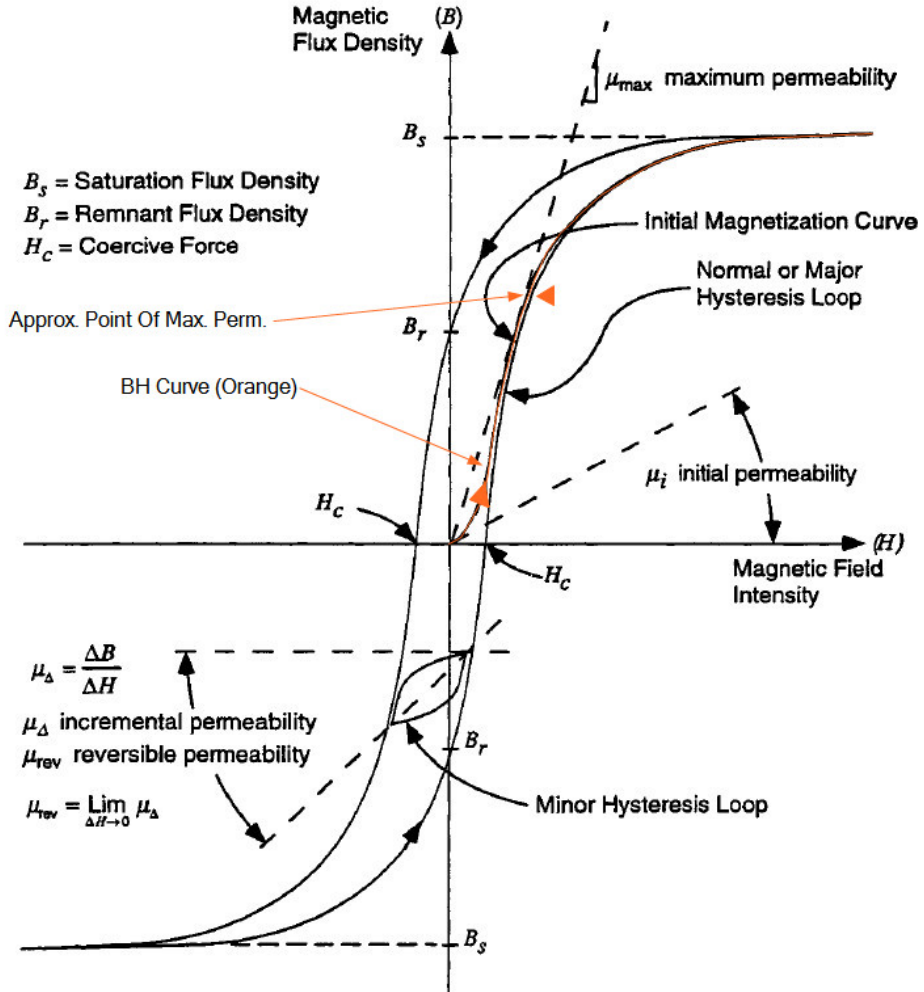


Figure 3.2: The hysteresis or  $B - H$  curve. Some commonly used terminology is shown.  $H_c$  or coercivity is a measure of the ability of the material to withstand external magnetic fields and is at  $B = 0$ . Initial permeability or  $\mu_i$  is the slope of the initial magnetization curve. The initial magnetization or idealization curve is achievable after degaussing the high  $\mu$  material.

the details of the  $B_m - H_m$  curve for the material in question, this normally means that  $\mu$  is quoted for the amplitude of  $H_m$  being at or near the coercivity of the material [109, 110], resulting in large values up to  $\mu_r = 4 \times 10^5$ .

It is well known that  $\mu$  measured in this fashion for toroidal, thin metal wound cores depends on the annealing process used for the core. There is a particularly strong dependence on the take-out or tempering temperature after the high-temperature portion of the annealing process has been completed [109, 110, 119]. Such studies normally suggest a take-out temperature of 490-500°C. This ensures that the large  $\mu_r = 4 \times 10^5$  is furthermore maximal at room temperature. Slight variations around room temperature, and assuming the take-out temperature is not controlled to better than a degree, imply a scale of possible temperature variation of  $\mu$  of approximately  $\left| \frac{1}{\mu} \frac{d\mu}{dT} \right| \simeq 0.3\text{-}1\%/\text{K}$  at room temperature [109, 110].

A challenge in applying these results to temperature stability of nEDM experiments is that, when used as DC magnetic shielding, the high-permeability alloys are usually

operated for significantly different parameters ( $B_m$ ,  $H_m$ , and frequencies).

For example, when used in a shielding configuration, the effective permeability is often measured to be typically  $\mu_r = 20,000$  rather than  $4 \times 10^5$ . This arises in part because  $H_m$  is well below the DC coercivity. As noted in Section 3.1, a more appropriate  $H_m$  for the innermost magnetic shield of an nEDM experiment is  $< 0.007$  A/m, whereas the coercivity is  $H_c = 0.4$  A/m [110]. The frequency dependence of the measurements could also be an issue. Typically, nEDM experiments are concerned with slow drifts at  $< 0.01$  Hz timescales whereas the previously reported  $\mu(T)$  measurements are performed in an AC mode at 50-60 Hz.

The goal of the experiments discussed in this chapter was to develop techniques to characterize the material properties of our own magnetic shields post-annealing, in regimes more relevant to nEDM experiments.

The magnetic shielding factors of each of our prototype four cylindrical shells, and of various combinations of them, were measured and found to be consistent with  $\mu_r \sim 20,000$ . In our studies of the material properties of these magnetic shields, two different approaches to measure  $\mu(T)$  were pursued. Both approaches involved experiments done using witness cylinders made of the same material and annealed at the same time as the prototype magnetic shields. We therefore expect they have the same magnetic properties as the larger prototype shields, and they have the advantage of being smaller and easier to perform measurements with.

The two techniques employed to determine  $\mu(T)$  were the following:

1. measuring the low-frequency AC axial magnetic shielding factor of the witness cylinder as a function of temperature, and
2. measuring the temperature dependence of the slope of a minor  $B - H$  loop, using the witness cylinder as a transformer core, similar to previous measurements of the temperature dependence of  $\mu$ , but for parameters closer to those encountered in nEDM experiments.

The details and results of each technique is presented below.

### 3.2.2 Axial Shielding Factor Measurements

In these measurements, a witness cylinder was used as a magnetic shield. The shield was subjected to a low-frequency AC magnetic field of  $\sim 1$  Hz. The amplitude of the shielded magnetic field  $B_s$  was measured at the center of the witness cylinder using a fluxgate magnetometer. Changes in  $B_s$  with temperature signify a dependence of the permeability  $\mu$  on temperature. The relative slope of  $\mu(T)$  can then be calculated using

$$\frac{1}{\mu} \frac{d\mu}{dT} = - \frac{\frac{1}{B_s} \frac{dB_s}{dT}}{\frac{\mu}{B_s} \frac{dB_s}{d\mu}}. \quad (3.3)$$

The numerator was taken from the measurements described above. The denominator was taken from finite-element simulations of the shielding factor for this geometry as a function of  $\mu$ .

This measurement technique was sufficiently robust to extract the temperature dependence of the shielding factor with some degree of certainty. Possible drifts and temperature dependence of the fluxgate magnetometer offset were mitigated by using an AC

magnetic field. Any temperature coefficients in the rest of the instrumentation were controlled by performing the same measurements with a copper cylindrical shell with the similar size and shape as the mu-metal witness cylinders in place of the mu-metal witness cylinder.

This technique is quite different than the usual transformer core measurements conducted by other groups. As shall be described, it offers an advantage that considerably smaller  $B_m$  and  $H_m$  fields can be accessed. Measuring the temperature dependence of the shielding factor is also considerably easier than measuring the temperature dependence of the reaction factor, since the sensitivity to changes in  $\mu(T)$  is considerably larger in magnitude for the shielding factor case where  $\frac{\mu}{B_s} \frac{dB_s}{d\mu} \sim -1$  compared to the reaction factor case where  $\frac{\mu}{B_0} \frac{dB_0}{d\mu} \sim 0.01$ .

### Experimental Apparatus for Axial Shielding Factor Measurements

The witness cylinder was placed within a homogeneous AC magnetic field. The field was created within the magnetically shielded volume of the prototype magnetic shielding system (described previously in Section 3.2.1) in order to provide a controlled magnetic environment. A short solenoid inside the shielding system was used to produce the magnetic field. The solenoid has 14 turns with 2.6 cm spacing between the wires. The solenoid was designed so that the field produced by the solenoid plus innermost shield approximates that of an infinite solenoid. The magnetic field generated by the solenoid was typically 1  $\mu\text{T}$  in amplitude. The solenoid current was varied sinusoidally at typically 1 Hz.

The witness cylinder was placed into this magnetic field generation system as shown schematically in Fig. 3.3. The cylinder was held in place by a wooden stand.

A Bartington fluxgate magnetometer Mag-03IEL70 [120] (low noise) measured the axial magnetic field at the center of the witness cylinder. The fluxgate was a “flying lead” model, meaning that each axis was available on the end of a short electrical lead, separable from the other axes. One flying lead was placed in the center of the witness cylinder, the axis of the fluxgate being aligned with that of the witness cylinder. The fluxgate was held in place rigidly by a plastic mounting fixture, which was itself rigidly mounted to the witness cylinder.

To increase the resolution of the measured signal from the fluxgate, a Bartington Signal Conditioning Unit (SCU) was used with a low-pass filter set to typically 10-100 Hz and a gain set to typically  $> 50$ . The signal from the SCU was demodulated by an SR830 lock-in amplifier [121] providing the in-phase and out-of-phase components of the signal. The sinusoidal output of the lock-in amplifier reference output itself was normally used to drive the solenoid generating the magnetic field. The time constant on the lock-in was typically set to 3 seconds with 12 dB/oct rolloff.

As shall be described in Section 3.2.2, a concern in the measurement was changes in the field measured by the fluxgate that could arise due to motion of the system components, or other temperature dependences. This could generate a false slope with temperature that might incorrectly be interpreted as a change in the magnetic properties of the witness cylinder.

To address possible motion of the witness cylinder with respect to the field generation system, another coil (the loop coil, also shown in Fig. 3.3) was wound on a plastic holder mounted rigidly to the witness cylinder. The coil was one loop of copper wire with a diameter of 9.7 cm. Plastic set screws in the holder fixed the loop coil to be coaxial with

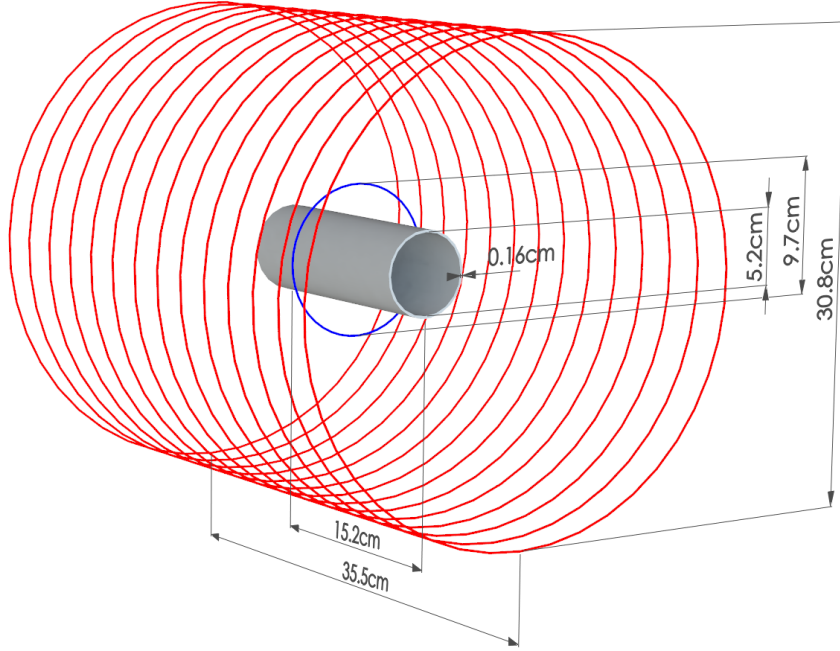


Figure 3.3: (color online) Axial shielding factor measurement setup. The witness cylinder with an inner diameter of 5.2 cm and a length of 15.2 cm is placed inside a solenoid (shown in red) with a diameter of 30.8 cm and a length of 35.5 cm, containing 14 turns. The thickness of the witness cylinder is  $1/16'' = 0.16$  cm. The loop coil (shown in blue) is mechanically coupled to the witness cylinder and has a diameter of 9.7 cm.

the witness cylinder.

Systematic differences in the results from the two coils (the solenoidal coil, and the loop coil) were used to search for motion artifacts. As well, some differences could arise due to the different magnetic field produced by each coil, and so such measurements could reveal a dependence on the profile of the applied magnetic field. This is described further in Section 3.2.2.

The temperature of the witness cylinder was measured by attaching four thermocouples at different points along the outside of the cylinder. This allowed us to observe the temperature gradient along the witness cylinder. To reduce any potential magnetic contamination, T-type thermocouples were used, which have copper and constantan conductors. (K-type thermocouples are magnetic.)

Thermocouple readings were recorded by a National Instruments NI-9211 temperature input module. The magnetic field (signified by the lock-in amplifier readout) and the temperature were recorded at a rate of 0.2 Hz.

Temperature variations in the experiment were driven by ambient temperature changes in the room, although forced air and other techniques were also tested. These are described further in Section 3.2.2.

## Data and Interpretation

An example of the typical data acquired is shown in Fig. 3.4. For these data, the field applied by the solenoid coil was  $1 \mu\text{T}$  in amplitude, at a frequency of 1 Hz. Fig. 3.4(a) shows the temperature of the witness cylinder over a 70-hr measurement. The temper-

ature changes of 1.4 K are caused by diurnal variations in the laboratory. The shielded magnetic field amplitude  $B_s$  within the witness cylinder is anti-correlated with the temperature trend as shown in Fig. 3.4(b). Here,  $B_s$  is the sum in quadrature of the amplitudes of the in-phase and out-of-phase components (most of the signal is in phase). The magnetic field is interpreted to depend on temperature, and the two quantities are graphed as a function of one another in Fig. 3.4(c). The slope in Fig. 3.4(c) has been calculated using a linear fit to the data. The relative slope at 23°C was found to be  $\frac{1}{B_s} \frac{dB_s}{dT} = -0.75\%/\text{K}$ .

Figs. 3.4(d), (e), and (f) show the same measurement with essentially the same settings, when the mu-metal witness cylinder is replaced by a copper cylinder. A similar relative vertical scale has been used in Figs. 3.4(e) and (f) as Figs. 3.4(b) and (c). This helps to emphasize the considerably smaller relative slope derived from panel (f) compared to panel (c). A variety of measurements of this sort were carried out multiple times for different parameters such as coil current. Running the coil at the same current tests for effects due to heating of the coil, whereas running the coil at a current which equalizes the fluxgate signal to its value when the mu-metal witness cylinder is present tests for possible effects related to the fluxgate. For all measurements the temperature dependence of the demodulated magnetic signal was  $< 0.1\%/\text{K}$ , giving confidence that unknown systematic effects contribute below this level.

Some deviations from the linear variation of  $B_s$  with  $T$  can be seen in the data, particularly in Figs. 3.4(a), (b), and (c). For example, when the temperature changes rapidly, the magnetic field takes some time to respond, resulting in a slope in  $B_s - T$  space that is temporarily different than when the temperature is slowly varying. This is typical of the data that we acquired, that the data would generally follow a straight line if the temperature followed a slow and smooth dependence with time, but the data would not be linear if the temperature varied rapidly or non-monotonically with time. We also tried other methods of temperature control, such as forced air, liquid flowing through tubing, and thermo-electric coolers. The diurnal cycle driven by the building's air conditioning system gave the most stable method of control and the most reproducible results for temperature slopes.

As mentioned earlier, data were acquired for both the solenoid coil and the loop coil. A summary of the data is provided in Table 3.1. Repeated measurements of temperature slopes using the loop coil fell in the range  $0.4\%/\text{K} < |\frac{1}{B_s} \frac{dB_s}{dT}| < 1.5\%/\text{K}$ . Similar measurements for the solenoidal coil yielded  $0.3\%/\text{K} < |\frac{1}{B_s} \frac{dB_s}{dT}| < 0.8\%/\text{K}$ .

In general, the slopes measured with the loop coil were larger than for the solenoidal coil. This is particularly evident for measurements 6-12, which were acquired daily over the course of a few weeks alternating between excitation coils but all used the same witness cylinder and otherwise without disturbing the measurement apparatus. A partial explanation of this difference is offered by the field profile generated by each coil, and its interaction with the witness cylinder. This is addressed further in Section 3.2.2.

The other difference between the loop coil and the solenoidal coil was that the loop coil was rigidly mounted to the witness cylinder, reducing the possibility of artifacts from relative motion. Given that this did not reduce the range of the measured temperature slopes we conclude that relative motion was well controlled in both cases.

Several other possible systematic effects were considered, all of which were found to give uncertainties on the measured slopes  $< 0.1\%/\text{K}$ . These included: thermal expansion of components including the witness cylinder itself, temperature variations of the magnetic shielding system within which the experiments were conducted, degaussing of

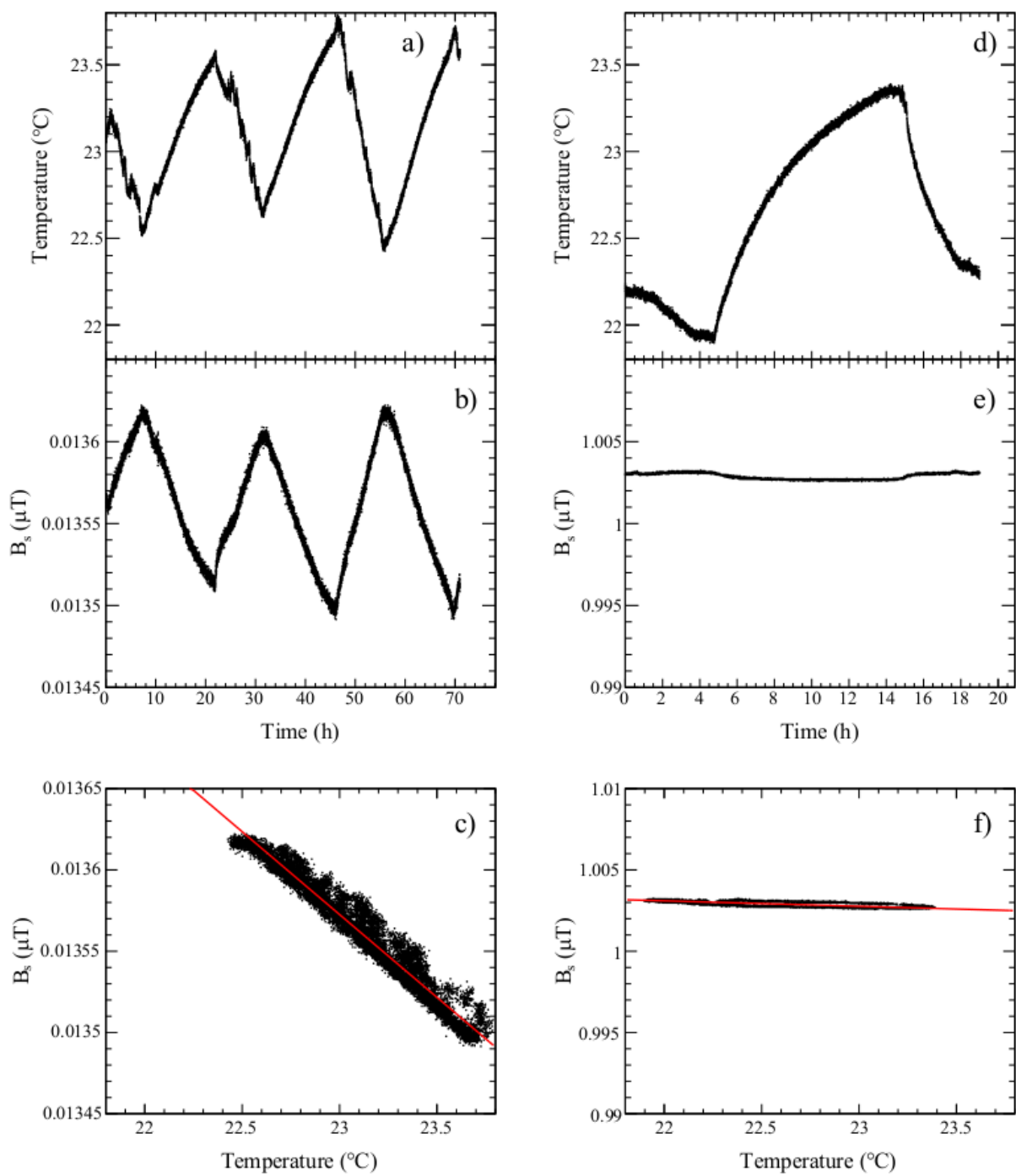


Figure 3.4: Ambient temperature and shielded magnetic field amplitude, measured over a 70 hour period. (a) temperature of the witness cylinder as a function of time. (b) magnetic field amplitude measured by fluxgate at center of witness cylinder vs. time. (c) magnetic field vs. temperature with linear fit to data giving  $\frac{1}{B_s} \frac{dB_s}{dT} = -0.75\%/\text{K}$  (evaluated at  $23^{\circ}\text{C}$ ). In panels (d), (e), and (f), the same quantities are shown for a 20-hour run with a copper cylinder in place of the witness cylinder with the linear fit giving  $\frac{1}{B_s} \frac{dB_s}{dT} = -0.03\%/\text{K}$ .

Trial #	$\frac{1}{B_s} \frac{dB_s}{dT}$ (%/K)	Coil type
1	-0.32	solenoid
2	-0.30	solenoid
3	-0.33	solenoid
4	-1.53	loop
5	-0.42	loop
6	-1.30	loop
7	-0.74	solenoid
8	-1.05	loop
9	-0.73	solenoid
10	-1.23	loop
11	-0.75	solenoid
12	-1.12	loop

Table 3.1: Summary of data acquired for the AC axial shielding factor measurements, in chronological order. Data with an applied field of  $\sim 1 - 6\mu T$  and a measurement frequency of 1 Hz are included. Data which used daily fluctuations of the temperature from 21-24°C over a 10-80 hour period are included. Other data acquired for systematic studies are not included in the table.

the witness cylinder, and temperature slopes of various components e.g. the fluxgate magnetometer and the lock-in amplifier.

As mentioned earlier in reference to Fig. 3.4(d), (e), and (f), the stability of the system was also tested by replacing the mu-metal witness cylinder with a copper cylinder and in all cases temperature slopes  $< 0.1\%/\text{K}$  were measured, giving confidence that other unknown systematic effects contribute below this level.

Based on the systematic effects that we studied, we conclude that they do not explain the ranges of values measured for  $\frac{1}{B_s} \frac{dB_s}{dT}$ . We suspect that the range measured is either some yet uncharacterized systematic effect, or a complicated property of the material. We use this range to set a limit on the slope of  $\mu(T)$

### Geometry correction and determination of $\mu(T)$

To relate the data on  $B_s(T)$  to  $\mu(T)$ , the shielding factor of the witness cylinder as a function of  $\mu$  must be known. Finite element simulations in FEMM and OPERA were performed to determine this factor. The simulations are also useful for determining the effective values of  $B_m$  and  $H_m$  in the material, which will be useful to compare to the case for typical nEDM experiments when the innermost shield is used as a flux return.

For closed objects, such as spherical shells [? ? ], the shielding factor approaches infinity as  $\mu \rightarrow \infty$ , and  $|\frac{\mu}{B_s} \frac{dB_s}{d\mu}| \rightarrow 1$ . Because the witness cylinders are open ended, the shielding factor asymptotically approaches a constant rather than infinity in the high- $\mu$  limit, and as a result  $|\frac{\mu}{B_s} \frac{dB_s}{d\mu}| < 1$  here. From the simulations the ratio  $\frac{\mu}{B_s} \frac{dB_s}{d\mu}$  was calculated. A linear model of the material was used where  $\mathbf{B}_m = \mu \mathbf{H}_m$  with  $\mu$  constant.

The simulations differed slightly in their results, dependent on whether OPERA or FEMM was used, and whether the solenoidal coil or loop coil were used. Based on the simulations, the result is  $|\frac{\mu}{B_s} \frac{dB_s}{d\mu}| = 0.42 - 0.50$  for the solenoidal coil, with the lower value being given by FEMM and the upper value being given by a 3D OPERA simulation, for

	$ \frac{\mu}{B_s} \frac{dB_s}{d\mu} $ (simulated)	$ \frac{1}{B_s} \frac{dB_s}{dT} $ (%/K) (measured)	$\frac{1}{\mu} \frac{d\mu}{dT}$ (%/K) (extracted)
Solenoidal Coil	0.42-0.50	0.3-0.8	0.6-1.9
Loop Coil	0.56-0.65	0.4-1.5	0.6-2.7

Table 3.2: Summary of OPERA and FEMM simulations and shielding factor measurements, resulting in extracted temperature slopes of  $\mu$ .

identical geometries. This is somewhat lower than the value suggested by Ref. [122] with fits to simulations performed in OPERA, which we estimate to be 0.6. We adopt our value since it is difficult to determine precisely from Ref. [122]. For the loop coil, we determine  $|\frac{\mu}{B_s} \frac{dB_s}{d\mu}| = 0.56 - 0.65$ , the range being given again by a difference between FEMM and OPERA.

Combining the measurement and the simulations, the temperature dependence of the effective  $\mu$  (at  $\mu_r = 20,000$  which is consistent with our measurements) can be calculated by equation (3.3). The results of the simulations and measurements are presented in Table 3.2. Combining the loop coil and solenoidal coil results, we find  $0.6\%/\text{K} < \frac{1}{\mu} \frac{d\mu}{dT} < 2.7\%/\text{K}$  to represent the full range for the possible temperature slope of  $\mu$  that observed in these measurements.

As stated earlier, the simulations also provided a way to determine the typical  $B_m$  and  $H_m$  internal to the material of the witness cylinder. According to the simulations, the  $B_m$  amplitude was typically  $100 \mu\text{T}$  and the  $H_m$  amplitude was typically  $0.004 \text{ A/m}$ . These are comparable to the values normally encountered in nEDM experiments, recalling from Section 3.1 that  $H_m < 0.007 \text{ A/m}$  for the innermost magnetic shield of an nEDM experiment. A caveat is that these measurements were typically conducted using AC fields at 1 Hz, as opposed to the DC fields normally used in nEDM experiments.

### 3.2.3 Transformer Core Measurements

An alternative technique similar to the standard method of magnetic materials characterization via magnetic induction was also used to measure changes in  $\mu$ . In this measurement technique, the witness cylinder was used as the core of a transformer. Two coils (primary and secondary) were wound on the witness cylinder using multistranded 20-gauge copper wire. The windings were made as tight as possible, but not so tight as to potentially stress the material. The windings were not potted in place. Three witness cylinders were tested. Data were acquired using different numbers of turns on both the primary and secondary coils (from 6 to 48 on the primary, and from 7 to 24 on the secondary).

Fig. 3.5 shows a picture of one of the witness cylinders, wound as described. It also shows a schematic diagram of the measurement setup, which we now use to describe the measurement principle.

The primary coil generated an AC magnetic field as a function of time  $H(t)$ , while the secondary coil was used to measure the emf induced by the time-varying magnetic flux proportional to  $dB(t)/dt$ . To a good approximation

$$H_m(t) = \frac{N_p I(t)}{2\pi R} \quad (3.4)$$

where  $N_p$  is the number of turns in the primary,  $I(t)$  is the current in the primary, and

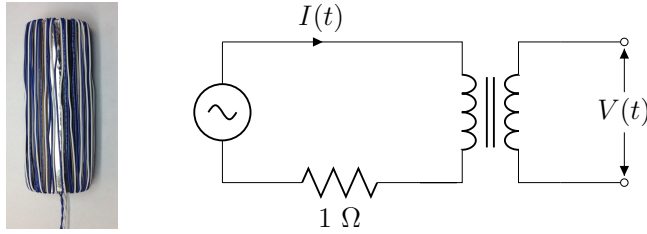


Figure 3.5: Photograph of a witness cylinder showing transformer windings (left) and schematic of the transformer measurement (right). The primary coil was driven by the sine-out of an SR830 lock-in amplifier, which was also used to demodulate induced voltage  $V(t)$  in the secondary coil. The driving current  $I(t)$  was sensed by measuring the voltage across a stable  $1 \Omega$  resistor.

$R$  is the radius of the witness cylinder, and

$$\frac{dB_m(t)}{dt} = \dot{B}_m(t) = \frac{V(t)}{b\ell} \quad (3.5)$$

where  $V(t)$  is the voltage generated in the secondary, and  $b$  and  $\ell$  are the thickness and length of the witness cylinder respectively. For a sinusoidal drive current  $I(t)$ , and under the assumption that  $B_m(t) = \mu H_m(t)$  with  $\mu$  being a constant, the voltage generated in the secondary  $V(t)$  should be sinusoidal and out of phase with the primary current.

The internal oscillator of an SR830 lock-in amplifier was used to generate  $I(t)$ . This was monitored by measuring the voltage across a  $1 \Omega$  resistor with small temperature coefficient in the primary loop. The lock-in amplifier was then used to demodulate  $V(t)$  into its in-phase  $V_X$  and out-of-phase  $V_Y$  components (or equivalently  $\dot{B}_m(t)$  being demodulated into  $\dot{B}_{m,X}$  and  $\dot{B}_{m,Y}$ , as in equation (A.21)). The experiment was done at 1 Hz with  $H_m(t)$  as small as possible, typically 0.1 A/m in amplitude, to measure the slope of the minor  $B_m - H_m$  loops near the origin of the  $B_m - H_m$  space.

The temperature of the core was measured continuously using the same thermocouple arrangement described previously. Measurements of  $V_Y$  as a function of temperature would then signify a change in  $\mu$  with temperature. In general, we used ambient temperature variations for the measurements, similar to the procedure used for our axial shielding factor measurements.

The naive expectation is that the out-of-phase  $V_Y$  component should signify a non-zero  $\mu$ , and the in-phase  $V_X$  component should be zero. In practice, due to a combination of saturation, hysteresis, eddy-current losses, and skin-depth effects, the  $V_X$  component is nonzero. It was found experimentally that keeping the amplitude of  $H_m(t)$  small compared to the apparent coercivity ( $\sim 3$  A/m for the 0.16 cm thick material at 1 Hz frequencies) ensured that the  $V_Y$  component was larger than the  $V_X$  component. This is displayed graphically in Fig. 3.6, where the dependence of  $\dot{B}_{m,Y}$  and  $\dot{B}_{m,X}$  on the amplitude of the applied  $H_m(t)$  is displayed, for a driving frequency of 1 Hz. Clearly the value of  $\dot{B}_{m,X}$  can be considerable compared to  $\dot{B}_{m,Y}$ , for larger  $H_m$  amplitudes near the coercivity. At larger amplitudes, the material goes into saturation. Both  $\dot{B}_{m,Y}$  and  $\dot{B}_{m,X}$  eventually decrease as expected at amplitudes much greater than the coercivity.

To understand the behavior in Fig. 3.6, a theoretical model of the hysteresis based on the work of Jiles [123] was used. The model contains a number of adjustable parameters. We adjusted the parameters based on our measurements of  $B_m - H_m$  loops including

the initial magnetization curve. These measurements were performed separately from our lock-in amplifier measurements, using an arbitrary function generator and a digital oscilloscope to acquire them. The measurements were done at frequencies from 0.01 to 10 Hz. It was found that the frequency dependence predicted by Ref. [123] gave relatively good agreement with the measured  $B_m - H_m$  loops once the five original (Jiles-Atherton [124, 125]) parameters were tuned.

For the parameters of the (static) Jiles-Atherton model, we used  $B_s = 0.45$  T,  $a = 3.75$  A/m,  $k = 2.4$  A/m,  $\alpha = 2 \times 10^{-6}$ ,  $c = 0.05$ , which were tuned to our  $B_m - H_m$  curve measurements. For classical losses, we used the parameters  $\rho = 5.7 \times 10^{-7}$  Ω·m,  $d = 1.6$  mm (the thickness of the material), and  $\beta = 6$  (geometry factor). These parameters were not tuned, but taken from data. For anomalous losses we used the parameters  $w = 0.005$  m and  $H_0 = 0.0075$  A/m, which we also did not tune, instead relying on the tuning performed in Ref. [123].

These parameters were then used to model the measurement presented in Fig. 3.6, including the lock-in amplifier function. As shown in Fig. 3.6, trends in the measurements and simulations are fairly consistent. The sign of  $\dot{B}_{m,X}$  relative to  $\dot{B}_{m,Y}$  is also correctly predicted by the model (we have adjusted them both to be positive, for graphing purposes). We expect that with further tuning of the model, even better agreement could be achieved.

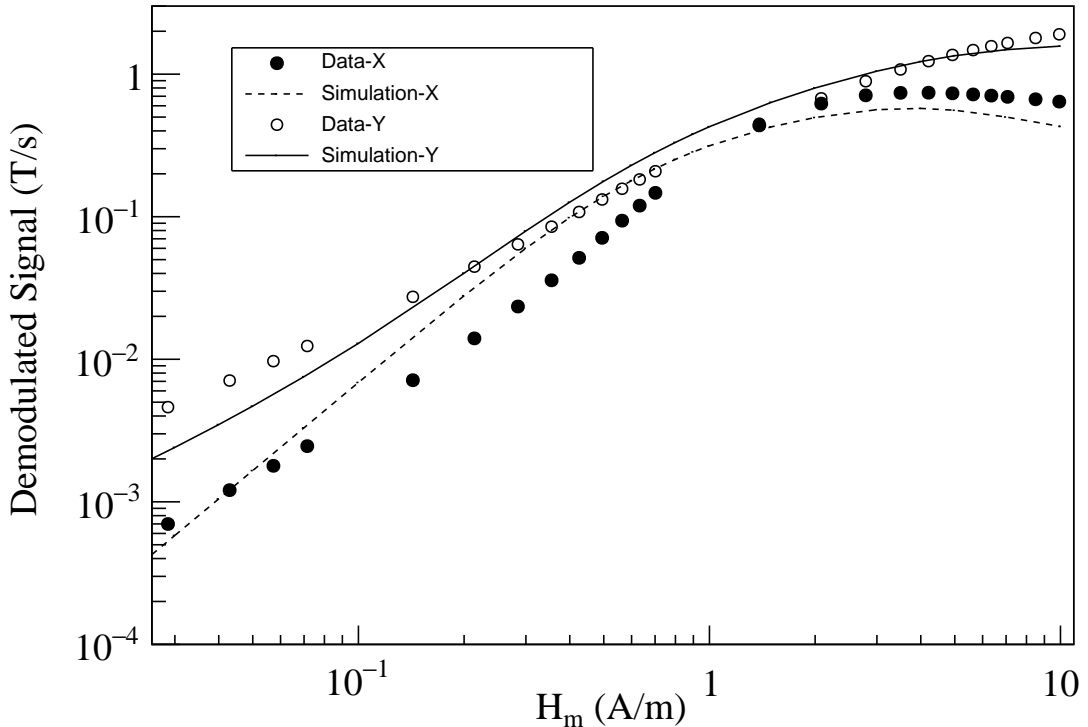


Figure 3.6:  $\dot{B}_{m,X}$  and  $\dot{B}_{m,Y}$  as a function of amplitude of the applied  $H_m$  field at 1 Hz. Points show the acquired data. Curves display the simulation based on the model described in the text.

The model of Ref. [123] makes no prediction of the temperature dependence of the parameters. Ideally, the temperature dependence of  $\dot{B}_{m,Y}$  and  $\dot{B}_{m,X}$  under various condi-

tions could be used to map out the temperature dependence of the parameters. However, this is beyond the scope of the present work.

We make the simplifying assumption that temperature dependence of  $\dot{B}_{m,Y}$  may be approximately interpreted as the temperature dependence of a single parameter  $\mu$ , i.e. that

$$\frac{1}{\dot{B}_{m,Y}} \frac{d\dot{B}_{m,Y}}{dT} = \frac{1}{\mu} \frac{d\mu}{dT}. \quad (3.6)$$

This is justified in part by our selection of measurement parameters (the amplitude of  $H_m = 0.1$  A/m and a measurement frequency of 1 Hz) which ensure that  $\dot{B}_{m,Y}$  dominates over  $\dot{B}_{m,X}$ .

We assign no additional systematic error for this simplification, and all our results are subject to this caveat. We comment further that in our measurements of the axial shielding factor (presented in Section 3.2.2), the same caveat exists. In that case the in-phase component dominates the demodulated fluxgate signal. In a sense, measuring  $\mu(T)$  itself is always an approximation, because it is actually the parameters of minor loops in a hysteresis curve which are measured. In reality, our results may be interpreted as a measure of the temperature-dependence of the slopes of minor loops driven by the stated  $H_m$ .

Measurements of  $\frac{1}{\dot{B}_{m,Y}} \frac{d\dot{B}_{m,Y}}{dT}$  as a function of  $T$  were made. In general, the data mimicked the behavior of the axial shielding factor measurements, giving a similar level of linearity with temperature as the data displayed in Fig. 3.4. Other similar behaviors to those measurements were also observed, for example: (a) when the temperature slope changed sign,  $\dot{B}_{m,Y}$  would temporarily give a different slope with temperature, (b) the measured value of  $\frac{1}{\dot{B}_{m,Y}} \frac{d\dot{B}_{m,Y}}{dT}$  depended on a variety of factors, most notably a dependence on which of the three witness cylinders was used for the measurement, and on differences between subsequent measurements using the same cylinder.

Table 3.3 summarizes our measurements of the relative slope  $\frac{1}{\dot{B}_{m,Y}} \frac{d\dot{B}_{m,Y}}{dT}$  for a variety of trials, witness cylinders, and numbers of windings. The data show a full range of  $0.03 - 2.15\%/\text{K}$  for  $\frac{1}{\mu} \frac{d\mu}{dT} = \frac{1}{\dot{B}_{m,Y}} \frac{d\dot{B}_{m,Y}}{dT}$ , again naively assuming the material to be linear as discussed above. The sign of the slope of  $\mu(T)$  was the same as the axial shielding factor technique.

A dominant source of variation between results in this method arose from properties inherent to each witness cylinder. One of the cylinders (referred to as  $\beta$  in Table 3.3) gave temperature slopes consistently larger  $\frac{1}{\mu} \frac{d\mu}{dT} \sim 0.88 - 2.15\%/\text{K}$  than the other two  $\frac{1}{\mu} \frac{d\mu}{dT} \sim 0.03 - 0.77\%/\text{K}$  (referred to as  $\alpha$  and  $\gamma$ , with some evidence that  $\gamma$  had a larger slope than  $\alpha$ ). We expect this indicates some difference in the annealing process or subsequent treatment of the cylinders, although to our knowledge the treatment was controlled the same as for all three cylinders. Since our goal is to provide input to future EDM experiments on the likely scale of the temperature dependence of  $\mu$  that they can expect, we phrase our result as a range covering all these results.

Detailed measurements of the effect of degaussing were conducted for this geometry. The ability to degauss led us ultimately to select a larger number of primary turns (48) so that we could fully saturate the core using only the lock-in amplifier reference output as a current source. A computer program was used to control the lock-in amplifier in order to implement degaussing. A sine wave with the measurement frequency (typically 1 Hz) was applied at the maximum lock-in output power. Over the course of several

Trial #	$\frac{1}{B_{m,Y}} \frac{dB_{m,Y}}{dT}$ (%/K)	core used
1	0.15	$\alpha$
2	0.03	$\alpha$
3	0.04	$\alpha$
4	0.06	$\alpha$
5	1.07	$\beta$
6	0.93	$\beta$
7	0.88	$\beta$
8	0.88	$\beta$
9	0.09	$\alpha$
10	1.23	$\beta$
11	2.15	$\beta$
12	1.85	$\beta$
13	1.20	$\beta$
14	0.77	$\gamma$

Table 3.3: Summary of data acquired for the transformer core measurements. Three different witness cylinders, arbitrarily labeled  $\alpha$ ,  $\beta$ , and  $\gamma$ , were used for the measurements. A 1 Hz excitation frequency was used with amplitudes for  $H_m$  ranging from 0.1 to 0.3 A/m. Fluctuations in the temperature ranged from 21-24°C and measurement times over a 10-80 hour period are included. Other data acquired for systematic studies are not included in the table.

thousand oscillations, the amplitude was decreased linearly to the measurement amplitude ( $\sim 0.1$  A/m). After degaussing with parameters consistent with the recommendations of Refs. [87, 106], the measured temperature slopes were consistent with our previous measurements where no degaussing was done.

Other systematic errors found to contribute at the  $< 0.1\%/\text{K}$  level were: motion of the primary and secondary windings, stability of the lock-in amplifier and its current source, and stability of background noise sources.

To summarize, the dominant systematic effects arose due to different similarly prepared cores giving different results, and due to variations in the measured slopes in multiple measurements on the same core. The second of these is essentially the same error encountered in our axial shielding factor measurements. We expect it has the same source; it is possibly a property of the material, or an additional unknown systematic uncertainty.

### 3.3 Relationship to nEDM experiments

Neutron EDM experiments are typically designed with the DC coil being magnetically coupled to the innermost magnetic shield. As discussed in Section 3.1, if the magnetic permeability of the shield changes, this results in a change in the field in the measurement region by an amount  $\frac{\mu}{B_0} \frac{dB_0}{d\mu} = 0.01$ .

The temperature dependence of  $\mu$  has been constrained by two different techniques using open-ended mu-metal witness cylinders annealed at the same time as our prototype

magnetic shields. We summarize the overall result as  $0.0\%/\text{K} < \frac{1}{\mu} \frac{d\mu}{dT} < 2.7\%/\text{K}$ , where the range is driven in part by material properties of the different mu-metal cylinders, and in part by day-to-day fluctuations in the temperature slopes.

We note the following caveats in relating this measurement to nEDM experiments:

- Although the measurement techniques rely on considerably larger frequencies and different  $H_m$ -fields than those relevant to typical nEDM experiments, we think it reasonable to assume the temperature dependence of the effective permeability should be of similar scale. For frequency, both techniques typically used a 1 Hz AC field, whereas for nEDM experiments the field is DC and stable at the 0.01 Hz level. Furthermore, in one measurement technique the amplitude of  $H_m$  was  $\sim 0.004 \text{ A/m}$  and in the other was  $\sim 0.1 \text{ A/m}$ . For nEDM experiments  $H_m < 0.007 \text{ A/m}$  and is DC.
- Both measurement techniques extract an effective  $\mu$  that describes the slope of minor loops in  $B_m - H_m$  space. A more correct treatment would include a more comprehensive accounting of hysteresis in the material, which is beyond the scope of this work.

Assuming our measurement of  $0.0\%/\text{K} < \frac{1}{\mu} \frac{d\mu}{dT} < 2.7\%/\text{K}$  and the generic EDM experiment sensitivity of  $\frac{\mu}{B_0} \frac{dB_0}{d\mu} = 0.01$  results in a temperature dependence of the magnetic field in a typical nEDM experiment of  $\frac{dB_0}{dT} = 0 - 270 \text{ pT/K}$ . To achieve a goal of  $\sim 1 \text{ pT}$  stability in the internal field for nEDM experiments, the temperature of the innermost magnetic shield in the nEDM experiment should then be controlled to the  $< 0.004 \text{ K}$  level if the worst-case dependence is to be taken into account. This represents a potentially challenging design constraint for future nEDM experiments.

As noted by others [126], the use of self-shielded coils to reduce the coupling of the  $B_0$  coil to the innermost magnetic shield is an attractive option for EDM experiments. The principle of this technique is to have a second coil structure between the inner coil and the shield, such that the net magnetic field generated by the two coils is uniform internally but greatly reduced externally. For a perfect self-shielded coil, the field at the position of the magnetic shield would be zero, resulting in perfect decoupling, which is to say a reaction factor that is identically unity. For ideal geometries, such as spherical coils [127–129] or infinitely long sine-phi coils [130–132], the functional form of the inner and outer current distributions are the same, albeit with appropriately scaled magnitudes and opposite sign. More sophisticated analytical and numerical methods have been used extensively in NMR and MRI to design self-shielded gradient [133, 134], shim [135, 136], and transmit coils [132, 137], and should be of value in the context of nEDM experiments, as well.

## 3.4 Conclusion

In the axial shielding factor measurement, we found  $0.6\%/\text{K} < \frac{1}{\mu} \frac{d\mu}{dT} < 2.7\%/\text{K}$ , with the measurement being conducted with a typical  $H_m$ -amplitude of  $0.004 \text{ A/m}$  and at a frequency of 1 Hz. In the transformer core case, we found  $0.0\%/\text{K} < \frac{1}{\mu} \frac{d\mu}{dT} < 2.2\%/\text{K}$ , with the measurement being conducted with a typical  $H_m$ -amplitude of  $0.1 \text{ A/m}$  and at a frequency of 1 Hz.

The primary caveat to these measurements is that both measurements (transformer core and axial shielding factor) do not truly measure  $\mu$ . Rather they measure observables

related to the slope of minor hysteresis loops in  $B_m - H_m$  space. They would be more appropriately described by a hysteresis model like that of Jiles [123], but to extract the temperature dependence of all the parameters of the model is beyond the scope of this work. Instead we acknowledge this fact and relate the temperature dependence of the effective  $\mu$  measured by each experiment.

We think it is interesting and useful information that the two experiments measure the same scale and sign of the temperature dependence of their respective effective  $\mu$ 's. This is a principal contribution of this work.

In future work, we plan to measure  $B_0(T)$  directly for nEDM-like geometries using precision atomic magnetometers. We anticipate based on the present work that self-shielded coil geometries will achieve the best time and temperature stability.

# Chapter 4

## Current UCN Facility at TRIUMF

The current vertical UCN cryostat at TRIUMF is the same UCN cryostat developed and tested at KEK-RCNP. In October 2016, the cryostat was shipped to triumf, and in 2017 it was installed at a dedicated spallation neutron source for further UCN experiments. The main purpose of such experiments were for better understanding of the vertical UCN source, and the design of the next generation UCN source for higher statistics. The 520 MeV cyclotron at TRIUMF provides up to  $40 \mu\text{A}$  of proton beam that can be diverted onto a tungsten spallation target. The vertical UCN source is placed above the target and is surrounded by graphite blocks serving as neutron reflectors.

The vertical source was modified to fulfill the Canadian safety requirements at TRIUMF. Those include installing pressure relief valves on the cryostat and the UCN guides, and additional radiation shielding. The extra shielding requires much longer UCN guides compared to RCNP. The current location of the vertical source is at the Meson Hall experimental area. A map of TRIUMF is shown in Fig. 4.1.

The unique feature of the UCN source at TRIUMF is the combination of spallation neutrons and superfluid helium for UCN production. The important elements of the UCN facility at TRIUMF are described below.

### 4.1 UCN Beam-line (BL1U)

TRIUMF produces negatively charged hydrogen ions  $H^-$  from an ion source. These ions are then accelerated in the 520 Mev cyclotron in an outward spiral trajectory. A thin graphite stripper foil removes the electrons from the hydrogen ion while protons can pass through. The proton, because it is a positively charged particle, is deflected in the outward direction due to the magnetic field, and is directed to a proton beam-line. The cyclotron has three independent extraction probes with various sizes of foils to provide protons to up to three beam-lines (BL) simultaneously (see Fig. 4.2).

The  $120 \mu\text{A}$  beam (BL1A) enters the Meson Hall, routinely delivers protons at 480 MeV to two target systems: T1 and T2 for the  $\mu\text{SR}$  experimental channels. Beam-line 1B (BL1B) separates off BL1 at the edge of the cyclotron vault, and provides international users with the Proton Irradiation Facility (PIF), which mimics space radiation for testing computer chips. The new BL1U provides beam to the UCN source. BL2A provides 480 MeV proton beams for the targets that produce exotic ion beams for a host of experiments in ISAC facilities.

The microstructure of BL1A is in pulses with approximately 1 ms periods of beam followed by a 50-100  $\mu\text{s}$  periods of no beam. This is shown in Fig. (4.4) [138]. A kicker

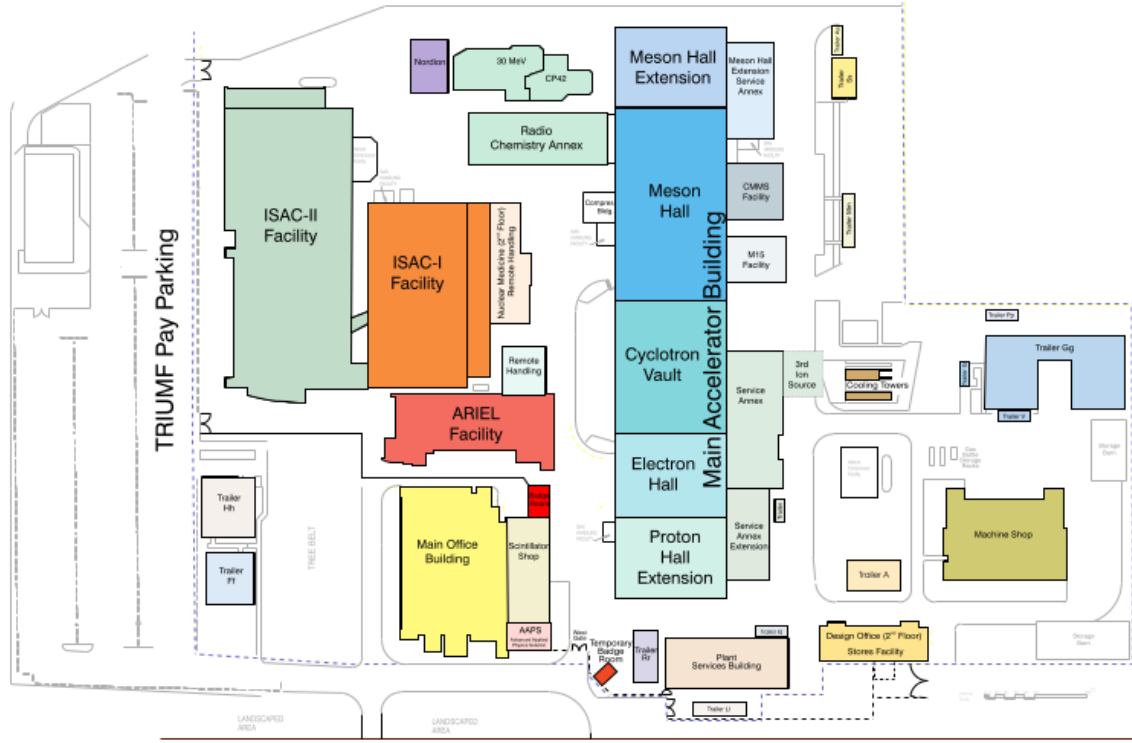


Figure 4.1: A map of TRIUMF. The UCN facility is located at the Meson Hall area shown in Blue.

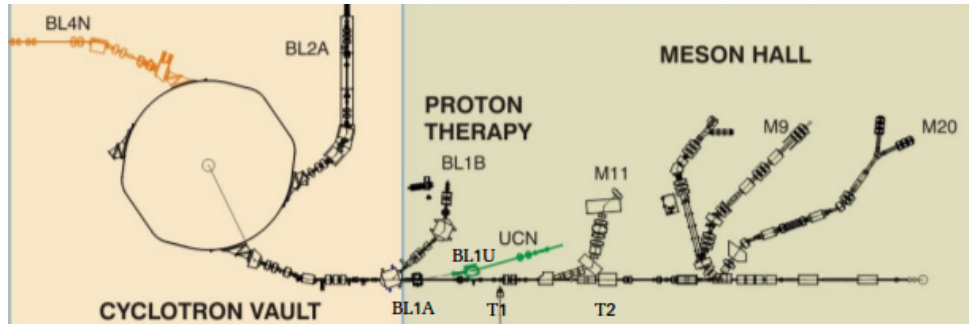


Figure 4.2: TRIUMF cyclotron and the three beam-lines.

magnet and the septum magnet kick away 1/3 of the beam from BL1A to BL1U and transport it to a conventional dipole (bender) magnet (see Fig. 4.3).

The vertical UCN cryostat is sitting above the tungsten target, and is designed for a maximum of 40  $\mu\text{A}$  beam on target. As a result, only one third of the beam can go to the UCN experimental area, and the rest is shared with other users.

After the bender magnet, the beam then passes through a cored shielding block, and reaches the two quadrupole magnets, providing the final focus of the beam onto a 12 cm thick tungsten spallation target. The target is located inside a hermetically-sealed target crypt, which also envelops the beam-line exit window that defines the end of BL1U. Upstream of the beam-line window, there is a collimator to reduce the halo from the proton beam, as well as to help reduce the amount of neutrons and photons streaming back into the beam-line from the target region (the collimator also increases the impedance for the

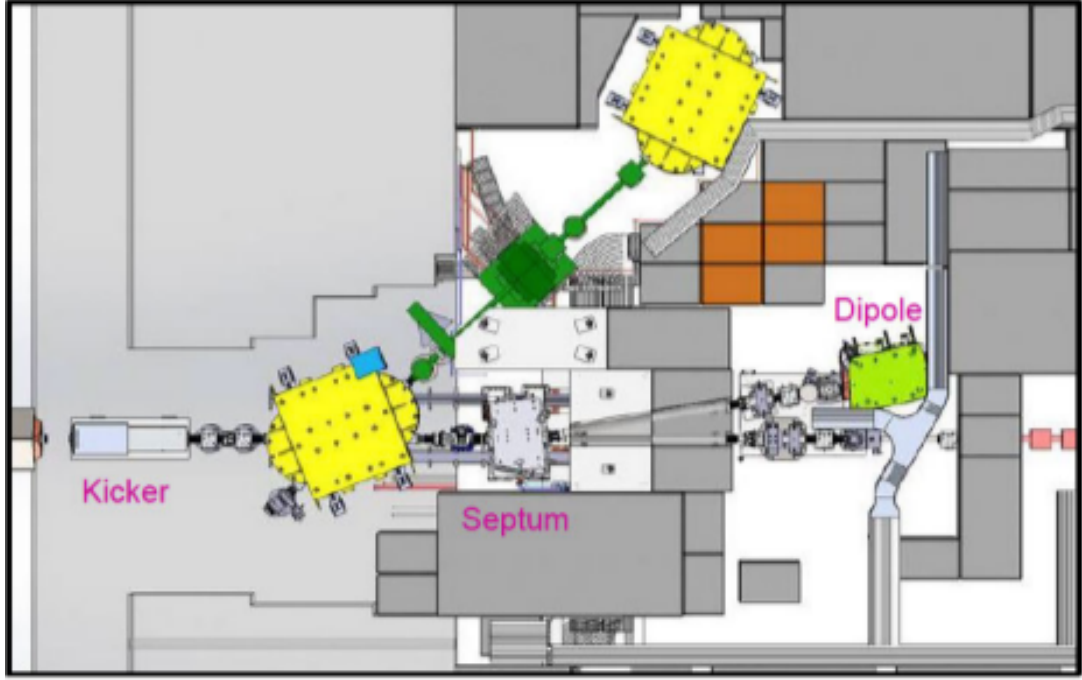


Figure 4.3: The kicker, septum and dipole (bender) magnets define the front two sections of BL1U.

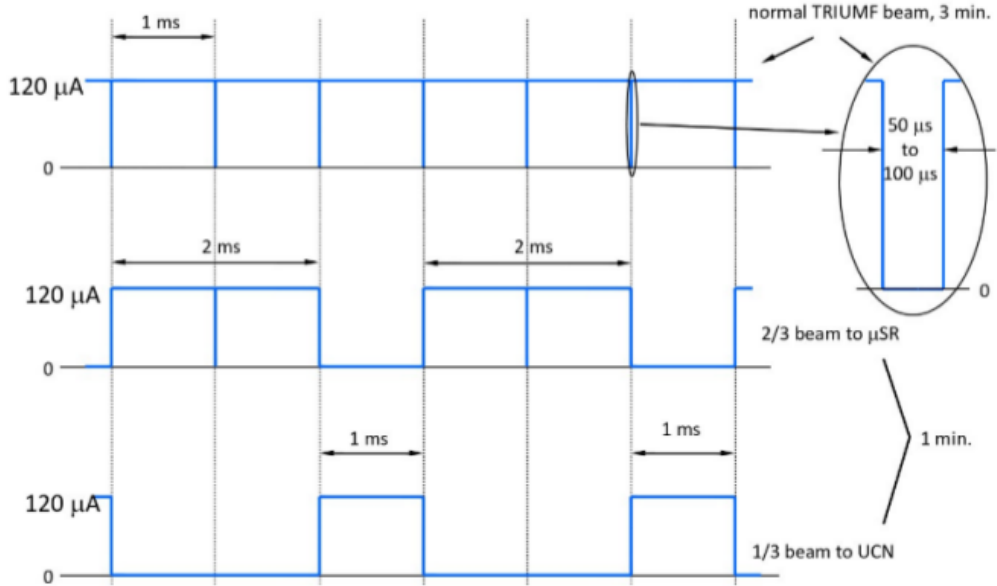


Figure 4.4: UCN beam structure. The top graph shows the  $120 \mu\text{A}$  BL1A in 1 ms period of beam followed by a 50-100  $\mu\text{s}$  of no beam. The middle graph shows the same beam-line when the kicker magnet is on. The bottom graph shows the 1/3 of the beam that goes to the UCN area.

passage of gas arising from any target or window failure, to allow time for the cyclotron fast valves to close). This last part of the beam-line also contains a variety of beam position and current monitors. The spallation target and UCN source, located downstream of the beam line-exit window, are enclosed in a large shielding pyramid Fig. 4.5.

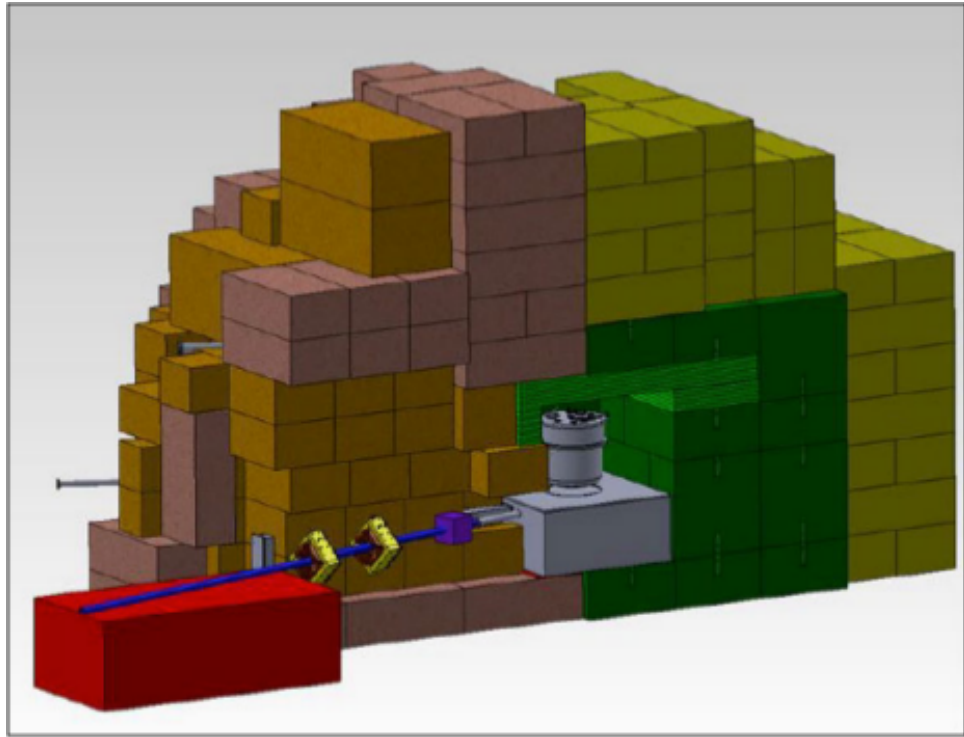


Figure 4.5: Two quadrupole magnets which focus the proton beam onto a 12 cm thick tungsten spallation target, located inside a hermetically-sealed target crypt. Also shown is the UCN shielding pyramid, which encases both the spallation target and the UCN source, and is designed to meet the dose rate requirements specified by the TRIUMF Safety Group.

## 4.2 Tungsten Spallation Target

The spallation target is located at the downstream end of BL1U. The UCN spallation target comprises a series of rectangular blocks, adding up to roughly one stopping length (11 cm) of tungsten, with a cross-section of  $\sim 6 \times 8 \text{ cm}^2$ . This geometry is very similar to (and motivated by) the neutron spallation target design used at KEK (KENS facility) [139]: five blocks of tungsten constitute the target with 78 mm height and 57 mm width, three with 20 mm length in beam direction and two with 30 mm length (see Fig. 4.6). The target requires a support and cooling system, and is designed to allow for remote-handling and ease of servicing. The target-cooling and remote-handling systems are designed for an instantaneous proton current of 40  $\mu\text{A}$  (10  $\mu\text{A}$  time-averaged). The target is being water-cooled. A water flow of approximately 0.8 L/s cools the target. Horizontal channels around the blocks create a uniform flow. To reduce the beam absorption in the water the last two blocks are thicker. Cooling water corrode tungsten. Therefore, a coating of tantalum with a thickness of  $< 0.1 \text{ mm}$  prevents corrosion by the water-cooling system. The estimated lifetime of the target is longer than 10 years. An extraction system allows to exchange the target when necessary.

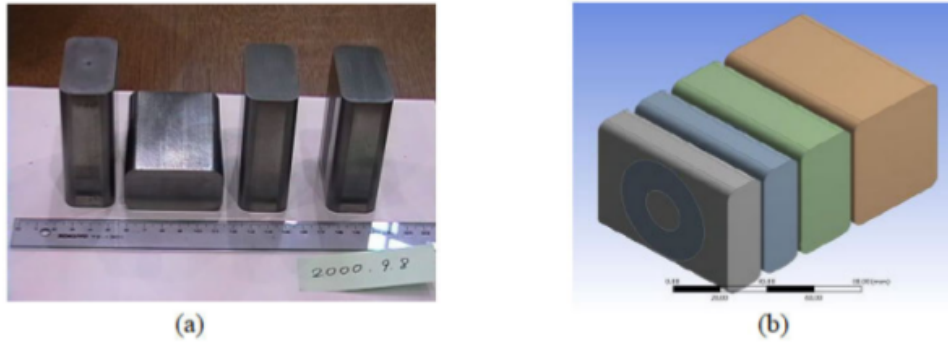


Figure 4.6: (a) Tungsten Target Blocks from the spallation target at KEK. The target blocks are plated with tantalum. (b) Present design for the tungsten spallation target at the TRIUMF UCN facility. The target blocks have a cross-section of  $5.7 \times 7.8 \text{ cm}^2$ , and thicknesses of 2.0, 2.0, 3.0, and 5.0 cm, respectively.

## 4.3 Vertical UCN Source at TRIUMF

At TRIUMF, neutrons are produced via the spallation process by hitting a tungsten target with a proton beam. Spallation is referred to a nuclear reaction where high energy particles interact with atomic nucleus. This process creates many high energy neutrons and background radiation. The target is surrounded by several blocks of lead and graphite. The fast neutrons are reflected and moderated down and enter the warm D<sub>2</sub>O moderator at room temperature (300 K) and become thermal neutrons with an energy of 0.025 eV, and the speed of 2.2 km/s. Iced heavy water at 10 K is used as a cold moderator. After passing through the warm D<sub>2</sub>O, thermal neutrons enter the cold moderator and become cold neutrons. These neutrons have the speed of several hundreds of meter per second. UCN are produced when the slow neutrons enter the isotopically pure superfluid helium at 0.84 to 0.92 K as a result of phonon transitions inside the superfluid helium as discussed in Section 1.5.

The schematic of the vertical source is shown in Fig. 4.7. The neutron moderators and the helium circulation system are explained below.

### 4.3.1 Neutron D<sub>2</sub>O Moderators

Deuterium is an isotope of hydrogen which has one proton and one neutron in the nucleus, and it has a lower probability to absorb neutrons. As a result, heavy water is used as a neutron moderator. The warm D<sub>2</sub>O moderator to create thermal neutrons from spallation neutrons is at room temperature. However, the cold moderator for the production of cold neutrons is at much lower temperatures ( $\sim 10$  K).

#### D<sub>2</sub>O Solidification

The Iced D<sub>2</sub>O vessel has a capacity of 100 L. About 14 L of liquid D<sub>2</sub>O is injected to the vessel initially. This is followed by adding 11 L of D<sub>2</sub>O to the vessel 8 times. After filling up the vessel, Gifford McMahon refrigerators solidify the heavy water and further cool it down to 20 K. The process of icing the heavy water takes about 6 days and cooling it down to 20 k takes another 7 days.

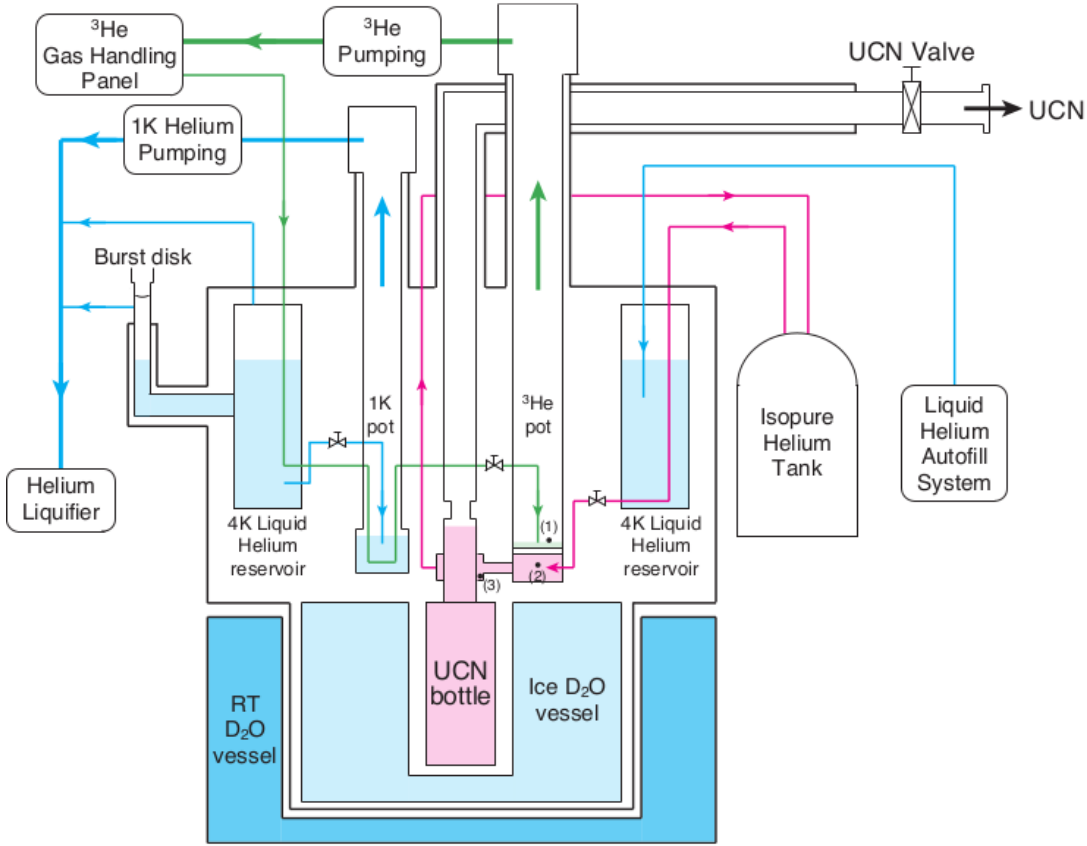


Figure 4.7: Schematic diagram of the vertical UCN source at TRIUMF. Spallation neutrons are moderated in warm  $D_2O$  vessel and become cold neutrons in Iced  $D_2O$ . The cold neutrons then enter the superfluid helium bottle where they become UCN by phonon excitations in the superfluid. The isotopically pure superfluid helium is cooled down to below 1 K via a  $^3He$  pot. The  $^3He$  pot is cooled down to 0.7 K via the 1 K pot and further pumping (see text for more details).

### 4.3.2 Helium Circulation and Superfluid Helium Condensation

The helium circulation and the superfluid helium condensation could get started once the temperature of  $D_2O$  is as low as 10 K. The stages towards superfluid helium condensation is presented below. The full operation and design details are available in Ref. [140].

#### 4 Kelvin Reservoir

The first step of the helium circulation is to fill up the helium reservoir with the commercially available 4.2 K helium. The full capacity of the helium reservoir is 50 L. In the 2017 experimental run, the TUCAN collaboration used a labview program to automatically fill up the reservoir using a 500 L dewar of 4.2 K helium. This dewar was referred to as the “stationary dewar”. This way, it is possible to set the desired minimum and maximum levels of the helium in the 4 K reservoir, and set it to automatically get filled once it hits the minimum value, and stop filling once it reaches the maximum value. The helium levels were measured by level meters. In addition, two flow meters were used to observe the gas flow and evaporation of the superfluid in the 4 K reservoir (FM4 and FM5 in Fig. D.1. The DAQ system and sensor positions are described in Section. 4.4 and the

gas flow diagram is available in Fig. D.1. The stationary dewar was filled up with 350 L dewars ( we reffered to them as “transfer dewar”) of 4 K helium from the meson hall liquifier. The helium autofill system is shown in Fig. 4.8.

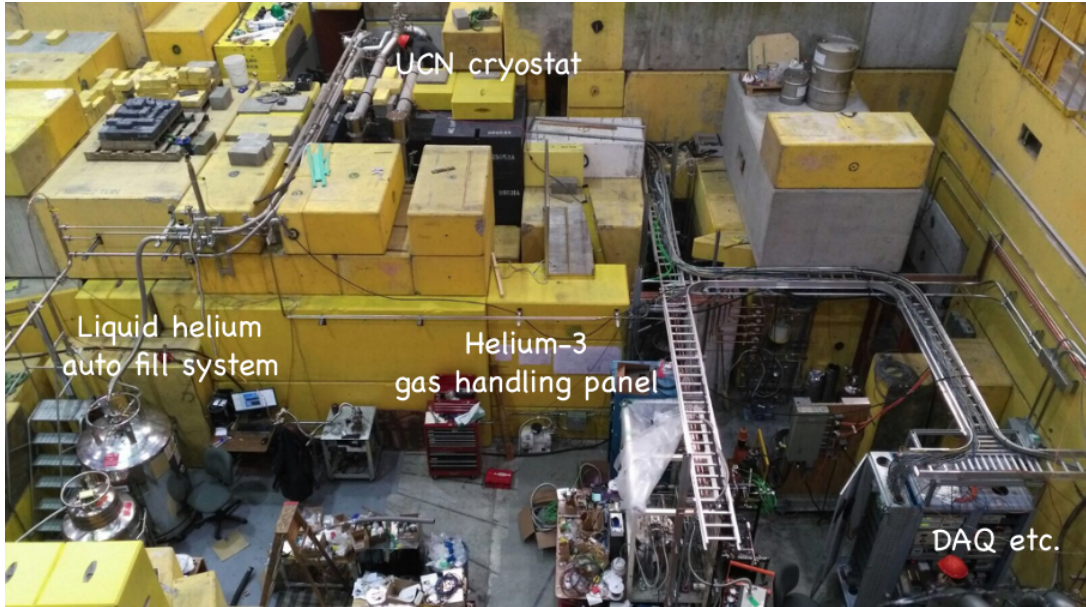


Figure 4.8: A photograph of the UCN experimental area during the mini shutdown in October 2017. Some experimental components are shown and are labeled. The yellow concrete blocks are blocking the radiation during the target irradiation times. The vertical UCN cryostat could be seen because of the removal of some radiation shielding.

Fig. 4.9 shows the 5 filling cycles of the 4 K reservoir on April 22, 2017 during the first cool down test. The liquid helium transfer starts once the liquid level in the 4 K reservoir reaches 20%. Once the transfer starts, the liquid level starts to decrease with a sharper slope. This is because of the introduced heat load to the reservoir. It takes some time to cool down the transfer line from the stationary dewar to the reservoir. The warm liquid helium causes a boil off in the 4 K reservoir. The boiled off helium gas goes through the recovery line to the liquifier. The liquid helium transfer stops once the 4 K reservoir is 60% filled.

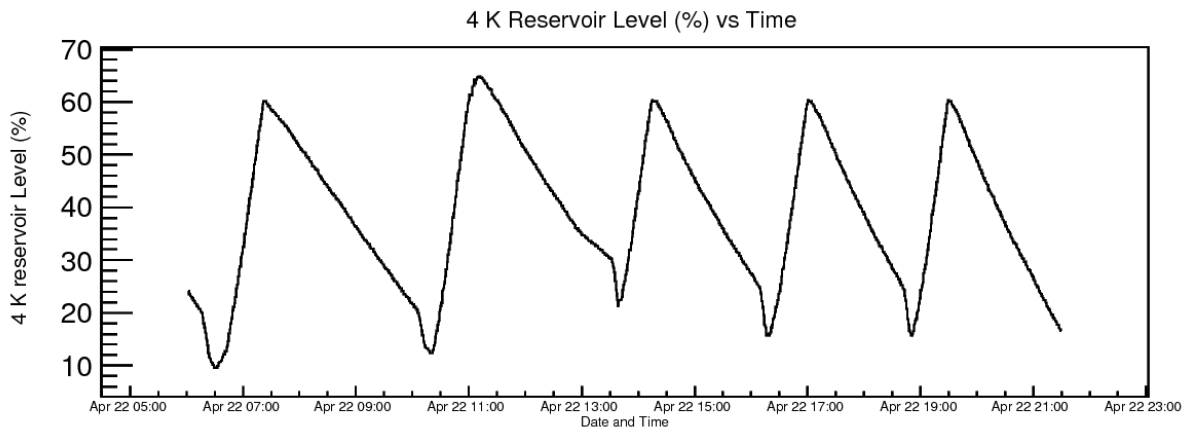


Figure 4.9: The 4 K reservoir filling during the cool down test in April 2017.

The efficiency of each transfer from the stationary dewar to the 4 K reservoir was about 40% to 60% on average.

## 1 Kelvin Pot

The 4.2 K liquid helium in the helium reservoir is transferred to a pot called “1 K pot”. The flow rate of the transferred liquid helium is controlled by a needle valve. The 1 K pot is always pumped by a pumping system to cool the 4.2 K helium down to about 1.4 K. The level of helium in the 1 K pot is measured by a liquid level meter. The maximum level of the 1.4 K liquid helium is about 15 cm. At this level, the volume of the 1.4 K liquid helium is about 1.3 L.

## $^3\text{He}$ Pot

Once the 1 K pot is ready, the  $^3\text{He}$  circulation starts to condense helium into the “ $^3\text{He}$  pot”. To start, the needle valve in the  $^3\text{He}$  reservoir is opened. A vacuum pump compresses the  $^3\text{He}$  gas. The  $^3\text{He}$  gas is then purified by a room temperature and a cold purifier and enters the 4 K reservoir to get precooled. The further cooling down to 1 K, and condensation happen via the 1 K pot. The liquid  $^3\text{He}$  is then transferred to the  $^3\text{He}$  pot, and is further cooled down to 0.7 K via pumping. The evaporated  $^3\text{He}$  is pumped out and goes through an oil filter and goes back to the beginning point of the circulation.

## Isopure Helium

After filling the  $^3\text{He}$  pot with 0.7 K liquid  $^3\text{He}$ , the condensation of the isotopically pure (isopure) superfluid helium starts. The isopure helium has much less  $^3\text{He}$  than  $^4\text{He}$  (less than  $10^{-10}$ ). Even though the natural abundance of  $^3\text{He}$  is  $1.37 \times 10^{-6}$  in the atmosphere, this value is still large because of the large neutron absorption cross section of  $^3\text{He}$ . The existence of  $^3\text{He}$  causes the UCN storage lifetime to decrease (see Section 1.5.1).

The isopure helium is stored in the isopure helium tank shown in Fig. 4.7. Before entering the cryostat, the isopure helium goes through a purifier. The purifier is composed of low temperature charcoals cooled by  $\text{LN}_2$ . The isopure He is precooled in the 4 K reservoir and goes into the heat exchange pot attached to the bottom of the  $^3\text{He}$  cryostat. The bottom of the  $^3\text{He}$  cryostat and the top of the heat exchange pot is connected via the copper heat exchanger. The isopure He in the heat exchange pot is cooled by the 0.7 K liquid  $^3\text{He}$  via the copper heat exchanger and becomes He-II. The condensed He-II fills the He-II bottle with a volume of 8.5 L and gets cooled down to  $\sim 0.83$  K.

## 4.4 Data Acquisition System

The TUCAN UCN DAQ system accumulates data from different devices and integrates them into a MIDAS file.

For the 2017 data acquisition, almost all the sensors such as temperature sensors, flow meters, pressure gauges and etc., were connected to a Programmable Logic Controller (PLC). The PLC receives information from the connected sensors or input devices, processes the data, and triggers outputs based on pre-programmed parameters. Depending on the inputs and outputs, a PLC can monitor and record data, automatically start and stop processes, generate alarms based on the applied limits, and more. A picture of the PLC is shown in Fig. 4.10.

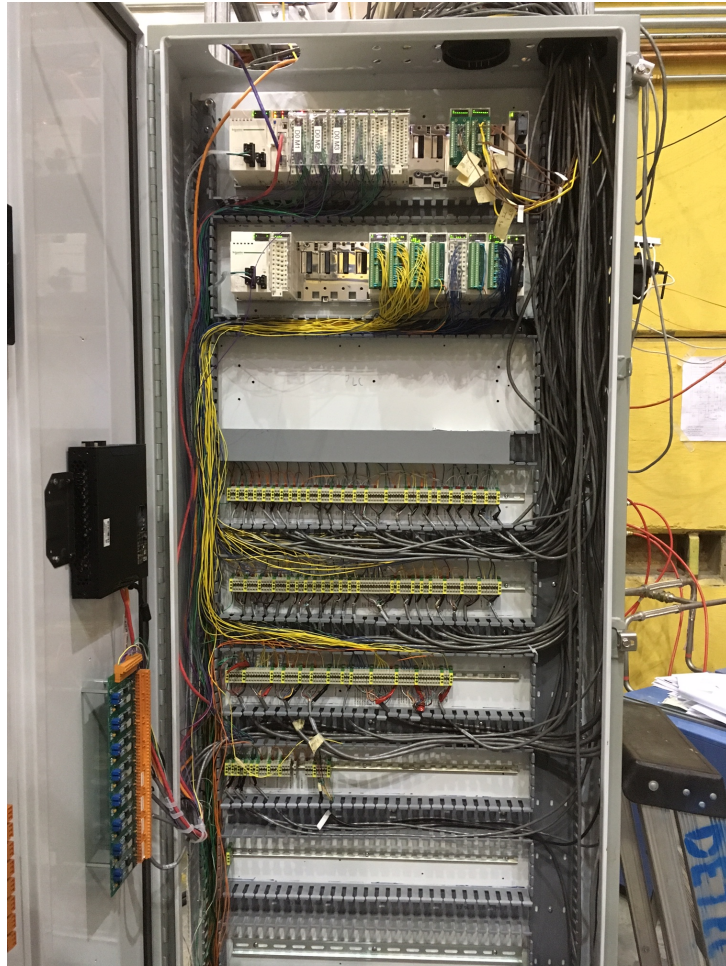


Figure 4.10: A photograph of the PLC in the meson hall. The grey terminal blocks are used to connect the signal from the devices to the computing modules. The first two top rows include the computing modules. Each sensor is connected to a specific terminal on a specific module. The bottom row is where the power supplies and the fuses are positioned.

The communication between the PLC and the screen is handled by EPICS. The EPICS screen defines the user interface for the controls. It provides readouts of variables, indications of device status, and various user input controls for turning devices on/off, resetting devices, etc. The screen shows the approximate physical layout of the apparatus being controlled, with each device and its controls placed in its actual location. The colours of the devices are used to indicate their current status [141]. Fig. 4.11 shows the thermal EPICS screen for the TUCAN vertical UCN source during the November 2017 experimental run. The gas flow screen (not shown, very similar to the thermal screen) is intended to contain all the information about pressures, flows, levels, and controls for pumps and valves.

MIDAS is a modern data acquisition system developed at PSI and TRIUMF written in C/C++ which runs on all operating systems. MIDAS logs data in two different ways: History logging where some data is saved periodically (every 1-10 s) and can be plotted from history page and file logging where all data is saved to MIDAS file to be analyzed later. The TUCAN MIDAS DAQ has a web interface shown in Fig. 4.12. The green color indicates that the equipment frontend is running. Each run can be started by pressing

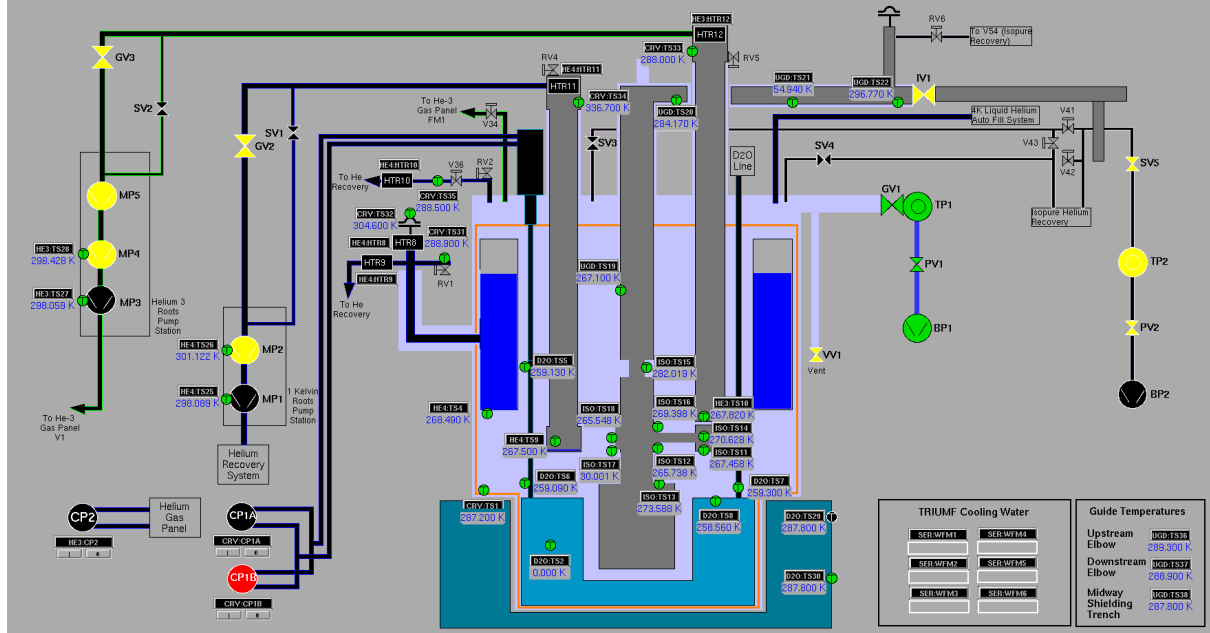


Figure 4.11: EPICS thermal screen. The approximate location of each temperature sensor is shown. The thermal screen is intended to contain all the information about temperatures, and controls for compressors and heaters.

the button at the top section.

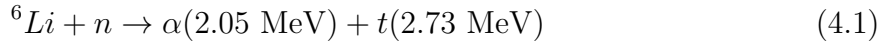
For the 2017 experimental run, each experiment had a unique MIDAS run number. The MIDAS files were then converted to ROOT files for data analysis. The result of the analysis is presented in Chapter 5.

## 4.5 UCN Detectors

For the TUCAN experimental runs in 2017, a  ${}^6\text{Li}$  and a  ${}^3\text{He}$  detector were used. The main reason for this was to check the consistency of the result, and the performance of each detector. The brief description of each detector is available below.

#### 4.5.1 ${}^6\text{Li}$ Detector

The main detector used during the UCN measurements (see Chapter 5) is a  ${}^6\text{Li}$  glass based scintillator detector designed and built at the University of Winnipeg for the TUCAN nEDM experiment at TRIUMF [83]. Since  ${}^6\text{Li}$  has a high neutron capture cross-section (order of  $10^5$  bn) at UCN energies, the scintillator glass is doped with it. The charged particles in the reaction



are detected. To reduce the effect of  $\alpha$  or triton escaping the glass, a layer of 60  $\mu\text{m}$  thick depleted  ${}^6\text{Li}$  glass (GS30), on top of a layer of 120  $\mu\text{m}$  thick dopped  ${}^6\text{Li}$  (GS20) were optically bonded. This design allows the resultant particles to deposit all of their energy within the scintillating glass. Table 4.5.1 shows the content and density of those  ${}^6\text{Li}$  scintillators.

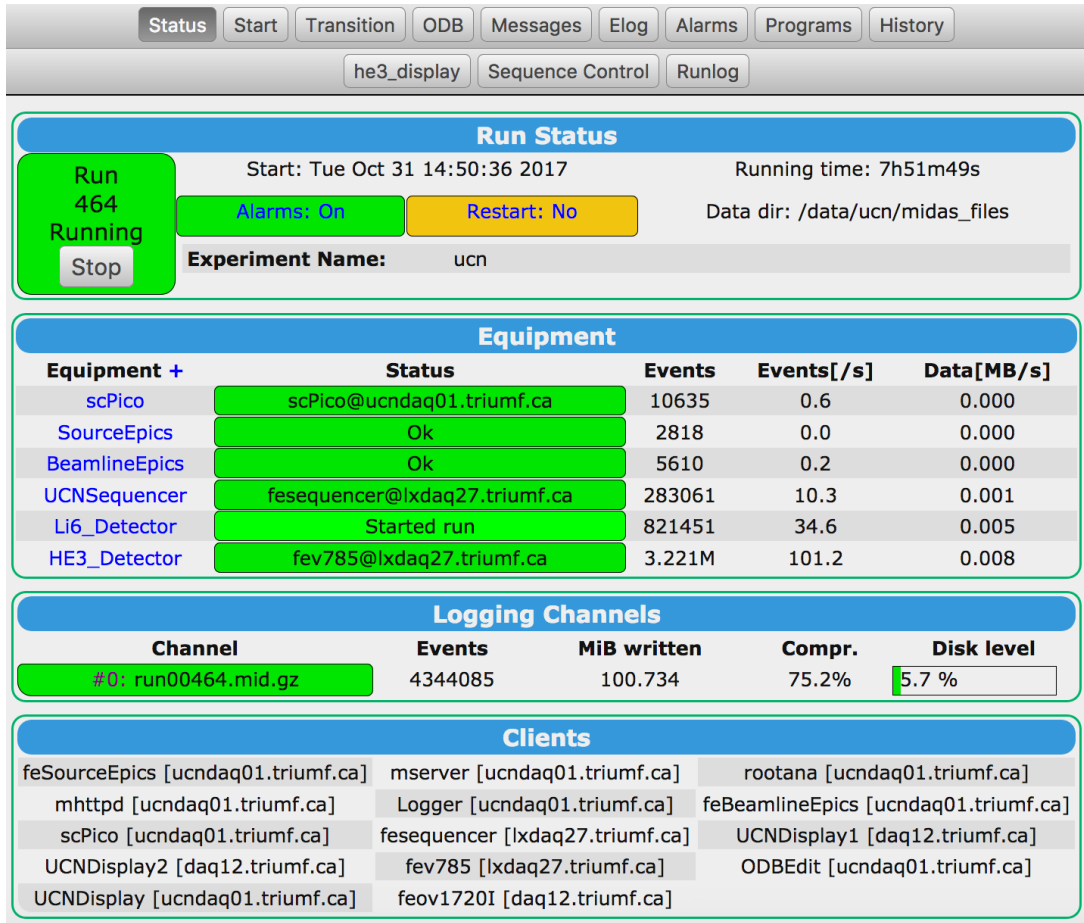


Figure 4.12: TUCAN MIDAS web interface

Scintillator	GS20 ( ${}^6\text{Li}$ Enriched)	GS30 ( ${}^6\text{Li}$ depleted)
Total Li content (%)	6.6	6.6
${}^6\text{Li}$ fraction (%)	95	0.01
${}^6\text{Li}$ desity ( $\text{cm}^{-3}$ )	$1.716 \times 10^{22}$	$1.806 \times 10^{18}$

Table 4.1: Properties of the glass scintillators

Making the scintillating Li glass as thin as possible reduces the sensitivity to  $\gamma$ -ray scintillating backgrounds, and thermal neutron captures. The mean range of the  $\alpha$  is  $5.3 \mu\text{m}$ , and the mean range of the triton is  $34.7 \mu\text{m}$ . This means, if the thickness of the scintillator is less than  $50 \mu\text{m}$ , the resultant particles escape before stopping which gives rise to an efficiency loss. In order to handle high UCN rates of up to  $\tilde{1} \text{ MHz}$ , the  ${}^6\text{Li}$  detector face is segmented into 9 tiles (see Fig. 4.13). The scintillation light is then guided through ultra-violet transmitting acrylic light-guide to its corresponding Photomultiplier Tube (PMT) outside the vacuum region of the detector.

The data acquisition with this detector includes a CAEN V1720 digitizer which has a Pulse-Shape Discrimination (PSD) firmware that triggers on pulses below a certain threshold for each channel. Every 4 ns the digitizer samples the waveform which is then digitized to a voltage on a 2 V scale into an ADC value between 0 and 4096. Each channel of the digitizer sends a trigger, whenever the number of counts in the ADC goes below a certain baseline (pedestal) value. The PSD calculates the sum of the signal below the

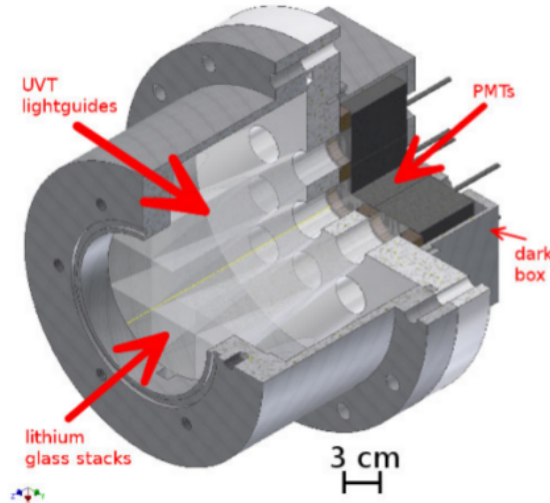


Figure 4.13: 3D drawing of the  ${}^6\text{Li}$  detector and its enclosure. The enclosure is made of Al, and the rim of the adapter flange which UCN can hit is ccoated with  $1 \mu\text{m}$  Ni by thermal evaporation.

baseline for two time windows:  $t_s = 40 \text{ ns}$  (short gate) and  $t_L = 200 \text{ ns}$  (long gate). The short gate is chosen in a way to contain all of the charge for the  $\gamma$ -ray interactions in the light-guide. The ADC sum for during the long gate below the baseline is calle  $Q_L$  (read charge long) and for during the short gate below the baseline is called  $Q_S$  (read charge short). Charge long has the total charge deposit for the neutron capture events. The PSD value is defined as

$$\text{PSD} = \frac{(Q_L - Q_S)}{Q_L}, \quad (4.2)$$

which is the amount of charge in the tail of an event.

Jamieson *et al.*, showed that the absolute efficiency of this detector is  $89.7^{+1.3}_{-1.9} \%$  with a background contamination of  $0.3 \pm 0.1 \%$  [83]. The detector is stable at the 0.06 % level or better, and that the variation in the efficiency between the detector tiles is less than 5 %.

### 4.5.2 ${}^3\text{He}$ Detector

The  ${}^3\text{He}$  detector used for the data acquisition is a Dunia-10 type which was shipped from RCNP.  ${}^3\text{He}$  provides an effective neutron detector material for neutron detection by absorbing neutrons via the following reaction



Before the start of the experiment, the  ${}^3\text{He}$  detector was tested with an AmBe source, and it showed consistent result with what was observed at RCNP. The detector was surrounded with paraffin blocks to moderate the neutrons (see Fig. 4.14).

More detail about the  ${}^3\text{He}$  detector could be found in Ref. [140].



Figure 4.14:  ${}^3\text{He}$  detector and paraffin blocks for neutron moderation.



# Chapter 5

## UCN Production and Detection

In November of 2017, the first UCN at TRIUMF were produced using the prototype vertical UCN source described in Section 4.3. Here the spallation neutrons are converted to UCN through phonon excitation in the isotopically pure superfluid helium. Several experiments were performed with the UCN including UCN yield measurements, UCN storage lifetime measurements and steady-state UCN production. These experiments are essential for the better understanding of the vertical source, and to design the next generation high intensity UCN source. In this chapter those experiments are described and the result of the data analysis is presented.

### 5.1 UCN Cycle of Measurement

Fig. 5.1 is a simple schematic of UCN production and detection volumes. This simplified sketch helps understand the UCN trade between different volumes and understand the concepts without getting distracted with too many details. Here volume  $V_1$  is the production and storage volume before the valve, where  $N_1$  number of UCN are produced.  $V_2$  is the secondary volume, where  $N_2$  number of UCN could enter after the valve is opened, and  $V_3$  is the detector volume where  $N_3$  number of UCN could reach the detector.

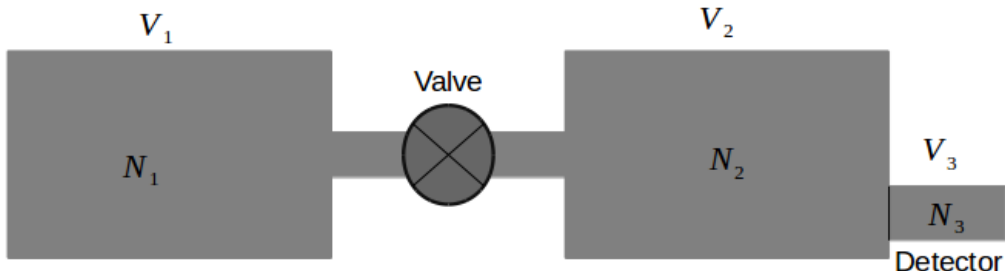


Figure 5.1: Schematic drawing of a simple UCN source.  $V_1$  is the production volume with  $N_1$  number of UCN,  $V_2$  is the secondary volume where  $N_2$  number of UCN exist, and  $V_3$  is the detector with  $N_3$  number of UCN.

At  $t = 0$ , when the beam is on and the valve is closed, the number of UCN in  $V_1$  goes up, while the total number of UCN in  $V_2$  and  $V_3$  is zero. This is described with

$$\frac{dN_1}{dt} = P - \frac{N_1}{\tau_1}, \quad (5.1)$$

where  $P$  is the UCN production rate in the source, as described in Section 1.5.2, and  $\tau_1$  is the UCN storage lifetime in the source. After the beam is turned off, the valve is opened, and UCN could travel to the volume  $V_2$  and eventually volume  $V_3$ . In our measurements, the valve is usually left open for 2 minutes. The UCN trade between  $V_1$ ,  $V_2$  and  $V_3$  is described by the differential Eqn. 5.2.

$$\begin{aligned} \frac{dN_1}{dt} &= -\frac{N_1}{\tau_{c,1}} - \frac{N_1}{\tau_1} + \frac{N_2}{\tau_{c,2}} \\ \frac{dN_2}{dt} &= \frac{N_1}{\tau_{c,1}} - \frac{N_2}{\tau_{c,2}} - \frac{N_2}{\tau_2} - \frac{N_2}{\tau_{c,3}} \\ \frac{dN_3}{dt} &= \frac{N_2}{\tau_{c,3}}. \end{aligned} \quad (5.2)$$

In these equations,  $\frac{dN_1}{dt}$  shows the change in the UCN counts over time in  $V_1$ ,  $\frac{dN_2}{dt}$  shows the change in the UCN counts in  $V_2$ , and  $\frac{dN_3}{dt}$  shows the change in the UCN count in  $V_3$ , after the valve is opened. Each term in the right side of the equations is described below.

The total number of UCN in  $V_1$  depends on three factors: the UCN that get into  $V_2$  ( $\frac{N_1}{\tau_{c,1}}$ ), the UCN that is lost with the storage lifetime  $\tau_1$ , and the UCN that bounce back from  $V_2$  to  $V_1$  ( $\frac{N_2}{\tau_{c,2}}$ ). In  $V_2$ , some UCN cross from  $V_1$  to  $V_2$  ( $\frac{N_1}{\tau_{c,1}}$ ), some get lost with the loss rate  $\tau_2$  ( $\frac{N_2}{\tau_2}$ ), some cross the gate valve and go back to  $V_1$  ( $\frac{N_2}{\tau_{c,2}}$ ), and some get to the detector ( $\frac{N_2}{\tau_{c,3}}$ ). The rate of the UCN detection  $\frac{dN_3}{dt}$  is the number of UCN crossing from  $V_2$ . In principle, solving these equations could give an estimate of the number of UCN in each volume.

A 3D drawing of the experimental setup is shown in Fig. 5.2. In this case,  $V_1$  is the UCN source bottle, and the horizontal section of the UCN guide before the UCN gate valve, and  $V_2$  and  $V_3$  are the volumes after the UCN valve and the detector volume respectively.

The process of UCN production described above is referred to the UCN production in the “batch mode”, since the UCN is accumulated in the source while the UCN valve is left closed. Here the target is irradiated, and the UCN are produced in the source. After the irradiation stops, the UCN valve is opened, and UCN could bounce off the guide walls and reach the detector volume. In our standard UCN production measurements, the applied beam current is  $1 \mu\text{A}$ , and the target is irradiated for 60 s. One cycle of measurement is shown in Fig. 5.3. The UCN valve is typically left open for 2 minutes. The end of a UCN cycle is defined by the UCN valve close time. Once the UCN valve is closed, a new cycle of measurement starts.

Another possible mode of operation is when we leave the UCN valve open while irradiating the target. This is called the “steady-state mode” where we have a constant stream of UCN to the main detector (see Section 5.3.4).

The following sections are focused on the result of the UCN yield optimization, the UCN storage lifetime measurements, UCN production in the steady-state mode and the comparison of those measurements with simulations.

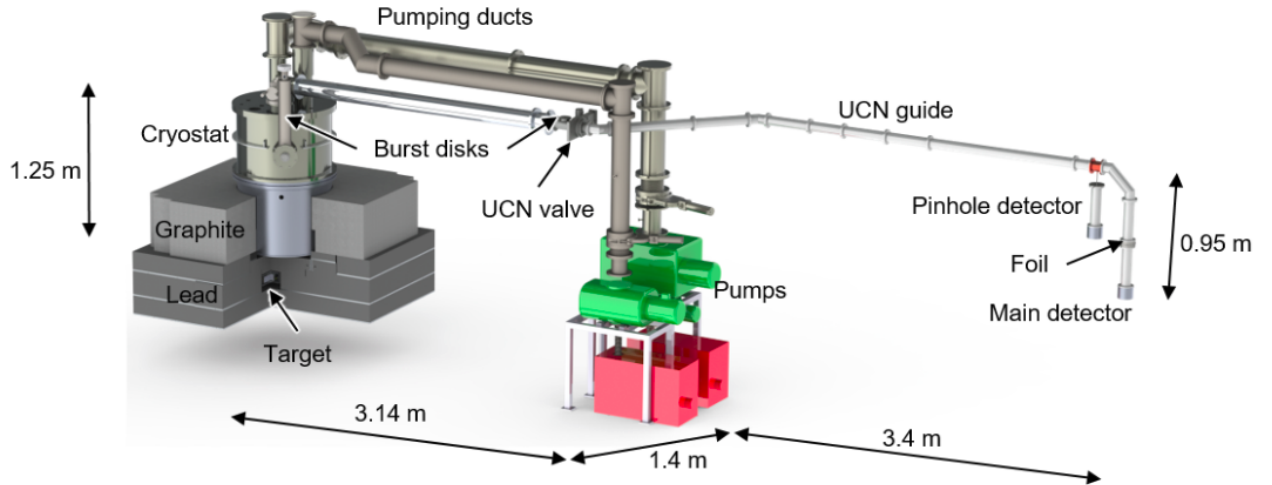


Figure 5.2: The UCN source and the guide geometry at TRIUMF

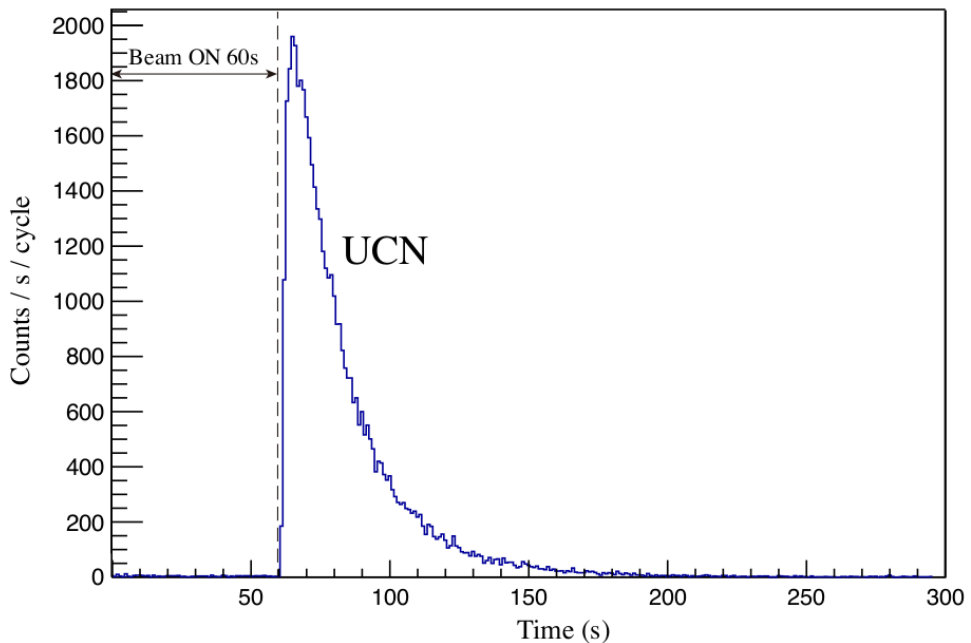


Figure 5.3: The figure shows the UCN rate at 60 s irradiation time, and 1  $\mu$ A beam current. In this case, the UCN gate valve is opened immediately after the end of target irradiation. At this time, the UCN rate reaches the peak of about 2000 UCN/s. The UCN rate decays down to the background level. The valve is left open for 120 s.

## 5.2 Data Quality Checks

During the 2017 experimental run, we performed about 35 experiments. For most of these experiments we used the  ${}^6\text{Li}$  glass based scintillator detector that was described in Section 4.5.1. The data that is described in this chapter is all acquired with the  ${}^6\text{Li}$  detector. To check the reliability of this data we performed some data quality checks that are reported here.

The PSD versus  $Q_L$  distribution from a UCN run is shown in Fig. 5.4 for all the PMTs combined. This is the most useful way of separating the signal and background.

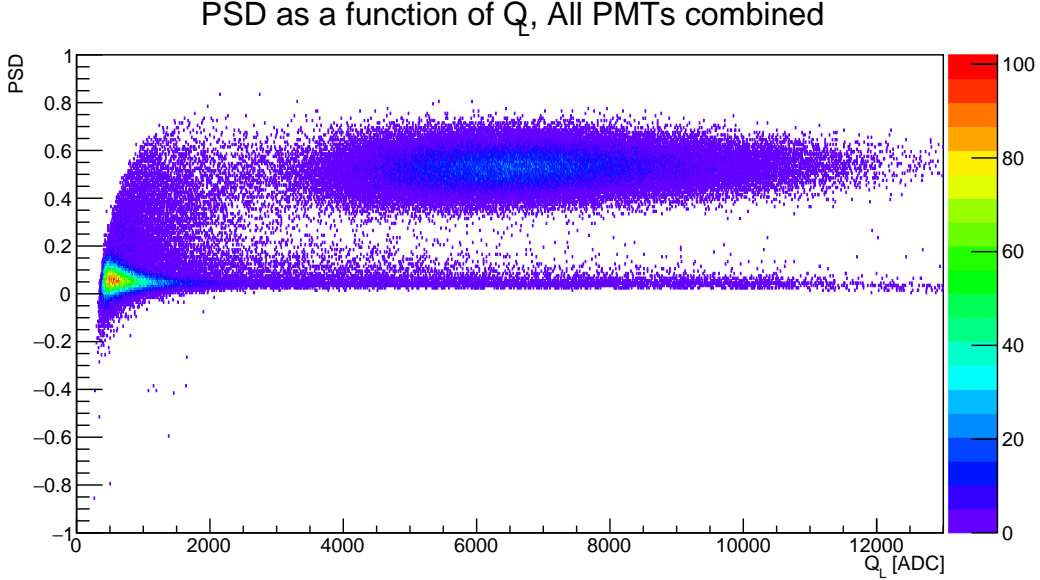


Figure 5.4: PSD versus  $Q_L$  for all of the PMTs for a standard  $1 \mu\text{A}$  proton beam current and 60 s target irradiation time

Here the UCN spectrum has an energy range of 3000 to 12000  $Q_L$  as expected, and a median PSD value of 0.5. The events at  $\text{PSD} \sim 0$  represent the  $\gamma$ -rays in the lightguides. To get the actual UCN counts, a PSD cut at 0.3 and a  $Q_L$  cut at 2000 were applied. Those cuts were confirmed with Monte-Carlo simulations to have an acceptance of 99% or higher. This ensures that only the UCN events are counted which are represented by the central oval-shaped region. Out of all 9 channels, the center channel counts the most number of UCN events, while the corner channels receive the least as expected (see Fig. 5.5).

The effect of the detector on the UCN counts could be categorized in three groups: Deadtime, Crosstalk and Pileup. Deadtime is the minimum time difference between two subsequent UCN events in the same PMT, which might give rise to loss in the UCN counts. Crosstalk is the multiple trigger events in neighboring PMTs originated from the same UCN events. This effect might increase the possibility of overestimating the total UCN counts. Pileup is the combination of multiple events into a single event. It includes UCN-UCN, UCN- $\gamma$ ,  $\gamma$ -UCN and  $\gamma$ - $\gamma$  pileups. The true number of UCN counts is estimated by

$$N_{\text{UCN}}^{\text{True}} = [N_{\text{UCN}}^{\text{raw}} \cdot (1 + \alpha_{pl} + \alpha_{ct})] \cdot A_{box}, \quad (5.3)$$

where  $\alpha_{pl}$  is the estimated pileup coefficient from data and independent calculations assuming Poisson statistics,  $\alpha_{ct}$  is the estimated time-coincidence analysis on data, and  $A_{box}$  is the UCN box efficiency estimated using Monte-Carlo simulations. Based on our Monte-Carlo simulations, the  $\gamma$ -UCN and UCN- $\gamma$  pileups are not a concern for UCN counting. In addition,  $\gamma$ - $\gamma$  pileup does not leak into the UCN box.

The result of such analyses showed the UCN box acceptance is at  $97. \pm 0.1 \%$ . The UCN-UCN pileup at  $1 \mu\text{A}$  beam current and 60 s irradiation of the target was measured to be at 0.075 Hz or has an effect of less than 1 %. The analysis indicated that cross-talk

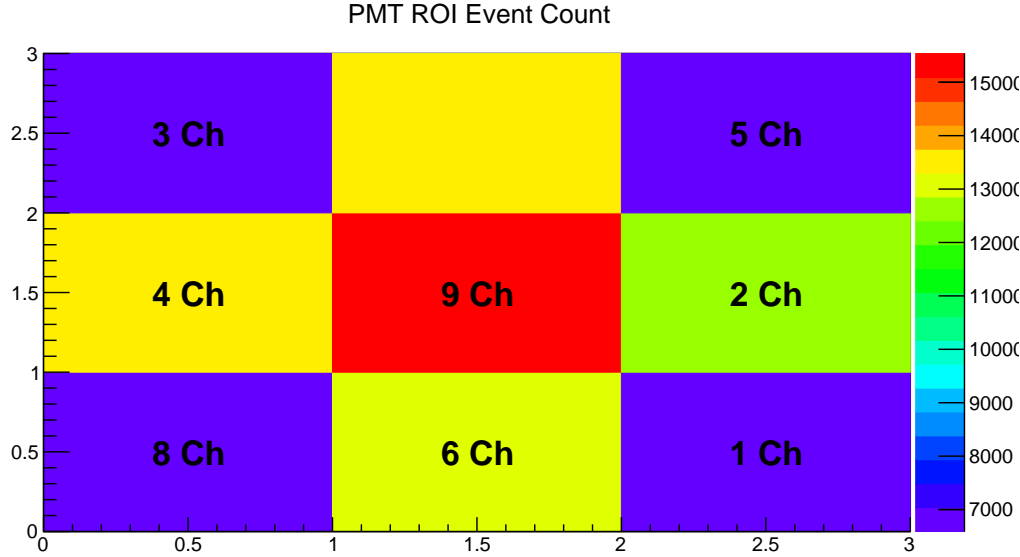


Figure 5.5: Number of UCN events for each channel. The total number of UCN events decrease as we move towards the corner channels.

has a negligible effect on the operating rates and deadtime affects the rates by less than 2 %.

### 5.3 UCN Count Measurements

The total number of produced UCN in the vertical source,  $N$ , at a certain time  $t_i$ , when the UCN valve is closed is the integration of Eqn. 5.1

$$N = P\tau_1 \left[ 1 - \exp \left( \frac{t_i}{\tau_1} \right) \right] , \quad (5.4)$$

where the UCN storage lifetime  $\tau_1$  is given by

$$\frac{1}{\tau_1} = \frac{f_1}{\tau_{\text{He}}} + \frac{1-f_1}{\tau_{\text{vapour}}} + \frac{1}{\tau_{\text{wall},1}} + \frac{1}{\tau_\beta} . \quad (5.5)$$

The storage lifetime consists of four terms: the loss rate in the superfluid helium  $f_1\tau_{\text{He}}^{-1}$ , the loss rate in the helium vapour  $(1-f_1)\tau_{\text{vapour}}^{-1}$ , the loss rate in the UCN guide walls  $\tau_{\text{wall},1}^{-1}$ , and the neutron  $\beta$  decay  $\tau_\beta^{-1}$ . The volume in which the UCN are produced includes the UCN bottle, as well as the horizontal guide section before the UCN valve (see Fig. 5.2). This volume is not fully filled with the superfluid helium. As a result,  $f_1$  is the probability of UCN being in the superfluid helium while the UCN valve is closed. After the valve is opened, the total UCN lifetime is

$$\frac{1}{\tau_2} = \frac{f_2}{\tau_{\text{He}}} + \frac{1-f_2}{\tau_{\text{vapour}}} + \frac{1}{\tau_{\text{wall},2}} + \frac{1}{\tau_d} + \frac{1}{\tau_\beta} , \quad (5.6)$$

where  $f_2$  is the probability of UCN being in the superfluid helium,  $\tau_{\text{wall},2}^{-1}$  is the UCN guide loss rate in the case where the valve is open and the target irradiation is stopped, and  $\tau_d^{-1}$  is the loss rate in the detector. Fig. 5.6 shows three measurement cycles at  $1 \mu\text{A}$

beam current, and 60 s irradiation time with zero second delay time between the end of the target irradiation and opening the UCN valve (here sometimes this is referred to as the cycle delay time or valve open delay time). The dashed lines indicate the start of the target irradiation for a cycle, the dotted lines show the end of the target irradiation, which in this case is the same as the UCN valve open time. The solid lines shows the valve close time.

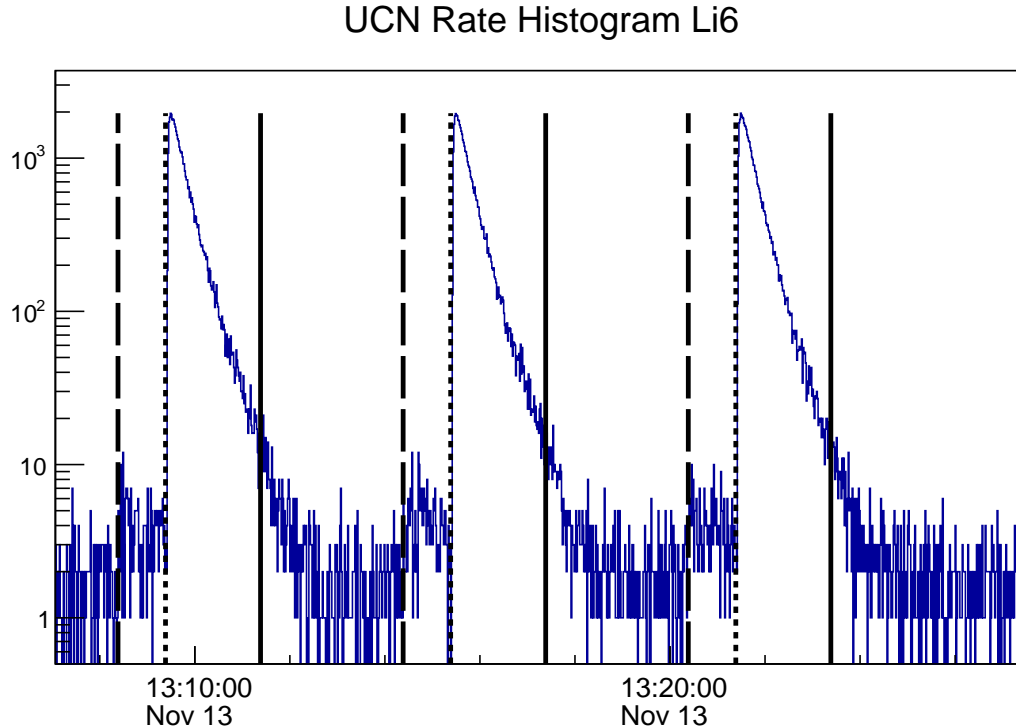


Figure 5.6: Three measurement cycles for 1  $\mu\text{A}$  beam current, 60 s irradiation time, and 0 s valve open delay time. The dashed lines show the start of the target irradiation, the dotted lines show the end of the irradiation and the valve open time for each cycle and the solid lines show the end of a cycle, which is the valve close time.

The total UCN counts are given by the integration of all the UCN events for the duration of the valve open time. However, this method of counting includes the measured background UCN as well. To subtract the background counts from the actual UCN counts, the UCN background rate is calculated before the start of the irradiation of that particular cycle. This rate is then multiplied by the valve open duration, which then gives an estimate of the total background UCN counts. The background rate is typically less than 5 UCN/s. The subtraction of the latter from the total UCN counts gives the actual number of UCN that are produced by the isopure helium converter, and detected by the detector. At low and moderate UCN counts, the statistical uncertainty is available by taking the square root of the number of measured events, as follows conveniently from Poisson statistics [142].

### 5.3.1 UCN Yield Versus Proton Beam Current

The UCN yield at different proton beam currents is also studied. Fig. 5.7 shows the total UCN counts versus the applied proton beam current in  $\mu\text{A}$  at 60 s irradiation time. The

background UCN is subtracted off from the detected UCN counts as explained earlier. The error bar on the UCN counts is calculated as  $\sqrt{N}$ . At lower beam currents, the total UCN counts increase linearly with the proton beam current. The dashed line shows the extrapolation to higher beam currents in an ideal case. However, at higher beam currents, the total UCN counts decrease due to an increase in the heat load on the isopure superfluid helium, and therefore, its temperature. Theoretically, the upscattering rate in the superfluid helium is proportional to its temperature as  $T^7$  (see Section 1.5.2). This has been confirmed by performing PENTrack simulations and comparing the result to the acquired data (see Section 5.5).

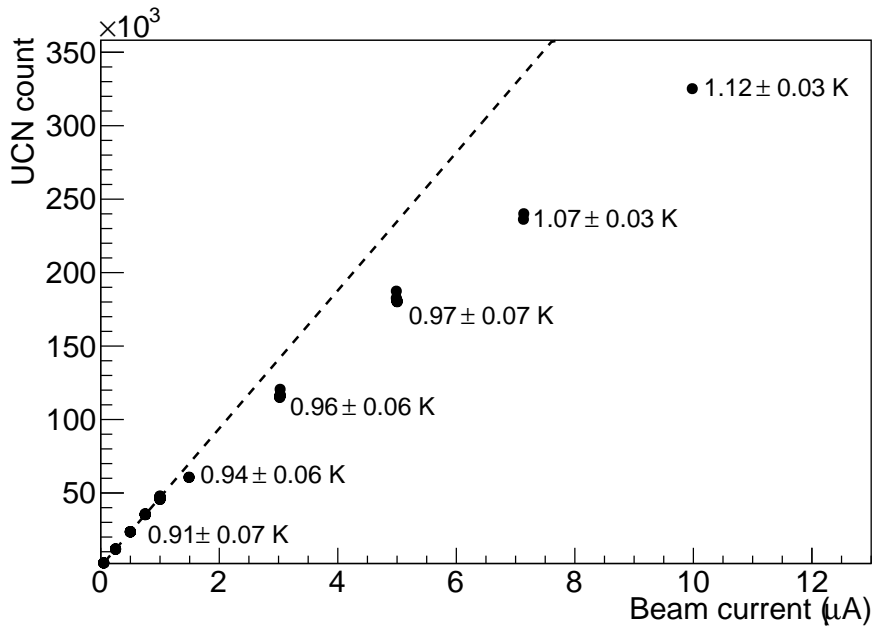


Figure 5.7: The total UCN counts versus the applied proton beam current. The labels show the full range of the superfluid helium temperature for that measurement. The dashed line is the fit to the UCN counts at low beam currents.

The labels in the graph show the full range of the isopure helium temperatures during the measurement cycle. Four temperature sensors were used to measure the superfluid helium temperature with the following names in our EPICS system: TS11, TS12, TS14 and TS16. The location of these sensors are shown in Fig. 5.8. The temperature sensor TS11 is located at the UCN heat exchanger bottom, the temperature sensor TS14 is located at the UCN heat exchanger top, the temperature sensor TS12 is located at the UCN double tube bottom, and the temperature sensor TS16 is located at the UCN double tube top. At low temperatures around 0.8 K, these temperature sensors show a maximum of 0.1 K discrepancy with TS16 showing the highest value, and TS12 showing the lowest value.

In summary, at lower beam currents, because of the low heat load on the superfluid helium, its temperature change is not significant, and it gives rise to a linear increase in the UCN counts versus various applied proton beam current. However, at higher proton beam currents, the temperature of the superfluid increases due to a higher heat load, and it gives rise to higher upscattering rate in the superfluid and lower UCN counts.

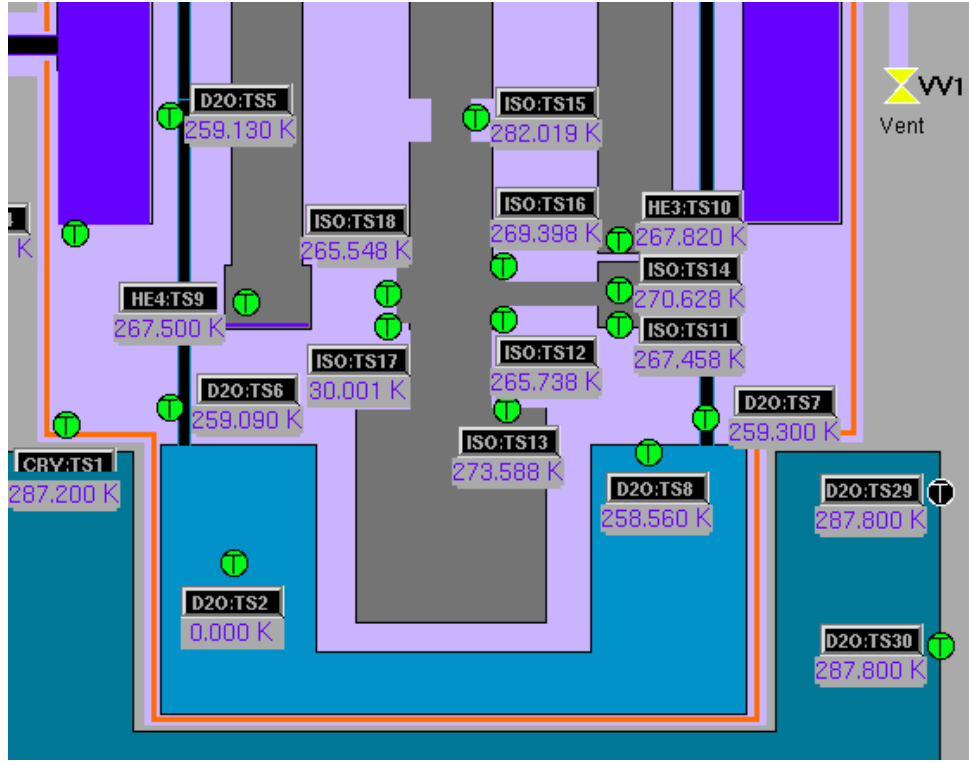


Figure 5.8: Zoomed in screenshot of the EPICS temperature monitoring screen 4.11. TS11 is located at the UCN heat exchanger bottom, TS12 is located at the UCN double tube bottom, TS14 is located at the heat exchanger double tube top and TS16 is located at the UCN double tube top. For further information about the source schematic see Section 4.3

### 5.3.2 UCN Yield Versus Target Irradiation Times

The total UCN counts is optimized by irradiating the target with different proton beam currents at different irradiation times. The result is shown in Fig. 5.9. In this graph, the vertical axis shows the total number of UCN counts where the background UCN are subtracted, and the horizontal axis shows the target irradiation times in seconds. Each marker represents a proton beam current. The dashed line is an exponential fit to those data points. The proton beam current and the extracted time constant from the fit are shown in the Figure.

At higher beam currents, the saturation time constant decreases due to the higher heat load and faster temperature increase in the superfluid helium. At higher beam currents and longer irradiation times, the total measured UCN counts are below the exponential extrapolation due to the higher temperature and higher upscattering rate in the superfluid helium.

### 5.3.3 UCN Yield Versus Isopure Helium Temperature

The UCN counts were also measured at different superfluid helium temperature (see Fig. 5.10). The vertical axis shows the number of UCN counts, and the horizontal axis shows the temperature of the superfluid helium for all four temperature sensors. The vertical error bars are  $\sqrt{N}$ , and the horizontal error bars are calculated as  $(T_{\max} - T_{\min})/2$  for each temperature sensor, where  $T_{\max}$  is the maximum value of the superfluid helium

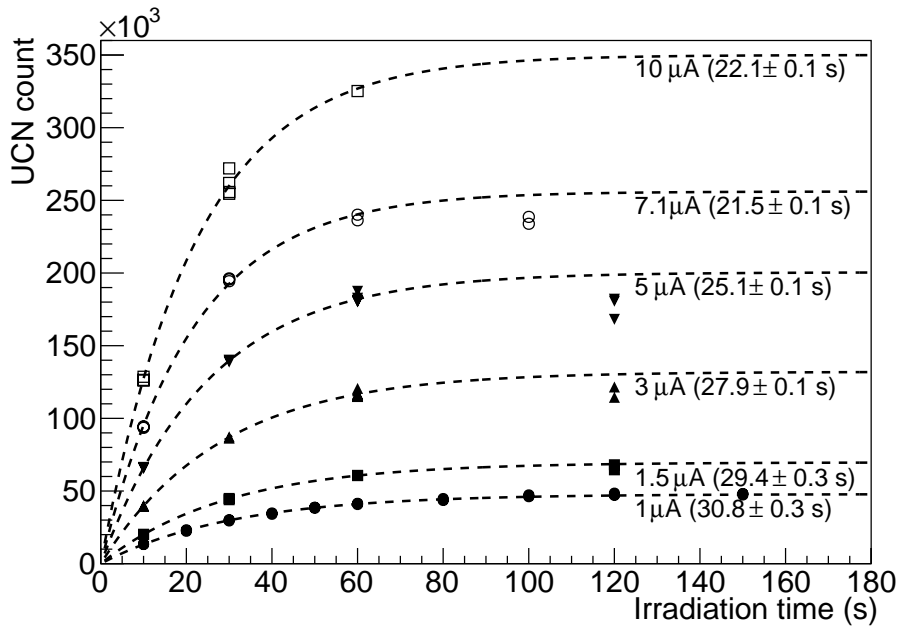


Figure 5.9: Number of UCN extracted from the source after irradiating the target for different times with different beam currents. The dashed lines extrapolate the data for irradiation times below 60 s using exponential saturation curves. The labels show the saturation time constant for each beam current.

temperature reading by one temperature sensor, and  $T_{\min}$  is the minimum value read for the same sensor.

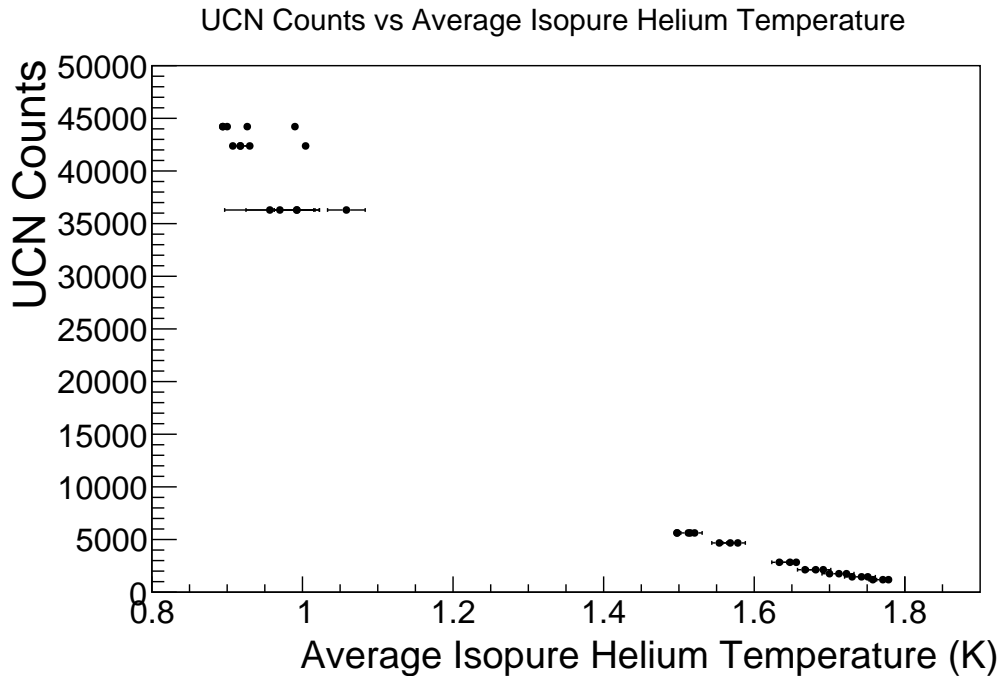


Figure 5.10: UCN yield versus the superfluid helium temperature. At a particular UCN counts, there are several values for the temperature of the superfluid helium. This is due to the discrepancy in the temperature sensor readings as described in the text.

As the temperature of the superfluid helium increases, the number of UCN counts in the detector decreases as expected. This is mainly due to the high UCN upscattering rate in the superfluid helium at higher temperatures.

### 5.3.4 Steady-state UCN Production

The result shown so far are achieved in the batch mode of operation. In addition to such measurements, the UCN rate was also measured at different beam currents in the steady-state mode of operation. In these measurements, the UCN valve was left open, and the target was irradiated for about 10 min. A typical UCN rate graph for  $0.3 \mu\text{A}$  beam current and 10 min target irradiation time is shown in Fig. 5.11.

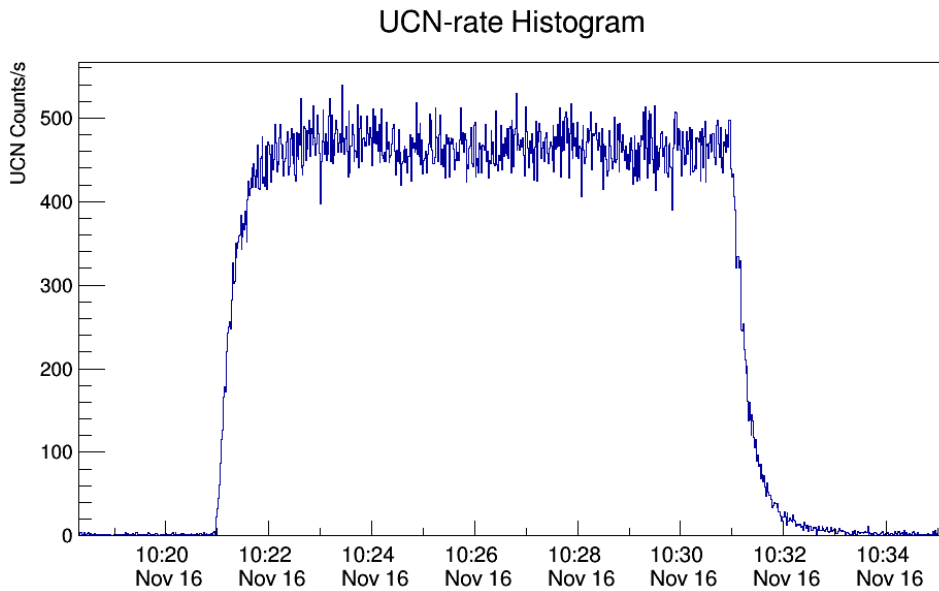


Figure 5.11: UCN rate at the steady-state production mode with  $0.3 \mu\text{A}$  proton beam current. The UCN rate reaches a constant value of 450 UCN counts/s.

At lower beam currents such as  $0.3 \mu\text{A}$ , the UCN rate remains constant throughout the whole target irradiation time as shown in Fig. 5.11. An example of a steady-state UCN production at  $3 \mu\text{A}$  is shown in Fig. 5.12. Since the proton beam current is high, the UCN rate does not remain constant. Here the maximum UCN rate is observed near the start of the target irradiation. As the target irradiation continues, the heat load on the cryostat increases the temperature, and the upscattering rate in the superfluid helium. As a result, the UCN rate decreases. The change in the temperature is shown in Fig. 5.13. Throughout the target irradiation time, the temperature of the superfluid helium increases. Once the irradiation stops, the temperature starts to decrease.

The steady-state UCN rate measurements were conducted at different proton beam currents, leading to different temperature changes for all temperature sensors. The result of all those measurements and comparison to simulations are discussed in Section 5.5.

### 5.3.5 UCN Yield Over the Experiment Period

The total UCN counts for our standard measurements at  $1 \mu\text{A}$  beam current and 60 s irradiation time over the course of the experimental run is shown in Fig. 5.14. The graph

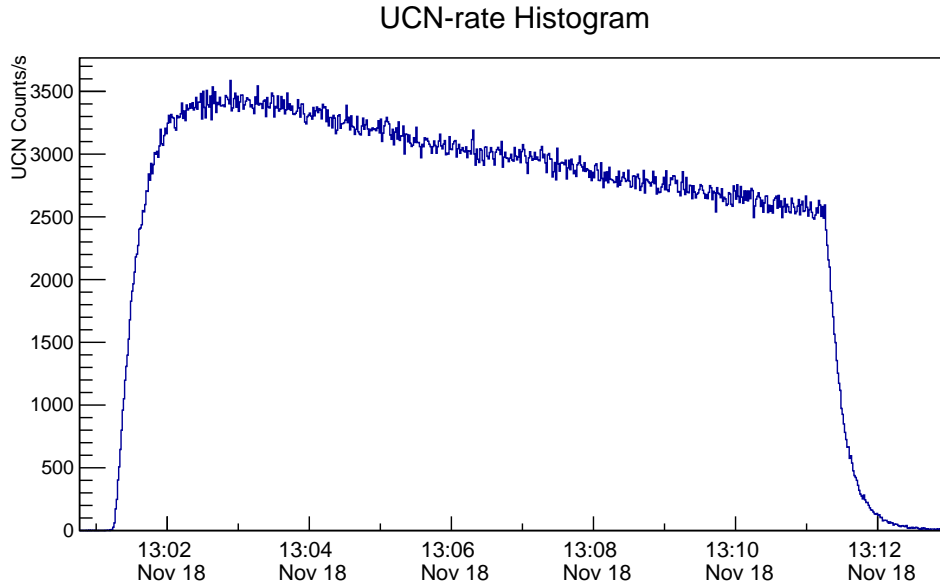


Figure 5.12: The UCN rate at  $3 \mu\text{A}$  beam current at 10 min irradiation time at the steady-state mode of operation. The UCN valve is left open throughout the measurement cycle. Quickly after the start of the target irradiation the UCN rate in the detector goes up. The target irradiation creates a heatload on the cryostat and the superfluid helium. This gives rise to a slow temperature increase in the source. As a result, the UCN rate goes down due to the higher upscattering rate.

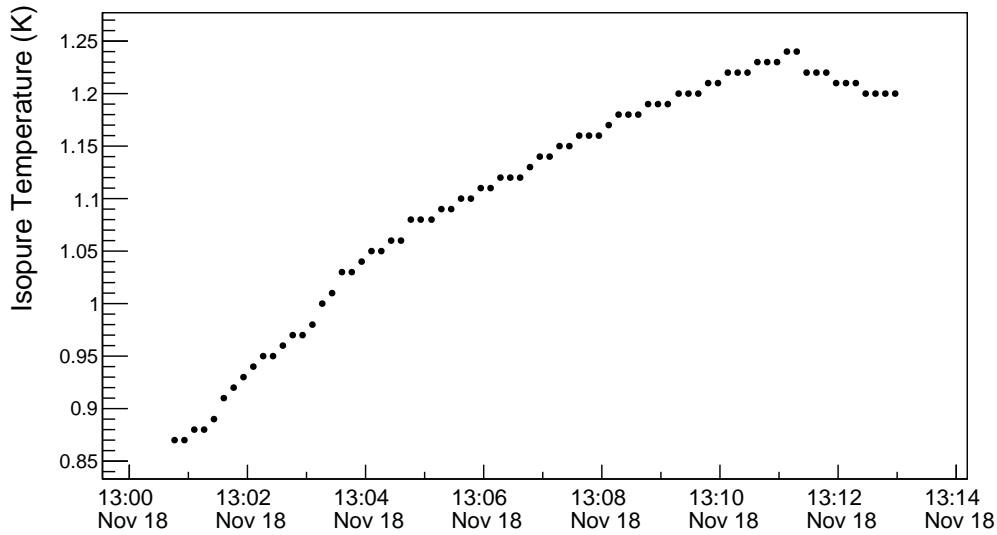


Figure 5.13: The temperature of the superfluid helium (TS12) for the steady state mode of operation at  $3 \mu\text{A}$  beam current and 10 min target irradiation. After the irradiation stops, the temperature starts to decrease.

shows an overall decrease of about  $\sim 40\%$  over the course of the eighteen days. The source volume is connected to a long UCN guide sealed with an O-ring. It is expected that the rest gas to contaminate the source every time the UCN valve is opened. This caused a decrease in the UCN yield (and storage lifetime as shown later in Section 5.4.3)

over the course of the measurement. In addition, the changes in the UCN guide geometry in the latter half of the run potentially affected this drop.

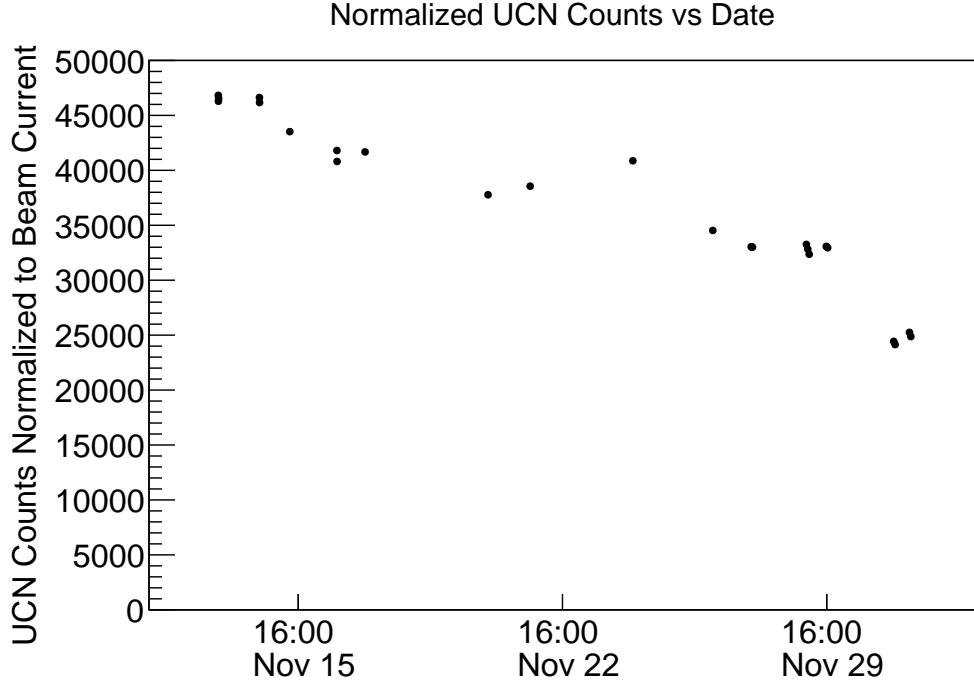


Figure 5.14: The total UCN counts extracted from the source for  $1 \mu\text{A}$  beam current and 60 s irradiation time at different days during the experimental run.

## 5.4 UCN Storage Lifetime

The total number of detected UCN strongly depends on the storage lifetime of the source  $\tau_1$  (see Eqn. 5.5) which indicates the performance of the UCN source. The storage lifetime of UCN is determined by measuring the detected UCN at different valve open delay times right after the irradiation stops. The typical chosen values are 0 s, 5 s, 10 s, 20 s, 30 s, 60 s, 80 s, 120 s and 170 s. The exponential decay constant in the fit to the total UCN counts without the background, for different valve open delay times, is the total storage lifetime in the source.

Fig. 5.15 shows several UCN cycles for the standard  $1 \mu\text{A}$  proton beam current and 60 s target irradiation time. The difference in the maximum detected UCN rate is due to different valve open delay times. Fig. 5.16 shows the total UCN counts (background subtracted) versus the valve open delay time for  $1 \mu\text{A}$  proton beam current and 60 s target irradiation time. The longer delay times give rise to lower UCN counts due to the loss mechanisms. The one exponential fit function

$$\text{UCN counts} = Ae^{-t/\tau_1} \quad (5.7)$$

determines the storage lifetime  $\tau_1$ . At 170 s valve open delay time, the total UCN counts are not consistent with what the fit function predicts due to low statistics. However, the result of the fit is not driven by this inconsistency as it has a negligible effect on the extracted storage lifetime.

Below the result of the storage lifetime measurements are presented.

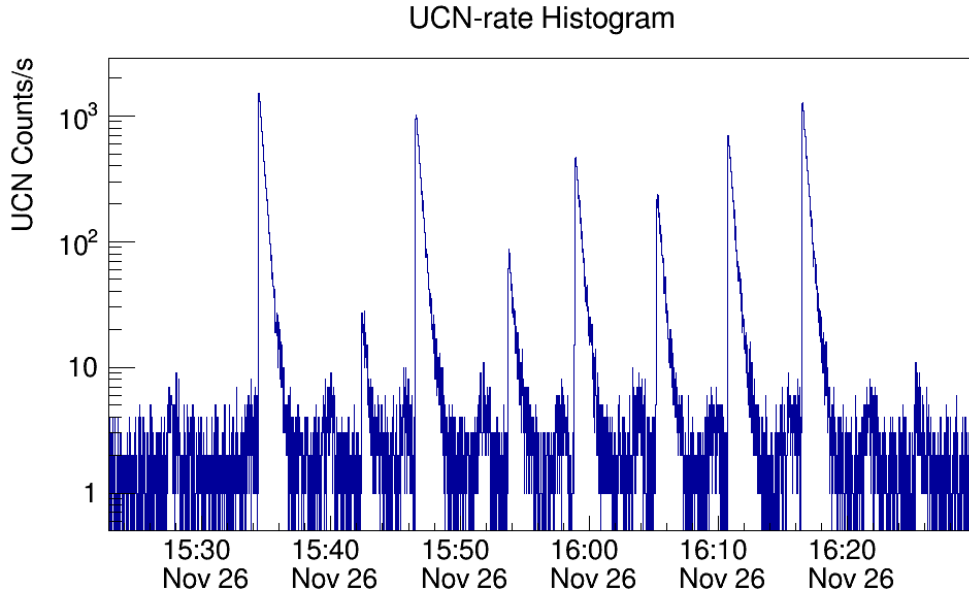


Figure 5.15: UCN cycles at different valve open delay times for  $1 \mu\text{A}$  beam current and 60 s target irradiation time.

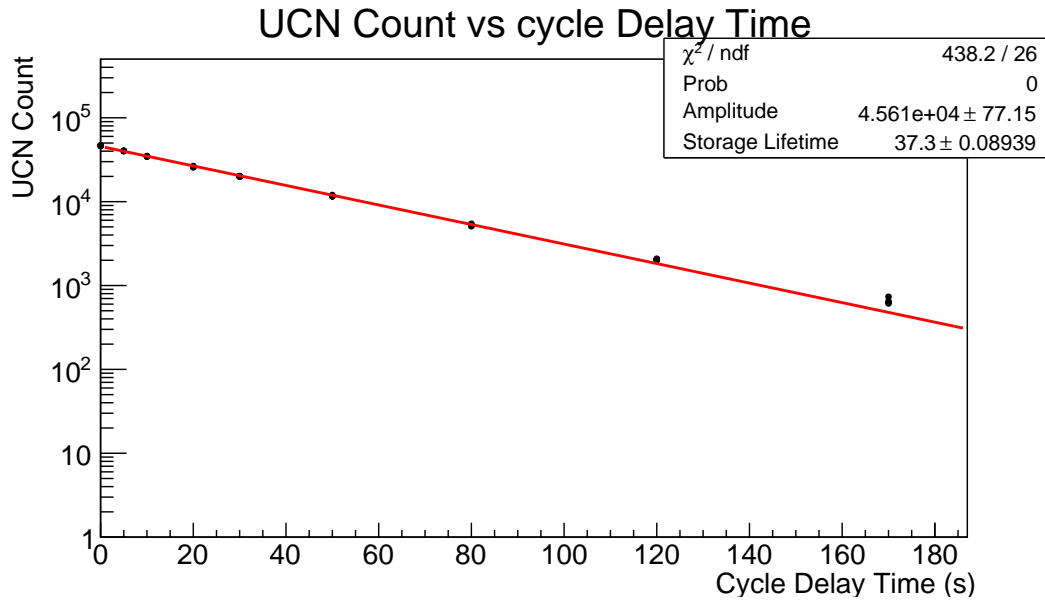


Figure 5.16: The total UCN counts at different valve open delay times for  $1 \mu\text{A}$  beam current and 60 s irradiation time. The red line is the one exponential fit.

#### 5.4.1 Storage Lifetime Versus Beam Current and Irradiation Time

The storage lifetime of UCN in the source is measured at different proton beam currents and different target irradiation times for better optimization of the source. The result of those measurements is shown in Fig. 5.17. Here the vertical axis shows the storage lifetime in the source in seconds, and the horizontal axis shows the proton beam current in  $\mu\text{A}$ . Each marker represents a target irradiation time. At lower beam currents, the duration of the target irradiation does not make a significant difference in the storage

lifetime. At higher proton beam currents, the longer the irradiation time takes, the lower the storage lifetime will be.

In summary, irradiating the target at high proton beam currents and longer irradiation times create a higher heat load on the UCN source, which leads to higher upscattering rates, and as a result, lower UCN storage lifetime in the source.

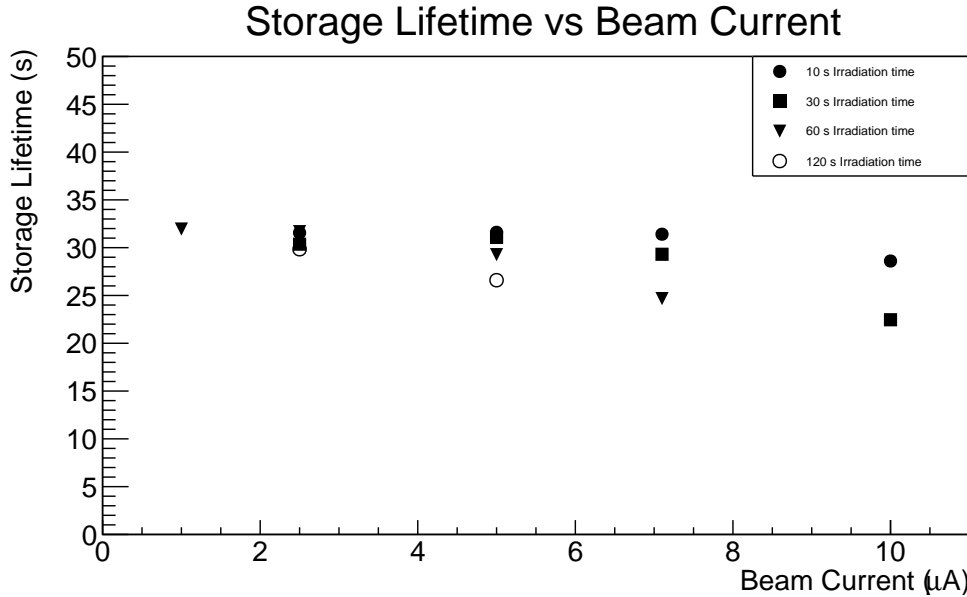


Figure 5.17: Storage lifetime in the source at different irradiation times and proton beam currents. Different markers refer to different target irradiation times. At longer irradiation times and higher beam currents, the storage lifetime decreases due to the increased heat load in the source, and an increase in the superfluid helium temperature.

### 5.4.2 Storage Lifetime Versus Isopure Helium Temperature

The storage lifetime of UCN was also measured at different temperatures of the superfluid helium. In this experiment, the temperature of superfluid was increased by using the heater tapes wrapped around the UCN bottle. The heater powers were set to increase the temperatures by a certain amount. Once the temperatures reached a stable state, the target irradiation started.

The result of this measurement is shown in Fig. 5.18. The vertical axis is the storage lifetime of UCN in seconds, and the horizontal axis is the temperature of the superfluid helium. As mentioned earlier, the four temperature sensors that measure the temperature of the superfluid show some discrepancy. As a result, for a given value of the storage lifetime, there are four different values for the temperature of the superfluid. The vertical error bars are equal to  $\sqrt{N}$ , and the horizontal error bars are set as  $(T_{\max} - T_{\min})/2$ , as discussed earlier. The data shows a downward trend. As the temperature of the superfluid helium increases, the storage lifetime in the source decreases. This is due to higher upscattering rate in the superfluid helium at higher temperatures.

### 5.4.3 Storage Lifetime Over Experimental Period

The standard storage lifetime measurements were performed on a daily basis over the course of the experimental run. This includes the irradiation of the target at  $1 \mu\text{A}$  proton

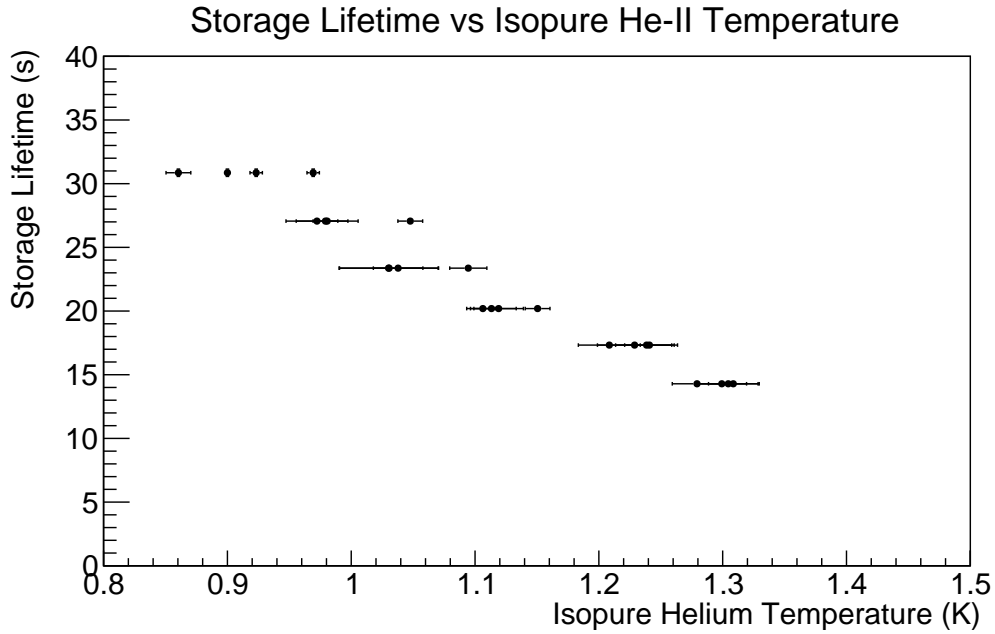


Figure 5.18: Storage lifetime of UCN at different isopure helium temperatures. In this experiment, the temperature of the superfluid helium was set using heater tapes around the UCN bottle. The vertical axis shows the storage lifetime in seconds and the horizontal axis shows the superfluid helium temperature in Kelvin. As the temperature increases, the storage lifetime decreases. This is due to higher upscattering rate in the superfluid helium at higher temperatures.

beam current for 60 s. The result of those measurements are shown in Fig. 5.19. Over a two week period, the storage lifetime decreased from 37 s to 27 s. This is possibly due to the contamination in the UCN source after opening the UCN valve.

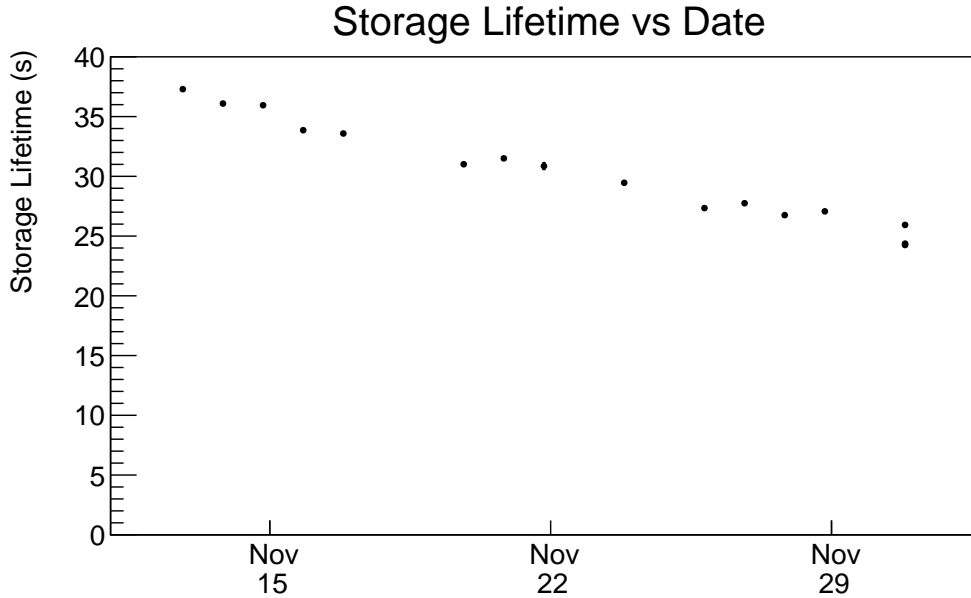


Figure 5.19: Storage lifetime of the source over the experimental run. A 2% daily decrease in the storage lifetime is observed possibly due to the contamination in the source after opening the UCN valve.

## 5.5 PENTrack Simulations

For better understanding of the loss mechanisms of UCN, the experiments were also simulated in PENTrack [143]. PENTrack is a particle tracking simulation software which simulates the trajectories of UCN and their decay products (e.g., Protons and Electrons) and their spin precession in complex geometries in Electric and Magnetic fields by solving the relativistic equation of motion.

To simulate the UCN storage and transport, an exact model of the UCN guides for PENTrack was build by the TUCAN team. Here the result of those simulations are presented.

### 5.5.1 UCN Guide Diffusivity

As discussed in Chapter 1, UCN interact with all four fundamental forces. To describe the interaction of UCN with matter, a complex optical potential is used to describe matters:

$$U = V - iW \quad (5.8)$$

where the real part,  $V$ , depends on the number densities and bound coherent scattering lengthes of each nucleus species. The imaginary part,  $W$ , depends on the loss cross-section for a given velocity. Upon the incidence of the UCN on a surface, it can be scatterd either specularly or diffusely. The specular reflection by definition is the reflection of light from a smooth surface at a defined angle. The diffuse reflection is the reflection by rough surfaces that tend to reflect light in all directions.

PENTrack simulations were performed to extract the diffusivity of the UCN guides (see Fig. 5.2). PENTrack uses two models to calculate the scattering distribution of the UCN impinging on the material surface: Lambert model or the Microroughness [144]. Experimental geometries imported in PENTrack are the StL files made through CAD models. For these simulations, the exact model of the vertical UCN source was used including the burst disk, the actual shape of the UCN valve in the open and close state, pinhole, foil and the detector.

The abosorption in the foil is set according to the measurements in [145]. The main decotor is modeled with its two scintillator layers [83] and their corresponding Fermi potentials and absorption cross-section, as stated in [146]. In the simulations, it is assumed that the spectrum of produced UCN is proportional to  $\sqrt{E}$  and that the upscattering rate in the superfluid helium follows  $\tau_{\text{He}} = BT^7$ , with  $B$  between  $0.008 \text{ s}^{-1}$  and  $0.016 \text{ s}^{-1}$  as measured by [50]. The wall loss parameters were tuned to give a storge lifetime in the source  $\tau_1$  between  $(29.81 \pm 0.18) \text{ s}$  and  $(31.07 \pm 0.19) \text{ s}$  matching the storage lifetime during the middle of the experimental run, and resulting in the material parameters shown in Table 5.1.

The helium vapour above the liquid was included with an upscattering rate  $\tau_{\text{vapour}}^{-1} = \langle v \rangle n \sigma_{\text{He,n}}$  depending on the average atomic velocity  $\langle v \rangle$  which is given by the vapour temperature, the vapour density  $n$  given by the saturated vapour pressure of the liquid and the vapour temperature, and the neutron-scattering cross-section of helium  $\sigma_{\text{He,n}} = 0.76 \text{ b}$ . It was assumed that the vapour has the same temperature gradient as measured by several temperature sensors on the outer guide wall. To include the temperature gradient in the simulation, the guide volume was split into 10 cm long sections and assigned each an averaged UCN upscattering rate in that section.

Material	Fermi pot. (neV)	Diffusivity
He-II	$18.8 - 0.5\hbar BT^7 i$	0.16
He vapour	$-0.5\hbar\tau_{\text{vapour}}^{-1} i$	0
Prod. volume (NiP)	$213 - 0.120 i$	0.05
Guides (stainl. steel)	$183 - 0.140 i$	0.03
Foil (aluminium)	$54.1 - 0.00281 i$	0.20
GS30 scintillator	$83.1 - 0.000123 i$	0.16
GS20 scintillator	$103 - 1.24 i$	0.16

Table 5.1: Material parameters used in PENTrack simulation. [145–147]

To better match the simulated UCN transport with reality, both the simulation and the measured UCN rate in the detector after opening the valve at  $t = 0$  are fitted with the function

$$R(t) = R_B \left[ 1 - \exp \left( -\frac{t - \Delta t}{\tau_{\text{rise}}} \right) \right] \exp \left( -\frac{t - \Delta t}{\tau_2} \right) + R_B \quad (5.9)$$

In this equation,  $\Delta t$  is the delay time between opening the valve and detecting the first UCN and it is 2 to 3 s. The parameter  $R_B$  is the background UCN rate in the experimental data and is zero in the simulations. The fit function, the rise time  $\tau_{\text{rise}}$  and the fall time  $\tau_2$  are shown in Fig. 5.20 for a given UCN cycle.

In the simulations, the Lambert model is used to tune the probability of UCN being diffusely reflected on the guide walls to match the rise time and fall time of the UCN rate in the storage lifetime measurements (see Fig. 5.21 and Fig. 5.22). The delay time  $\Delta t$  matches in all scenarios. In the graphs, the data is shown by the boxes and the simulation results for different UCN guide diffusivity are shown by different markers.

Diffuse reflection probabilities of 1% and 10% clearly result in too short and too long time constants. The experimental fall time can be matched with diffuse reflection probabilities of 3% and 5%. The rise time is best matched with 3%. This value is similar to values reported for a range of UCN guides [148–150].

### 5.5.2 UCN Yield and Storage Lifetime Simulations

To estimate the UCN production, a model of accurate target, moderator and UCN converter geometries were build for MCNP6.1, taking into account material impurities determined from assays and fill levels of liquid moderator vessels (see Fig. 5.23). The full source is then simulated: the proton beam hitting the target, secondary neutrons, protons, photons, and electrons, and neutron moderation in graphite and heavy water. In contrast to liquid heavy water, there is no detailed data on thermal neutron scattering in solid heavy water available. Instead, we relied on a free-gas model with an effective temperature of 80 K, as this seems to be the minimum effective neutron temperature achieved with solid heavy water moderators [151]. From the simulated cold neutron flux in the UCN production volume and UCN production cross sections from [41, 152], a production rate of  $(20600 \pm 200) \text{ s}^{-1}$  in an energy range up to 233.5 neV was determined.

Fig. 5.24 and 5.25 show the measured UCN counts and storage lifetime versus the superfluid helium temperature for all four temperature sensors and their simulations. In these graphs, the filled circles represent the measured data, and the empty squares and triangles represent the simulations. The lines are only shown for readability and are

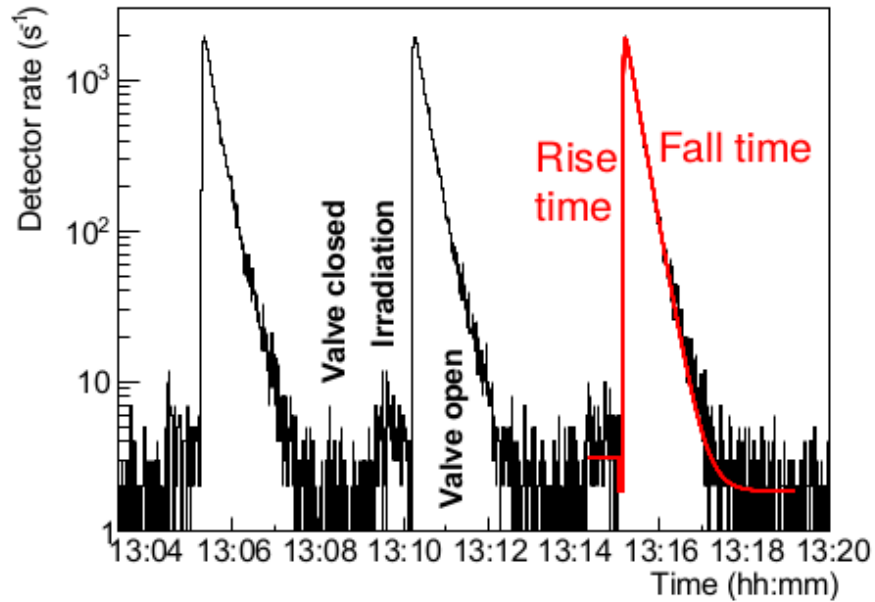


Figure 5.20: UCN rate with two exponential fit shown in red. The rise time and fall time are labeled.

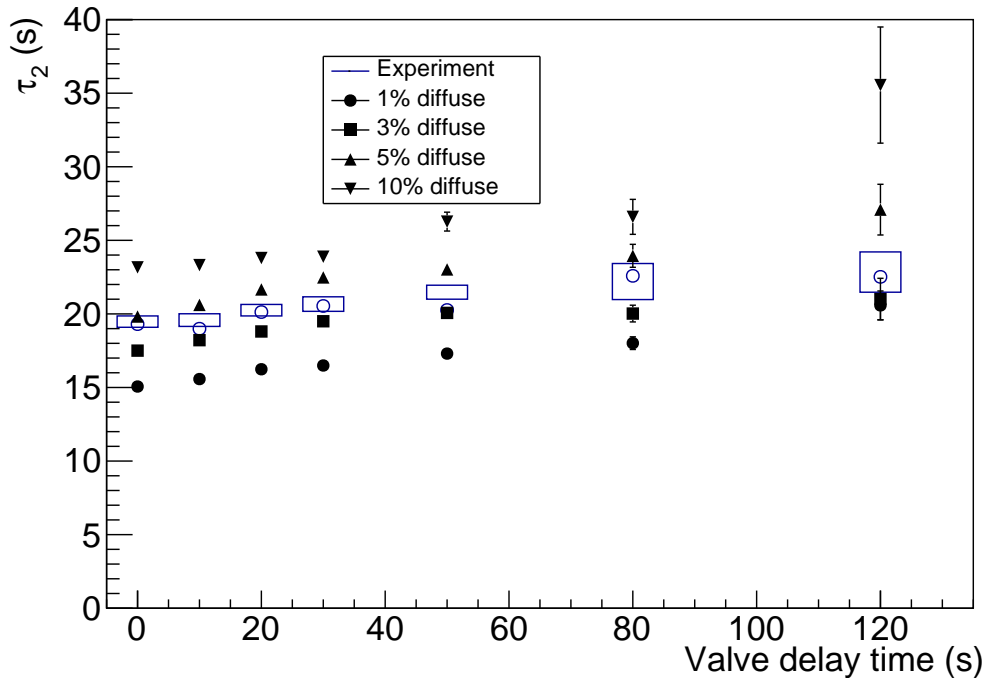


Figure 5.21: Comparison of fall time  $\tau_2$  in the experimental data and the simulations with different diffuse-reflection probabilities. The boxes indicate the second and third quartile of the experimental data. The empty circle indicates its average.

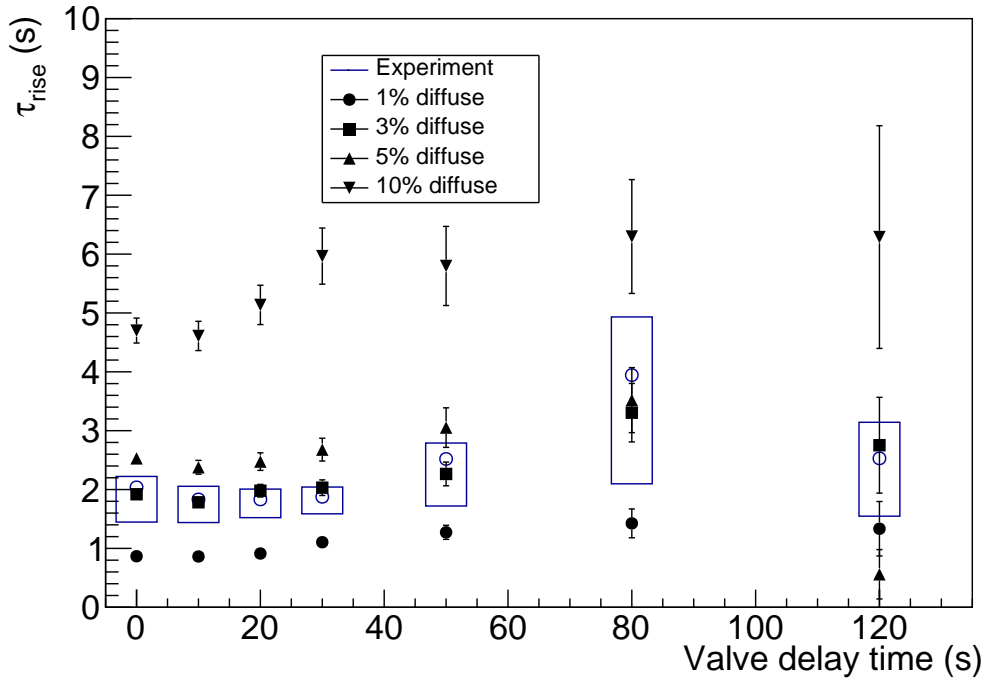


Figure 5.22: Comparison of rise time  $\tau_{\text{rise}}$  in experimental data and simulations with different diffuse-reflection probabilities. The boxes indicate the second and third quartile of the experimental data. The empty circles indicate the average.

interpolation of the simulated points. The empty squares are the simulations where the helium vapour above the superfluid helium liquid is included, and empty triangles are the simulations without the helium vapour. The interpolations for the squares are shown in solid lines and the interpolations for the empty triangles are shown with dotted lines.

The simulations include two values for the upscattering parameter  $B$ :  $B = 0.016 \text{ s}^{-1}$  which is shown in red, and  $B = 0.008 \text{ s}^{-1}$  which is shown in blue. The red solid lines show the simulations for  $B = 0.016 \text{ s}^{-1}$  where the measured data and simulations match very well. Simulations without vapour upscattering (empty triangles) show significant differences at higher liquid temperatures. In this model, the storage lifetime and the UCN yield at higher temperatures are overestimated. The reason for this is because of the high upscattering rate of UCN in the helium vapour.

The UCN rate in the steady-state mode of operation was measured at different proton beam currents, leading to increased temperature in the superfluid helium. The overall result of those measurements and their simulations are shown in Fig. 5.26. Here again, the empty squares represent the simulations where the helium vapour above the superfluid helium is included in the simulations, and the empty triangles represent the case where the helium vapour is excluded. The interpolation of the simulations are shown in lines. The simulated data with a liquid helium upscattering parameter of  $B = 0.016 \text{ s}^{-1}$  (red solid line) slightly overestimates the drop in the rate with temperature. With  $B = 0.008 \text{ s}^{-1}$  (blue solid line), it slightly overestimates the UCN rate, but better matches the drop with temperature.

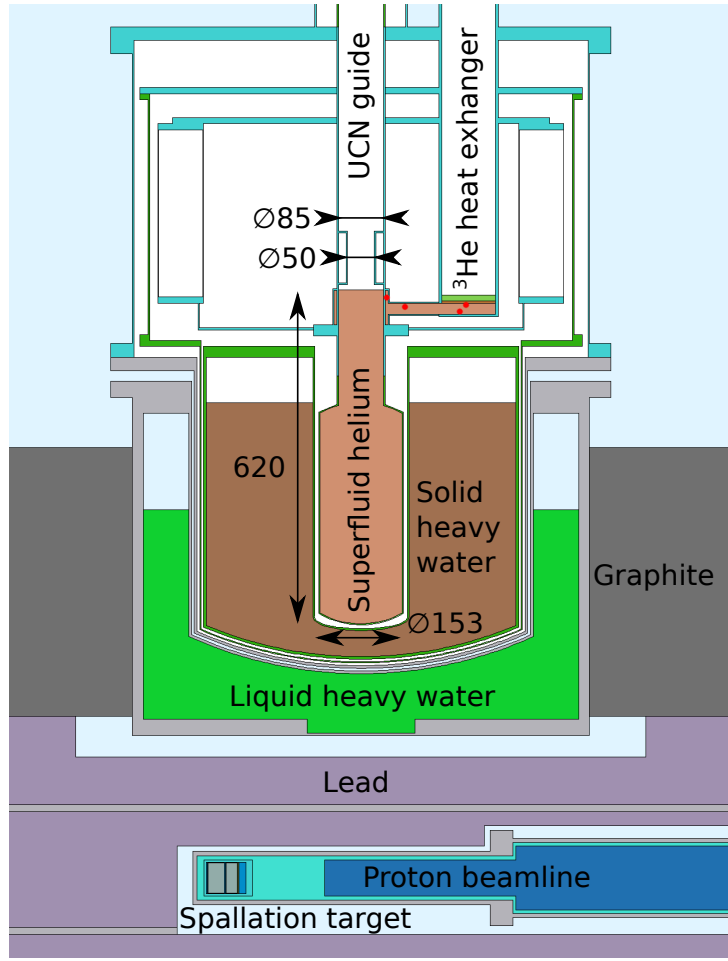


Figure 5.23: MCNP model of the source. Red dots indicate the temperature sensors used to determine the temperature of the superfluid.

### 5.5.3 Heater Test Versus Proton Beam Current

One of the UCN experiments was designed to match the heater power from the heaters wrapped around the UCN bottle with the proton beam current. This type of measurements helps in the understanding of the input heat load on the cryostat.

The result of the heater tests were discussed in Appendix E. Applying heat to the superfluid helium bottle gives rise to a temperature increase in the superfluid helium, as well as a flow rate increase in the  $^3\text{He}$  pot. The amount of this heat load is known simply by knowing the applied current to the heater tapes. However, the input heat load is not known in the case of the target irradiation. As a result, the steady-state UCN yield were measured at different proton beam currents. The target irradiation at higher beam currents give rise to a temperature change in the superfluid helium. In addition, the increase in the heat load increases the  $^3\text{He}$  flow rate in the  $^3\text{He}$  pot. The comparison of the temperature and flow rate increase between these experiments give an idea of the amount of applied heat load on the superfluid helium bottle for each given proton beam current.

Even though the result of the data analysis for this experiment was not conclusive, it gave an idea of the stability and the behaviour of the helium cryostat, and a better experimental plan for the future.

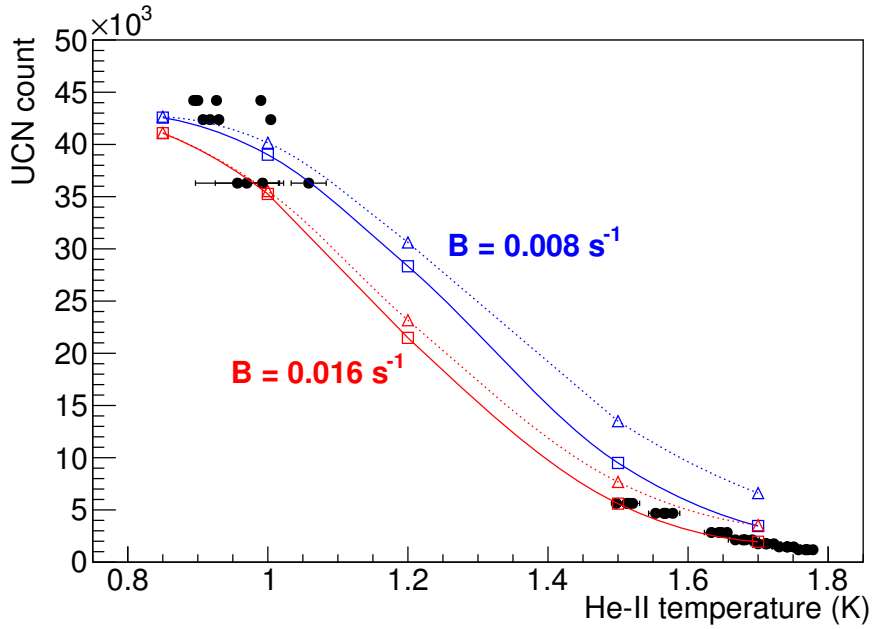


Figure 5.24: Number of UCN extracted from the source at different superfluid helium temperatures after irradiating the target with  $1 \mu\text{A}$  proton beam current for 60 s(filled circles). The lines are interpolations of simulated data to guide the eye.

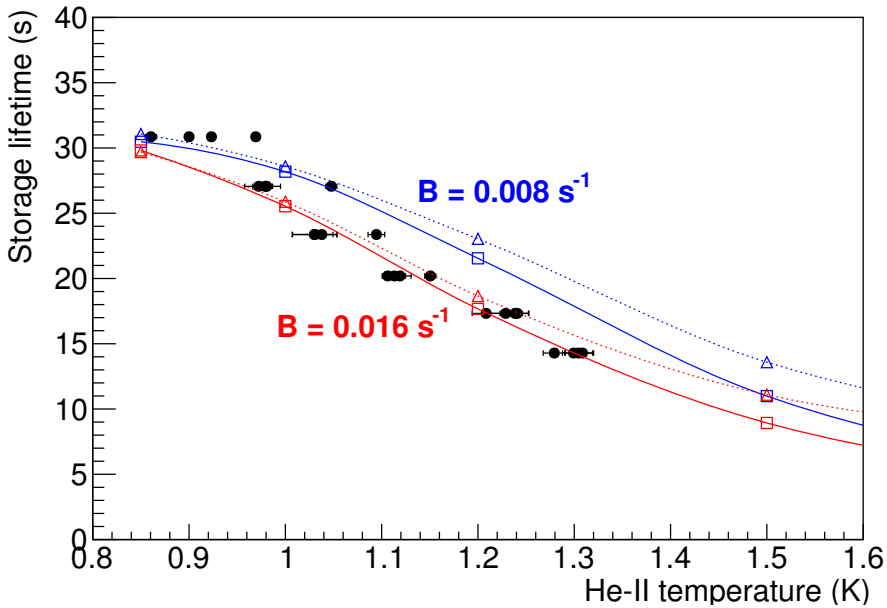


Figure 5.25: Storage lifetime of UCN in the source at different superfluid helium temperatures (filled circules). The lines are interpolations of simulated data to guide the eye.

Some unexpected anomalies were observed during the measurements. For instance, when the 4 K resorvoir was being filled, the flow rate in the  ${}^3\text{He}$  pot as well as the temperature in the superfluid helium was not stable. Another problem arose from the wait time between the measurements. Before conducting a new measurement, it is essential

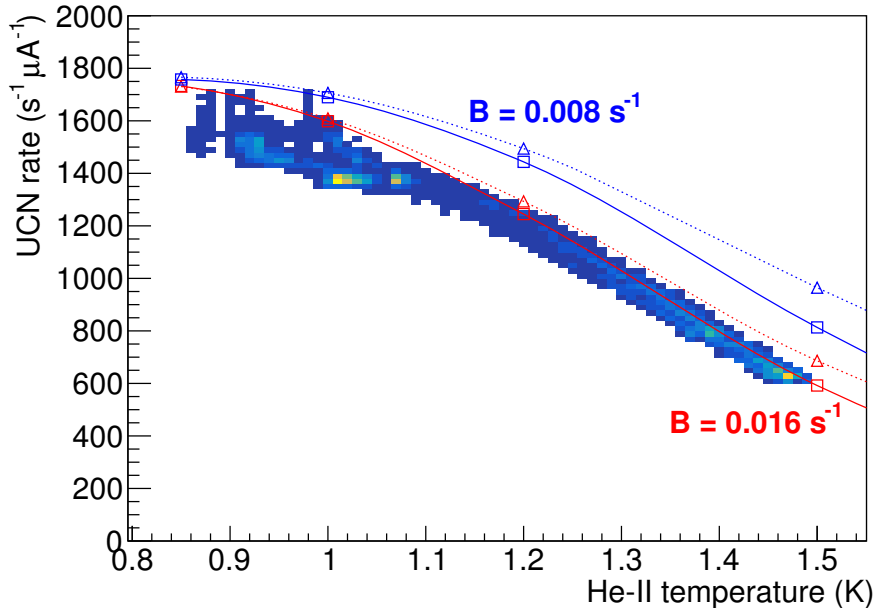


Figure 5.26: Histogram of measured UCN rates and temperatures from all four temperature sensors while the target is continuously irradiated with the UCN valve open. The simulated data (empty squares and triangles) slightly overestimate the UCN rate. The lines are interpolations of simulated data to guide the eye.

to wait long enough so that the superfluid helium temperature and  $^3\text{He}$  flow rate get down to a stable value. In some cases, the wait time between the measurements was not long enough, and so it was not possible to assign a change in the superfluid helium temperature or  $^3\text{He}$  flow rate. In addition, target irradiation should be long enough so that the temperature and the  $^3\text{He}$  flow rate reach a stable value.

Fig. 5.27 shows an inconclusive run. The top graph shows the UCN rate over time. This shows an increase in the UCN rate after starting the target irradiation. At the end of the irradiation, the UCN rate decays to the typical background rate. The middle graph shows the temperature of the superfluid helium from the temperature sensor TS12 over time. Here the irradiation of the target stopped before the superfluid helium could reach a stable saturation value. The bottom graph shows the flow rate in the  $^3\text{He}$  from sensor FM1 (see Fig. D.1 to see the position of the sensor). At the beginning of the run, the flow rate was still going down, and it did not reach a minimum stable value. Typically this value was around 14 SLM. In addition, the flow rate did not reach a maximum saturation value due to short target irradiation time. Therefore, the change in the flow rate is not inclusively due to the target irradiation and is not conclusive.

## 5.6 Summary

The result of the first UCN production with the vertical UCN source at TRIUMF were discussed in this chapter. The measurements include the UCN yield experiments, UCN storage lifetime experiments, and steady-state UCN production experiments.

The maximum number of UCN achieved for the standard  $1 \mu\text{A}$  proton beam current at 60 s target irradiation time was 40000 and the highest number of UCN counts was

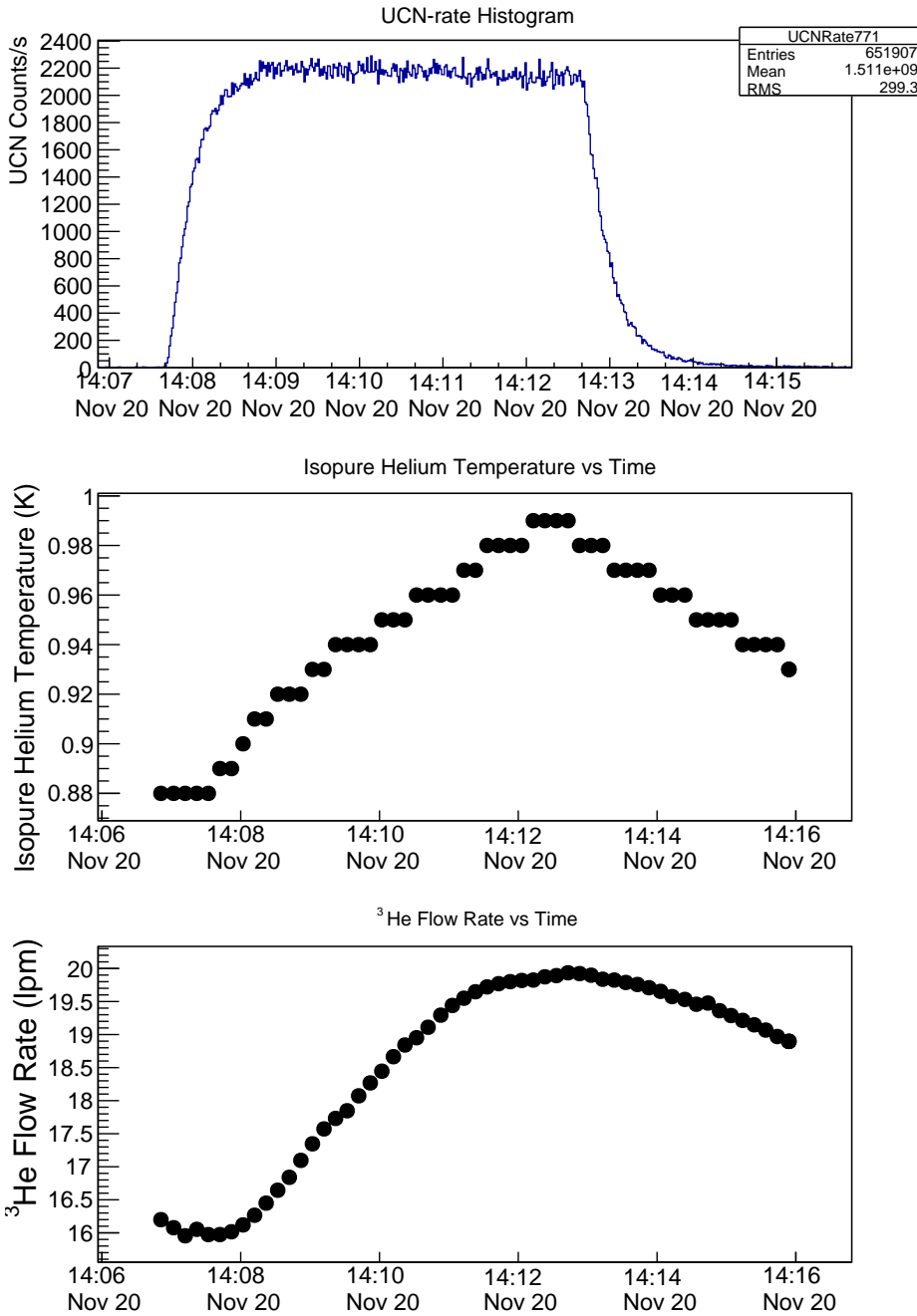


Figure 5.27: Steady-state UCN production data for  $1.5 \mu\text{A}$  proton beam current. The top graph shows the UCN rate over time, the middle graph shows the superfluid helium temperature (TS12) over time and the bottom graph shows the  $^3\text{He}$  flow rate versus time. Detail provided in text.

325000 at  $10 \mu\text{A}$  beam current and 60 s target irradiation time. The experimental period took about two weeks. In this time, the storage lifetime of UCN decreased from 37 s to 27 s with about 2 % decrease per day due to the source contamination after opening the UCN valve. The UCN counts also showed a decrease of about 40 % due to the source contamination as well as different experimental configuration at later dates. The steady-state UCN rate showed to be around  $1600 \text{ UCN/s}/\mu\text{A}$ .

To decrease the temperature of the superfluid by 0.1 K, a 5 min wait between the cycles is necessary. It is also concluded that, if interested in the  $^3\text{He}$  flow rate, the data acquisition should happen after the 4 K reservoir filling.

# Chapter 6

## Conclusion

The work presented in this thesis is part of the R&D studies towards the future nEDM experiment at TRIUMF. The existence of a non-zero nEDM confirms beyond the standard model theories that provide extra sources of CP violation. Based on Sakharov conditions, these sources are essential to create the observed Baryon asymmetry in the universe.

The focus of the research in this thesis is on the two aspects of the nEDM measurement: magnetic field stability, and UCN production and storage.

To measure the nEDM, an ensemble of polarized neutrons are placed in the presence of aligned electric and magnetic fields. The Larmor precession frequency of the UCN is measured once when the electric and magnetic fields are parallel, and once when they are anti-parallel. The frequency shift between these two geometries is proportional to the nEDM. In this process, the existence of a very stable and homogeneous magnetic environment is essential. The applied DC magnetic field should be held constant. To achieve the magnetic requirements several layers of magnetic shielding are employed including active and passive shielding. Internal coils are placed inside the passive shielding to create the DC magnetic field. These are called the shield-coupled coils. In this case, a change in the properties of the passive shields, such as magnetic permeability  $\mu$ , would affect the magnetic field measured internally. One of the factors that can cause such changes in  $\mu$  is the changes in the environmental temperature.

In Chapter 3 the result of the studies of the changes of  $\mu$  with temperature were presented and discussed. Two methods were pursued to study the correlation of the changes in the measured internal magnetic field with respect to the changes in temperature. In method one, a witness cylinder with a length of 15.2 cm and a diameter of 5.2 cm was put inside a coil system that produced a low-frequency magnetic field. The axial shielding factor was then measured with a magnetometer as a function of temperature. The temperature was measured via non-magnetic temperature sensors attached on the witness cylinder. These measurements were repeated with two different coils to study the systematic effects. In the second technique, which is more common, the witness cylinder was used as a core of a transformer. A primary and a secondary coil were wound on the witness cylinder. Here the slopes of the minor  $B - H$  loops as a function of temperature were measured.

The overall result of the  $B(T)$  measurements are presented in Tables 3.1 and 3.3. These measurements were conducted in AC fields with frequencies around 1 Hz as opposed to the DC fields in the actual nEDM experiments. To relate these measurements to  $\mu(T)$ , finite element simulations were performed to find the shielding factor of the witness cylinders as a function of  $\mu$ . Combining the measurements and the simulations, in the first

method it was found that  $0.6\%/\text{K} < \frac{1}{\mu} \frac{d\mu}{dT} < 2.7\%/\text{K}$  with  $H_m$ -amplitude of 0.004 A/m at 1 Hz. In the second method, it was found that  $0.0\%/\text{K} < \frac{1}{\mu} \frac{d\mu}{dT} < 2.2\%/\text{K}$  with a typical  $H_m$ -amplitude of 0.1 A/m at 1 Hz.

Considering the overall value of  $0.0\%/\text{K} < \frac{1}{\mu} \frac{d\mu}{dT} < 2.7\%/\text{K}$  and the generic EDM experiment sensitivity of  $\frac{\mu}{B_0} \frac{dB_0}{d\mu} = 0.01$ , the temperature dependence of the magnetic field in a typical nEDM experiment would be  $\frac{dB_0}{dT} = 0 - 270 \text{ pT/K}$ . This means, to achieve the magnetic stability goal of 1 pT in the interal field, the temperature of the innermost magnetic shield in the nEDM experiment should be controlled to  $< 0.004 \text{ K}$  level which puts a challenging constraint on the future nEDM experiment design.

The second half of this thesis was focused on the current UCN facility at TRIUMF. In 2016 the prototype vertical UCN source, previously built and tested in Japan, was shipped to TRIUMF. The unique feature of this facility is producing UCN by combining spallation neutrons with a helium converter. In Chapter 4 the facility was described.

In November 2017 the first UCN were produced with the prototype vertical source. Those experiments and the result of data analysis were presented in Chapter 5. Such experiments are essential for a better understanding of the cryostat and for the design of the next generation UCN source. Around 40000 UCN were produced at the standard measurement of 1  $\mu\text{A}$  proton beam current while irradiating the target for 60 s. The maximum number of produced UCN were 325000 at 10  $\mu\text{A}$  proton beam current. In about three weeks of experimental period, the measured storage lifetime of UCN dropped from 37 s to 27 s. This was due to the contamination in the source by opening the UCN valve. The UCN yield also dropped by about 40%. Other than the source contamination, different experimental configuration in the second half of the experimental run period caused this drop. Some measurements with the heater tapes were also performed to find the amount of heat load on the cryostat when applying the proton beam. Even though the result of those experiments was not conclusive, it gave valuable insight for the future experimental plan.

# Appendices



# Appendix A

## Review of Quantum Mechanics [153]

### A.1 Spin-1/2 Particle in a Magnetic Field

The Hamiltonian  $H$  for a particle at rest with spin  $\vec{S}$  in a magnetic field  $\vec{B}$  is

$$H = -\gamma \vec{S} \cdot \vec{B}, \quad (\text{A.1})$$

where  $\gamma$  is the gyromagnetic ratio. If the magnetic field  $\vec{B} = B_0 \hat{k}$ , then

$$H = -\gamma B_0 \vec{S} \cdot \hat{k} = -\gamma B_0 S_z \quad (\text{A.2})$$

where  $S_z$  is the projection of the particles spin along the z-axis. For spin-1/2 particles

$$S_z = \begin{pmatrix} \frac{\hbar}{2} & 0 \\ 0 & -\frac{\hbar}{2} \end{pmatrix} = \frac{\hbar}{2} \sigma_z,$$

where  $\sigma_z$  is the Pauli spin matrix

$$\sigma_z = \begin{pmatrix} 1 & 0 \\ 0 & -1 \end{pmatrix},$$

with eigenvalues  $\lambda_{1,2} = \pm 1$ , and corresponding eigenvectors

$$\vec{\chi}_{1,2} = \begin{pmatrix} 1 \\ 0 \end{pmatrix}, \begin{pmatrix} 0 \\ 1 \end{pmatrix} \quad (\text{A.3})$$

which can be relabeled as

$$\chi_1 = |\uparrow\rangle = \begin{pmatrix} 1 \\ 0 \end{pmatrix}, \quad \chi_2 = |\downarrow\rangle = \begin{pmatrix} 0 \\ 1 \end{pmatrix} \quad (\text{A.4})$$

The Hamiltonian is then

$$H = -\gamma B_0 \frac{\hbar}{2} \sigma_z = \omega_0 \frac{\hbar}{2} \sigma_z, \quad (\text{A.5})$$

where  $\omega_0 = \gamma B_0$ . The eigenvalues, or energies of this Hamiltonian are

$$E_\uparrow = -\omega_0 \frac{\hbar}{2} \quad \text{and} \quad E_\downarrow = \omega_0 \frac{\hbar}{2}. \quad (\text{A.6})$$

The corresponding eigenvectors evolve with time as

$$|\uparrow(t)\rangle = |\uparrow\rangle e^{-i \frac{E_\uparrow t}{\hbar}} = |\uparrow\rangle e^{i \frac{\omega_0 t}{2}} \quad (\text{A.7})$$

and

$$|\downarrow(t)\rangle = |\downarrow\rangle e^{-i\frac{E_{\downarrow}t}{\hbar}} = |\downarrow\rangle e^{-i\frac{\omega_0 t}{2}}. \quad (\text{A.8})$$

The state of the system at time  $t$  is

$$|\psi(t)\rangle = a_0 |\uparrow(t)\rangle + b_0 |\downarrow(t)\rangle = \begin{pmatrix} a_0 e^{i\frac{\omega_0 t}{2}} \\ b_0 e^{-i\frac{\omega_0 t}{2}} \end{pmatrix} \quad (\text{A.9})$$

with

$$|\psi(0)\rangle = \begin{pmatrix} a_0 \\ b_0 \end{pmatrix}. \quad (\text{A.10})$$

For normalization, it is require that  $|a_0|^2 + |b_0|^2 = 1$ . Let  $a_0 = \cos(\alpha/2)$  and  $b_0 = \sin(\alpha/2)$ , then

$$|\psi(t)\rangle = \cos(\alpha/2) |\uparrow\rangle e^{i\frac{\omega_0 t}{2}} + \sin(\alpha/2) |\downarrow\rangle e^{-i\frac{\omega_0 t}{2}} = \begin{pmatrix} \cos(\alpha/2) e^{i\frac{\omega_0 t}{2}} \\ \sin(\alpha/2) e^{-i\frac{\omega_0 t}{2}} \end{pmatrix}. \quad (\text{A.11})$$

This is the time-varying wavefunction of a spin-1/2 particle in a static magnetic field  $\vec{B} = B_0 \hat{k}$ .

## A.2 Larmor precession

Using Eqn. A.11, we can determine  $\langle S_x \rangle$ ,  $\langle S_y \rangle$ , and  $\langle S_z \rangle$ , where

$$S_x = \begin{pmatrix} 0 & \frac{\hbar}{2} \\ \frac{\hbar}{2} & 0 \end{pmatrix} = \frac{\hbar}{2} \sigma_y, \quad \text{and} \quad S_y = \begin{pmatrix} 0 & -i\frac{\hbar}{2} \\ i\frac{\hbar}{2} & 0 \end{pmatrix} = \frac{\hbar}{2} \sigma_y,$$

and

$$\langle S \rangle = \langle \psi(t) | S | \psi(t) \rangle.$$

$$\begin{aligned} \langle S_x \rangle &= \left( \cos(\alpha/2)^* e^{-i\frac{\omega_0 t}{2}} \ \sin(\alpha/2)^* e^{i\frac{\omega_0 t}{2}} \right) \begin{pmatrix} 0 & \hbar/2 \\ \hbar/2 & 0 \end{pmatrix} \begin{pmatrix} \cos(\alpha/2) e^{i\frac{\omega_0 t}{2}} \\ \sin(\alpha/2) e^{-i\frac{\omega_0 t}{2}} \end{pmatrix} \\ &= \left( \cos(\alpha/2) e^{-i\frac{\omega_0 t}{2}} \ \sin(\alpha/2) e^{i\frac{\omega_0 t}{2}} \right) \begin{pmatrix} \frac{\hbar}{2} \sin(\alpha/2) e^{-i\frac{\omega_0 t}{2}} \\ \frac{\hbar}{2} \cos(\alpha/2) e^{i\frac{\omega_0 t}{2}} \end{pmatrix} \\ &= \frac{\hbar}{2} \cos(\alpha/2) \sin(\alpha/2) e^{-i\omega_0 t} + \frac{\hbar}{2} \sin(\alpha/2) \cos(\alpha/2) e^{-i\omega_0 t} \\ &= \hbar \cos(\alpha/2) \sin(\alpha/2) \left( \frac{e^{-i\omega_0 t} + e^{i\omega_0 t}}{2} \right) \\ &= \hbar \cos(\alpha/2) \sin(\alpha/2) \cos(\omega_0 t) \\ &= \frac{\hbar}{2} \sin(\alpha) \cos(\omega_0 t) \end{aligned} \quad (\text{A.12})$$

$$\begin{aligned}
\langle S_y \rangle &= \left( \cos(\alpha/2)^* e^{-i\frac{\omega_0 t}{2}} \sin(\alpha/2)^* e^{i\frac{\omega_0 t}{2}} \right) \begin{pmatrix} 0 & -i\hbar/2 \\ i\hbar/2 & 0 \end{pmatrix} \begin{pmatrix} \cos(\alpha/2) e^{i\frac{\omega_0 t}{2}} \\ \sin(\alpha/2) e^{-i\frac{\omega_0 t}{2}} \end{pmatrix} \\
&= \left( \cos(\alpha/2) e^{-i\frac{\omega_0 t}{2}} \sin(\alpha/2) e^{i\frac{\omega_0 t}{2}} \right) \begin{pmatrix} -i\frac{\hbar}{2} \sin(\alpha/2) e^{-i\frac{\omega_0 t}{2}} \\ i\frac{\hbar}{2} \cos(\alpha/2) e^{i\frac{\omega_0 t}{2}} \end{pmatrix} \\
&= -i\frac{\hbar}{2} \cos(\alpha/2) \sin(\alpha/2) e^{-i\omega_0 t} + i\frac{\hbar}{2} \sin(\alpha/2) \cos(\alpha/2) e^{i\omega_0 t} \\
&= -\hbar \cos(\alpha/2) \sin(\alpha/2) \left( \frac{e^{i\omega_0 t} - e^{-i\omega_0 t}}{2i} \right) \\
&= -\hbar \cos(\alpha/2) \sin(\alpha/2) \sin(\omega_0 t) \\
&= -\frac{\hbar}{2} \sin(\alpha) \sin(\omega_0 t)
\end{aligned} \tag{A.13}$$

$$\begin{aligned}
\langle S_z \rangle &= \left( \cos(\alpha/2)^* e^{-i\frac{\omega_0 t}{2}} \sin(\alpha/2)^* e^{i\frac{\omega_0 t}{2}} \right) \begin{pmatrix} \hbar/2 & 0 \\ 0 & -\hbar/2 \end{pmatrix} \begin{pmatrix} \cos(\alpha/2) e^{i\frac{\omega_0 t}{2}} \\ \sin(\alpha/2) e^{-i\frac{\omega_0 t}{2}} \end{pmatrix} \\
&= \left( \cos(\alpha/2) e^{-i\frac{\omega_0 t}{2}} \sin(\alpha/2) e^{i\frac{\omega_0 t}{2}} \right) \begin{pmatrix} \frac{\hbar}{2} \cos(\alpha/2) e^{i\frac{\omega_0 t}{2}} \\ -\frac{\hbar}{2} \sin(\alpha/2) e^{-i\frac{\omega_0 t}{2}} \end{pmatrix} \\
&= \frac{\hbar}{2} (\cos^2(\alpha/2) - \sin^2(\alpha/2)) \\
&= \frac{\hbar}{2} (\cos^2(\alpha/2) - 1 + \cos^2(\alpha/2)) \\
&= \frac{\hbar}{2} (2\cos(\alpha/2)^2 - 1) \\
&= \frac{\hbar}{2} (2 \left( \frac{1 + \cos(\alpha)}{2} \right) - 1) \\
&= \frac{\hbar}{2} \cos(\alpha)
\end{aligned} \tag{A.14}$$

### A.3 Effect of RF Pulses and NMR Lineshape

In this section the effect of adding an oscillating field at resonance, perpendicular to the static  $B_0$  field is studied. Consider

$$\begin{aligned}
\vec{B}_0 &= B_0 \hat{z}, \quad \vec{B}_1 = B_1 \cos(\omega t) \hat{i} - B_1 \sin(\omega t) \hat{j} \\
\vec{B} &= \vec{B}_0 + \vec{B}_1 = B_0 \hat{z} + B_1 (\cos(\omega t) \hat{i} - \sin(\omega t) \hat{j}).
\end{aligned} \tag{A.15}$$

The Hamiltonian would be

$$\begin{aligned}
H &= -\vec{\mu} \cdot \vec{B} = -\gamma \vec{S} \cdot \vec{B} = -\gamma (B_0 S_z + B_1 \cos(\omega t) S_x - B_1 \sin(\omega t) S_y) \\
&= -\gamma \frac{\hbar}{2} (B_0 \sigma_z + B_1 \cos(\omega t) \sigma_x - B_1 \sin(\omega t) \sigma_y).
\end{aligned} \tag{A.16}$$

In matrix form

$$\begin{aligned}
H &= -\gamma \frac{\hbar}{2} \begin{pmatrix} B_0 & B_1 (\cos(\omega t) + i \sin(\omega t)) \\ B_1 (\cos(\omega t) - i \sin(\omega t)) & -B_0 \end{pmatrix} \\
&= -\gamma \frac{\hbar}{2} \begin{pmatrix} B_0 & B_1 e^{i\omega t} \\ B_1 e^{-i\omega t} & -B_0 \end{pmatrix}.
\end{aligned} \tag{A.17}$$

The Schrödinger equation

$$H|\psi(t)\rangle = i\hbar \frac{\partial}{\partial t} |\psi(t)\rangle \quad (\text{A.18})$$

would then become

$$-\gamma \frac{\hbar}{2} \begin{pmatrix} B_0 & B_1 e^{i\omega t} \\ B_1 e^{-i\omega t} & -B_0 \end{pmatrix} \begin{pmatrix} a(t) \\ b(t) \end{pmatrix} = i\hbar \frac{\partial}{\partial t} \begin{pmatrix} a(t) \\ b(t) \end{pmatrix}. \quad (\text{A.19})$$

This gives two coupled differential equations to solve. Letting  $\gamma B_0 = \omega_0$ , and  $\gamma B_1 = \omega_1$ , then

$$\dot{a}(t) = \frac{i}{2} [\omega_0 a(t) + \omega_1 e^{i\omega t} b(t)]. \quad (\text{A.20})$$

and

$$\dot{b}(t) = \frac{i}{2} [\omega_1 e^{-i\omega t} a(t) - \omega_0 b(t)]. \quad (\text{A.21})$$

Eqn. A.20 and Eqn. A.21 could be solved by taking the second order derivative of  $a(t)$

$$\ddot{a} = \frac{i}{2} (\omega_0 \dot{a} + i\omega \omega_1 e^{i\omega t} b + \omega_1 e^{i\omega t} \dot{b}). \quad (\text{A.22})$$

Using Eqn. A.20 and solving for  $b$  in terms of  $a$  and  $\dot{a}$

$$b = \frac{-i2\dot{a} - \omega_0 a}{\omega_1} e^{-i\omega t}. \quad (\text{A.23})$$

Plugging Eqn. A.21 and Eqn. A.23 into Eqn. A.22 gives

$$\ddot{a} = i\omega \dot{a} - \frac{a}{4} (\omega^2 + \omega_0^2 - 2\omega\omega_0), \quad (\text{A.24})$$

which has a solution of the form  $a = a_0 e^{i\alpha t}$ , where  $a_0$  and  $\alpha$  are parameters to be determined. Plugging this into Eqn. A.24 gives

$$0 = \alpha^2 - \omega\alpha - \frac{\omega_1^2 + \omega_0^2 - 2\omega\omega_0}{4} \quad (\text{A.25})$$

and therefore

$$\alpha_{\pm} = \frac{\omega \pm \omega'}{2}, \quad \omega' = \sqrt{\omega_1^2 + (\omega_0 - \omega)^2}. \quad (\text{A.26})$$

General solution of  $a(t)$  could be written as

$$a(t) = c_1 e^{i\alpha_+ t} + c_2 e^{i\alpha_- t}, \quad (\text{A.27})$$

where  $c_1$  and  $c_2$  are constants to be determined from initial conditions. Plugging Eqn. A.27, and it's first order time-derivative into Eqn. A.23 gives the general solution for  $b(t)$

$$b(t) = \frac{1}{\omega_1} [c_1(2\alpha_+ - \omega_0) e^{i\alpha_+ t} + c_2(2\alpha_- - \omega_0) e^{i\alpha_- t}] e^{-i\omega t}. \quad (\text{A.28})$$

At  $t = 0$ , the solutions of  $a(t)$  and  $b(t)$  become

$$\begin{aligned} a(0) &= a_0 = c_1 + c_2 \\ b(0) &= b_0 = \frac{1}{\omega_1} [c_1(2\alpha_+ - \omega_0 + c_2(2\alpha_- - \omega_0))]. \end{aligned} \quad (\text{A.29})$$

Solving for  $c_1$  and  $c_2$  in terms of  $a_0$  and  $b_0$  gives

$$\begin{aligned} c_1 &= a_0 \left( \frac{\omega' - \omega + \omega_0}{2\omega'} \right) + \frac{\omega_1 b_0}{2\omega'} \\ c_2 &= \frac{1}{\omega'} [a_0(\omega + \omega' - \omega_0) - \omega_1 b_0]. \end{aligned} \quad (\text{A.30})$$

Plugging  $c_1$  and  $c_2$  into the general solutions of  $a(t)$  and  $b(t)$  gives

$$\begin{aligned} a(t) &= \left\{ a_0 \cos(\omega' t/2) + \frac{i}{\omega'} [a_0(\omega_0 - \omega) + b_0 \omega_1] \sin(\omega' t/2) \right\} e^{\frac{i\omega t}{2}} \\ b(t) &= \left\{ b_0 \cos(\omega' t/2) + \frac{i}{\omega'} [b_0(\omega - \omega_0) + a_0 \omega_1] \sin(\omega' t/2) \right\} e^{\frac{-i\omega t}{2}}. \end{aligned} \quad (\text{A.31})$$

If the particle starts out at  $t = 0$  with spin up (*i.e.*,  $a_0 = 1$ ,  $b_0 = 0$ ),

$$\begin{aligned} a(t) &= \left\{ \cos(\omega' t/2) + \frac{i}{\omega'} (\omega_0 - \omega) \sin(\omega' t/2) \right\} e^{\frac{i\omega t}{2}} \\ b(t) &= \frac{i}{\omega'} \sin(\omega' t/2) e^{\frac{-i\omega t}{2}} \end{aligned} \quad (\text{A.32})$$

and the probability of a transition to spin down, as a function of time, is then

$$\begin{aligned} P(t) &= |b(t)|^2 \\ &= \left| \frac{-i}{\omega'} \sin(\omega' t/2) e^{\frac{i\omega t}{2}} \right|^2 \left| \frac{i}{\omega'} \sin(\omega' t/2) e^{\frac{-i\omega t}{2}} \right|^2 \\ &= \frac{\omega_1^2}{\omega'^2} \sin^2\left(\frac{\omega' t}{2}\right) \\ &= \frac{\omega_1^2}{\omega_1^2 + (\omega_0 - \omega)^2} \sin^2\left(\frac{\omega' t}{2}\right) \\ &= \frac{\omega_1^2}{\omega_1^2 + (\omega_0 - \omega)^2} \frac{1 - \cos(\omega' t)}{2}. \end{aligned} \quad (\text{A.33})$$

A maximum will occur on resonance when  $\omega = \omega_0$ , and when  $\omega' t = \pi$ . Then for  $\omega'$  would become

$$\begin{aligned} \omega' &= \sqrt{\omega_1^2 + (\omega_0 - \omega)^2} \\ &= \sqrt{\omega_1^2 + (\omega_0 - \omega_0)^2} \\ &= \omega_1 \quad , \end{aligned} \quad (\text{A.34})$$

which gives a pulse length of

$$t = \frac{\pi}{\omega'} = \frac{\pi}{\omega_1} \quad . \quad (\text{A.35})$$

Defining a dimensionless parameter  $x = (\frac{\omega_0 - \omega}{\omega_1})^2$ , and setting  $\omega_1 t = \pi$  gives

$$P(x) = \frac{1}{1+x^2} \sin^2\left(\sqrt{(x^2+1)} \frac{\pi}{2}\right). \quad (\text{A.36})$$

It is clear from Fig. A.1 that the probability of a transition from spin-up to spin-down is most likely to occur when  $x = 0$ , which corresponds to  $\omega = \omega_0$ .  $\omega_0$  is then considered to be the resonant frequency of this system, and is known as the Larmor precession frequency.

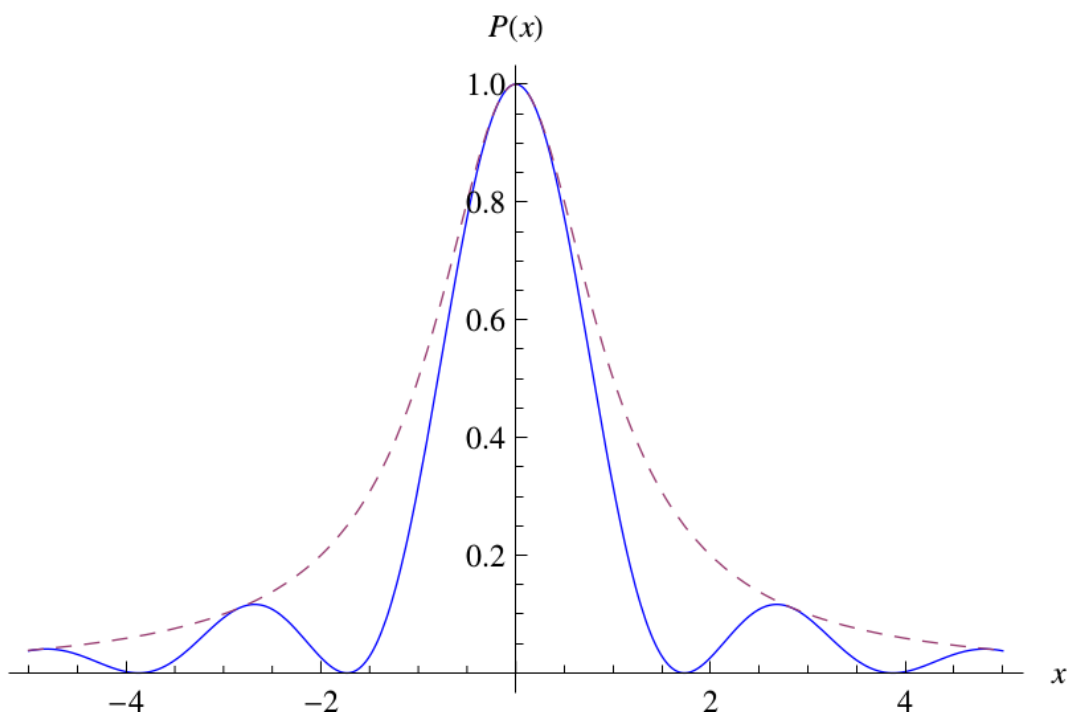


Figure A.1: The solid blue line shows the probability of the transition from spin-up to spin-down with  $\omega_1 t = \pi$ . The dashed line shows the envelope of the transition probability, which is the simply  $1/(1+x^2)$ .

## Appendix B

# Derivation of Ramsey's Method [153]

Here is a review of the Ramsey technique for the molecular beam resonance experiments. In previous studies, the oscillating fields were extended uniformly throughout the regions in which the energy levels of the system were investigated. This was not efficient since the amplitude and the phase of the oscillating field might change along the path of the beam. As a different approach, Ramsey suggested to confine the oscillating fields to small regions; one at the beginning of the space which the energy levels are being studied and the other one at the end. In this case, there is no oscillating field in between.

Consider a system which is subjected to an oscillatory perturbation at time  $t_1$ . This induces a transition between the eigenstates p and q:

$$V = \begin{pmatrix} 0 & \hbar b e^{i\omega t} \\ \hbar b e^{-i\omega t} & 0 \end{pmatrix} \quad (\text{B.1})$$

An example of such perturbation is a system with a magnetic moment entering a region with rotating magnetic field with angular velocity  $\omega$ . The general wave function for this system is

$$\psi(t) = C_p(t)\psi_p + C_q(t)\psi_q. \quad (\text{B.2})$$

Therefore, the time dependent Schrödinger equations will have the form

$$i\hbar\dot{C}_p(t) = W_p C_p(t) + \hbar b e^{i\omega t} C_q(t) \quad (\text{B.3})$$

$$i\hbar\dot{C}_q(t) = \hbar b e^{-i\omega t} C_p(t) + W_q C_q(t). \quad (\text{B.4})$$

In matrix form Eqns. B.3 and B.4 could be written as

$$i\hbar \frac{d}{dt} \begin{pmatrix} C_p \\ C_q \end{pmatrix} = \begin{pmatrix} W_p & \hbar b e^{i\omega t} \\ \hbar b e^{-i\omega t} & W_q \end{pmatrix} \begin{pmatrix} C_p \\ C_q \end{pmatrix} \quad (\text{B.5})$$

It is assumed that, at  $t = t_1$ ,  $C_p$  and  $C_q$  have the values  $C_p(t_1)$  and  $C_q(t_1)$  respectively. The  $2 \times 2$  matrix on the right side could be written as

$$\begin{aligned} \begin{pmatrix} W_p & \hbar b e^{i\omega t} \\ \hbar b e^{-i\omega t} & W_q \end{pmatrix} &= \begin{pmatrix} W_p & \hbar b \cos \omega t + i\hbar b \sin \omega t \\ \hbar b \cos \omega t - i\hbar b \sin \omega t & W_q \end{pmatrix} \\ &= \begin{pmatrix} W_p & 0 \\ 0 & W_q \end{pmatrix} - \hbar b \sin \omega t \sigma_2 + \hbar b \cos \omega t \sigma_1. \end{aligned} \quad (\text{B.6})$$

Here  $\sigma_1$  and  $\sigma_2$  are Pauli matrices. Replacing Eqn. B.6 in Eqn. B.5

$$\frac{d}{dt} \begin{pmatrix} C_p \\ C_q \end{pmatrix} = -i \left[ \begin{pmatrix} \frac{W_p}{\hbar} & 0 \\ 0 & \frac{W_q}{\hbar} \end{pmatrix} + b\sigma_1 \cos \omega t - b\sigma_2 \sin \omega t \right] \begin{pmatrix} C_p \\ C_q \end{pmatrix}. \quad (\text{B.7})$$

The first matrix on the right could be written as

$$\begin{aligned} \begin{pmatrix} \frac{W_p}{\hbar} & 0 \\ 0 & \frac{W_q}{\hbar} \end{pmatrix} &= \begin{pmatrix} \frac{W_p+W_q}{2\hbar} + \frac{W_p-W_q}{2\hbar} & 0 \\ 0 & \frac{W_p+W_q}{2\hbar} - \frac{W_p-W_q}{2\hbar} \end{pmatrix} \\ &= \begin{pmatrix} \Omega + \omega_0/2 & 0 \\ 0 & \Omega - \omega_0/2 \end{pmatrix} \\ &= \Omega + \frac{\omega_0}{2} \sigma_3 \end{aligned} \quad (\text{B.8})$$

where

$$C = \begin{pmatrix} C_p \\ C_q \end{pmatrix}, \Omega = \frac{W_p + W_q}{2\hbar}, \omega_0 = \frac{W_q - W_p}{\hbar}. \quad (\text{B.9})$$

Therefore the Schrödinger equation takes the form

$$\frac{d}{dt} C = -i \left[ \Omega - \frac{\omega_0}{2} \sigma_3 + b(\sigma_1 \cos \omega t - \sigma_2 \sin \omega t) \right] C. \quad (\text{B.10})$$

The term  $(\sigma_1 \cos \omega t - \sigma_2 \sin \omega t)$  is like a rotation. In general, we have

$$e^{-i\vec{\sigma} \cdot \hat{n}\frac{\theta}{2}} \vec{a} \cdot \vec{\sigma} e^{i\vec{\sigma} \cdot \hat{n}\frac{\theta}{2}} = [\hat{n}(\hat{n} \cdot \vec{a}) + \cos \theta(\vec{a} - \hat{n}(\hat{n} \cdot \vec{a})) + \sin \theta(\hat{n} \times \vec{a})] \vec{\sigma}. \quad (\text{B.11})$$

If  $\hat{n} = -\hat{k}$  and  $\vec{a} = \hat{x}$ , then

$$\sigma_1 \cos \omega t - \sigma_2 \sin \omega t = e^{i\frac{\omega t}{2} \sigma_3} \sigma_1 e^{-i\frac{\omega t}{2} \sigma_3}. \quad (\text{B.12})$$

Hence, the Schrödinger equation will be

$$\dot{C} = -ie^{i\frac{\omega t}{2} \sigma_3} \left[ \Omega - \frac{\omega_0}{2} \sigma_3 + b\sigma_1 \right] e^{-i\frac{\omega t}{2} \sigma_3} C. \quad (\text{B.13})$$

Rewriting the Schrödinger equation in terms of variable  $D$

$$\dot{D} = -i \left[ \left( \frac{\omega - \omega_0}{2} \right) \sigma_3 + b\sigma_1 \right] D, \quad (\text{B.14})$$

where

$$C = e^{i\frac{\omega t}{2} \sigma_3} e^{-i\Omega t} D \quad (\text{B.15})$$

or

$$\dot{D} = \frac{ia}{2} [\sigma_3 \cos \theta - \sigma_1 \sin \theta] D \quad (\text{B.16})$$

where  $a := [(\omega_0 - \omega)^2 + (2b)^2]^{\frac{1}{2}}$ ,  $\cos \theta = \frac{\omega_0 - \omega}{a}$  and  $\sin \theta = \frac{2b}{a}$ . Hence, at  $t = t_1 + T$ , the solution to the Eqn. B.16 is

$$D(t_1 + T) = e^{\left[ \frac{ia}{2} (\sigma_3 \cos \theta - \sigma_1 \sin \theta) T \right]} D(t_1). \quad (\text{B.17})$$

Using  $e^{i\vec{\sigma} \cdot \hat{n}\frac{\phi}{2}} = I \cos \frac{\phi}{2} + i(\vec{\sigma} \cdot \hat{n}) \sin \frac{\phi}{2}$  with  $\phi = aT$  and  $\vec{\sigma} \cdot \hat{n} = \sigma_3 \cos \theta - \sigma_1 \sin \theta$ , then

$$D(t_1 + T) = \left[ \cos \frac{aT}{2} + i(\sigma_3 \cos \theta - \sigma_1 \sin \theta) \sin \frac{aT}{2} \right] D(t_1) \quad (\text{B.18})$$

and therefore  $C(t_1 + T)$  would be

$$\begin{aligned} C(t_1 + T) &= e^{i\frac{\omega}{2}(t_1+T)\sigma_3} e^{-i\Omega T} \left[ \cos \frac{aT}{2} + i(\sigma_3 \cos \theta - \sigma_1 \sin \theta) \sin \frac{aT}{2} \right] \\ &\quad \times e^{-i\frac{\omega t_1}{2}\sigma_3} C(t_1), \end{aligned} \quad (\text{B.19})$$

or equivalently

$$\begin{aligned} C_p(t_1 + T) &= \left\{ \left[ i \cos \theta \sin \frac{aT}{2} + \cos \frac{aT}{2} \right] C_p(t_1) \right. \\ &\quad \left. - \left[ i \sin \theta \sin \frac{aT}{2} e^{i\omega t_1} \right] C_q(t_1) \right\} e^{\left\{ i \left[ \frac{1}{2}\omega - \frac{(W_p+W_q)}{2\hbar} \right] T \right\}} \\ C_q(t_1 + T) &= \left\{ - \left[ i \sin \theta \sin \frac{aT}{2} e^{-i\omega t_1} \right] C_p(t_1) \right. \\ &\quad \left. + \left[ -i \cos \theta \sin \frac{aT}{2} + \cos \frac{aT}{2} \right] C_q(t_1) \right\} e^{\left\{ i \left[ -\frac{\omega}{2} - \frac{W_p+W_q}{2\hbar} \right] T \right\}}. \end{aligned} \quad (\text{B.20})$$

These are the general solutions for a system with energy eigenstates  $p$  and  $q$ . As a comparison, if  $C_p(t_1 + T) = a(t)$ ,  $C_q(t_1 + T) = b(t)$ ,  $a = \omega'$ ,  $2b = \omega_1$  then Eqn. A.31. In this case,  $W_p$  and  $W_q$  are energies of the spin up and spin down configurations.

As a special case, if  $b = 0$  (no perturbation), then  $\cos \theta = 1$  and  $\sin \theta = 0$ . Hence, the solutions would be

$$\begin{aligned} C_p(t_1 + T) &= e^{-i\frac{W_p}{\hbar}T} C_p(t_1) \\ C_q(t_1 + T) &= e^{-i\frac{W_q}{\hbar}T} C_q(t_1). \end{aligned} \quad (\text{B.21})$$

Now, consider a system which is subjected to perturbation for time  $\tau$  and length  $l$ , then the perturbation goes off for time  $T$  and length  $L$  and again the perturbation goes on for another time  $\tau$ . To achieve greater generality, corresponding to the experimental impossibility of attaining completely uniform magnetic fields, it is assumed that energy levels  $p$  and  $q$  are not constant in the intermediate state when  $b = 0$ , which means, it is divided to sub-regions with duration  $\Delta t_k$  and energies are  $W_{p,k}$  and  $W_{q,k}$  respectively. Assuming

$$C_p(0) = 1, \quad C_q(0) = 0, \quad (\text{B.22})$$

it means, the system is at state  $p$  before it enters the first perturbation region. Hence, the amplitudes would be

$$\begin{aligned} C_p(\tau) &= \left[ i \cos \theta \sin \frac{a\tau}{2} + \cos \frac{a\tau}{2} \right] e^{i \left[ \frac{\omega}{2} - \left( \frac{W_p+W_q}{2\hbar} \right) \right] \tau} \\ C_q(\tau) &= \left[ -i \sin \theta \sin \frac{a\tau}{2} \right] e^{i \left[ -\frac{\omega}{2} - \left( \frac{W_p+W_q}{2\hbar} \right) \right] \tau}. \end{aligned} \quad (\text{B.23})$$

And after entering the intermediate region,

$$\begin{aligned} C_p(\tau + T) &= \Pi_k e^{-iW_{p,k}\Delta t_k} C_p(\tau) \\ &= e^{-\frac{i}{\hbar}\Sigma_k W_{p,k}\Delta t_k} C_p(\tau) \\ C_p(\tau + T) &= e^{-i\frac{\bar{W}_p T}{\hbar}} C_p(\tau) \end{aligned} \quad (\text{B.24})$$

$$C_q(\tau + T) = e^{-i\frac{\bar{W}_q T}{\hbar}} C_q(\tau). \quad (\text{B.25})$$

It is impossible to have completely uniform magnetic fields in the experiment. Therefore, it is assumed that the energies of the  $p$  and  $q$  states are not constant in this region, and the region is divided into a number of sub-regions such that in the  $k^{th}$  sub-region of duration  $\Delta t_k$  the energies are  $W_{p,k}$  and  $W_{q,k}$ . In addition,  $\bar{W}_p = \frac{1}{T} \sum_k W_{p,k} \Delta t_k = \frac{1}{L} \sum_k W_{p,k} \Delta L_k$ , which is the space mean value of  $W_p$ . There is a similar interpretation for  $W_q$  as well. After entering the final perturbation region,

$$\begin{aligned} C_p(2\tau + T) &= \left\{ \left[ i \cos \theta \sin \frac{a\tau}{2} + \cos \frac{a\tau}{2} \right] C_p(\tau + T) \right. \\ &\quad \left. - \left[ i \sin \theta \sin \frac{a\tau}{2} e^{i\omega(\tau+T)} \right] C_q(\tau + T) \right\} \times e^{i\left[\frac{\omega}{2} - \frac{(W_p+W_q)}{2\hbar}\right]\tau} \\ C_q(2\tau + T) &= \left\{ - \left[ i \sin \theta \sin \frac{a\tau}{2} e^{-i\omega(\tau+T)} \right] C_p(\tau + T) \right. \\ &\quad \left. + \left[ -i \cos \theta \sin \frac{a\tau}{2} + \cos \frac{a\tau}{2} \right] C_q(\tau + T) \right\} \times e^{i\left[\frac{-\omega}{2} - \frac{(W_p+W_q)}{2\hbar}\right]\tau} \end{aligned} \quad (\text{B.26})$$

or it could be rewritten as

$$\begin{aligned} C_q(2\tau + T) &= 2i \sin \theta \left[ \cos \theta \sin^2 \frac{a\tau}{2} \sin \frac{\lambda T}{2} - \frac{1}{2} \sin a\tau \cos \frac{\lambda T}{2} \right] \\ &\quad \times e^{-i\left[\frac{\omega}{2} + \frac{(W_p+W_q)}{2\hbar}\right]\tau} (2\tau + T) + \left[ \frac{\bar{W}_q - W_p + \bar{W}_p - W_q}{2\hbar} T \right], \end{aligned} \quad (\text{B.27})$$

where

$$\lambda = \left( \frac{\bar{W}_q - \bar{W}_p}{\hbar} \right) - \omega. \quad (\text{B.28})$$

Therefore, the probability that the system changes from state  $p$  to state  $q$  is

$$P_{p,q} = |C_q|^2 = 4 \sin^2 \theta \sin^2 \frac{a\tau}{2} \left[ \cos \frac{\lambda T}{2} \cos \frac{a\tau}{2} - \cos \theta \sin \frac{\lambda T}{2} \sin \frac{a\tau}{2} \right]^2. \quad (\text{B.29})$$

Defining a dimensionless parameter  $x$  as

$$x := \frac{\omega_0 - \omega}{2b}, \quad (\text{B.30})$$

and therefore,  $a$  would take the form

$$a = 2b\sqrt{1+x^2}. \quad (\text{B.31})$$

Setting  $b\tau = \frac{\pi}{4}$  (which is similar to Section A.3 where  $\omega_1 t = \pi$ ) and  $T = 8\tau$ , then

$$\begin{aligned} P(x) &= \frac{4}{1+x^2} \left[ \sin \left( \sqrt{1+x^2} \frac{\pi}{4} \right) \right]^2 \\ &\quad \times \left[ \cos(2\pi x) \cos \left( \sqrt{1+x^2} \frac{\pi}{4} \right) - \frac{x}{1+x^2} \sin \left( \sqrt{1+x^2} \frac{\pi}{4} \right) \right]^2, \end{aligned} \quad (\text{B.32})$$

and is plotted in Fig. B.1.

An important special case of this relation is that corresponding to a nuclear magnetic moment of spin- $\frac{1}{2}$  with gyromagnetic ratio  $\gamma$ , in a fixed field of strength  $B_0$ , with a weak field of strength  $B_1$  perpendicular to  $B_0$  and rotating about  $B_0$ . In this case, the above equation applies with

$$\omega_0 = \gamma B_0, \lambda = \omega_0 - \omega \quad (\text{B.33})$$

$$2b = \gamma B_1 = \frac{\omega_0 B_1}{B_0} \quad (\text{B.34})$$

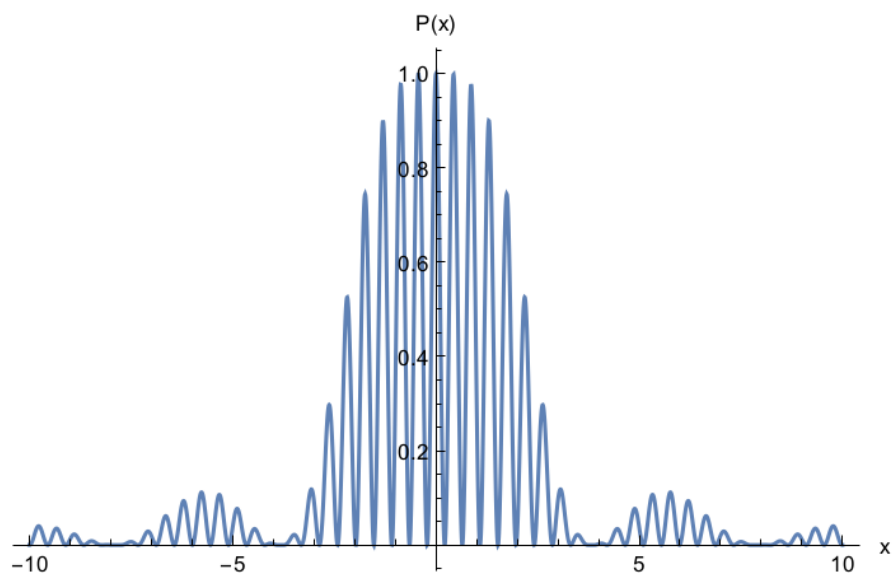


Figure B.1: The graph above shows the transition probability of spin down using Ramsey technique of separated oscillating fields. In this graph  $T = 8\tau$  and  $b\tau = \frac{\pi}{4}$ .



# Appendix C

## Geometric phase effect [153]

### C.1 Geometric phase effect as a Bloch-Siegert shift

Experiments designed to measure the Electric Dipole Moment (EDM), typically observe particles of interest as they move through a region of uniform and aligned  $\vec{E}$  and  $\vec{B}_0$  fields. The particles under question are usually neutral and have a total spin angular momentum  $\vec{J}$ . The external field interaction Hamiltonian is

$$H_{ext} = \frac{\mu_a}{J} \vec{J} \cdot \vec{B}_0 - \frac{d_a}{J} \vec{J} \cdot \vec{E}, \quad (\text{C.1})$$

where  $\mu_a$  and  $d_a$  are the magnetic and electric dipole moments, respectively. The Larmor precesssion frequencies, for parallel and antiparallel  $\vec{B}_0$  and  $\vec{E}$ , are given by the expressions

$$\omega_{L\uparrow\uparrow} = -\frac{(\mu_a B_{0\uparrow\uparrow} + d_a E)}{J\hbar}, \quad \omega_{L\uparrow\downarrow} = -\frac{(\mu_a B_{0\uparrow\downarrow} - d_a E)}{J\hbar} \quad (\text{C.2})$$

An EDM will reveal itself by causing a reduction or enhancement of the accumulated precession frequency according to whether the fields are parallel or anti-parallel.

If the particles are moving through static, but non-uniform fields, there exists motion of the fields in the frame of any particle. This causes geometric phases (GP's) in the precession of the total spin of the ensemble, which is generally independent of the precession caused by an EDM. Therefore, the terms  $+\epsilon_{geo\uparrow\uparrow}/T$  and  $+\epsilon_{geo\uparrow\downarrow}/T$  should be added to the right-hand sides of Equations C.2 respectively. The accumulated phase measured int he time interval  $T$  will be

$$(|\omega_{L\uparrow\uparrow}| - |\omega_{L\uparrow\downarrow}|)T = \frac{|\mu_a|(B_{0\uparrow\uparrow} - B_{0\uparrow\downarrow})T}{J\hbar} \pm \frac{2d_a ET}{J\hbar} \pm (\epsilon_{geo\uparrow\uparrow} - \epsilon_{geo\uparrow\downarrow}), \quad (\text{C.3})$$

where the sign alternative has to be chosen to be the same as the sign of  $\mu_a$ . If  $B_0$  remains constant while  $\vec{E}$  is reversed, then the first term becomes zero. The geometric phase term will result in a false EDM  $d_{af}$  given by

$$d_{af} = -(\epsilon_{geo\uparrow\uparrow} - \epsilon_{geo\uparrow\downarrow}) \frac{J\hbar}{2ET} = -(\Delta\omega_{geo\uparrow\uparrow} - \Delta\omega_{geo\uparrow\downarrow}) \frac{J\hbar}{2E}, \quad (\text{C.4})$$

where  $\Delta\omega_{geo\uparrow\uparrow}$  is the average rate of accumulation of the GP proportional to  $E$  for the particle ensemble of spins in parallel fields.

As a particle moves through the electric field with velocity  $v$ , it experiences an effective magnetic field

$$\vec{B}_v = \frac{\vec{E} \times \vec{v}}{c^2}, \quad (\text{C.5})$$

which interacts with the particles magnetic moment  $\mu_a$ , creating a geometric phase. This is independent of the interaction of a genuine EDM with the  $\vec{E}$  field. A gradient  $\partial B_{0z}/\partial z$ , in the case of cylindrical symmetry, has the associated components in the  $xy$  plane,

$$\vec{B}_{0xy} = \vec{B}_{0r} = - \left( \frac{\partial B_{0z}}{\partial z} \right) \frac{\vec{r}}{2}, \quad (\text{C.6})$$

at all radial positions  $\vec{r}$  relative to the axis of symmetry.

A geometric phase is caused by the combination of  $\vec{B}_v$  and  $\vec{B}_{0xy}$ , thus

$$\vec{B}_{xy} = (\vec{B}_{0xy} + \vec{B}_v). \quad (\text{C.7})$$

These fields are varying with position in the trap. Here it is assumed that inhomogeneities in  $\vec{E}$  are small enough that they only effect  $\vec{B}_v$  to second order, and thus they will not be considered.

The particles are assumed to be moving in conditions where  $mc^2 \gg mv^2 \gg |\mu_a B_0|$ . Thus, no relativity is needed other than Eqn. C.5.

Ramsey considered a neutral particle with spin and magnetic moment precessing with an angular velocity  $\omega_L = \omega_0 = -\gamma B_{0z}$  in a constant magnetic field  $\vec{B}_{0z}$  and the addition of a magnetic field of strength  $B_{xy}$  in the  $xy$  plane rotating in the plane at angular velocity  $\omega_r$ . He found that, the Larmor precession frequency  $\omega_L$  is shifted away from  $\omega_0$ , and to first order, this shift  $\Delta\omega = \omega_L - \omega_0$  is given by

$$\Delta\omega = \frac{\omega_{xy}^2}{2(\omega_0 - \omega_r)}, \quad (\text{C.8})$$

where  $\omega_{xy} = -\gamma B_{xy}$  [154]. Here this is referred to as the Ramsey-Bloch-Siegert (RBS) shift. It is useful to note that the numerator  $\omega_{xy}^2$  is

$$\omega_{xy}^2 = \gamma^2 \vec{B}_{xy}^2 = \gamma^2 (\vec{B}_{0xy}^2 + \vec{B}_v^2 + 2\vec{B}_{0xy} \cdot \vec{B}_v). \quad (\text{C.9})$$

The first term takes into account the influence of  $\vec{B}_{xy}$  on  $\omega_L$  in the absence of an  $\vec{E}$  field. The second term is proportional to  $(\vec{E} \times \vec{v})^2$ , and is involved in the calculation of the second order  $(\vec{E} \times \vec{v})$  shift. The third term is the one that causes the GP shifts linear in  $E$ .

Consider a particle in a cylindrical storage vessel with the shape shown in Fig. C.1. The  $z$  axis points along the cylinder axis of the trap. Circular electrodes in the  $xy$  plane form the roof and floor of the trap, and the walls are fully specular in terms of reflections of particles. It is also assumed that there is no particle-particle collisions.

It can also be assumed that the particle's motion is confined to the  $xy$  plane with velocity  $v_{xy}$ , since any motion in the  $z$  direction does not contribute to the GP's under investigation ( $\vec{E} \times \vec{v} = 0$ ). The  $\vec{B}_0$  field is taken to be nearly uniform with a small gradient  $\partial \vec{B}_{0z}/\partial z$  that is to first order independent of position. As in C.6, also

$$\vec{B}_{0xy} = \vec{B}_{0r} = -\frac{\partial B_{0z}}{\partial z} \frac{\vec{r}}{2} = B_{0r} \frac{\vec{r}}{r}. \quad (\text{C.10})$$

Very close to the wall of the trap,  $\vec{B}_{0r}$  and  $\vec{B}_v$  are nearly parallel and aligned with the radius  $\vec{r}$ . Therefore, a particle moving along the edge of the trap experiences rotating radial magnetic field of amplitudes

$$\text{for } \vec{B}_{0\uparrow} \text{ and } \vec{E}_{\uparrow}, \quad B_{xy+} = B_{0r} - |B_v|, \quad B_{xy-} = B_{0r} + |B_v|, \quad (\text{C.11})$$

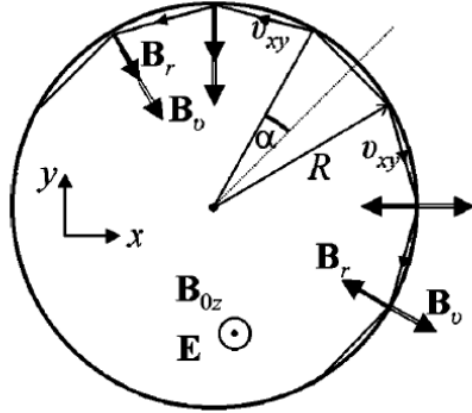


Figure C.1: Effective magnetic field in the rotating coordinate system

and

$$\text{for } \vec{B}_{0\uparrow} \text{ and } \vec{E}_\downarrow, \quad B_{xy+} = B_{0r} + |B_v|, \quad B_{xy-} = B_{0r} - |B_v|, \quad (\text{C.12})$$

where the (+) case is the sense with the particles angular momentum vector parallel to  $\vec{B}_0$  and the (-) case is the opposite sense. This peripheral motion has  $|\omega_r| = v_{xy}/R$ , where  $R$  is the trap radius. As a result,

$$|B_v| = \frac{|v_{xy}| |E|}{c^2}, \quad |\omega_0| = |\gamma B_{0z}|, \quad |\omega_r| = \frac{|v_{xy}|}{R}, \quad (\text{C.13})$$

$$B_{0r} \rightarrow \left\{ B_{0R} = -\frac{\partial B_{0z}}{\partial z} \frac{R}{2} \right\} \text{ as } \alpha \rightarrow 0.$$

These rotating fields induce shifts in the Larmor frequency, which is described by the RBS shift equation. In mechanical equilibrium, any particle is equally likely to move in either direction around the trap. To get the ensemble average shift, the shifts of the two senses of circulation are equally weighted giving

$$\Delta\omega = \frac{(\gamma B_{xy+})^2}{4(\omega_0 - |\omega_r|)} + \frac{(\gamma B_{xy-})^2}{4(\omega_0 + |\omega_r|)}. \quad (\text{C.14})$$

Inserting the expressions for  $B_{xy\pm}$  gives

$$\begin{aligned} \Delta\omega_{\uparrow\uparrow} &= \frac{\gamma^2(B_{0R}^2 + B_v^2)}{4} \left[ \frac{1}{(\omega_0 - |\omega_r|)} + \frac{1}{(\omega_0 + |\omega_r|)} \right] \\ &\quad - \frac{\gamma^2 B_{0R} |B_v|}{2} \left[ \frac{1}{(\omega_0 - |\omega_r|)} - \frac{1}{(\omega_0 + |\omega_r|)} \right], \end{aligned} \quad (\text{C.15})$$

$$\begin{aligned} \Delta\omega_{\uparrow\downarrow} &= \frac{\gamma^2(B_{0R}^2 + B_v^2)}{4} \left[ \frac{1}{(\omega_0 - |\omega_r|)} + \frac{1}{(\omega_0 + |\omega_r|)} \right] \\ &\quad + \frac{\gamma^2 B_{0R} |B_v|}{2} \left[ \frac{1}{(\omega_0 - |\omega_r|)} - \frac{1}{(\omega_0 + |\omega_r|)} \right]. \end{aligned} \quad (\text{C.16})$$

And taking their difference gives

$$\begin{aligned} (\Delta\omega_{\uparrow\uparrow} - \Delta\omega_{\uparrow\downarrow}) &= -\gamma^2 B_{0R}|B_v| \left[ \frac{1}{(\omega_0 - |\omega_r|)} - \frac{1}{(\omega_0 + |\omega_r|)} \right] \\ &= -2\gamma^2 B_{0R}|B_v| \frac{|\omega_r|}{(\omega_0^2 - \omega_r^2)}, \end{aligned} \quad (\text{C.17})$$

The Eqn. C.17 shows that only the cross terms involving  $B_{0R}|B_v|$  contribute to the GP that is linear in  $E$ . The factor  $(\omega_0^2 - \omega_r^2)^{-1}$  has a sharp peak and changes sign at the boundary between the ranges  $|\omega_r| < |\omega_0|$  and  $|\omega_r| > |\omega_0|$ .

Typical nEDM measurements using UCN work in the nearly adiabatic regime where  $|\omega_r| < |\omega_0|$ . In this case, Eqn. C.17 could be written as

$$(\Delta\omega_{\uparrow\uparrow} - \Delta\omega_{\uparrow\downarrow}) = -2\gamma^2 B_{0R}|B_v| \frac{|\omega_r|}{\omega_0^2} \left[ 1 - \frac{\omega_r^2}{\omega_0^2} \right]^{-1}. \quad (\text{C.18})$$

Comparing this with  $(\Delta\omega_{geo\uparrow\uparrow} - \Delta\omega_{geo\uparrow\downarrow})$  from Eqn. C.4, and using the relations in Eqn. C.13 gives

$$d_{af} = -\frac{J\hbar}{2} \left( \frac{\partial B_{0z}/\partial z}{B_{0z}^2} \right) \frac{v_{xy}^2}{c^2} \left[ 1 - \frac{\omega_r^2}{\omega_0^2} \right]^{-1}, \quad (\text{C.19})$$

for particles moving in peripheral orbits.

### C.1.1 T1,T2, GPE redux

An alternative approach to determining the geometric phase effect provides a more general theory, valid for an arbitrary shape of the magnetic field as well as for arbitrary geometry of the confinement cell [155].

The frequency shift induced by a fluctuating transverse field is given by the Lamoreaux-Golub expression [98]:

$$\begin{aligned} \delta\omega &= \frac{1}{2} \int_0^\infty d\tau \cos(\omega_0 t) \langle \omega_x(0)\omega_y(\tau) - \omega_y(0)\omega_x(\tau) \rangle \\ &\quad + \frac{1}{2} \int_0^\infty d\tau \sin(\omega_0 t) \langle \omega_x(0)\omega_x(\tau) - \omega_y(0)\omega_y(\tau) \rangle, \end{aligned} \quad (\text{C.20})$$

where the bracket refers to the ensemble average of the quantity of particles in the trap. We can write the frequency shift in powers of the magnetic and electric field:

$$\delta\omega = \delta\omega_{B^2} + \delta\omega_{E^2} + \delta\omega_{BE}. \quad (\text{C.21})$$

If we flip the direction of the electric field, only the linear term in  $E$

$$\delta\omega_{BE} = \frac{\gamma^2 E}{c^2} \int_0^\infty d\tau \cos(\omega_0 \tau) \langle B_x(0)v_x(\tau) + B_y(0)V_y(\tau) \rangle \quad (\text{C.22})$$

generates a frequency shift (as long as the field amplitude doesn't change). Therefore, it generates a false EDM of the form

$$d_{\text{False}} = \frac{\hbar}{4E} [\delta\omega(E) - \delta\omega(-E)] = \frac{\hbar}{4E} \delta\omega_{BE}(E). \quad (\text{C.23})$$

The frequency shifts  $\delta\omega_{B^2}$ ,  $\delta\omega_{E^2}$ , and  $\delta\omega_{BE}$  involve Fourier transforms (evaluated at the Larmor frequency) of correlation functions involving field and velocity components. In the adiabatic regime these can be expanded in perturbation series using integration by parts

$$\begin{aligned} \int_0^\infty d\tau \cos(\omega_0\tau) \langle B_x(0)v_x(\tau) \rangle &= [\cos(\omega_0\tau) \langle B_x(0)x(\tau) \rangle]_0^\infty \\ &\quad + \omega_0 \int_0^\infty d\tau \sin(\omega_0\tau) \langle B_x(0)x(\tau) \rangle, \end{aligned} \quad (\text{C.24})$$

where the second term vanishes in the nonadiabatic limit ( $\omega_0\tau_c \ll 1$ ). Using this expansion with Eqn.C.22, we arrive at a false EDM:

$$d_{\text{False}} = -\frac{\hbar\gamma^2}{2c^2} \langle xB_x + yB_y \rangle, \quad (\text{C.25})$$

which is valid for arbitrary field inhomogeneities in the nonadiabatic regime.

### C.1.2 Why is it called a geometric phase?

In the nEDM experiment, it is important to understand how UCN move adiabatically through a magnetic field gradient. In the frame of reference of the UCN, the magnetic field is changing with time, which results in a Berry phase shift as the particle moves through a closed curve. Since the UCN is moving slowly with respect to the change in magnetic field, its spin will follow the field adiabatically. The change in field strength with time is then reflected in the geometry of the container that the UCN are moving in, and therefore, the phase accrued is geometric in origin.

#### Adiabatic Approximation

Consider a Hamiltonian that depends on some set of parameters. If these parameters change “slowly” with time, then the energy eigenvalues will also change as the parameters themselves change. Here slowly means that the parameters change on a time scale  $T$  that is much greater than  $\frac{2\pi\hbar}{E_{ab}}$  for some difference  $E_{ab}$  in energy eigenstates.

Starting from the eigenvalue equation for Hamiltonian

$$H(t)|n; t\rangle = E_n(t)|n; t\rangle, \quad (\text{C.26})$$

the Schrödinger equation can be written as

$$i\hbar \frac{d}{dt} |\alpha; t\rangle = H(t)|\alpha; t\rangle. \quad (\text{C.27})$$

Here  $|\alpha; \rangle$  could be written in terms of Hamiltonian eigenkets

$$|\alpha; t\rangle = \sum_n c_n(t) e^{i\theta_n(t)} |n; t\rangle, \quad (\text{C.28})$$

where

$$\theta_n(t) \equiv -\frac{1}{\hbar} \int_0^t E_n(t') dt'. \quad (\text{C.29})$$

Substituting Eqn. C.28 into Eqn. C.27 gives

$$\sum_n e^{i\theta_n(t)} \left[ \dot{c}_n(t)|n; t\rangle + c_n(t) \frac{\partial}{\partial t} |n; t\rangle \right] = 0. \quad (\text{C.30})$$

Multiplying the above equation with  $\langle m; t|$  and using orthonormality of Hamiltonian eigenstates at equal times gives

$$\dot{c}_m(t) = - \sum_n c_n(t) e^{i[\theta_n(t) - \theta_m(t)]} \langle m; t| \left[ \frac{\partial}{\partial t} |n; t\rangle \right]. \quad (\text{C.31})$$

The next step is to calculate  $\langle m; t| \left[ \frac{\partial}{\partial t} |n; t\rangle \right]$  in terms of the Hamiltonian and its eigenvalues. Taking the time derivative of Eqn. C.26, and then multiplying it on the left by  $\langle m; t|$  gives

$$\langle m; t| \dot{H}|n; t\rangle = [E_n(t) - E_m(t)] \langle m; t| \left[ \frac{\partial}{\partial t} |n; t\rangle \right]. \quad (\text{C.32})$$

Therefore, Eqn. C.31 becomes

$$\dot{c}_m(t) = -c_m(t) \langle m; t| \left[ \frac{\partial}{\partial t} |n; t\rangle \right] - \sum_{n \neq m} c_n(t) e^{i(\theta_n - \theta_m)} \frac{\langle m; t| \dot{H}|n; t\rangle}{E_n - E_m}. \quad (\text{C.33})$$

This is the solution to the general time-dependent problem. It means, as time goes on, states with  $n \neq m$  will mix with  $|m; t\rangle$  because of the time dependence of the Hamiltonian. In the adiabatic limit, the second term could be neglected which means,

$$\frac{\langle m; t| \dot{H}|n; t\rangle}{E_{nm}} \equiv \frac{1}{\tau} \ll \langle m; t| \left[ \frac{\partial}{\partial t} |m; t\rangle \right] \sim \frac{E_m}{\hbar}. \quad (\text{C.34})$$

In other words, the Hamiltonian changes with time much slower than the inverse natural frequency of the state-phase factor. Hence,

$$c_n(t) = e^{i\gamma_n(t)} c_n(0), \quad (\text{C.35})$$

where,

$$\gamma_n(t) \equiv i \int_0^t \langle n; t'| \left[ \frac{\partial}{\partial t'} |n; t'\rangle \right] dt', \quad (\text{C.36})$$

is a real quantity. This is called the geometric phase, and it is the result of the adiabatic approximation. So, Eqn. C.28 could be written as

$$|\alpha^{(n)}; t\rangle = e^{i\gamma_n(t)} e^{i\theta_n(t)} |n; t\rangle. \quad (\text{C.37})$$

### Berry's Phase

The accumulated phase for systems that travel in a closed loop is generally called Berry's phase, although Berry himself refers to it as a "geometric phase".

Assume that the time dependence of the Hamiltonian is represented by a parameter  $\vec{R}(t)$ . For example, it can be a magnetic field for a spin- $\frac{1}{2}$  system. Therefore,  $E_n(t) = E_n(\vec{R}(t))$  and  $|n; t\rangle = |n(\vec{R}(t))\rangle$ , and also

$$\langle n; t| \left[ \frac{\partial}{\partial t} |n; t\rangle \right] = \langle n; t| \left[ \vec{\nabla}_{\vec{R}} |n; t\rangle \right] \cdot \frac{d\vec{R}}{dt}. \quad (\text{C.38})$$

Combining equation C.36 and C.38 gives

$$\begin{aligned}\gamma_n(T) &= i \int_0^T \langle n; t | [\vec{\nabla}_R |n; t\rangle] \cdot \frac{d\vec{R}}{dt} dt \\ &= i \int_{\vec{R}(0)}^{\vec{R}(t)} \langle n; t | [\vec{\nabla}_R |n; t\rangle] \cdot d\vec{R}.\end{aligned}\quad (\text{C.39})$$

If  $T$  is the period for one full cycle, then  $\vec{R}(0) = \vec{R}(t)$  and therefore, the geometric phase for a closed loop could be calculated in which the vector  $\vec{R}$  traces a curve  $C$

$$\gamma_n(C) = i \oint \langle n; t | [\vec{\nabla}_R |n; t\rangle] \cdot d\vec{R}. \quad (\text{C.40})$$

Defining

$$\vec{A}_n(\vec{R}) \equiv i \langle n; t | [\vec{\nabla}_R |n; t\rangle], \quad (\text{C.41})$$

and so, the geometric phase will take the form

$$\gamma_n(C) = \oint_c \vec{A}_n(\vec{R}) \cdot d\vec{R}. \quad (\text{C.42})$$

Using Stokes' theorem gives

$$\gamma_n(C) = \int [\vec{\nabla}_R \times \vec{A}_n(\vec{R})] \cdot d\vec{a}. \quad (\text{C.43})$$

Thus, Berry's Phase is determined by the “flux” of a generalized field

$$\vec{B}_n(\vec{R}) \equiv \vec{\nabla}_R \times \vec{A}_n(\vec{R}). \quad (\text{C.44})$$

Eqn. C.42 has an interesting property. If the energy eigenkets are multiplied by an arbitrary phase, the value of  $\gamma_n(c)$  will not be affected, because the curl of a gradient is zero. This means, the geometric phase does not depend on the phase behaviour along the path and it only depends on the geometry of the path traced out by  $\vec{R}(t)$ , which is why it is called a “geometric phase”.

By doing a little math Berry's phase could be written as

$$\vec{B}_n(\vec{R}) = i \sum_{n \neq m} \frac{\langle n; t | \vec{\nabla}_R H | m; t \rangle \times \langle m; t | \vec{\nabla}_R H | n; t \rangle}{(E_m - E_n)^2}. \quad (\text{C.45})$$

### Example: Berry's Phase for Spin-1/2

The geometric phase for a spin- $\frac{1}{2}$  particle manipulated slowly through a time-varying magnetic field could be easily calculated. As before, the Hamiltonian could be written as

$$H = -\frac{2\mu}{\hbar} \vec{S} \cdot \vec{R}(t) = -\gamma \vec{S} \cdot \vec{R}(t). \quad (\text{C.46})$$

Here  $R(t)$  represents the magnetic field to avoid confusion with Berry's phase  $\vec{B}_n(\vec{R})$ . Consider  $|\pm; t\rangle$  to be the eigenstates of  $S_z$ . Writing

$$\vec{S} = \frac{1}{2}(S_+ + S_-)\hat{x} + \frac{1}{2i}(S_+ - S_-)\hat{y} + S_z\hat{z}, \quad (\text{C.47})$$

then

$$\langle \pm; t | \vec{S} | \mp; t \rangle = \frac{\hbar}{2} (\hat{x} \mp i\hat{y}). \quad (\text{C.48})$$

Combining these results finally gives

$$\gamma_{\pm}(C) = \mp \frac{1}{2} \int \frac{\hat{\vec{R}} \cdot d\vec{a}}{R^2} = \mp \frac{1}{2} \Omega, \quad (\text{C.49})$$

where  $\Omega$  is the “solid angle” subtended by the path through which the parameter vector  $\vec{R}(t)$  travels, relative to an origin  $\vec{R} = 0$  that is the source point for the field  $\vec{B}$ . This implies that the specifics of the path do not matter, so long as the solid angle subtended by the path is the same. This is also independent of the magnetic moment  $\mu$ .

# Appendix D

## Vertical Source Gas Flow Diagram

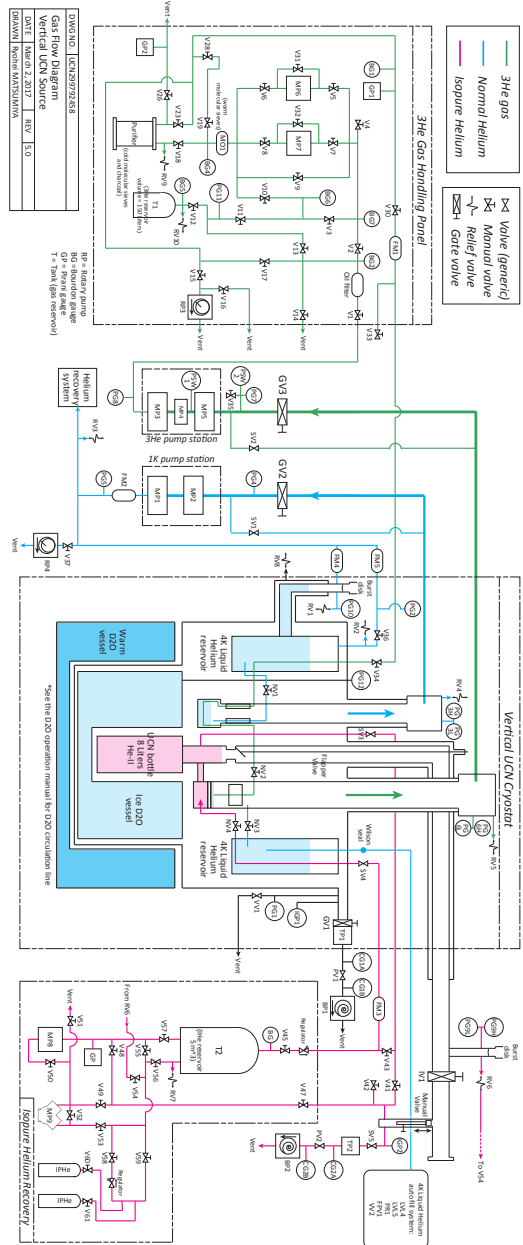


Figure D.1: Gas flow diagram for the vertical UCN source



## Appendix E

# Heat Conductivity in Superfluid Helium [156]

There are several sources of heat input on the UCN cryostat such as the cooling process or the target irradiation. The heat load on the UCN cryostat creates a temperature gradient along the heat exchanger to the superfluid helium bottle (see Fig. D.1. The temperature gradient in the superfluid helium is described by its heat conductivity. Lower heat conductivities give rise to larger temperature gradients.

The temperature dependence of the heat conductivity in the superfluid helium is describe by theoretical models from the lambda point at 2.17 K down to around 1.4 K which is above the temperatures for the UCN production (< 1 K). Since it is difficult to reach such low temperatures, the mechanism of heat transfer in temperatures below 1.4 K is not fully understood. To check the validity of the theoretical models, here the extrapolation to lower temperatures is compared to the acquired data with the vertical UCN source.

In order to create a temperature gradient along the channel from heat exchanger to the superfluid helium bottle, the heater tapes that are wrapped around the superfluid helium bottle are used. This temperature gradient can be measured using the temperature sensors shown in Fig. 5.8.

The heater test procedure is the following; The heater tape around the superfluid helium bottle is turned on when the temperature of the superfluid helium is stable. Here this temperature is referred to as the *base* temperature. The applied heat load could easily be calculated since the applied current and voltage are known. After the heater is turned on, the temperature of the superfluid helium starts to increase. This causes an increase in the flow rate in the  $^3\text{He}$  pot. After some time, the temperature of the superfluid helium starts to settle and reach a new equilibrium. This temperature is referred to as the *saturation* temperature. At this point, the heater could be turned off which causes the superfluid temperature and the flow rate of the  $^3\text{He}$  to get back to the initial conditions.

In 2017, two sets of heater tests were performed on the vertical UCN source: The April heat test and the November heat test. In April, the base temperature of the superfluid helium was slightly higher than in November. In addition, there was no proton beam during the April cooling of the cryostat and it was purely a cryostat cooling test. Table. E.1 shows the heat load and the temperatures of the superfluid helium for those tests.

Heater Power (mW)	$T_{\text{base,TS10}}$ (K)	$T_{\text{sat.,TS10}}$ (K)	$T_{\text{base,TS11}}$ (K)	$T_{\text{sat.,TS11}}$ (K)	$T_{\text{base,TS12}}$ (K)	$T_{\text{sat.,TS12}}$ (K)	$T_{\text{base,TS14}}$ (K)	$T_{\text{sat.,TS14}}$ (K)	$T_{\text{base,TS16}}$ (K)	$T_{\text{sat.,TS16}}$ (K)
<b>April Heat Test</b>										
2.5	0.717	0.718	0.93	0.931	0.926	0.9271	0.93	0.931	1.012	1.013
12.5	0.717	0.7185	0.93	0.9315	0.924	0.929	0.93	0.9315	1.011	1.015
25	0.719	0.723	0.928	0.931	0.919	0.929	0.928	0.931	1.008	1.015
75	0.7195	0.7255	0.9285	0.937	0.922	0.952	0.928	0.937	1.01	1.03
250	0.7175	0.7375	0.93	0.9475	0.93	1	0.93	0.947	1.01	1.065
<b>November Heat Test</b>										
25	0.724	0.73	0.892	0.9	0.84	0.86	0.92	0.923	0.96	0.97
50	0.741	0.75	0.895	0.91	0.84	0.9	0.92	0.93	0.96	0.99
75	0.73	0.74	0.9	0.91	0.85	0.92	0.92	0.93	0.96	1
100	0.73	0.769	0.9	0.936	0.85	0.96	0.92	0.952	0.96	1.04
150	0.73	0.755	0.9	0.93	0.84	0.99	0.92	0.945	0.96	1.06
200	0.73	0.9	0.9	1.26	0.84	1.23	0.92	1.25	0.96	1.26
250	0.73	0.94	0.895	1.385	0.84	1.345	0.92	1.363	0.97	1.375

Table E.1: The heater power, and the base and saturation temperatures from the temperature sensors in the superfluid helium, and in the  $^3\text{He}$  pot, for the April and November heat tests [156]

### E.0.1 Theoretical Models

The relationship between the heat flux and the temperature gradient in a one dimensional channel is written as

$$q^m = f^{-1}(T, p) \frac{dT}{dx} \quad (\text{E.1})$$

where  $q$  is the input heat flux,  $T$  is the temperature,  $p$  is the pressure,  $\frac{dT}{dx}$  is the temperature gradient along the channel and  $f(T, p)$  is the heat conductivity function which controls the temperature gradient of the heat flux which could be written as

$$f(T, p) = \frac{A_{\text{GM}} \rho_n}{\rho_s^3 s^4 T^3}. \quad (\text{E.2})$$

Here  $\rho_n$  is the density of the normal fluid component,  $\rho_s$  is the density of the superfluid component,  $s$  is the specific entropy,  $T$  is the temperature and  $A_{\text{GM}}$  is the Gorter-Mellink parameter which describes the friction between the normal fluid component and the superfluid component.

Since the Gorter-Mellink parameter is unknown, it is difficult to calculate  $f(T, p)$  in the form of Eqn. E.2. However, there are other models to describe the behaviour of the heat conductivity functions. There are two models that are considered here at the saturated vapour pressure. This means, the pressure dependence could be neglected. The models are the theory model from Van Sciver [157] and the HEPAK model [158].

The heat conductivity function for the Van Sciver and the HEPAK theoretical models are shown in Fig. E.1. As the graph shows, both models tend to agree at higher heat inputs. However, at lower heat inputs, the heat conductivity function values for the Van Sciver model lie below the values for the HEPAK model. In addition, as the temperature of the superfluid helium increases, the heat conductivity function tends to look more linear. Since the Van Sciver model is more well known, it is used for comparison with experimental data.

## E.1 Measurement Result

The data shown in Table. E.1 is from all the heater tests in 2017. If the heat load on the cryostat is higher than its cooling power, the temperature of the superfluid helium would increase linearly without reaching an equilibrium. This phenomena has been observed for higher heater powers *e.g.* 1 W. As a result, that data is discarded.

Fig. E.2 shows the result of the April heat test. For a given heat input to the superfluid helium, the temperature difference between the base and the saturation temperatures for each temperature sensor is calculated (see table E.1). The average of all of those temperature differences give the overall  $\Delta T$  across the channel (see Ref. [156] for more information on this). Those are shown with black dots in Fig. E.2 as the raw data. However, the heat input for each data point should be corrected since the total heat input is a combination of the added heat from the heater tapes and the background heat load on the cryostat which has not been taken into account.

The two other sources of heat input to be considered are the *Joule-Thomson* expansion, and the the background heat load on the  ${}^3\text{He}$  pot, due to the thermal radiation, and to the superfluid helium bottle. The Joule-Thomson expansion happens when a gas or liquid passes through a valve which has different temperatures and pressures on both

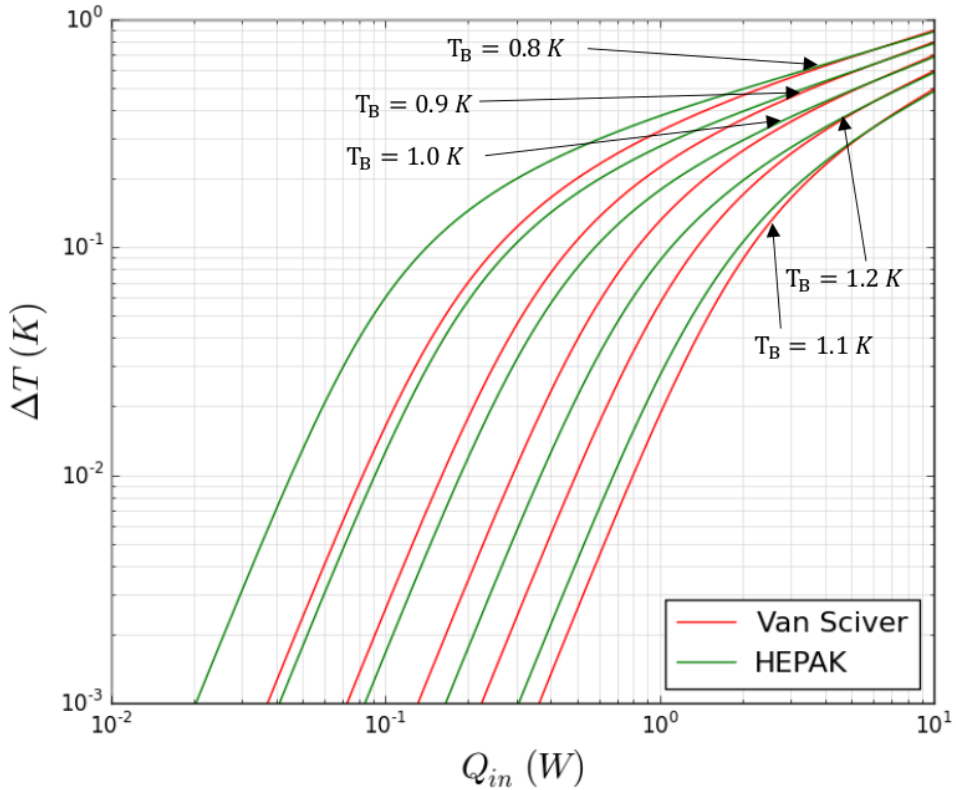


Figure E.1: The heat conductivity function of the Van Sciver and HEPAK models. The vertical axis shows the temperature gradient along the channel and the horizontal axis shows the input heat flux [156]. The arrows on the graph indicate the temperature of the superfluid helium

sides while there is no heat exchange to the environment. Here, in the vertical UCN source, the  ${}^3\text{He}$  flows into the heat exchanger and passes through a valve with different pressures and temperatures on two sides. Because of the Joule-Thomson expansion, some liquid changes into vapor, which is then directly pumped out of the system, and does not contribute to the cooling process. For the background heat load, based on the estimations of the heat sources to the bottle alone, combined with the measurements of the mass flow of  ${}^4\text{He}$  from the top of the bottle when the  ${}^3\text{He}$  system is switched off, a heat load of  $\simeq 50 \text{ mW}$  is a reasonable estimation. In Fig. E.2, the assumed values are the sum of the 50 mW background heat and the heat input from the heaters, and the Joule-Thomson values are the sum of the heat input from the heaters plus the calculated 232 mW background heat from the Joule-Thomson effect [156].

Fig. E.3 shows the measured data in November 2017 with the heaters as well as the theoretical model of Van Sciver for the heat conductivity. Each color represents a temperature range. The markers are the measured data points.

At all the temperature ranges, the acquired data shows a lower heat load compared to the theoretical model. At the range of 1.2-1.3 K, the data point with the smaller  $\Delta T$  is acquired at a higher He-II base temperature, whereas the data point with higher  $\Delta T$  is acquired at the standard He-II base temperature. However, the large error bars indicate that these values could be anywhere in between. For a complete discussion on how the error bars are calculated see Ref. [156]. The data points which are closer to the theoretical models are acquired at lower base temperature for the superfluid helium.

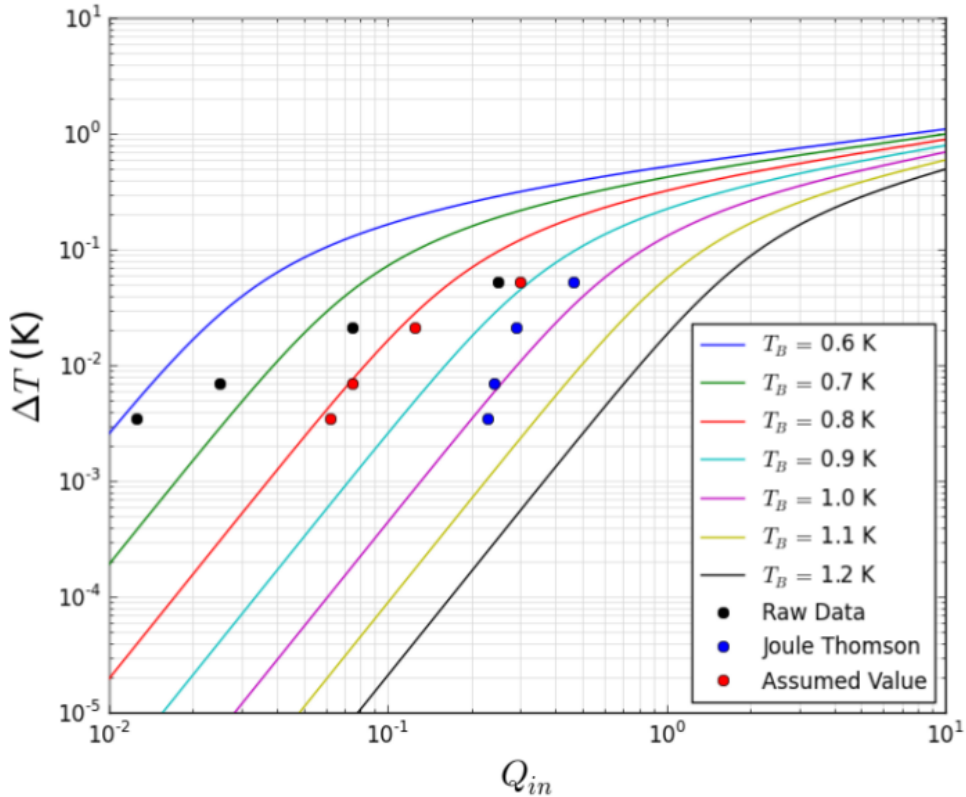


Figure E.2: The comparison between the April heater test data and the Van Sciver theoretical model of heat conductivity. The lines show the Van Sciver model's heat conductivity function at different superfluid helium bath temperatures. The black data points show the measured raw data of the heater tests. The blue points are the the values where the Joule-Thomson effect is considered and its heat input is added to the raw data plus the calculated background heat. The red points show the raw data with the assumed 50 mW background heat input.

Since the measured data show bigger temperature differences compared to the theoretical model of Van Sciver, it suggests that the theory is assuming higher heat conductivity. Looking back at Fig. E.1, it shows that using the HEPAK model might solve this problem since the HEPAK model shows lower heat conductivity.

One reason for the disagreement between the measurements and the theory could be the fact that these theoretical models are only measured down to 1.4 K and they are extrapolated to lower temperatures. Another reason could lie in the geometry difference. The theoretical models are valid for a one-dimensional channel while there is a 90° bend in the vertical UCN source setup which can cause a higher temperature differnece across the channel [156]. One other reason might be the uncertainty in the measured temperature due to the calibration of the temperature sesnors. There might be other unknown sources of systematic error affecting the measurements.

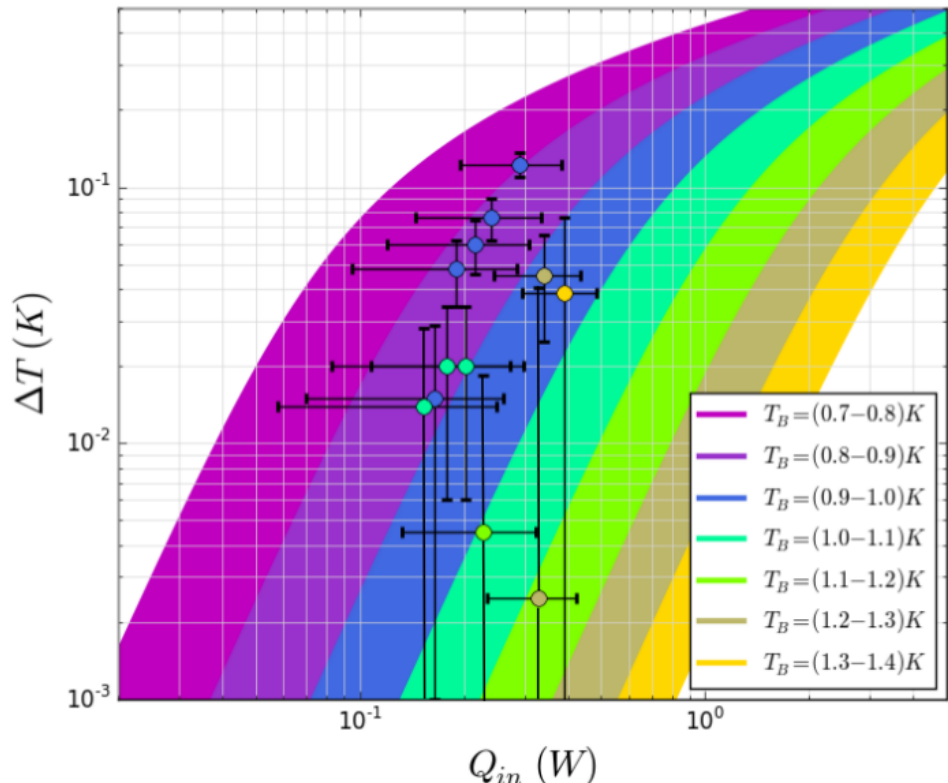


Figure E.3: Theoretical model of Van Sciver for the superfluid helium heat conductivity at different temperature ranges and the November heater test data. The vertical axis shows the temperature difference between the base and the saturation temperature for temperature sensors. The horizontal axis shows the heat input from the heaters plus the background heat.

# References

- [1] M. Pospelov and A. Ritz, Annals of physics **318**, 119 (2005).
- [2] T. D. Lee and C.-N. Yang, Physical Review **105**, 1671 (1957).
- [3] C. S. Wu, E. Ambler, R. W. Hayward, D. D. Hoppes, and R. P. Hudson, Phys. Rev. **105**, 1413 (1957).
- [4] R. L. Garwin, L. M. Lederman, and M. Weinrich, Phys. Rev. **105**, 1415 (1957).
- [5] J. I. Friedman and V. Telegdi, Physical Review **106**, 1290 (1957).
- [6] L. Landau, Nuclear Physics **3**, 127 (1957).
- [7] J. D. Jackson, S. B. Treiman, and H. W. Wyld, Phys. Rev. **106**, 517 (1957).
- [8] J. Smith, E. Purcell, and N. Ramsey, Physical Review **108**, 120 (1957).
- [9] J. Pendlebury, S. Afach, N. Ayres, C. Baker, G. Ban, G. Bison, K. Bodek, M. Burghoff, P. Geltenbort, K. Green, *et al.*, Physical Review D **92**, 092003 (2015).
- [10] J. M. Cline, (2006), arXiv:hep-ph/0609145 [hep-ph].
- [11] A. Sakharov, Pisma Zh.Eksp.Teor.Fiz. **5**, 32 (1967).
- [12] E. W. Kolb and M. S. Turner, Front. Phys., Vol. 69, **1** (1990).
- [13] A. G. Cohen, D. Kaplan, and A. Nelson, Annual Review of Nuclear and Particle Science **43**, 27 (1993).
- [14] C. Baker, D. Doyle, P. Geltenbort, K. Green, M. Van der Grinten, P. Harris, P. Iaydjiev, S. Ivanov, D. May, J. Pendlebury, *et al.*, Physical Review Letters **97**, 131801 (2006).
- [15] A. Serebrov, P. Geltenbort, I. Shoka, G. Shmelev, A. Kharitonov, A. Vassiliev, I. Krasnoshekova, M. Lasakov, E. Siber, A. Fomin, *et al.*, Nuclear Instruments and Methods in Physics Research Section A: Accelerators, Spectrometers, Detectors and Associated Equipment **611**, 263 (2009).
- [16] S. Lamoreaux and R. Golub, Journal of Physics G: Nuclear and Particle Physics **36**, 104002 (2009).
- [17] I. Altarev, G. Ban, G. Bison, K. Bodek, M. Burghoff, Z. Chowdhuri, M. Daum, C. Düsing, M. Fertl, P. Fierlinger, *et al.*, Nuclear Physics A **844**, 47c (2010).

- [18] J. Pendlebury, S. Afach, N. Ayres, C. Baker, G. Ban, G. Bison, K. Bodek, M. Burghoff, P. Geltenbort, K. Green, *et al.*, Physical Review D **92**, 092003 (2015).
- [19] S. Paul, Nuclear Instruments and Methods in Physics Research Section A: Accelerators, Spectrometers, Detectors and Associated Equipment **611**, 157 (2009).
- [20] F. E. Wietfeldt and G. L. Greene, Reviews of Modern Physics **83**, 1173 (2011).
- [21] S. Arzumanov, L. Bondarenko, S. Chernyavsky, W. Drexel, A. Fomin, P. Geltenbort, V. Morozov, Y. Panin, J. Pendlebury, and K. Schreckenbach, Physics Letters B **483**, 15 (2000).
- [22] A. Serebrov, V. Varlamov, A. Kharitonov, A. Fomin, Y. Pokotilovski, P. Geltenbort, J. Butterworth, I. Krasnoschekova, M. Lasakov, R. Tal'daev, *et al.*, Physics Letters B **605**, 72 (2005).
- [23] P. R. Huffman, C. Brome, J. Butterworth, K. Coakley, M. S. Dewey, S. Dzhosyuk, R. Golub, G. Greene, K. Habicht, S. K. Lamoreaux, *et al.*, Nature **403**, 62 (2000).
- [24] M. P. Mendenhall, R. W. Pattie, Y. Bagdasarova, D. B. Berguno, L. J. Broussard, R. Carr, S. Currie, X. Ding, B. W. Filippone, A. García, P. Geltenbort, K. P. Hickerson, J. Hoagland, A. T. Holley, R. Hong, T. M. Ito, A. Knecht, C.-Y. Liu, J. L. Liu, M. Makela, R. R. Mammei, J. W. Martin, D. Melconian, S. D. Moore, C. L. Morris, A. Pérez Galván, R. Picker, M. L. Pitt, B. Plaster, J. C. Ramsey, R. Rios, A. Saunders, S. J. Seestrom, E. I. Sharapov, W. E. Sondheim, E. Tatar, R. B. Vogelaar, B. VornDick, C. Wrede, A. R. Young, and B. A. Zeck (UCNA Collaboration), Phys. Rev. C **87**, 032501 (2013).
- [25] L. Broussard and U. Collaboration, AIP Conference Proceedings **1560**, 149 (2013), <https://aip.scitation.org/doi/pdf/10.1063/1.4826741>.
- [26] .
- [27] O. Zimmer, Physics Letters B **685**, 38 (2010).
- [28] S. Baessler, V. Nesvizhevsky, K. Protasov, and A. Y. Voronin, Physical Review D **75**, 075006 (2007).
- [29] A. P. Serebrov, O. Zimmer, P. Geltenbort, A. K. Fomin, S. Ivanov, E. Kolomensky, I. Krasnoschekova, M. Lasakov, V. M. Lobashev, A. Pirozhkov, *et al.*, JETP letters **91**, 6 (2010).
- [30] S. Afach, G. Ban, G. Bison, K. Bodek, M. Burghoff, M. Daum, M. Fertl, B. Franke, Z. Grujić, V. Helaine, *et al.*, Physics Letters B **745**, 58 (2015).
- [31] I. Altarev, Phys. Rev. Lett. **103**, 081602 (2009).
- [32] V. V. Nesvizhevsky, H. Börner, A. Gagarski, A. Petoukhov, G. Petrov, H. Abele, S. Baeßler, G. Divkovic, F. Rueß, T. Stöferle, *et al.*, Physical Review D **67**, 102002 (2003).
- [33] M. Tanabashi, K. Hagiwara, K. Hikasa, K. Nakamura, and Y. Sumino *et al.*, .

- [34] A. Steyerl, H. Nagel, F.-X. Schreiber, K.-A. Steinhauser, R. Gähler, W. Gläser, P. Ageron, J. Astruc, W. Drexel, G. Gervais, *et al.*, Physics Letters A **116**, 347 (1986).
- [35] A. Steyerl, Nuclear Instruments and Methods **125**, 461 (1975).
- [36] R. Golub, D. Richardson, and S. Lamoureaux, *Ultra-cold neutrons, Adam Hilger, Bristol, Philadelphia, New York*, Tech. Rep. (ISBN 0-7503-0115-5, 1991).
- [37] A. R. Young (JGU Mainz, Germany, 2016).
- [38] R. Golub, J.M. Pendlebury, Physics Letters A **53**, 133 (1975).
- [39] R. Golub and J. Pendlebury, Physics Letters A **62**, 337 (1977).
- [40] C. R. Brome, J. Butterworth, S. Dzhosyuk, C. Mattoni, D. McKinsey, J. Doyle, P. Huffman, M. Dewey, F. Wietfeldt, R. Golub, *et al.*, Physical review C **63**, 055502 (2001).
- [41] E. Korobkina, R. Golub, B. Wehring, and A. Young, Physics Letters A **301**, 462 (2002).
- [42] P. Schmidt-Wellenburg, K. Andersen, and O. Zimmer, Nuclear Instruments and Methods in Physics Research Section A: Accelerators, Spectrometers, Detectors and Associated Equipment **611**, 259 (2009), particle Physics with Slow Neutrons.
- [43] K. Kirch, B. Lauss, P. Schmidt-Wellenburg, and G. Zsigmond, Nuclear Physics News **20**, 17 (2010), <https://doi.org/10.1080/10619121003626724>.
- [44] G. L. Squires, *Introduction to the Theory of Thermal Neutron Scattering*, 3rd ed. (Cambridge University Press, 2012).
- [45] M. Gibbs, W. Stirling, K. Andersen, and H. Schober, Journal of low temperature physics **120**, 55 (2000).
- [46] M. Gibbs, K. Andersen, W. Stirling, and H. Schober, Journal of Physics: Condensed Matter **11**, 603 (1999).
- [47] K. H. Andersen, W. G. Stirling, R. Scherm, A. Stunault, B. Fak, H. Godfrin, and A. J. Dianoux, Journal of Physics: Condensed Matter **6**, 821 (1994).
- [48] W. Schott, J.M. Pendlebury, I. Altarev, S. Gröger, E. Gutzmiedl, F.J. Hartmann, S. Paul, G. Petzoldt, P. Schmidt-Wellenburg, and U. Trinks, Eur. Phys. J. A **16**, 599 (2003).
- [49] B. Fåk and K. Andersen, Physics Letters A **160**, 468 (1991).
- [50] K. K. H. Leung, S. Ivanov, F. M. Piegza, M. Simson, and O. Zimmer, Phys. Rev. C **93**, 025501 (2016).
- [51] F. Atchison, K. Bodek, B. van den Brandt, T. Brys, M. Daum, P. Fierlinger, P. Geltenbort, M. Giersch, P. Hautle, M. Hino, R. Henneck, M. Kasprzak, K. Kirch, J. Kohlbrecher, J. Konter, G. Kühne, M. Kuźniak, K. Mishima, A. Pichlmaier, and J. Zmeskal, *Journal of research of the National Institute of Standards and Technology*, **110** (2005).

- [52] A. Frei, E. Gutsmiedl, C. Morkel, A. R. Müller, S. Paul, S. Rols, H. Schober, and T. Unruh, EPL (Europhysics Letters) **92**, 62001 (2010).
- [53] A. Frei, E. Gutsmiedl, C. Morkel, A. R. Müller, S. Paul, M. Urban, H. Schober, S. Rols, T. Unruh, and M. Hölzel, Phys. Rev. B **80**, 064301 (2009).
- [54] T. V. F., *Slow Neutrons*, 3rd ed. (Israel Program for Scientific Translations, 1965).
- [55] F. Atchison, B. Blau, K. Bodek, B. van den Brandt, T. Bryś, M. Daum, P. Fierlinger, A. Frei, P. Geltenbort, P. Hautle, R. Henneck, S. Heule, A. Holley, M. Kasprzak, K. Kirch, A. Knecht, J. A. Konter, M. Kuźniak, C.-Y. Liu, C. L. Morris, A. Pichlmaier, C. Plonka, Y. Pokotilovski, A. Saunders, Y. Shin, D. Tortorella, M. Wohlmuther, A. R. Young, J. Zejma, and G. Zsigmond, Phys. Rev. Lett. **99**, 262502 (2007).
- [56] Z.-C. Yu, S. S. Malik, and R. Golub, Zeitschrift für Physik B Condensed Matter **62**, 137 (1986).
- [57] C.-Y. Liu, A. R. Young, and S. K. Lamoreaux, Phys. Rev. B **62**, R3581 (2000).
- [58] C. L. Morris, J. M. Anaya, T. J. Bowles, B. W. Filippone, P. Geltenbort, R. E. Hill, M. Hino, S. Hoedl, G. E. Hogan, T. M. Ito, T. Kawai, K. Kirch, S. K. Lamoreaux, C.-Y. Liu, M. Makela, L. J. Marek, J. W. Martin, R. N. Mortensen, A. Pichlmaier, A. Saunders, S. J. Seestrom, D. Smith, W. Teasdale, B. Tipton, M. Utsuro, A. R. Young, and J. Yuan, Phys. Rev. Lett. **89**, 272501 (2002).
- [59] R. Golub and K. Böning, Zeitschrift für Physik B Condensed Matter **51**, 95 (1983).
- [60] Salvat, D. J., Gutsmiedl, E., Liu, C.-Y., Geltenbort, P., Orecchini, A., Paul, S., and Schober, H., EPL **103**, 12001 (2013).
- [61] F. Atchison, B. Blau, K. Bodek, B. van den Brandt, T. Bryś, M. Daum, P. Fierlinger, A. Frei, P. Geltenbort, P. Hautle, R. Henneck, S. Heule, A. Holley, M. Kasprzak, K. Kirch, A. Knecht, J. Konter, M. Kuźniak, C.-Y. Liu, C. Morris, A. Pichlmaier, C. Plonka, Y. Pokotilovski, A. Saunders, Y. Shin, D. Tortorella, M. Wohlmuther, A. Young, J. Zejma, and G. Zsigmond, Nuclear Instruments and Methods in Physics Research Section A: Accelerators, Spectrometers, Detectors and Associated Equipment **611**, 252 (2009), particle Physics with Slow Neutrons.
- [62] E. Alsolami, *An examination of keystroke dynamics for continuous user authentication*, Ph.D. thesis, Queensland University of Technology (2012).
- [63] A. Serebrov (Neutron Electric Dipole Moment Workshop, Ascona, Switzerland, 2014).
- [64] F. M. Piegsa, M. Fertl, S. N. Ivanov, M. Kreuz, K. K. H. Leung, P. Schmidt-Wellenburg, T. Soldner, and O. Zimmer, Phys. Rev. C **90**, 015501 (2014).
- [65] O. Zimmer and R. Golub, Phys. Rev. C **92**, 015501 (2015).
- [66] T. Ito (Neutron Electric Dipole Moment Workshop, Ascona, Switzerland, 2014).
- [67] D. Ries (Neutron Electric Dipole Moment Workshop, Ascona, Switzerland, 2014).

- [68] J. Karch, Y. Sobolev, M. Beck, K. Eberhardt, G. Hampel, W. Heil, R. Kieser, T. Reich, N. Trautmann, and M. Ziegner, *The European Physical Journal A* **50**, 78 (2014).
- [69] A. Kolarkar, AIP Conference Proceedings **1200**, 861 (2010), <https://aip.scitation.org/doi/pdf/10.1063/1.3327748>.
- [70] S. Imajo *et al.*, PTEP **2016**, 013C02 (2016), arXiv:1507.07223 [physics.ins-det].
- [71] R. Picker (Neutron Electric Dipole Moment Workshop, Ascona, Switzerland, 2014).
- [72] A. P. Serebrov, E. Kolomenskiy, A. Pirozhkov, I. Krasnoschekova, A. Vassiljev, A. Polushkin, M. Lasakov, A. K. Fomin, I. Shoka, V. Solovey, *et al.*, *JETP letters* **99**, 4 (2014).
- [73] A. Serebrov, S. Boldarev, A. Erykalov, V. Ezhov, V. Fedorov, A. Fomin, V. Ilatovskiy, K. Keshyshev, K. Konoplev, A. Krivshitch, *et al.*, *Physics Procedia* **17**, 251 (2011).
- [74] K. Kirch, in *AIP Conference Proceedings*, Vol. 1560 (AIP, 2013) pp. 90–94.
- [75] C. Baker, G. Ban, K. Bodek, M. Burghoff, Z. Chowdhuri, M. Daum, M. Fertl, B. Franke, P. Geltenbort, K. Green, *et al.*, *Physics Procedia* **17**, 159 (2011).
- [76] I. Altarev, D. Beck, S. Chesnevskaya, T. Chupp, W. Feldmeier, P. Fierlinger, A. Frei, E. Gutzmiedl, F. Kuchler, P. Link, *et al.*, *Nuovo Cimento-C* **35**, 122 (2012).
- [77] R. Golub and S. K. Lamoreaux, *Physics Reports* **237**, 1 (1994).
- [78] T. M. Ito, nEdm Collaboration, *et al.*, in *Journal of Physics: Conference Series*, Vol. 69 (IOP Publishing, 2007) p. 012037.
- [79] R. Picker, in *Proceedings of the 14th International Conference on Meson-Nucleon Physics and the Structure of the Nucleon (MENU2016)* (2017) p. 010005.
- [80] N. F. Ramsey, *Phys. Rev.* **78**, 695 (1950).
- [81] P. Schmidt-Wellenburg, *Proceedings, 11th Latin American Symposium on Nuclear Physics and Applications: Medellin, Colombia*, AIP Conf. Proc. **1753**, 060002 (2016), arXiv:1602.01997 [nucl-ex].
- [82] J. M. Pendlebury, W. Heil, Y. Sobolev, P. G. Harris, J. D. Richardson, R. J. Baskin, D. D. Doyle, P. Geltenbort, K. Green, M. G. D. van der Grinten, P. S. Iaydjiev, S. N. Ivanov, D. J. R. May, and K. F. Smith, *Phys. Rev. A* **70**, 032102 (2004).
- [83] B. Jamieson, L. A. Rebenitsch, S. Hansen-Romu, B. Lauss, T. Lindner, R. Mammei, J. W. Martin, and E. Pierre, *The European Physical Journal A* **53**, 3 (2017).
- [84] B. Franke, *Investigations of the internal and external magnetic fields of the neutron electric dipole moment experiment at the Paul Scherrer Institute*, Ph.D. thesis, ETH Zurich (2013).

- [85] S. Afach, G. Bison, K. Bodek, F. Burri, Z. Chowdhuri, M. Daum, M. Fertl, B. Franke, Z. Grujic, V. Hélaine, *et al.*, Journal of Applied Physics **116**, 084510 (2014).
- [86] I. Altarev, E. Babcock, D. Beck, M. Burghoff, S. Chesnevskaya, T. Chupp, S. De-genkob, I. Fan, P. Fierlinger, A. Frei, *et al.*, Review of scientific instruments **85**, 075106 (2014).
- [87] I. Altarev, P. Fierlinger, T. Lins, M. Marino, B. Nießen, G. Petzoldt, M. Reisner, S. Stuiber, M. Sturm, J. T. Singh, *et al.*, Journal of Applied Physics **117**, 233903 (2015).
- [88] J. W. Martin, R. R. Mammei, W. Klassen, C. Cerasani, T. Andalib, C. P. Bidinosti, M. Lang, and D. Ostapchuk, Nuclear Instruments and Methods in Physics Research Section A: Accelerators, Spectrometers, Detectors and Associated Equipment **778**, 61 (2015).
- [89] T. Bryś, S. Czekaj, M. Daum, P. Fierlinger, D. George, R. Henneck, M. Kasprzak, K. Kirch, M. Kuźniak, G. Kuehne, *et al.*, Nuclear Instruments and Methods in Physics Research Section A: Accelerators, Spectrometers, Detectors and Associated Equipment **554**, 527 (2005).
- [90] W. C. Griffith, M. D. Swallows, T. H. Loftus, M. V. Romalis, B. R. Heckel, and E. N. Fortson, Phys. Rev. Lett. **102**, 101601 (2009).
- [91] E. M. Purcell and N. F. Ramsey, Phys. Rev. **78**, 807 (1950).
- [92] B. Graner, Y. Chen, E. Lindahl, and B. Heckel, arXiv preprint arXiv:1601.04339 (2016).
- [93] B. Lauss (Neutron Electric Dipole Moment Workshop, Harrison Hot Springs, BC, Canada, 2017).
- [94] S. Afach, C. A. Baker, G. Ban, G. Bison, K. Bodek, Z. Chowdhuri, M. Daum, M. Fertl, B. Franke, P. Geltenbort, K. Green, M. G. D. van der Grinten, Z. Grujic, P. G. Harris, W. Heil, V. Hélaine, R. Henneck, M. Horras, P. Iaydjiev, S. N. Ivanov, M. Kasprzak, Y. Kermaïdic, K. Kirch, P. Knowles, H.-C. Koch, S. Komposch, A. Kozela, J. Krempel, B. Lauss, T. Lefort, Y. Lemière, A. Mtchedlishvili, O. Naviliat-Cuncic, J. M. Pendlebury, F. M. Piegza, G. Pignol, P. N. Prashant, G. Quéméner, D. Rebreyend, D. Ries, S. Roccia, P. Schmidt-Wellenburg, N. Severijns, A. Weis, E. Wursten, G. Wyszynski, J. Zejma, J. Zenner, and G. Zsigmond, The European Physical Journal D **69**, 225 (2015).
- [95] S. Afach, N. J. Ayres, G. Ban, G. Bison, K. Bodek, Z. Chowdhuri, M. Daum, M. Fertl, B. Franke, W. C. Griffith, Z. D. Grujić, P. G. Harris, W. Heil, V. Hélaine, M. Kasprzak, Y. Kermaïdic, K. Kirch, P. Knowles, H.-C. Koch, S. Komposch, A. Kozela, J. Krempel, B. Lauss, T. Lefort, Y. Lemière, A. Mtchedlishvili, M. Musgrave, O. Naviliat-Cuncic, J. M. Pendlebury, F. M. Piegza, G. Pignol, C. Plonka-Spehr, P. N. Prashanth, G. Quéméner, M. Rawlik, D. Rebreyend, D. Ries, S. Roccia, D. Rozpedzik, P. Schmidt-Wellenburg, N. Severijns, J. A. Thorne, A. Weis, E. Wursten, G. Wyszynski, J. Zejma, J. Zenner, and G. Zsigmond, Phys. Rev. Lett. **115**, 162502 (2015).

- [96] H.-C. Koch, G. Bison, Z. D. Grujić, W. Heil, M. Kasprzak, P. Knowles, A. Kraft, A. Pazgalev, A. Schnabel, J. Voigt, and A. Weis, The European Physical Journal D **69**, 202 (2015).
- [97] J.-C. Peng, Modern Physics Letters A **23**, 1397 (2008).
- [98] S. K. Lamoreaux and R. Golub, Phys. Rev. A **71**, 032104 (2005).
- [99] S. Clayton (Neutron Electric Dipole Moment Workshop, Harrison Hot Springs, BC, Canada, 2017).
- [100] I. Altarev, D. Beck, S. Chesnevskaya, T. Chupp, W. Feldmeier, P. Fierlinger, A. Frei, E. Gutsmiedl, F. Kuchler, P. Link, T. Lins, M. Marino, J. McAndrew, S. Paul, G. Petzoldt, A. Pichlmaier, R. Stoepler, S. Stuiber, and B. Taubenheim, Nuovo Cimento della Societa Italiana di Fisica C **35**, 122 (2012).
- [101] A. P. Serebrov, E. A. Kolomenskiy, A. N. Pirozhkov, I. A. Krasnoshekova, A. V. Vasiliev, A. O. Polyushkin, M. S. Lasakov, A. N. Murashkin, V. A. Solovey, A. K. Fomin, I. V. Shoka, O. M. Zherebtsov, P. Geltenbort, S. N. Ivanov, O. Zimmer, E. B. Alexandrov, S. P. Dmitriev, and N. A. Dovator, Physics of Particles and Nuclei Letters **12**, 286 (2015).
- [102] I. Altarev, M. Bales, D. Beck, T. Chupp, K. Fierlinger, P. Fierlinger, F. Kuchler, T. Lins, M. Marino, B. Niessen, *et al.*, Journal of Applied Physics **117**, 183903 (2015).
- [103] A. Serebrov (Neutron Electric Dipole Moment Workshop, Ascona, Switzerland, 2014).
- [104] B. Patton, E. Zhivun, D. Hovde, and D. Budker, Physical review letters **113**, 013001 (2014).
- [105] J. Voigt, S. Knappe-Grüneberg, A. Schnabel, R. Körber, and M. Burghoff, Metrology and Measurement Systems **20**, 239 (2013).
- [106] F. Thiel, A. Schnabel, S. Knappe-Grüneberg, D. Stollfuß, and M. Burghoff, Review of scientific instruments **78**, 035106 (2007).
- [107] Z. Sun, M. Reisner, P. Fierlinger, A. Schnabel, S. Stuiber, and L. Li, Journal of Applied Physics **119**, 193902 (2016).
- [108] B. Franke, Ph.D. thesis, ETH Zürich (2013).
- [109] G. Couderchon and J. Tiers, Journal of Magnetism and Magnetic Materials **26**, 196 (1982).
- [110] Krupp VDM Magnifer 7904, *Material Data Sheet No. 9004*, Tech. Rep. (Krupp VDM, Aug. 2000).
- [111] K. Gupta, K. Raina, and S. Sinha, Journal of alloys and compounds **429**, 357 (2007).
- [112] R. Bozorth, “Ferromagnetism, american telephone and telegraph company, 1978,” (1993).

- [113] C. Bidinosti and J. Martin, AIP Advances **4**, 047135 (2014).
- [114] L. Urankar and R. Oppelt, IEEE transactions on biomedical engineering **43**, 697 (1996).
- [115] A. Knecht, *Towards a New Measurement of the Neutron Electric Dipole Moment*, Ph.D. thesis, Zurich (2009).
- [116] “Finite Element Method Magnetics FEMM, version 4.2, available from <http://www.femm.info.> ,” .
- [117] R. H. Lambert and C. Uphoff, Review of Scientific Instruments **46**, 337 (1975).
- [118] T. Sumner, Journal of Physics D: Applied Physics **20**, 692 (1987).
- [119] F. Pfeifer and C. Radloff, Journal of magnetism and magnetic materials **19**, 190 (1980).
- [120] “Bartington Instruments Ltd., 10 Thorney Leys Business Park, Witney, Oxon, OX28 4GG, England.” .
- [121] “Stanford Research Systems, 1290-D Reamwood Ave., Sunnyvale, CA 94089.” .
- [122] E. Paperno, IEEE transactions on magnetics **35**, 3940 (1999).
- [123] D. C. Jiles, Journal of Applied Physics **76**, 5849 (1994).
- [124] D. C. Jiles and D. L. Atherton, Journal of applied physics **55**, 2115 (1984).
- [125] D. C. Jiles and D. L. Atherton, Journal of magnetism and magnetic materials **61**, 48 (1986).
- [126] I. B. Khriplovich and S. K. Lamoreaux, *CP violation without strangeness* (Springer, 1997).
- [127] W. F. Brown Jr and J. H. Sweer, Review of Scientific Instruments **16**, 276 (1945).
- [128] H. A. Wheeler, Proceedings of the IRE **46**, 1595 (1958).
- [129] E. M. Purcell, American Journal of Physics **57**, 18 (1989), <https://doi.org/10.1119/1.15860> .
- [130] R. Beth, “Brookhaven National Laboratory Report,” (), BNL-10143 (1966).
- [131] R. Beth, (), US Patent 3466499, September 9, 1969.
- [132] C. Bidinosti, I. Kravchuk, and M. Hayden, Journal of Magnetic Resonance **177**, 31 (2005).
- [133] R. Turner and R. M. Bowley, Journal of Physics E: Scientific Instruments **19**, 876 (1986).
- [134] H.-T. S.S., Concepts in Magnetic Resonance Part A **36A**, 223, <https://onlinelibrary.wiley.com/doi/pdf/10.1002/cmr.a.20163> .

- [135] B. M. A., F. L. K., and C. Stuart, Concepts in Magnetic Resonance **14**, 9, <https://onlinelibrary.wiley.com/doi/pdf/10.1002/cmr.10000> .
- [136] L. K. Forbes and S. Crozier, Journal of Physics D: Applied Physics **36**, 68 (2003).
- [137] V. V. Kuzmin, C. P. Bidinosti, M. E. Hayden, and P.-J. Nacher, Journal of Magnetic Resonance **256**, 70 (2015).
- [138] N. Christopher, “Bachelor Thesis, An amalgamation of work on the ultra-cold neutron source and neutron electric dipole moment experiment at TRIUMF,” (2016).
- [139] M. Kawai, K. Kikuchi, H. Kurishita, J.-F. Li, and M. Furusaka, Journal of nuclear materials **296**, 312 (2001).
- [140] R. Matsumiya, *Study of He-II Spallation UCN Source*, Ph.D. thesis, Osaka University (2013).
- [141] S. Vanbergen, “UCN cryostat controls development and maintenance manual,” (2017).
- [142] S. Pomme, R. Fitzgerald, and J. Keightley, Metrologia **52**, S3 (2015).
- [143] W. Schreyer, T. Kikawa, M. J. Losekamm, S. Paul, and R. Picker, Nuclear Instruments and Methods in Physics Research Section A: Accelerators, Spectrometers, Detectors and Associated Equipment **858**, 123 (2017).
- [144] A. Steyerl, Zeitschrift für Physik A Hadrons and nuclei **254**, 169 (1972).
- [145] F. Atchison, B. Blau, A. Bollhalder, M. Daum, P. Fierlinger, P. Geltenbort, G. Hampe, M. Kasprzak, K. Kirch, S. Köchli, *et al.*, Nuclear Instruments and Methods in Physics Research Section A: Accelerators, Spectrometers, Detectors and Associated Equipment **608**, 144 (2009).
- [146] G. Ban, G. Bison, K. Bodek, Z. Chowdhuri, P. Geltenbort, W. C. Griffith, V. Hélaine, R. Henneck, M. Kasprzak, Y. Kermaidic, K. Kirch, S. Komposch, P. A. Koss, A. Kozela, J. Krempel, B. Lauss, T. Lefort, Y. Lemière, A. Mtchedlishvili, M. Musgrave, O. Naviliat-Cuncic, F. M. Piegsa, E. Pierre, G. Pignol, G. Quéméner, M. Rawlik, D. Ries, D. Rebreyend, S. Roccia, G. Rogel, P. Schmidt-Wellenburg, N. Severijns, E. Wursten, J. Zejma, and G. Zsigmond, The European Physical Journal A **52**, 326 (2016).
- [147] V. F. Sears, Neutron news **3**, 26 (1992).
- [148] M. Daum, B. Franke, P. Geltenbort, E. Gutzmiedl, S. Ivanov, J. Karch, M. Kasprzak, K. Kirch, A. Kraft, T. Lauer, B. Lauss, A. Müller, S. Paul, P. Schmidt-Wellenburg, T. Zechlau, and G. Zsigmond, Nuclear Instruments and Methods in Physics Research Section A: Accelerators, Spectrometers, Detectors and Associated Equipment **741**, 71 (2014).
- [149] S. Wlokka, P. Fierlinger, A. Frei, P. Geltenbort, S. Paul, T. Pöschl, F. Schmid, W. Schreyer, and D. Steffen, (2017), arXiv:1701.07431 [physics.ins-det] .

- [150] F. Atchison, M. Daum, R. Henneck, S. Heule, M. Horisberger, M. Kasprzak, K. Kirch, A. Knecht, M. Kužniak, B. Lauss, A. Mtchedlishvili, M. Meier, G. Petzoldt, C. Plonka-Spehr, R. Schelldorfer, U. Straumann, and G. Zsigmond, The European Physical Journal A **44**, 23 (2010).
- [151] J. J. Rush, D. W. Connor, and R. S. Carter, Nuclear Science and Engineering **25**, 383 (1966), <https://doi.org/10.13182/NSE66-A18558>.
- [152] P. Schmidt-Wellenburg, J. Bossy, E. Farhi, M. Fertl, K. K. H. Leung, A. Rahli, T. Soldner, and O. Zimmer, Phys. Rev. C **92**, 024004 (2015).
- [153] T. Andalib, M. Lang, L. Rebenitsch, “NMR Internal Notes,” .
- [154] N. F. Ramsey, Phys. Rev. **100**, 1191 (1955).
- [155] G. Pignol and S. Roccia, Phys. Rev. A **85**, 042105 (2012).
- [156] F. Rehm, “Bachelor Thesis, Heat conductivity in superfluid helium and ultracold neutron source cryogenics,” (2018).
- [157] S. W. Van Sciver, *Helium cryogenics* (Springer Science & Business Media, 2012).
- [158] V. Arp, R. McCarty, and F. Jeffrey, Inc, Data Program (2005).